I. Ultrasensitive Surface NMR Using Parahydrogen Spin Labeling

II. High-Resolution Optical NMR of Semiconductor Heterostructures Using Larmor Beat Detection

Thesis by
Paul Jonathan Carson

In Partial Fulfillment of the Requirements
for the Degree of
Doctor of Philosophy

California Institute of Technology
Pasadena, California

1997

(Submitted June 9, 1997)

I. Ultrasensitive Surface NMR Using Parahydrogen Spin Labeling

II. High-Resolution Optical NMR of Semiconductor Heterostructures Using Larmor Beat Detection

Thesis by Paul Jonathan Carson
Adviser: Daniel P. Weitekamp, Associate Professor of Chemical Physics
California Institute of Technology
Pasadena, California
1997

Abstract

This dissertation presents two techniques for ultrasensitive high-resolution nuclear magnetic resonance. The first exploits the spin order inherent in spin-symmetry enriched H_2 to achieve orders of magnitude improvement in the sensitivity of surface NMR over traditional techniques. The second uses a Larmor beat method to allow real-time optical detection of NMR transients in single epitaxial heterostructures and achieves orders of magnitude improvement in spectral resolution over previous steady-state techniques.

Molecular addition of para-enriched hydrogen to sites in which the protons are magnetically inequivalent results in large nonequilibrium spin population differences, detected as enhanced NMR signals in coupled spin systems. This PASADENA technique (parahydrogen and synthesis allow dramatically enhanced nuclear alignment) has previously been applied to liquids, with the potential for improvement in sensitivity of up to four orders of magnitude. The extension of the technique to the solid state is described here. Enhanced spectra of hydrogen chemisorbed on powdered ZnO are observed, revealing a reversible binding site. The spectra show a strong dipolar coupling which is not detected without PASADENA enhancement. This indicates the selectivity of the

method for molecular binding and its potential for structural and mechanistic studies. A random comparison of theoretical lineshapes with the data yields clustering of possible interproton distances around 1.8 Å, and 2.3-2.5 Å, although other distances are not rigorously excluded. The inverse technique, in which the branching fraction of ortho and para molecules desorbed after spin evolution reports on the surface NMR spectrum, is also discussed.

Next, the Larmor beat method for optical detection of NMR in III-V semiconductors is presented. The technique utilizes modulation of the circular polarization of luminescence, via a Hanle effect, at the difference in Larmor precession frequencies of two nuclear species. Order-of-magnitude improvements in both sensitivity and resolution over previous methods for studying single epitaxial structures are observed. High-resolution spectra of a GaAs heterojunction reveal weak quadrupole splittings that report on the electric field gradient at nuclear sites. The spectra also allow spin thermometry, indicating that optically pumped nuclear spin polarizations on the order of 10% are achieved with less than 5 seconds of optical nuclear polarization.

Acknowledgments

I would like to thank my advisor, Dan Weitekamp, for his endless scientific wisdom, for the opportunity to work in his laboratory, for his truly inspiring source of ideas, and for his patience. It has been a privilege to be exposed to the depth of his scientific insight.

I am also grateful for the scientific and personal interactions I have had with Weitekamp group members, both past and present. In particular: John Marohn, Len Mueller, Jack Hwang, Michael Miller, Jim Kempf, Russ Bowers, Steve Buratto, Herman Cho, and David Shykind. It has been, without a doubt, my good fortune to work with such bright and creative people. I would especially like to thank John and Len for always being ready to discuss quantum mechanics, NMR, mathematics, physics...the list goes on. They have inspired me and taught me in more ways than they know.

I would like to thank my father and mother, Vance and Gail, and my two brothers, Devin and Trevor, for their continuous love and support. This thesis is dedicated to them. I have truly been blessed to have such a wonderful family.

Finally, I would like to thank my home group. They are Harry, Frank, Nick, Mark, Tom, Ray, Carlos, David, Anne Marie, Susie, Joyce, Naomi, Karen, Jackie, Alicia, and Laura. I did not learn what true friendship is until I met these people—despite more than my fair share of examples in my life. I am forever grateful to them. These people have taught me what it means to enjoy life.

Table of Contents

Chapter I. The PASADENA Effect

1. Introduction

The use of parahydrogen as a high-sensitivity spin label for nuclear magnetic resonance (NMR) was first proposed [1] and then demonstrated [2-6] to be of value in studying species which are formed from the molecular addition of hydrogen. The phenomenon known as the PASADENA effect derives from the fact that deviation of the parahydrogen mole fraction in a sample of H_2 from its statistical high-temperature limit of 1/4 is associated with an inherent form of spin order. Upon molecular addition of the two protons from a single molecule into magnetically inequivalent environments, this order is manifested as large nonequilibrium spin population differences across allowed NMR transitions. Signal enhancements of up to four orders of magnitude are possible.

Since its prediction and initial demonstration, the PASADENA effect has been applied to several systems involving homogeneous catalysis. It has been used to detect hydrogenation intermediates,[7-10] as well as to study reaction mechanisms,[10-17] and kinetics.[18,19] The extension of the PASADENA method to the solid-state[20,21] is described here.

2. The Symmetrization Postulate

The source of enhanced spin order that gives rise to the PASADENA effect is the deviation of the ortho and para mole fractions of molecular hydrogen before reaction from their high-temperature values. The ability to enrich a sample of hydrogen in one of its two spin-symmetry forms with relative ease, for example by interconversion or separation, is an indirect result of the *symmetrization postulate* of quantum mechanics. The symmetrization postulate [22,23] states that the total wavefunction of any system of identical particles has definite symmetry with respect to permutations of particle indices. It postulates (with no known exceptions) that for a system of bosons (particles with integer spin) the overall wavefunction is symmetric with respect to exchange of particle labels between any two identical particles. Conversely, the wavefunction for a system of fermions (particles with half-integer spin) is antisymmetric with respect to exchange of particle labels between any two identical particles.

To apply the symmetrization postulate to the nuclei in a homonuclear diatomic molecule, the Born-Oppenheimer approximation is used to factor the wavefunction into separate electronic and nuclear parts. The nuclear wavefunction is then further factored into separate translational, vibrational, rotational, and spin wavefunctions:

$$\Phi_n = \psi_{trans}\,\psi_{vib}\,\psi_{rot}\,\psi_{spin} \qquad (1)$$

The symmetry of the individual wavefunctions comprising the total nuclear wavefunction must be examined separately. Since the translational and vibrational wavefunctions for a homonuclear diatomic are both symmetric with respect to nuclear exchange, the

symmetry of the overall wavefunction is governed by the product of the rotational and spin wavefunctions, whose individual symmetries are discussed in the next section.

3. Spin-Symmetry Restrictions on the States of Molecular Hydrogen

For any homonuclear diatomic with spin-1/2 nuclei, such as dihydrogen, the coupled nuclear spin system of the free molecule divides into two manifolds, a triplet manifold and a singlet manifold, characterized by their total spin quantum numbers. The triplet manifold, corresponding to a total spin quantum number of 1, is of greater statistical weight and is thus referred to as the ortho manifold. The singlet manifold is referred to as the para manifold. The spin states comprising the two manifolds can be expressed in the uncoupled basis (or "simple-product" basis) as

$$\begin{aligned} \text{ortho} & \begin{cases} |\psi_{1,1}\rangle = |\alpha\alpha\rangle \\ |\psi_{1,0}\rangle = 1/\sqrt{2}\left(|\alpha\beta\rangle + |\beta\alpha\rangle\right) \\ |\psi_{1,-1}\rangle = |\beta\beta\rangle \end{cases} \\ \text{para} & \; |\psi_{0,0}\rangle = 1/\sqrt{2}\left(|\alpha\beta\rangle - |\beta\alpha\rangle\right) \end{aligned} \tag{2}$$

As seen in this basis, the ortho spin states are symmetric with respect to nuclear exchange while the para state is antisymmetric.

The rotational wavefunction has the following dependence on the angular nuclear coordinates ϑ and φ:

$$\psi_{\text{rot}} \propto e^{im_j\varphi} P_j^{m_j}(\cos\vartheta) \tag{3}$$

with j and m_j the quantum numbers corresponding to the total rotational angular momentum and its projection onto the axis defined by $\vartheta = 0$, respectively. Exchange of

the two protons corresponds to reflection of their coordinates through the origin ($\vartheta \mapsto \pi - \vartheta$, and $\varphi \mapsto \varphi + \pi$). The sign of ψ_{rot} is preserved upon nuclear exchange for even j and is reversed upon exchange for odd j. The symmetrization postulate thus dictates that even rotational states are strictly correlated with ortho spin states and odd rotational states are strictly correlated with para spin states.

The energy of the j^{th} rotational state is given by

$$E_{\text{rot},j} = \hbar^2 \frac{j(j+1)}{2I} \tag{4}$$

where I is the moment of inertia of the H_2 molecule. From the expression for the rotational energies and the rotational partition function, the ratio of ortho to para hydrogen can be derived:

$$\frac{N_o}{N_p} = \frac{3\sum_{j=1,3,\ldots}(2j+1)e^{-j(j+1)\Theta_{\text{rot}}/T}}{\sum_{j=0,2,\ldots}(2j+1)e^{-j(j+1)\Theta_{\text{rot}}/T}} \tag{5}$$

where the characteristic rotational temperature is given by

$$\Theta_{\text{rot}} = \frac{\hbar^2}{2I k_B} \tag{6}$$

For H_2, $\Theta_{\text{rot}} = 85.4$ K, and for D_2, $\Theta_{\text{rot}} = 42.7$ K. The temperature dependence of the ortho and para mole fractions for H_2 and D_2 are shown in Fig. 1. For equilibration of H_2 gas at 300 K, $N_o/N_p \approx 3.0$. For equilibration of H_2 at 77 K (liquid nitrogen), $N_o/N_p \approx 1.0$.

One straightforward method of enriching [24,25] a sample of H_2 or D_2 gas in one of its spin-symmetry isomers is to bring it into contact with a solid paramagnetic catalyst at cryogenic temperatures. In the absence of such a catalyst, ortho-para transitions are forbidden. Rotational population equilibration without a catalyst occurs rapidly only

within each manifold (i.e., odd j states are in rapid thermal equilibrium only with other odd j states, and likewise for even j states). The catalyst breaks the magnetic symmetry of the molecule and allows rapid interconversion between the ortho and para manifolds. In the presence of a catalyst the ensemble is thus free to equilibrate its rotational distribution without symmetrization restrictions. At low temperatures, the result for H_2 is enrichment in the para form, since this form correlates with the lowest ($j = 0$) rotational state. The fact that this enrichment can be made large at easily achievable temperatures (e.g. 77 K) is a direct consequence of the relatively large rotational splitting indicated by Θ_{rot}. For D_2, the result is enrichment in the ortho form, for the same reason. Enrichment of D_2 is, however, more difficult because of the smaller Θ_{rot}. Since ortho-para interconversion is slow in the absence of a catalyst, a spin-symmetry enriched sample can be warmed to room temperature and stored for days without significant loss of enrichment. A sample prepared in this way can be used as a reagent for NMR enhancement via the PASADENA effect.

4. Nuclear Spin Density Operator for H_2

For most of the spin dynamics calculations performed in this thesis, a spin density operator approach is used. This approach provides a convenient way to describe an ensemble whose members are not all in the same quantum state. An equivalent statement is that the density operator allows for easy representation of ensembles for which the net (ensemble-averaged) coherence between two states that are populated has a magnitude less than the geometric mean of the two populations. Such a density operator necessarily

has more than one matrix element in its own eigenbasis. Such ensembles are called statistical mixtures of pure states and are not easily treated using state-vector notation. By itself, the density operator approach makes no distinction between cases where a particular coherence between two states is not represented among individual members of the ensemble and where it is represented (possibly in spectroscopically distinct subpopulations), but because of its distribution of phases, it averages to zero across the ensemble.

The density operators for the separate spin eigenstates of molecular hydrogen have the form

$$\rho_{\psi_{I,m}} = \left|\psi_{I,m}\right\rangle\left\langle\psi_{I,m}\right| \tag{7}$$

It will be convenient to expand these and other density operators encountered into linear combinations of other, more easily manipulated, basis operators. Common operator bases use operators formed by products and/or sums of individual spin angular momentum operators. The density operators for the pure eigenstates of H_2 can be expanded in an operator basis whose members are diagonal when expressed in the singlet-triplet basis:

$$\begin{aligned}
\rho_{\psi_{1,\pm1}} &= \frac{1}{4}\mathbb{1} + \frac{1}{2}(I_{1z} + I_{2z}) + \frac{1}{3}(3I_{1z}I_{2z} - \mathbf{I}_1\cdot\mathbf{I}_2) + \frac{1}{3}\mathbf{I}_1\cdot\mathbf{I}_2 \\
\rho_{\psi_{1,0}} &= \frac{1}{4}\mathbb{1} - \frac{2}{3}(3I_{1z}I_{2z} - \mathbf{I}_1\cdot\mathbf{I}_2) + \frac{1}{3}\mathbf{I}_1\cdot\mathbf{I}_2 \\
\rho_{\psi_{0,0}} &= \frac{1}{4}\mathbb{1} - \mathbf{I}_1\cdot\mathbf{I}_2
\end{aligned} \tag{8}$$

For simplicity in forming the density operator for a mixture of ortho and para hydrogen, the ortho fraction is assumed to be unpolarized. In reality, the ortho manifold will become slightly polarized in a strong magnetic field by the same relaxation mechanisms as in any other ordinary spin system. Signal from the *gas-phase* ortho

fraction polarized in this way is clearly seen in surface-PASADENA spectra shown in Chapter III. However, sensitivity to these spins in the same spectrum as the parahydrogen enhanced signal is possible only because the gas-phase H_2 is orders of magnitude more abundant than the sites detected with the PASADENA effect. Only the two proton system *after* reaction with the surface is of interest here. The "Curie-law polarization" of the ortho fraction before reaction is ignored in the density operator treatment since it is several orders of magnitude smaller than the spin ordering that gives rise to the PASADENA effect.

The density operator for an arbitrary mixture of ortho and para hydrogen is formed by taking the weighted sum of the density operators in Eq. (8). If x_o is the ortho mole fraction and x_p is the para mole fraction, then an unpolarized mixture has the form

$$\begin{aligned}\rho &= \frac{x_o}{3}\left(\rho_{\psi_{1,1}} + \rho_{\psi_{1,0}} + \rho_{\psi_{1,-1}}\right) + x_p \rho_{\psi_{0,0}} \\ &= \frac{1}{4}1 - \left(x_p - \frac{1}{3}x_o\right)\mathbf{I}_1 \cdot \mathbf{I}_2\end{aligned} \tag{9}$$

This is taken as the starting density operator, $\rho(0)$, *before* reaction of the H_2 with a substrate, for all of the PASADENA experiments discussed in this thesis. Defining

$$f = x_p - \frac{1}{3}x_o = \frac{1}{3}\left(4x_p - 1\right) \tag{10}$$

allows the density operator to be written

$$\rho(0) = \frac{1}{4}1 - f\,\mathbf{I}_1 \cdot \mathbf{I}_2 . \tag{11}$$

Expressed as a matrix in the singlet-triplet basis the density operator is

$$\rho(0) \mapsto \begin{array}{c} \\ \langle\psi_{1,1}| \\ \langle\psi_{1,0}| \\ \langle\psi_{1,-1}| \\ \langle\psi_{0,0}| \end{array} \begin{array}{c} \begin{array}{cccc} |\psi_{1,1}\rangle & |\psi_{1,0}\rangle & |\psi_{1,-1}\rangle & |\psi_{0,0}\rangle \end{array} \\ \begin{pmatrix} \frac{1-f}{4} & 0 & 0 & 0 \\ 0 & \frac{1-f}{4} & 0 & 0 \\ 0 & 0 & \frac{1-f}{4} & 0 \\ 0 & 0 & 0 & \frac{3f+1}{4} \end{pmatrix} \end{array} \tag{12}$$

For pure parahydrogen $f = 1$, and for pure orthohydrogen $f = -1/3$. In a statistical mixture of ortho and parahydrogen at room temperature, $f \approx 0$. In a statistical mixture at 77 K, as used in these experiments, $f \approx 0.33$. The spin order that leads to large enhancements in the PASADENA effect, as well as to the characteristic phase pattern in the PASADENA spectrum, is the scalar order seen in Eq. (11) when f deviates from 0.

5. The Hamiltonian for the Two-Spin System after Chemical Reaction

The spin dynamics which describe the PASADENA effect start with the density operator $\rho(0)$ in Eq. (11). The effect is initiated by the interaction of a spin-symmetry enriched H_2 sample ($f \neq 0$) with a substrate system, usually involving breaking of the H_2 bond. The substrate can be, for example, a molecule in solution, whether it is a catalyst molecule, a catalytic intermediate, or a final product species. It can also be a reactive solid surface, which is the subject of the following three chapters, or a heteromolecule adsorbed to a surface, or a gas phase molecule just released from a surface after reaction with H_2. The primary requirement of the product system is that the two protons that originated from a single H_2 molecule end up magnetically inequivalent to each other. Magnetic inequivalence can be conferred either by a difference in chemical environments (leading to a difference in chemical shifts in the NMR spectrum) or by different spin-spin

couplings to a possible third spin in the product system, regardless of whether the ι spin has a symmetry partner with respect to the two added protons. Another requirement of the product system is that the two added protons remain magnetically coupled to *each other* throughout the PASADENA measurement process.

For the purpose of describing the essential spin dynamics leading to the PASADENA effect, only the two-proton system formed by addition of H_2 to a substrate will be considered. In certain situations, couplings to other spins in the product system or transfer of the spin order to surrounding spins may be of chemical interest. Each such unique product spin system and/or experimental strategy must be addressed with separate spin dynamics calculations, all starting with the same form for the precursor H_2 spin order. The essential PASADENA spin physics is illustrated, however, by a two-proton product system that is isolated magnetically from surrounding spins.

The truncated, rotating-frame spin Hamiltonian [26] for an isolated two-spin system in a strong magnetic field aligned with the *z*-axis is

$$\mathcal{H} = \omega_{1z} I_{1z} + \omega_{2z} I_{2z} + D\left(3I_{1z}I_{2z} - \mathbf{I}_1 \cdot \mathbf{I}_2\right) + J\mathbf{I}_1 \cdot \mathbf{I}_2 \qquad (13)$$

where the units are radians/second and the parameters are defined below. This will occasionally be referred to as the *internal* Hamiltonian, since it contains only interactions that are due to the immediate environment of the two spins. The first and second terms represent the chemically-shifted Zeeman interaction between the protons and the applied magnetic field. The third term represents the direct (through space) dipolar coupling between the two spins. The dipolar coupling parameter is given by

$$D = \frac{1}{2}\omega_D\left(1 - 3\cos^2\theta\right) \qquad (14)$$

where

$$\omega_D = \frac{\gamma_n^2 \hbar}{r^3} \tag{15}$$

The parameter γ_n is the gyromagnetic ratio of the two spins, and r is the internuclear distance. The angle θ subtends the internuclear vector and applied magnetic field vector. The fourth term in the Hamiltonian represents the indirect scalar coupling between the spins mediated by surrounding bonding electrons. In general in solids, as discussed in Chapter II, this interaction is usually negligible relative to the dipolar interaction.

In calculating the eigenvectors and eigenvalues of the Hamiltonian $\mathcal{H}$, parameters for the average chemical shift of the two spins and the chemical shift difference are defined:

$$\begin{aligned} \overline{\omega} &= \frac{1}{2}(\omega_{1z} + \omega_{2z}) \\ \Delta &= \omega_{1z} - \omega_{2z} \end{aligned} \tag{16}$$

Also defined is a parameter κ which helps to summarize the dependence of the spin dynamics on the quantities Δ and $(D - J)$:

$$\kappa = \mathrm{Arg}[\Delta + i(J - D)] \tag{17}$$

Diagonalization of the Hamiltonian $\mathcal{H}$ yields the following eigenstates expanded in the uncoupled basis.

$$\begin{aligned} |1\rangle &= |\alpha\alpha\rangle \\ |2\rangle &= \cos\frac{\kappa}{2}|\alpha\beta\rangle + \sin\frac{\kappa}{2}|\beta\alpha\rangle \\ |3\rangle &= -\sin\frac{\kappa}{2}|\alpha\beta\rangle + \cos\frac{\kappa}{2}|\beta\alpha\rangle \\ |4\rangle &= |\beta\beta\rangle \end{aligned} \tag{18}$$

The corresponding eigenvalues are

$$\begin{aligned} E_1 &= \overline{\omega} + \frac{D}{2} + \frac{J}{4} \\ E_2 &= -\frac{D}{2} - \frac{J}{4} + \frac{1}{2}\sqrt{(J-D)^2 + \Delta^2} \\ E_3 &= -\frac{D}{2} - \frac{J}{4} - \frac{1}{2}\sqrt{(J-D)^2 + \Delta^2} \\ E_4 &= -\overline{\omega} + \frac{D}{2} + \frac{J}{4} \end{aligned} \tag{19}$$

The sign of Δ can be thought of as serving to label the two spins. Since none of the spin physics can depend on which spin is given which label in the isolated proton pair, it follows that no calculation starting from a symmetric spin-symmetry enriched precursor will ultimately depend on the sign of Δ, despite the explicit dependence of κ on the sign of Δ. This can be seen as follows. First, the effect of a swap in spin labels on the energy eigenstates can be seen with a very small amount of amount of algebra to be at most a change in the overall phase factor of one of the two states with nonzero singlet character. Second, there is no effect on the energy eigenvalues. There is thus no overall effect of a change in the sign of Δ. There is however, an explicit dependence of the PASADENA signal on the signs of J and D. Care must be taken when computing the value of κ from the arctangent function to use the correct branch of the function.

6. The Sudden Approximation

When a hydrogen molecule reacts with a substrate system, the Hamiltonian for the two protons changes. If the change occurs rapidly on the time scale of the evolution of the spin system, the *sudden approximation* of quantum mechanics applies. Under the sudden

approximation [23], the density operator is not changed by the sudden change in the Hamiltonian. The eigenstates of the new Hamiltonian which become populated by the rapid change are not necessarily those that connect by continuity with the eigenstates populated under the previous Hamiltonian. They are, rather, those which have nonvanishing *projection* onto the formerly populated eigenstates. The correlation between populations of the initial eigenstates of H_2 and the final product eigenstates is shown in Fig. 2 for the case of a pure parahydrogen precursor. The diagram shows that large nonequilibrium population differences across dipole-allowed transitions can result from the sudden change in Hamiltonian. The sudden approximation is assumed valid for the present case since the spin Hamiltonian changes on the time scale of the chemical reaction (picoseconds) while spin evolution takes place on the time scale of milliseconds. The spin system that is formed by reaction is subject to the same spin-lattice relaxation mechanisms as any ordinary spin system that has the same substrate and surrounding medium, if any. As a result, the enhanced population differences in the PASADENA effect must be used for NMR before a period roughly on the order of T_1, a requirement which is easily met in most systems.

For an isolated spin system, magnetic equivalence corresponds to the condition $\left|(J-D)/\Delta\right| \gg 1$, in which case $|\kappa| \approx \pi/2$. If this condition is met for the two protons after reaction with the substrate, the singlet-triplet basis remains the eigenbasis of the new Hamiltonian, and the states that were populated before reaction remain populated after reaction. If the precursor is enriched in one of the two unpolarized spin-symmetry isomers, the high degree of spin order that this represents remains present after reaction. However, this spin order is inaccessible to any NMR experiment because, just as in the

precursor, it does not consist of population differences across dipole-allowed transitions. It can neither be converted into such population differences by rf irradiation, nor can it evolve into such differences under unitary evolution.

In the case of hydrogenation reactions in the liquid state, rapid reorientation of the product species averages the dipolar coupling interaction to its isotropic value of zero. It is further often the case that $J \ll \Delta$, a situation referred to as the weak-coupling limit. If the weak-coupling limit applies, $\kappa \approx 0$ and the eigenstates of the product Hamiltonian are approximated by the uncoupled basis states $|\alpha\alpha\rangle$, $|\alpha\beta\rangle$, $|\beta\alpha\rangle$, and $|\beta\beta\rangle$. Also in this case, the populations become equal between any two states related by inversion of both spins together (i.e., the density operator in the new eigenbasis is symmetric about the antidiagonal). Such a limiting case simplifies the calculation of the spin dynamics for NMR experiments. In the calculations below, however, no assumptions are made about κ so that the results are general to both solid-state and liquid state PASADENA experiments.

Whenever the precursor and product Hamiltonians do not share eigenstates (which is the only case of interest in connection with the PASADENA effect), coherences between at least some of the populated eigenstates of the product Hamiltonian are formed automatically under the sudden approximation. These coherences do not represent new spin order beyond what was present before the reaction. They are the result of re-expressing the unchanged density operator in the new eigenbasis, in which it is no longer diagonal.

Since the density operator is not changed under the sudden approximation, the density operator after reaction of a spin-symmetry enriched H_2 sample with a substrate

remains $\rho(0)$ as given in Eq. (11). In the basis of the product Hamiltonian given in Eq. (13), this density operator can be represented as follows.

$$\rho(0) \mapsto \begin{array}{c} \\ \langle 1| \\ \langle 2| \\ \langle 3| \\ \langle 4| \end{array} \begin{array}{c} \begin{array}{cccc} |1\rangle & |2\rangle & |3\rangle & |4\rangle \end{array} \\ \begin{pmatrix} \frac{1-f}{4} & 0 & 0 & 0 \\ 0 & \frac{1+f}{4} - \frac{f}{2}\sin\kappa & -\frac{f}{2}\cos\kappa & 0 \\ 0 & -\frac{f}{2}\cos\kappa & \frac{1+f}{4} + \frac{f}{2}\sin\kappa & 0 \\ 0 & 0 & 0 & \frac{1-f}{4} \end{pmatrix} \end{array} \tag{20}$$

7. The Time-Averaged Initial Density Operator

Zero-quantum coherence can be seen in the matrix representation of $\rho(0)$ in Eq. (20), which follows the reaction of H_2 with a substrate. The phase of this coherence will immediately begin to evolve under the product Hamiltonian. This evolution and its consequences for the density operator of an ensemble with a spread of reaction times will be discussed in this section.

The equation of motion for the density operator is the usual Liouville-von Neumann equation [26]:

$$\frac{d\rho(t)}{dt} = -i\left[\mathcal{H}, \rho(t)\right] \tag{21}$$

The solution to this equation has the form

$$\rho(t) = U(t)\rho(0)U^{\dagger}(t) \tag{22}$$

For a time-independent Hamiltonian, the unitary evolution operator in Eq. (22) is

$$U(t) = e^{-i\mathcal{H}t} \tag{23}$$

It is seen from Eqs. (22) and (23) that in the eigenbasis of the Hamiltonian, the time dependence of a matrix element of ρ is given by

$$\rho_{ij}(t) = \rho_{ij}(0)\, e^{-i\omega_{ij}t} \tag{24}$$

where

$$\omega_{ij} = \frac{E_i - E_j}{\hbar} \tag{25}$$

This summarizes the general result of quantum mechanical systems under unitary evolution that populations (diagonal elements of the density matrix in the eigenbasis) do not evolve and coherences between states (off-diagonal elements) evolve at a frequency proportional to the difference in energy between the states in question.

Applying this to the density operator in Eq. (20) for the two-proton system after reaction, the populations formed immediately after reaction are stationary (neglecting spin-lattice relaxation) . The zero-quantum coherence that is initiated evolves at the frequency

$$\omega_{23} = \frac{E_2 - E_3}{\hbar} = \sqrt{(J-D)^2 + \Delta^2} \tag{26}$$

In the experiments described in this thesis, the distribution of reaction times within the ensemble is spread out over many periods of the zero-quantum evolution. To see the effect of this on the resulting ensemble density operator, it is convenient to view the density operator as an average of the density operators for the individual molecules in the ensemble. The single-molecule density operators are labeled with an index k. Let t_k be the time at which the k^{th} molecule undergoes reaction, and let t_0 be some *later* time after the entire ensemble has undergone reaction and before the NMR experiment begins. At

time t_0, the zero-quantum matrix element of the density operator for the k^{th} molecule is found from Eqs. (20) and (24) to be

$$\rho_{23}^{k}(t_0) = -\frac{f\cos\kappa}{2} e^{-i\omega_{23}(t_0 - t_k)} \tag{27}$$

with its Hermitian mate given by $\rho_{32}^{k}(t_0) = \left[\rho_{23}^{k}(t_0)\right]^*$. The diagonal matrix elements of the density operators ρ^k do not depend on t_k and are those given by Eq. (20).

The ensemble-averaged density operator at t_0 for N total molecules is

$$\rho(t_0) = \frac{1}{N}\sum_{k=1}^{N} \rho^{k}(t_0) \tag{28}$$

If the reaction times t_k for large N are distributed randomly over a period several times longer than $2\pi/\omega_{23}$ then the zero-quantum coherence is averaged to zero in the ensemble average:

$$\rho_{23}(t_0) = -\frac{f\cos\kappa}{2}\frac{1}{N}\sum_{k=1}^{N} e^{-i\omega_{23}(t_0 - t_k)} = 0 \tag{29}$$

The ensemble-averaged density operator after reaction is thus diagonal in the eigenbasis of the Hamiltonian:

$$\begin{aligned} \rho(t_0) &= \sum_i \langle i|\rho(0)|i\rangle |i\rangle\langle i| \\ &= \sum_i \langle i|\tfrac{1}{4} - f\,\mathbf{I}_1\cdot\mathbf{I}_2|i\rangle |i\rangle\langle i| \end{aligned} \tag{30}$$

Choosing an appropriate orthogonal operator basis, $\rho(t_0)$ can be expanded as follows:

$$\rho(t_0) = \frac{1}{4}1 - f\left[\frac{1}{2}\sin\kappa\cos\kappa(I_{1z} - I_{2z})\right.$$
$$+\frac{1}{3}\cos^2\kappa(3I_{1z}I_{2z} - \mathbf{I}_1\cdot\mathbf{I}_2) \qquad (31)$$
$$\left.+\left(1-\frac{2}{3}\cos^2\kappa\right)\mathbf{I}_1\cdot\mathbf{I}_2\right]$$

This is the density operator that describes the state of the two-proton ensemble described above after reaction and before the subsequent NMR experiment. It will henceforth be referred to as the *initial condition* for the PASADENA experiment. The first term in Eq. (31) is proportional to the identity operator and is of no direct interest since it exhibits no dynamics. The second term represents the amount of "difference magnetization" in the initial condition. The third and fourth terms represent dipolar order and scalar order, respectively.

The coefficients weighting the terms in the initial condition depend on the parameter κ, which in turn depends on the chemical shifts and spin-spin couplings between the two protons. This highly-sensitive dependence of the initial condition on the parameters of the internal NMR Hamiltonian is one of the unique features of the PASADENA effect. It is not found, for example, in conventional NMR.

In the weak-coupling limit ($\kappa \approx 0$), the initial condition well approximated by

$$\rho_{\kappa=0}(t_0) = \frac{1}{4}1 - f I_{1z}I_{2z} \qquad (32)$$

indicating that only J order is present after reaction of the ensemble. While this is often the situation in liquids, as mentioned in Sec. 6, it is not, in general, the case for a solid-state product such as the surface-bound proton system discussed in Chapters II-IV.

8. The PASADENA Signal

The simplest PASADENA experiment requires a single resonant radio-frequency pulse following a reaction that leads to the initial condition in Eq. (31). Transverse magnetization can then be measured using a high-Q NMR probe as in conventional NMR. The Fourier transform of the free-induction decay gives the PASADENA spectrum, with typically orders of magnitude enhancement in spectral intensities over ordinary NMR, as will be shown in the next section.

An rf pulse of duration τ_p and rotating-frame amplitude $\omega_1 = \gamma_n B_1$ (in rad/s), rotates magnetization transverse to the pulse in the rotating frame by an angle $\Theta = \omega_1 \tau_p$. For most purposes, it is sufficient to assume that the pulse is strong enough (and hence brief enough) that no appreciable evolution due to the internal Hamiltonian takes place during the pulse. This simplifies calculations in that the action of the pulse can be represented by a simple angular momentum rotation operator.

Following a single pulse, only the difference magnetization and the dipolar order in the initial condition are converted into single-quantum coherence. These single-quantum terms are the only terms which can evolve into observable magnetization during free evolution under the Hamiltonian $\mathcal{H}$. After a pulse of flip angle Θ along the y direction in the rotating frame, the observable part of the density operator becomes

$$\rho_{SQ}(0) = f\left[\frac{1}{2}\sin\kappa\cos\kappa\sin\Theta(I_{2x} - I_{1x}) - \cos^2\kappa\sin\Theta\cos\Theta(I_{1z}I_{2x} + I_{1x}I_{2z})\right] \tag{33}$$

where the subscript SQ indicates that only terms with single-quantum coherence have been retained. Time zero is now taken to be immediately following the pulse.

The signal measured in the NMR experiment is proportional to

$$S(t) = \langle I_+(t) \rangle = \mathrm{Tr}\{I_+ \rho(t)\} \tag{34}$$

where ρ in this case corresponds to ρ_{SQ}. The time dependence of ρ_{SQ} is computed using Eqs. (22) and (23):

$$\rho_{SQ}(t) = e^{-i\mathcal{H}t} \rho_{SQ}(0)\, e^{i\mathcal{H}t} \tag{35}$$

Using this and the trace relation of Eq. (34), the PASADENA signal is found:

$$\begin{aligned} S(t) = \frac{1}{4} f \cos^2\kappa \sin\Theta \{ & [-1+(1-\cos\Theta)(1+\sin\kappa)] e^{i\omega_{12}t} + \\ & [-1+(1-\cos\Theta)(1-\sin\kappa)] e^{i\omega_{13}t} + \\ & [\ 1-(1-\cos\Theta)(1+\sin\kappa)] e^{i\omega_{24}t} + \\ & [\ 1-(1-\cos\Theta)(1-\sin\kappa)] e^{i\omega_{34}t} \} \end{aligned} \tag{36}$$

The transition frequencies are

$$\begin{aligned} \omega_{12} &= \overline{\omega} + D + \frac{J}{2} - \frac{1}{2}\sqrt{(J-D)^2 + \Delta^2} \\ \omega_{13} &= \overline{\omega} + D + \frac{J}{2} + \frac{1}{2}\sqrt{(J-D)^2 + \Delta^2} \\ \omega_{24} &= \overline{\omega} - D - \frac{J}{2} + \frac{1}{2}\sqrt{(J-D)^2 + \Delta^2} \\ \omega_{34} &= \overline{\omega} - D - \frac{J}{2} - \frac{1}{2}\sqrt{(J-D)^2 + \Delta^2} \end{aligned} \tag{37}$$

The transition frequencies are plotted in Fig. 3 as functions of J and D separately for fixed Δ.

A few characteristics of the PASADENA signal can be examined using the expression in Eq. (36). Two lines are always absorptive and two are always emissive. The identity of the absorptive and emissive lines depends on the values of κ and Θ. For all values of κ and Θ, however, $S(0) = 0$. The result is that the net integrated area of the

spectrum is always zero. In liquids in the weak-coupling limit ($\kappa \approx 0$), the $\sin\kappa$ terms disappear and the spectrum consists of two antiphase doublets chemically shifted from each other by Δ with a splitting for each doublet of J. This situation corresponds to Fig. 2(a) for small J. The maximum signal in this case is obtained with a pulse flip angle of either $\pi/4$ or $3\pi/4$.

Fig. 4 shows the transition amplitude for one of the four transitions as a function of κ and Θ. The functional form of the other three transition amplitudes can be obtained by appropriate symmetry operations. Antisymmetry about $\Theta = \pi/2$ occurs only for $\kappa = 0$ and $|\kappa| = \pi/2$; i.e., it occurs only when there is *not* a mixture of the different types of spin order in the initial condition that lead to single-quantum coherence. The pulse flip angle which maximizes the signal now depends on κ.

Fig. 5 shows the signal energy of the PASADENA spectrum, in arbitrary units, as a function of κ and Θ. The signal energy is defined as the sum of the squared amplitudes of the four transitions. Implicit in this calculation of the signal energy is the assumption that none of the lines overlap to cancel each other out (due to antiphase intensities). The figure shows that for $\kappa = 0$, the largest signal energy is realized for a pulse flip angle Θ of either $\pi/4$ or $3\pi/4$. For all other values of κ, the largest signal energy is realized for a pulse angle in the near vicinity of $3\pi/4$ only. For comparison, the integrated magnitude spectrum is shown in Fig. 6. The integrated magnitude is defined as the sum of the absolute values of the four transition amplitudes, again assuming that none of the lines overlap.

9. PASADENA Enhancement over Ordinary NMR

The enhancement in spectral intensity that stems from the use of spin-symmetry enriched H_2 as a precursor can be quantified by comparing the signal strength in the PASADENA experiment to the signal strength in an ordinary NMR experiment. A convenient point of reference is the signal that arises from an initial condition of thermal equilibrium in a high-field magnet. Since a ratio will be taken to compute the enhancement factor, no instrument-dependent sensitivity factors will affect the calculation.

Recall that the PASADENA effect arises from a novel choice for the *initial condition* and does not depend on manipulation of the *Hamiltonian* after reaction. The Hamiltonian governing the spins for the ordinary NMR experiment is, therefore, just that of Eq. (13). However, to compute the equilibrium density operator it is necessary to use the full lab-frame Hamiltonian, of which $\mathcal{H}$ in Eq. (13) is the rotating-frame counterpart. For a spin system in a strong magnetic field, the lab-frame Zeeman interaction so dominates the Hamiltonian that the parameters of the internal Hamiltonian $\mathcal{H}$ are inconsequential in computing the equilibrium density operator. The lab-frame Hamiltonian for the purposes of this calculation can thus be written

$$\mathcal{H}_{\text{Lab}} = -\hbar\omega_0(I_{1z} + I_{2z}) \tag{38}$$

where $\omega_0 = \gamma_n B_0$ is the Larmor frequency in a field of strength B_0. Note that this Hamiltonian is written in units of energy and not radians/second.

The equilibrium density operator is given by

$$\rho_{eq} = \frac{\exp\left(-\frac{\mathcal{H}_{Lab}}{k_B T}\right)}{\mathrm{Tr}\left\{\exp\left(-\frac{\mathcal{H}_{Lab}}{k_B T}\right)\right\}} \tag{39}$$

where k_B is the Boltzmann constant and T is the temperature in kelvins. Combining Eqs. (38) and (39) gives

$$\rho_{eq} = \frac{1}{4}1 + \frac{\zeta}{2}(I_{1z} + I_{2z}) + \frac{\zeta^2}{2} I_{1z} I_{2z} \tag{40}$$

where

$$\zeta = \tanh\left(\frac{\hbar\omega_0}{2k_B T}\right) \tag{41}$$

Note that the parameter ζ in this case is just the equilibrium polarization defined by

$$P_{eq} \equiv \frac{\langle I_z \rangle}{N_s I} = \zeta \tag{42}$$

where N_s is the number of spins, in this case 2. The equilibrium density operator is seen to contain, in general, both Zeeman and J order. The amount of J order, however, is significant only at extremely low temperatures (~ 10 mK).

The operator ρ_{eq} has the same matrix representation in both the eigenbasis of $\mathcal{H}$ and the uncoupled basis:

$$\rho_{eq} \mapsto \begin{pmatrix} \frac{1}{4}(1+\zeta)^2 & 0 & 0 & 0 \\ 0 & \frac{1}{4}(1-\zeta^2) & 0 & 0 \\ 0 & 0 & \frac{1}{4}(1-\zeta^2) & 0 \\ 0 & 0 & 0 & \frac{1}{4}(1-\zeta)^2 \end{pmatrix} \tag{43}$$

At $T = 0$ K, $\zeta = 1$ for a magnetic field oriented along the positive z axis. The matrix representation shows that in this case only the $|\alpha\alpha\rangle$ state is occupied.

In the high-temperature limit $(T >> \hbar\omega_0/2k_B)$, the parameter ζ can be approximated by

$$\zeta \to \frac{\hbar\omega_0}{2k_B T} \tag{44}$$

The density operator in this limit is

$$\rho_{\text{eq, high-T}} \approx \frac{1}{4}1 + \frac{\hbar\omega_0}{4k_B T}(I_{1z} + I_{2z}) \tag{45}$$

which shows that only Zeeman order is present at high temperatures. This density operator corresponds to Curie-law magnetization.

As in the PASADENA experiment, the simplest ordinary NMR experiment consists of a single resonant rf pulse followed by detection of precessing magnetization. The signal measured is computed from the expectation value in Eq. (34). For a pulse of flip angle Θ, the signal is proportional to

$$\begin{aligned} S_{\text{equilib.}}(t) = \frac{1}{4}\zeta \sin\Theta \big[& (1+\zeta\cos\Theta)(1+\sin\kappa)e^{i\omega_{12}t} + \\ & (1+\zeta\cos\Theta)(1-\sin\kappa)e^{i\omega_{13}t} + \\ & (1-\zeta\cos\Theta)(1+\sin\kappa)e^{i\omega_{24}t} + \\ & (1-\zeta\cos\Theta)(1-\sin\kappa)e^{i\omega_{34}t} \big] \end{aligned} \tag{46}$$

A few observations can be made about the difference between this signal and the PASADENA signal. The parameter f in the PASADENA experiment and the parameter ζ in the equilibrium-polarization experiment are analogous to each other. They both give a measure of the degree of spin order present. In both cases this parameter appears as a

prefactor scaling the overall signal strength. The reason the *relative* intensities within the ordinary NMR signal also depend on this parameter is because the relative contributions of different types of spin order in the equilibrium density operator depend on this parameter. In the PASADENA experiment, the relative contributions of different types of spin order do not depend on f. This is a result of the fact that the ortho and para states span the entire Hilbert space of the two-spin system. As a result, a statistical mixture (3:1) of unpolarized ortho and para density operators gives the identity operator for the initial condition, which leads to zero net signal. Since the computation of the signal constitutes a linear operation this proves that the ortho and para signals must have the same functional form but be of opposite intensity (and in the ratio 1:3). It follows from this that the parameter f, which tabulates the ratio of ortho to para, can only affect the overall intensity of the signal and cannot affect relative intensities within the spectrum.

The maximum signal energy in the ordinary NMR experiment is realized for a pulse angle of $\pi/2$, independent of κ. The signal for $\Theta = \pi/2$ is

$$S_{\text{equilib.}}(t) = \frac{1}{4}\zeta\Big[(1+\sin\kappa)\left(e^{i\omega_{12}t}+e^{i\omega_{24}t}\right)+ (1-\sin\kappa)\left(e^{i\omega_{13}t}+e^{i\omega_{34}t}\right)\Big] \tag{47}$$

The enhancement in signal amplitude for equilibration at 0 K versus 300 K in a 4.7 T magnetic field is

$$\frac{\left|S_{\text{equilib.}}(0\,\text{K})\right|}{\left|S_{\text{equilib.}}(300\,\text{K})\right|} = \frac{\zeta_{0\text{K}}}{\zeta_{300\text{K}}} = 6.2\times10^{4} \tag{48}$$

For comparison of the PASADENA signal strength with the ordinary NMR signal strength, a judicious choice of transition amplitudes must be made. From the ordinary

NMR spectrum it is meaningful to select not the corresponding transition amplitude but the *largest* transition amplitude, since comparison with an increasingly forbidden transition (as $|\kappa| \rightarrow \pi/2$) is of little value. This selection is accomplished by replacing $\pm\sin\kappa$ with $+|\sin\kappa|$ in either one of the transition amplitudes in Eq. (47).

The PASADENA enhancement factor for the $|1\rangle \rightarrow |2\rangle$ and $|2\rangle \rightarrow |4\rangle$ transitions as a function of κ and Θ over the largest ordinary NMR transition at $\Theta = \pi/2$ is given by the ratio

$$\left|\frac{S_{\text{PASADENA}}}{S_{\text{equilib.}}}\right| = \left|\frac{f\cos^2\kappa\sin\Theta\left[1-(1-\cos\Theta)(1+\sin\kappa)\right]}{\zeta\left(1+|\sin\kappa|\right)}\right| \tag{49}$$

This ratio is plotted in Fig. 7 for the case of enhancement over ordinary NMR at $T = 300$ K. Notice that the absolute value of the $\sin\kappa$ term in the denominator of Eq. (49) leads to a discontinuous first derivative with respect to κ at $\kappa = 0$.

The maximum enhancement is found to occur for $\kappa \approx 0.3$ and $\Theta \approx 2.3$. In this case the enhancement is

$$\left|\frac{S_{\text{PASADENA}}}{S_{\text{equilib.}}(300\ K)}\right|_{\text{max}} = 3.8\times10^4 f \tag{50}$$

In the weak-coupling limit ($\kappa \approx 0$), the largest enhancement is realized for a $\pi/4$ or $3\pi/4$ pulse. In this case, the enhancement is

$$\left|\frac{S_{\text{PASADENA}}}{S_{\text{equilib.}}(300\ K)}\right|_{\substack{\text{max,}\\ \text{weak coupling}}} = 3.1\times10^4 f \tag{51}$$

It should be emphasized that the enhancement factor plotted in Fig. 7 assumes that all of the lines are well-resolved. Situations in liquid-state experiments where this may

not be the case are when the *J*-coupling is either too small (relative to the linewidths), leading to destructive interference within each antiphase doublet, or when the *J*-coupling is too large, leading to destructive interference between the two "allowed" transitions. The destructive interference in this latter case can be anticipated from Fig. 3(a). The near magnetic equivalence that corresponds to large J/Δ, however, will, in most cases, severely limit the enhancement before destructive interference limits it.

In the solid state for a single fixed orientation, the quantity ($J/2 - D$) must be large enough to prevent destructive interference within antiphase doublets. The anomalous overlap seen in Fig 3(b) at $D = \Delta/\sqrt{3}$ (for $J = 0$) will also lead to destructive interference. For the case of powdered samples, the effect of multiple random orientations of the dipolar coupling tensor and chemical shift tensors must be taken into account. In Chapter III, the enhancement for a "powder-averaged" spin system will be shown to be diminished by destructive interference between lines of opposite intensities in spectra from different crystallite orientations.

10. References

[1] C.R. Bowers and D.P. Weitekamp, Phys. Rev. Lett. **57**, 2645 (1986).

[2] C.R. Bowers and D.P. Weitekamp, J. Am. Chem. Soc. **109**, 5541 (1987).

[3] T.C. Eisenschmid, R.U. Kirss, P.P. Deutsch, S.I. Hommeltoft, R. Eisenberg, J. Bargon, R.G. Lawler and A.L. Balch, J. Am. Chem. Soc. **109**, 8089 (1987).

[4] M.G. Pravica and D.P. Weitekamp, Chem. Phys. Lett. **145**, 255 (1988).

[5] R.U. Kirss, T.C. Eisenschmid and R. Eisenberg, J. Am. Chem. Soc. **110**, 8564 (1988).

[6] C.R. Bowers, D.H. Jones, N.D. Kurur, J.A. Labinger, M.G. Pravica and D.P. Weitekamp, Adv. Magn. Reson. **14**, 269 (1990).

[7] J. Bargon, J. Kandels, P. Kating, A. Thomas and K. Woelk, Tetrahedron Lett. **31**, 5721 (1990).

[8] J. Bargon, J. Kandels and P. Kating, J. Chem. Phys. **98**, 6150 (1993).

[9] S.B. Duckett, C.L. Newell and R. Eisenberg, J. Am. Chem. Soc. **116**, 10548 (1994).

[10] P. Kating, A. Wandelt, R. Selke and J. Bargon, J. Phys. Chem. **97**, 13313 (1993).

[11] R.U. Kirss and R. Eisenberg, J. Organomet. Chem. **359**, C22 (1989).

[12] A. Thomas, M. Haake, F.W. Grevels and J. Bargon, Angew. Chem. Int. Ed. Engl. **33**, 755 (1994).

[13] A. Harthun, K. Woelk, J. Bargon and A. Weigt, Tetrahedron **51**, 11199 (1995).

[14] A. Harthun, R. Giernoth, C.J. Elsevier and J. Bargon, Chem. Commun. 2483 (1996).

[15] M. Jang, S.B. Duckett and R. Eisenberg, Organomet. **15**, 2863 (1996).

[16] M. Haake, J. Barkemeyer and J. Bargon, J. Phys. Chem. **99**, 17539 (1995).

[17] G. Buntkowsky, J. Bargon and H.H. Limbach, J. Am. Chem. Soc. **118**, 8677 (1996).

[18] M.S. Chinn and R. Eisenberg, J. Am. Chem. Soc. **114**, 1908 (1992).

[19] K. Woelk and J. Bargon, Z. Phys. Chem. **182**, 155 (1993).

[20] P.J. Carson, C.R. Bowers and D.P. Weitekamp, Abstracts of the 31st Experimental Nuclear Magnetic Resonance Conference (1991).

[21] C.R. Bowers, S.K. Buratto, P.J. Carson, H.M. Cho, J.Y. Hwang, L.J. Mueller, P.J. Pizarro, D.N. Shykind and D.P. Weitekamp, SPIE Optical Methods for Ultrasensitive Detection and Analysis: Techniques and Applications **1435**, 36 (1991).

[22] C. Cohen-Tannoudji, B. Diu and F. Laloë, Quantum Mechanics, Volume 2, (Wiley-Interscience, New York, 1977).

[23] L.D. Landau and E.M. Lifshitz, Quantum Mechanics, Volume 3, Third Edition, (Pergamon Press, Oxford, 1977).

[24] I.F. Silvera, Rev. Mod. Phys. **52**, 393 (1968).

[25] A. Farkas, Orthohydrogen, Parahydrogen and Heavy Hydrogen, (Cambridge University Press, London, 1935).

[26] M. Mehring, High Resolution NMR in Solids, Second Edition, (Springer-Verlag, Berlin, 1983).

Fig. 1. (a) Equilibrium mole fractions of the ortho and para forms of molecular hydrogen as a function of temperature. In PASADENA experiments performed to date, equilibration has been performed at 77 K, with subsequent warming to room temperature in the absence of the equilibration catalyst so that the mole fractions are maintained. (b) Equilibrium mole fractions of the ortho and para forms of molecular deuterium. Spin degeneracy considerations for D_2 eliminate the crossover of the mole fractions that is seen for H_2.

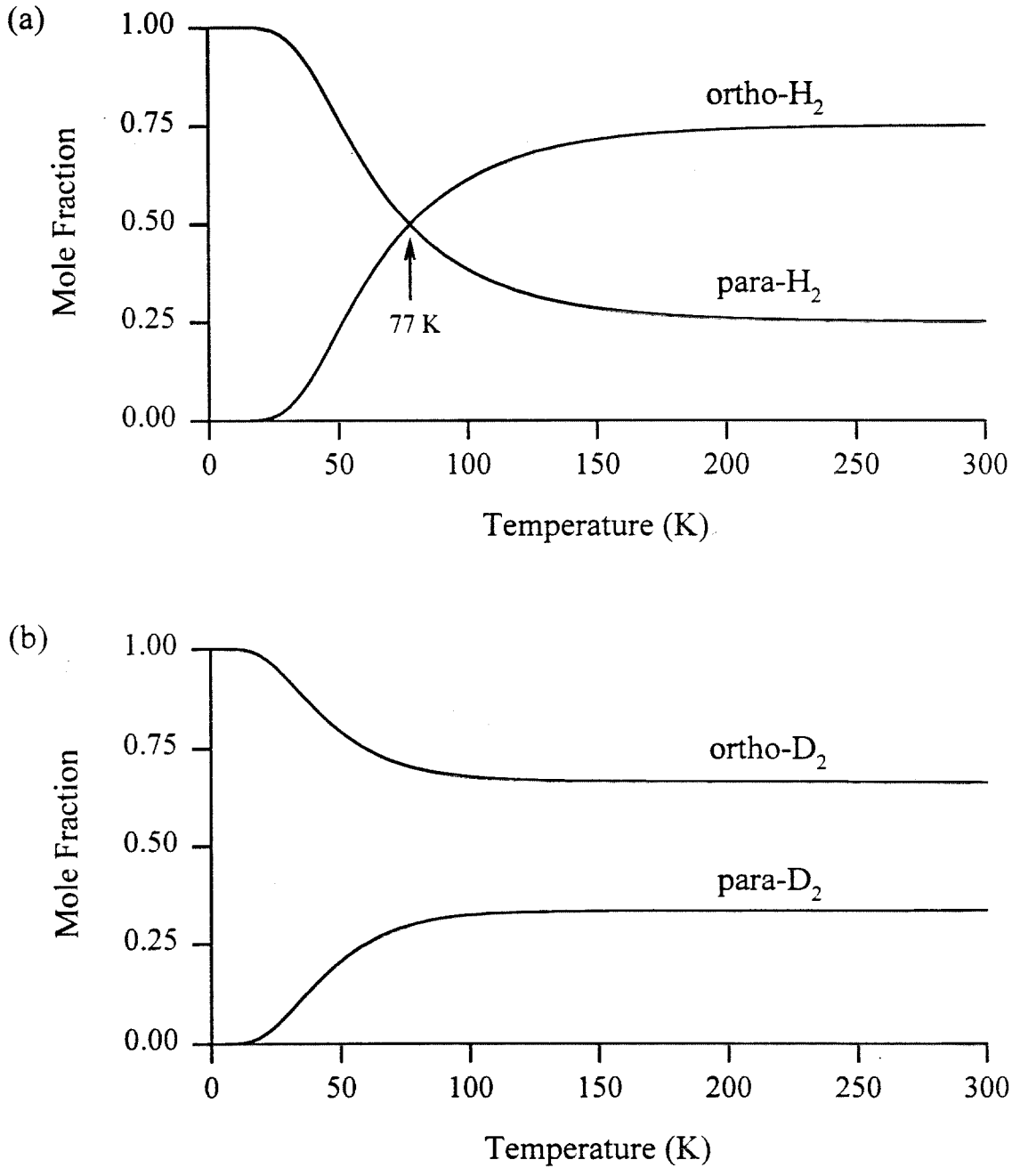

Fig. 2. PASADENA correlation diagram showing precursor molecular hydrogen spin states on the left and product spin states (after reaction of the H_2 with a substrate) on the right. The case of pure parahydrogen precursor is shown. The sudden change in Hamiltonian distributes all of the population between the two center states, with the exact distribution a function of the spectral parameter $\kappa = \tan^{-1}(J-D)/|\Delta|$. In the weak coupling case, $(J-D)/\Delta \approx 0$ and the two center populations are nearly equal. Except in the case of magnetic equivalence, for which $|(J-D)/\Delta| \gg 1$, large nonequilibrium population differences across NMR transitions result.

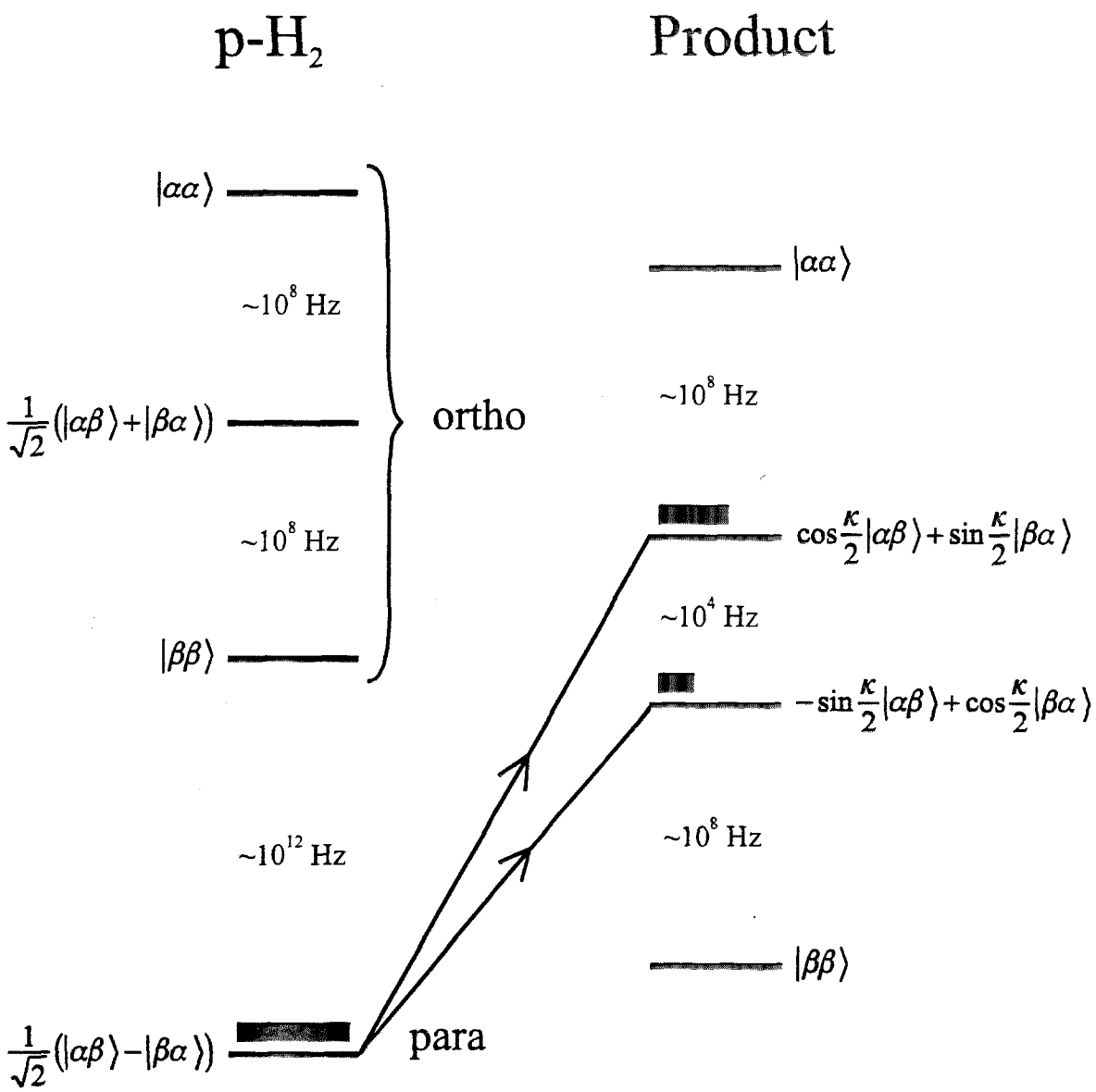

Fig. 3. Eigenfrequencies for a system of two spin-1/2 nuclei for fixed chemical shift difference Δ. (a) The four spectral frequencies are plotted as a function of J on the vertical axis, with $D = 0$. Dashed lines indicate negative transition amplitudes for small pulse angles. The average rotating-frame chemical shift $\overline{\omega}$ is taken to be zero. Both the spectral frequencies and J are shown in units of the chemical shift difference, which is assumed positive. (b) The four spectral frequencies are plotted as a function of D on the vertical axis, with $J = 0$.

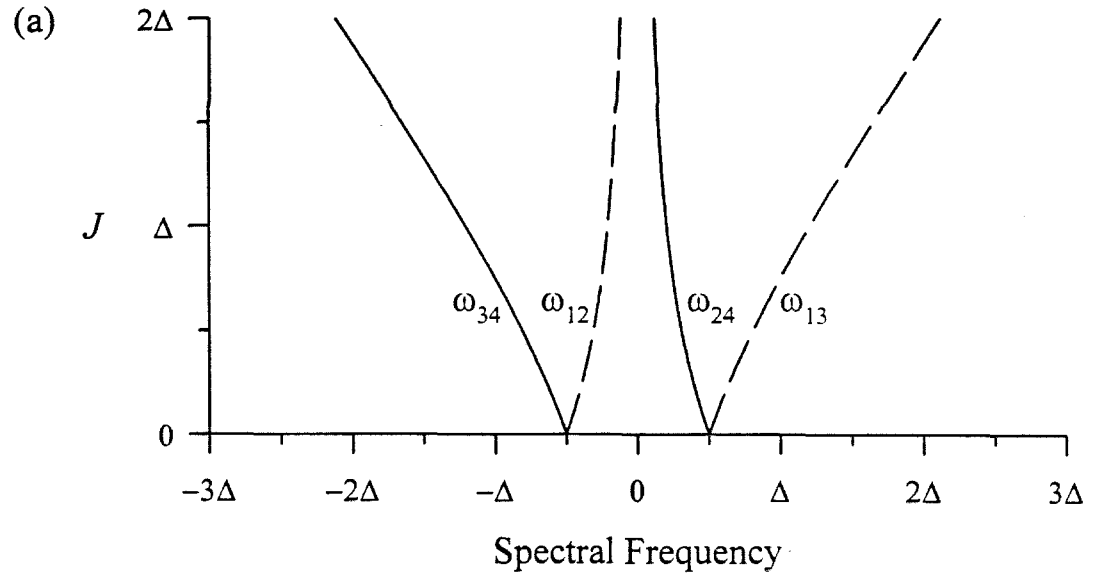

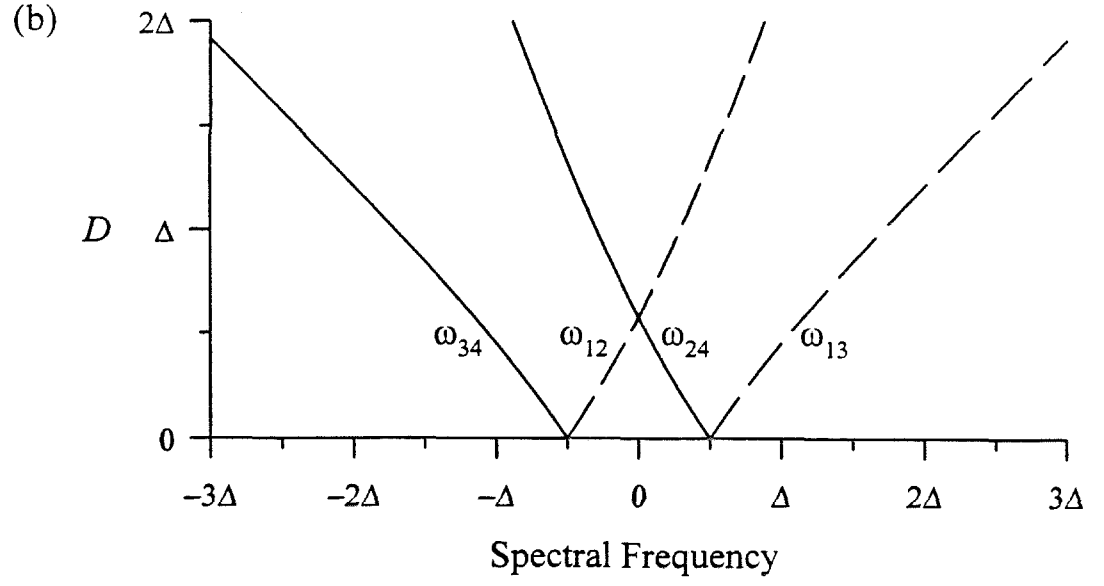

Fig. 4. Two different plots of the PASADENA transition amplitude for the $|2\rangle \rightarrow |4\rangle$ transition as a function of the spectral parameter $\kappa = \tan^{-1}(J-D)/|\Delta|$ and the pulse flip angle Θ. For the $|1\rangle \rightarrow |2\rangle$ transition the amplitude shown above is negated. The $|1\rangle \rightarrow |3\rangle$ and $|3\rangle \rightarrow |4\rangle$ transition amplitudes are identical to the $|1\rangle \rightarrow |2\rangle$ and $|2\rangle \rightarrow |4\rangle$ amplitudes, respectively, but with the κ-axis reversed.

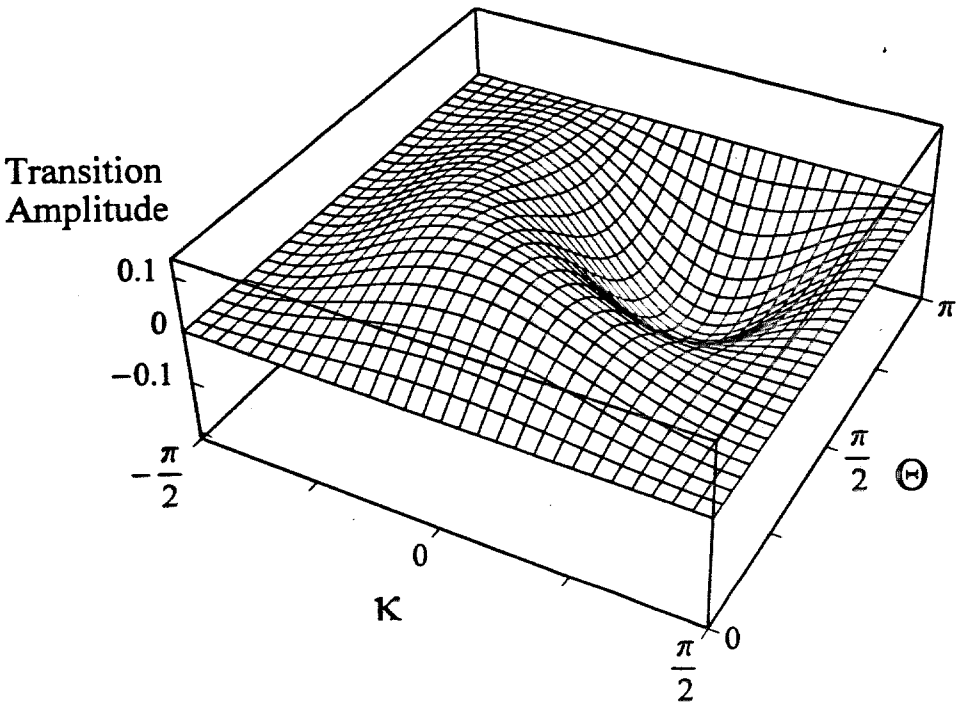
Transition
Amplitude
0.1
0
−0.1
$-\frac{\pi}{2}$
0
κ
$\frac{\pi}{2}$
0
$\frac{\pi}{2}$
Θ
π

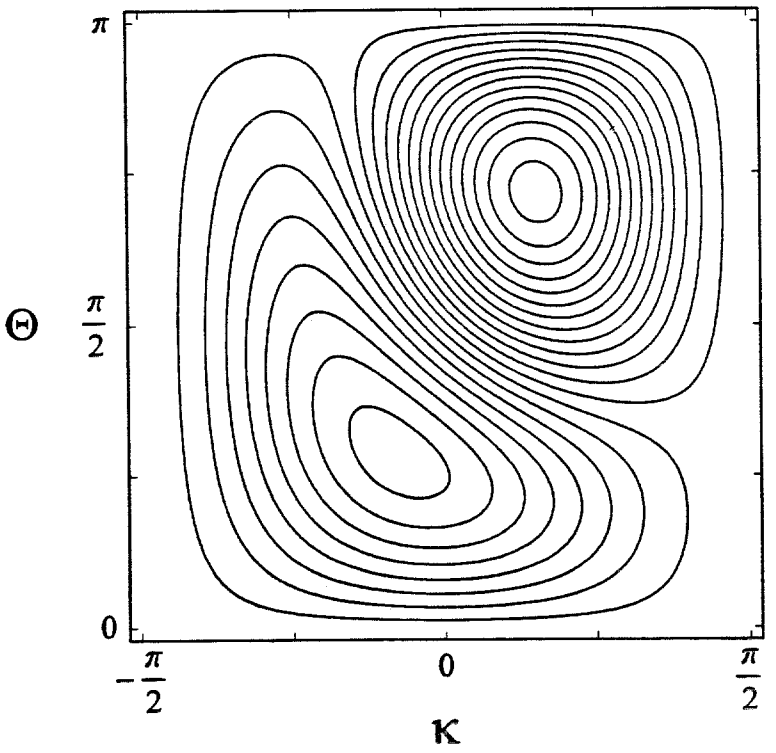
π
Θ
$\frac{\pi}{2}$
0
$-\frac{\pi}{2}$
0
$\frac{\pi}{2}$
κ

Fig. 5. Two different plots of the PASADENA signal energy as a function of κ and Θ. This calculation of the signal energy assumes that there is no overlap of the lines within the spectrum corresponding to any given point in the κ-Θ plane. The largest signal energy is always realized for a pulse angle in the near vicinity of $3\pi/4$. For $\kappa = 0$, this gives the same signal energy as a pulse angle of $\pi/4$.

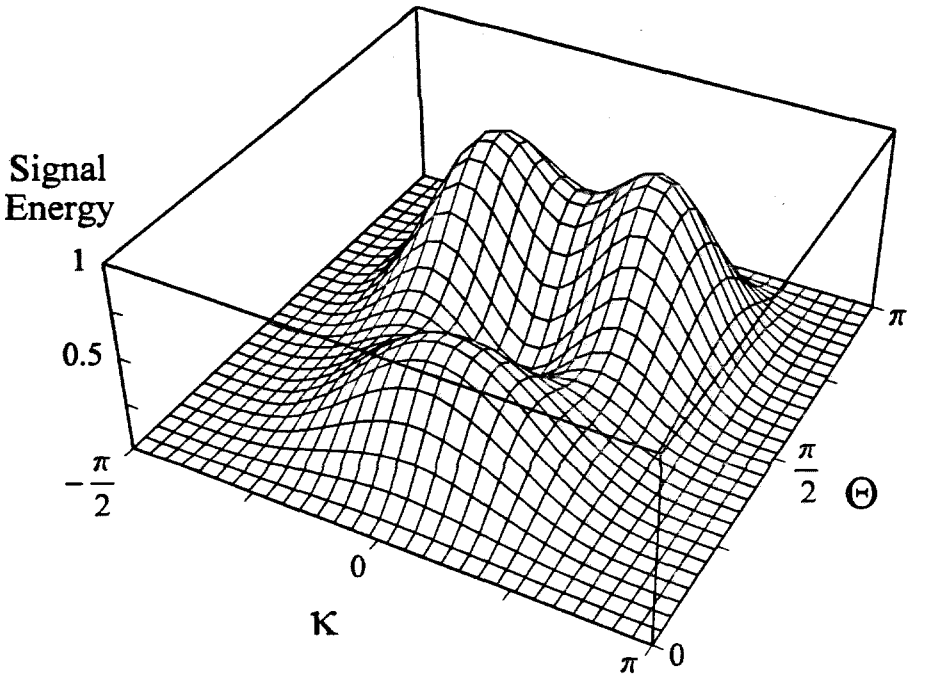
Signal
Energy
1
0.5
$-\frac{\pi}{2}$
0
$\frac{\pi}{2}$
π
Θ
κ
π
0

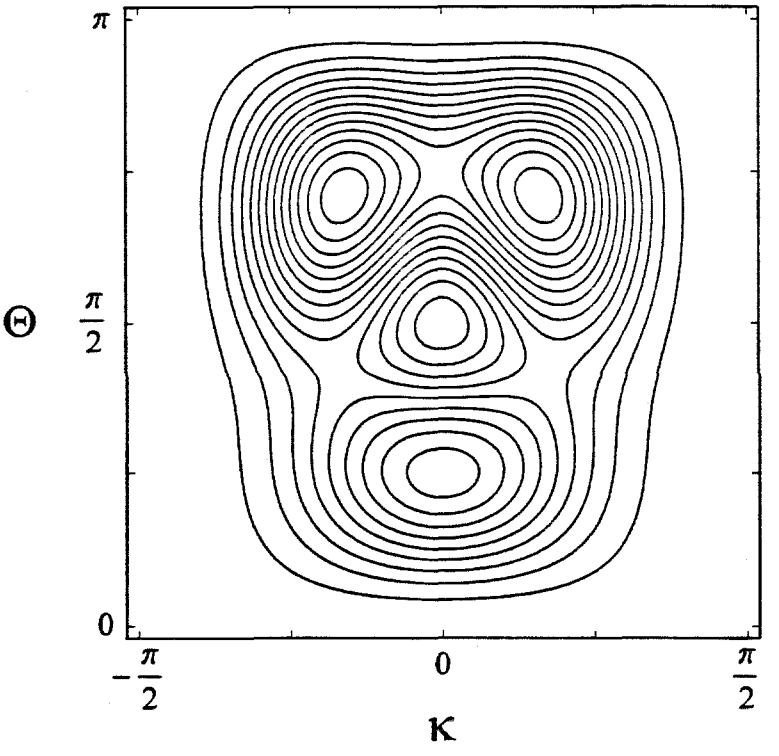
π
Θ
$\frac{\pi}{2}$
0
$-\frac{\pi}{2}$
0
$\frac{\pi}{2}$
κ

Fig. 6. Two different plots of the integrated magnitude of the PASADENA spectrum as a function of κ and Θ. This calculation assumes that there is no overlap of the lines within the spectrum.

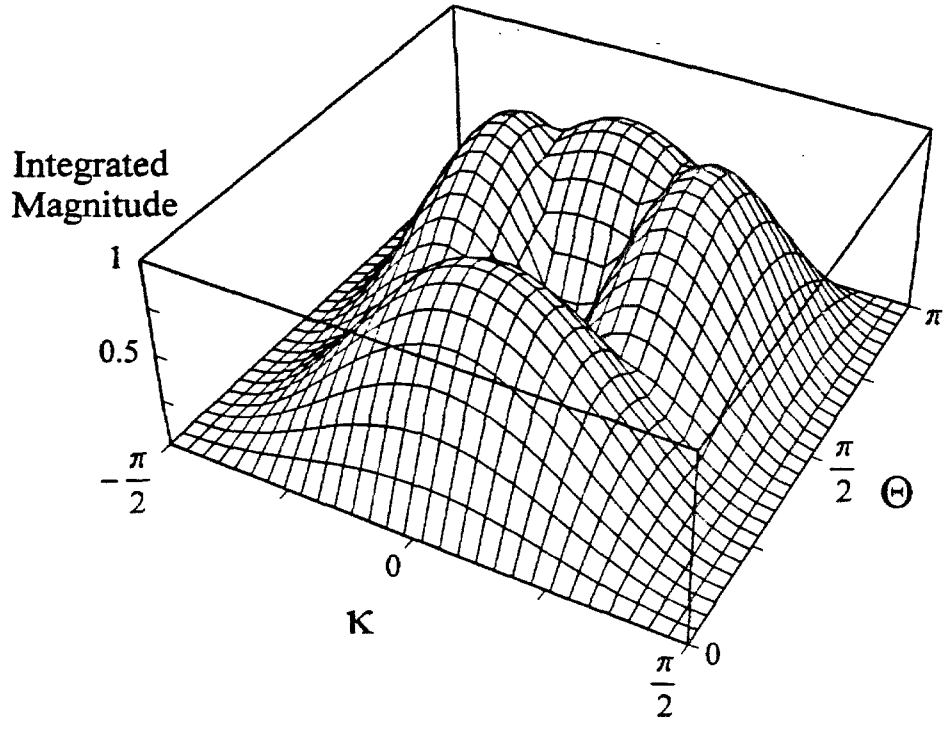

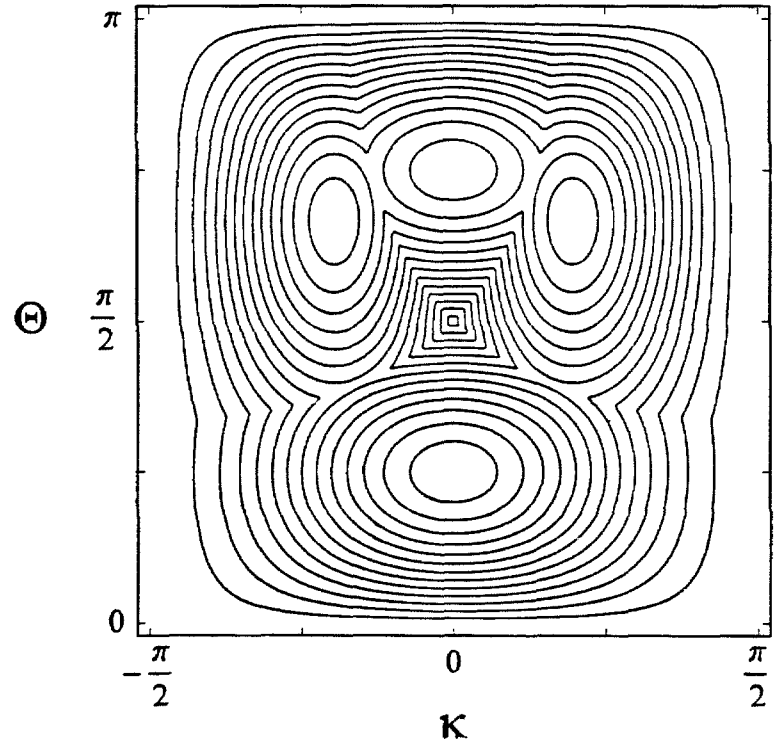

Fig. 7. Two different plots of the enhancement factor of the $|1\rangle \rightarrow |2\rangle$ and $|2\rangle \rightarrow |4\rangle$ PASADENA transition amplitudes over ordinary NMR as a function of κ and Θ for pure parahydrogen precursor ($f = 1$). The enhancement factor for the $|1\rangle \rightarrow |3\rangle$ and $|3\rangle \rightarrow |4\rangle$ transitions is obtained by reversing the κ axis. The initial condition for the ordinary NMR spectrum is equilibrium in a 4.7 T magnetic field (200 MHz) at 300 K. The discontinuous first derivative as a function of κ at $\kappa = 0$ is due to the abrupt change in the choice of transition amplitude in the ordinary NMR spectrum that is used for comparison. This choice ensures that the PASADENA signal is always compared with the largest transition in the ordinary spectrum as $\kappa \rightarrow \pm\pi/2$ (and not to the smallest transition, which represents an increasingly forbidden transition as $\kappa \rightarrow \pm\pi/2$).

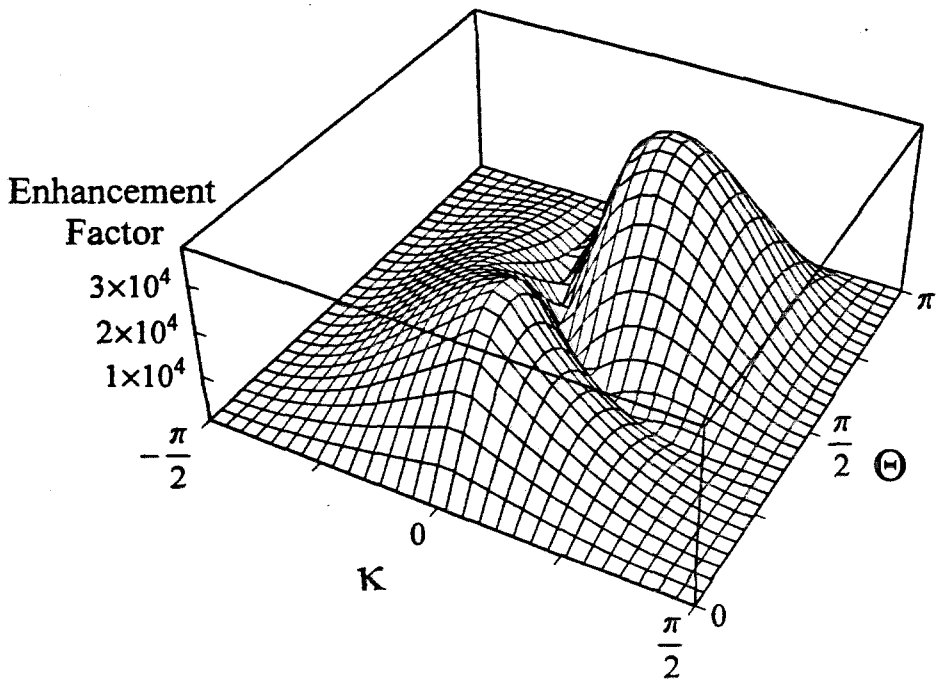
Enhancement
Factor
3×10^4
2×10^4
1×10^4
-π/2
0
π/2
κ
0
π/2
π
Θ

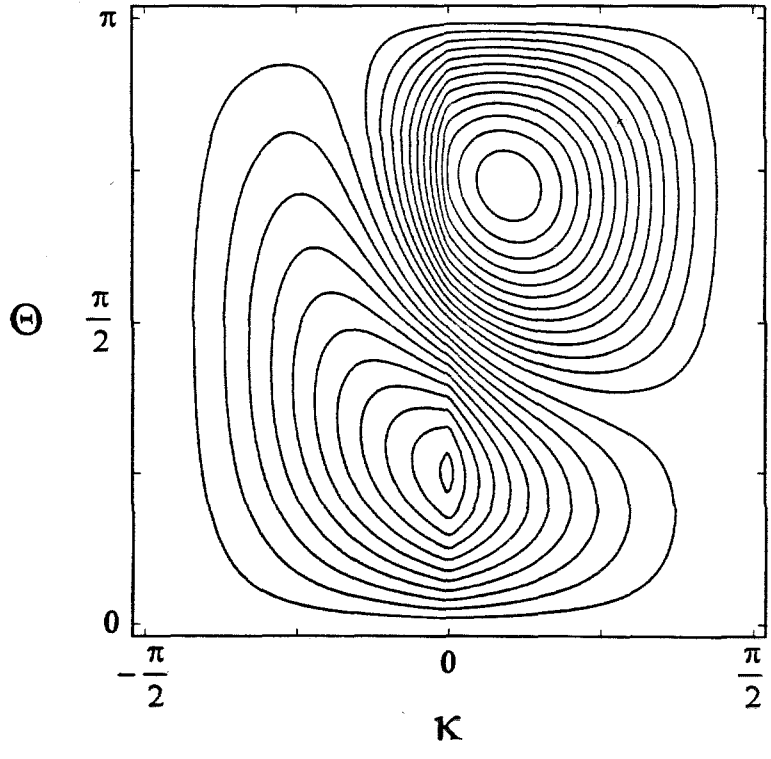
π
Θ
π/2
0
-π/2
0
π/2
κ

Chapter II. Surface PASADENA Theory

1. PASADENA in the Solid State

The application of the PASADENA effect to solid-state systems differs in important respects from its application in liquids. In liquids, as discussed in Chapter I, rapid tumbling of the molecules reduces the interactions in the Hamiltonian to their isotropic parts. One result is that each spin in the spin system has a single isotropic chemical shift throughout the ensemble, ignoring magnetic field inhomogeneity. Another result is that the dipolar coupling interaction is averaged to zero. The scalar coupling is unaffected since it is wholly isotropic. Liquid-state motional averaging typically results in narrow spectral lines that are easily resolved in systems with coupled, magnetically inequivalent spins.

In the solid state, the spin system remains fixed in its orientation and the anisotropic nature of the chemical shift and dipolar coupling interactions becomes observable. The Hamiltonian for an isolated two-spin system is that given by Eq. (13) in Chapter I:

$$\mathcal{H} = \omega_{1z} I_{1z} + \omega_{2z} I_{2z} + D(3I_{1z}I_{2z} - \mathbf{I}_1 \cdot \mathbf{I}_2) + J\mathbf{I}_1 \cdot \mathbf{I}_2 \qquad (1)$$

In order to compute the spectrum for a spin system in the solid state, the orientation dependence of the chemical shift and dipolar coupling interactions in $\mathcal{H}$ must be included.

The general form of the chemical shift interaction for the i^{th} spin is

$$\mathcal{H}^i_{CS} = \gamma_n \mathbf{I}_i \cdot \tilde{\sigma}^i \cdot \mathbf{B}_0 \qquad (2)$$

where $\tilde{\sigma}^i$ is the chemical shielding tensor and B_0 is the applied magnetic field vector. In high-field NMR the *nonsecular* terms in $\mathcal{H}^i_{CS}$ (terms which don't commute with I_z) are averaged to zero on the time scale of the spin evolution and are thus dropped, leaving the truncated form of the chemical shift interaction appearing in Eq. (1). The chemical shift ω_{iz} in the truncated Hamiltonian depends on the tensorial interaction in a complicated manner, as will be shown below.

The shielding tensor is a second-rank Cartesian tensor and reflects the chemical environment of the spin. It is generally assumed to be a symmetric tensor (i.e., it is assumed that its antisymmetric part is negligible). The implication of this symmetry is that the full tensor can be specified by six independent components (instead of nine). Three of these are conveniently chosen to be the *principal components* (eigenvalues) of the tensor, σ^i_{11}, σ^i_{22}, and σ^i_{33}. The other three are the set of Euler angles $\Omega_i = \{\alpha_i, \beta_i, \gamma_i\}$ which relate the principal axis system of the tensor to a specified molecular or crystal-fixed axis system.

In computing the chemical shift of a spin in an oriented system it is useful to define three new quantities in terms of the principal shielding components. The isotropic shift is defined as

$$\sigma_i = \mathrm{Tr}\{\tilde{\sigma}^i\} = \frac{1}{3}\left(\sigma^i_{11} + \sigma^i_{22} + \sigma^i_{33}\right) \tag{3}$$

The reduced anisotropy is defined as

$$\delta_i = \sigma^i_{33} - \sigma_i \tag{4}$$

(with the standard anisotropy equal to (3/2) δ_i). The asymmetry parameter is defined as

$$\eta_i = \frac{\left(\sigma^i_{22} - \sigma^i_{11}\right)}{\delta_i} \tag{5}$$

In order to keep η_i in the range $0 \le \eta_i \le 1$, the convention is to choose σ^i_{22} to be the component closest to the isotropic shift and σ^i_{33} to be the component farthest from the isotropic shift. This is summarized as

$$\left|\sigma^i_{33} - \sigma_i\right| \ge \left|\sigma^i_{11} - \sigma_i\right| \ge \left|\sigma^i_{22} - \sigma_i\right| \tag{6}$$

Once a molecular reference frame is chosen for a given system, the Euler angles relating the principal axis system of the shielding tensor to the molecular frame are specified. Only two angles are required to relate the molecular frame to the lab frame since all of the interactions, including the interaction with the rf field in the rotating-wave approximation, have rotational symmetry about the direction of the static field. A convenient choice for these two angles is to specify the direction of the magnetic field in the molecular frame using the polar angles θ and ϕ, corresponding to the longitudinal and azimuthal angles, respectively.

Spherical tensor operator methods can be used to compute the high-field rotating-frame chemical shift [1] for the i^{th} spin in terms of the principal components of the shielding tensor and the angles relating the three reference frames to each other. The chemical shift expression thus derived can be written

$$\begin{aligned}\omega_{iz} = \sigma_i + (8\pi/15)^{1/2}\delta_i \sum_m Y_{2,-m}(\theta,\phi) \\ \times\left[(3/2)^{1/2}\ \mathcal{D}^2_{0m}(\Omega_i) + (1/2)\eta_i\left\{\mathcal{D}^2_{2m}(\Omega_i) + \mathcal{D}^2_{-2m}(\Omega_i)\right\}\right]\end{aligned} \tag{7}$$

where the Y_{lm} are the normalized spherical harmonics, and the $\mathcal{D}^2_{m'm}$ are the elements of the second-rank Wigner rotation matrix. The chemical shift in Eq. (7) is the quantity that appears in $\mathcal{H}$ in Eq. (1) for each spin.

The general form of the dipolar coupling interaction between two homonuclear spins is

$$\mathcal{H}_D = \frac{\gamma_n^2\hbar}{r^3}\left[\mathbf{I}_1\cdot\mathbf{I}_2 - \frac{3(\mathbf{I}_1\cdot\mathbf{r})(\mathbf{I}_2\cdot\mathbf{r})}{r^2}\right] \tag{8}$$

where $\mathbf{r}$ is the internuclear vector. If a molecular reference frame is chosen such that its z-axis is parallel to the internuclear vector, then the angle θ defined above for the chemical shift interaction is also the angle between the internuclear vector and the applied magnetic field. With this definition for θ, the truncated high-field dipolar Hamiltonian [2] can be written

$$\mathcal{H}'_D = \frac{1}{2}\omega_D\left(1-3\cos^2\theta\right)\left(3I_{1z}I_{2z} - \mathbf{I}_1\cdot\mathbf{I}_2\right) \tag{9}$$

where

$$\omega_D = \frac{\gamma_n^2 \hbar}{r^3} \tag{10}$$

The Hamiltonian $\mathcal{H}_D'$ appears as the third term in Eq. (1). The dipolar coupling leads to a splitting of the transition frequencies for each of the two spins. In the limit that $\Delta = \omega_{1z} - \omega_{2z} = 0$, this splitting is equal to $(3/2)\omega_D(1-3\cos^2\theta)$. Regardless of the size of Δ, the splitting goes to zero at the "magic angle" $\left(\theta = \cos^{-1}\sqrt{1/3} \approx 54.7^\circ\right)$ and has opposite sign on either side of the magic angle.

Fig. 1 depicts graphically the anisotropic chemical shift and dipolar coupling parameters for an oriented two-spin system. Each ellipsoid fully describes the chemical shift interaction for a given spin. The molecular frame is shown in the lower right, with the *z*-axis taken to be parallel to the internuclear vector. The polar angles defining the orientation of the magnetic field with respect to the molecular frame are also shown.

A total of thirteen parameters from the internal Hamiltonian can be seen in Fig. 1, although only twelve are independent in the powder average, as discussed in the next section. The thirteen shown are the internuclear distance, and the six parameters describing each chemical shift tensor.

2. Powder Averaging

For a polycrystalline sample, or "powder," all possible orientations of the magnetic field in the molecular frame are represented in the sample. The resulting spectrum is the sum of individual spectra from each orientation. In the frequency domain, the "powder-averaged" spectrum can be written

$$S_{\text{powder}}(\omega) = \int_0^{2\pi} \int_0^{\pi} S(\theta, \phi, \omega) \sin\theta \, d\theta \, d\phi \tag{11}$$

where the spectrum from an individual cyrstallite orientation is given by the function $S(\theta, \phi, \omega)$.

If the angles α_i, β_i, and γ_i for each tensor are defined to be the set of Euler angles that rotate the molecular frame into coincidence with the tensor axes, then only two of the three angles α_1, α_2, and ϕ are independent (with ϕ defined as in Section 1). For example, for any arbitrary set of parameters, α_2 and ϕ can always be referenced to the angle α_1, and α_1 set to zero, without changing the Hamiltonian. Note that this is a separate issue from rotational invariance in the lab frame. This dependence, combined with the fact that all direct information about the orientation of the molecular frame with respect to the crystal frame is lost in powder averaging, leaves a total of twelve independent parameters needed to uniquely specify the powder average.

For an isolated two-spin system, the spectra from a single crystallite orientation is generally "liquid-like" (i.e., containing narrow, well-resolved lines). The spectrum for a powdered sample of the same isolated system, however, is generally orders of magnitude broader, depending on the anisotropies of the chemical shift interactions and the size of the dipolar coupling. Fig. 2 shows theoretical powder line shapes for a few simple cases of anisotropic Hamiltonians, where the initial spin order is Curie-law magnetization. For these simple cases, all of the relevant parameters in the Hamiltonian are manifestly recognizable in the spectra. For more complicated Hamiltonians, such as two dipolar coupled spins with anisotropic chemical shift interactions, the parameters of the Hamiltonian cannot, in general, be easily visually correlated with the spectrum.

In general, analytical solutions to the integral in Eq. (11) do not exist [3], and numerical methods must be used to predict the powder average for an arbitrary spin system. Software written primarily by Bowers [4] and based on the method of Alderman et al. [3] has been employed to calculate powder lineshapes for the PASADENA experiment. The calculations start with the expression for the PASADENA signal given in Chapter I, Eq. (37). The method produces a real channel frequency domain powder average using a linear interpolation scheme for rapid convergence compared to other methods.

In the case of powdered systems, the distribution of crystallite orientations necessarily leads to overlap of spectra from individual crystallites. For the PASADENA experiment this leads to unavoidable partial cancellation between these spectra due to the characteristic antiphase nature of the signal. Fig. 3 shows the variety of lineshapes that are possible in principle when the PASADENA technique is applied to powdered systems. The lineshapes reflect the antiphase character expected from the sum PASADENA spectra for individual cyrstallite orientations. As in liquid-state PASADENA, the net integral of the spectrum in the powder case is zero. In general, however, the lineshapes are too complicated to visually reveal in any straightforward fashion the parameters of the internal Hamiltonian.

The powder-PASADENA spectrum can be explored further by looking at the effect on lineshape of changing a single parameter in the Hamiltonian. A convention for units is used in which it is understood that when a Hamiltonian parameter is equated with a value in units of kHz, the parameter should be multiplied by 2π (to convert it to rad/s) before insertion into the Hamiltonian.

Fig. 4 shows a series of powder-PASADENA simulations in which only the isotropic shift difference Δ_0 between the two chemical shift tensors is varied. The other shift tensor parameters and the dipolar coupling parameter are held constant. For large Δ_0, distinct powder lineshapes for each of the two spins, separated by roughly Δ_0, are visible. This represents the weak-coupling limit for each crystallite in the powder. As Δ_0 is increased further, the two distinct lineshapes to not change either in shape or intensity. As Δ_0 approaches zero, both destructive interference and the increasingly forbidden character of the transitions diminish the intensity of the spectrum. The limit in this direction is not, however, zero intensity (defined here as zero integrated magnitude), since the anisotropies of the shift tensors are nonzero and fixed.

Fig. 5 shows a series of powder-PASADENA simulations in which only the dipolar coupling parameter ω_D is varied while the chemical shift tensor parameters are held constant. The spectrum approaches zero intensity for large ω_D (defined as $\omega_D >> \delta_1, \delta_2$ and Δ_0) due to the increasing magnetic equivalence of the spins. As discussed in Chapter I, this diminishes the size of the population differences across dipole allowed transitions following the reaction of spin-symmetry enriched H_2 with a substrate. Even for large ω_D, the dipolar coupling still vanishes for those crystallites in the powder having θ equal to the magic angle. However, the fraction of crystallites for which the spins are effectively magnetically inequivalent via this mechanism nonetheless goes to zero as ω_D is increased. At the other extreme, as ω_D goes to zero, the doublet splitting for each crystallite in the sample goes to zero. In this case, the destructive interference *within* each doublet causes the powder-averaged spectrum to approach zero intensity. This occurs as a

result of the antiphase character of the signal combined with the nonzero homogeneous linewidth within the spectra from each crystallite. As such, it is a form of destructive interference that occurs regardless of the additional destructive interference due to powder averaging.

Fig. 6 shows a series of powder-PASADENA simulations in which only the pulse flip angle Θ is varied while the internal Hamiltonian parameters remain fixed. The lineshape is seen to undergo a complete transformation in appearance from $\Theta = \pi/8$ to $\Theta = 7\pi/8$. The complicated dependence of the lineshape on Θ stems from the presence of more than one type of spin order in the initial condition, as seen in Chapter I, Eqs. (32) and (34). Recall that this includes the reasonable assumption for most experiments of a spread in reaction times that well exceeds the evolution period of the zero-quantum coherence. The expression for the PASADENA signal in Chapter I, Eq. (37), valid for a single value of κ (in this case, a single crystallite orientation), shows a more complicated Θ dependence than just an overall Θ-dependent prefactor for the signal.

Fig. 7 shows the integrated magnitude of the powder-PASADENA spectrum as a function of Θ for the same set of simulation parameters used in Fig. 6. The positions and ratios of the two local maxima and the nontrivial local minimum are qualitatively anticipated from the calculation shown in Chapter I, Fig. 5, of the integrated magnitude of a single narrow-line PASADENA spectrum as a function of κ and Θ. Note that the integrated magnitude of the powder-PASADENA spectrum is sensitive to the homogeneous and inhomogeneous broadening for the *individual* crystallite orientations, as will be discussed in Chapter III, along with a presentation of theoretical enhancement factors.

3. References

[1] U. Haeberlen, High Resolution NMR in Solids: Selective Averaging, (Advances in Magnetic Resonance Supplement I, J. S. Waugh, Series Ed.), (Academic Press, New York, 1976).

[2] M. Mehring, High Resolution NMR in Solids, Second Edition, (Springer-Verlag, Berlin, 1983).

[3] D.W. Alderman, M.S. Solum and D.M. Grant, J. Chem. Phys. **84**, 3717 (1986).

[4] C.R. Bowers, Ph.D. Thesis, California Institute of Technology (1991).

Fig. 1. Graphical representation of anisotropic Hamiltonian parameters for an oriented two-spin system. The chemical shift tensors are depicted as ellipsoids rotated by their respective Euler angles Ω_i. The three principal radii of an ellipse represent the principal components of the tensor, referenced to a common chemical shift. The length and direction of the internuclear vector determines the strength of the dipolar coupling. The orientation of the magnetic field with respect to the molecular frame is depicted in the lower right.

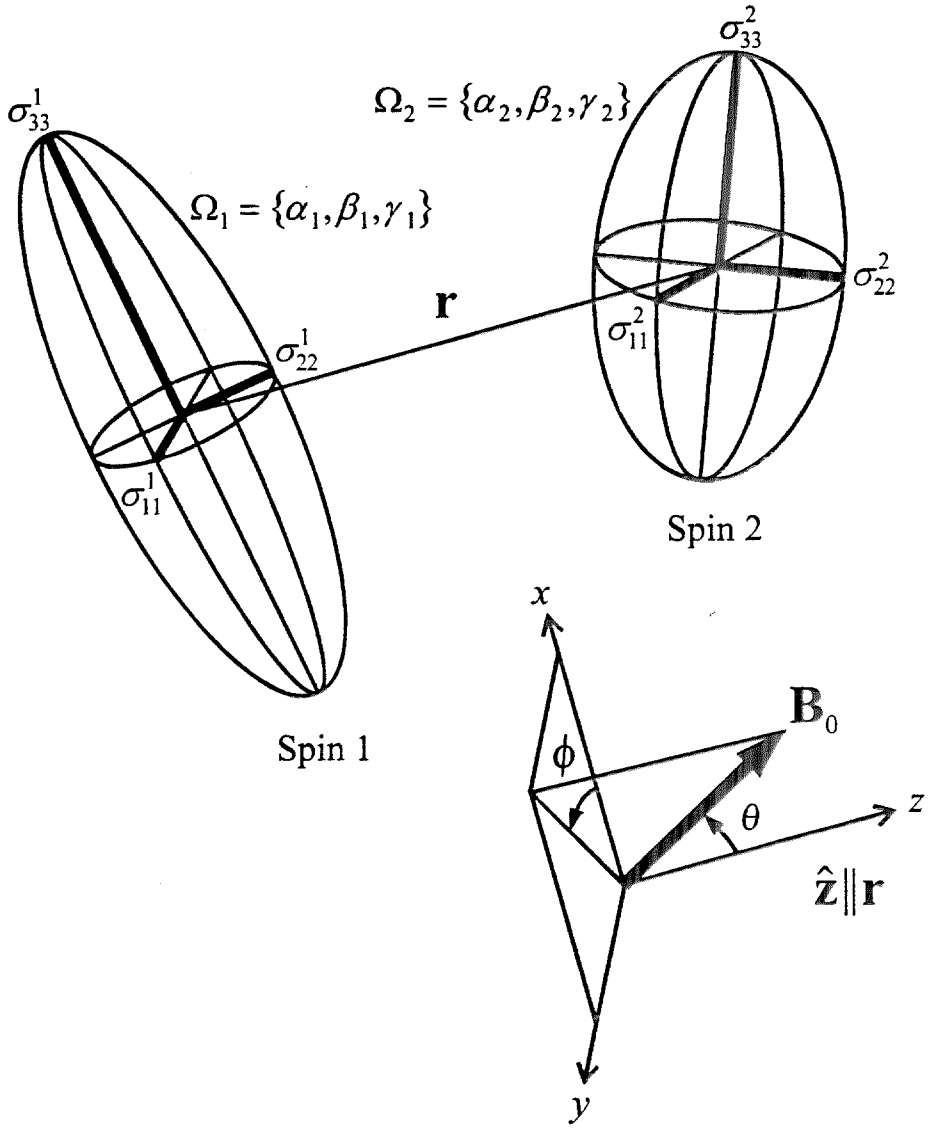

Fig. 2. Simulated powder-spectrum line shapes for three simple cases of anisotropic interactions in the Hamiltonian, identified below. The initial spin order is Curie-law magnetization. The spectra have been broadened by convolution with a Lorentzian lineshape having a FWHM of ~2% of the spectral bandwidth. (a) Two magnetically equivalent spins coupled through space with a dipolar coupling parameter of ω_D $\left(=\gamma^2\hbar/r^3\right)$. The powder pattern that results is the familiar Pake doublet. (b) A single spin with an axially symmetric chemical shift tensor ($\eta = 0$). The principal components of the tensor are shown. (c) A single spin with an arbitrary chemical shift tensor ($\eta \neq 0$).

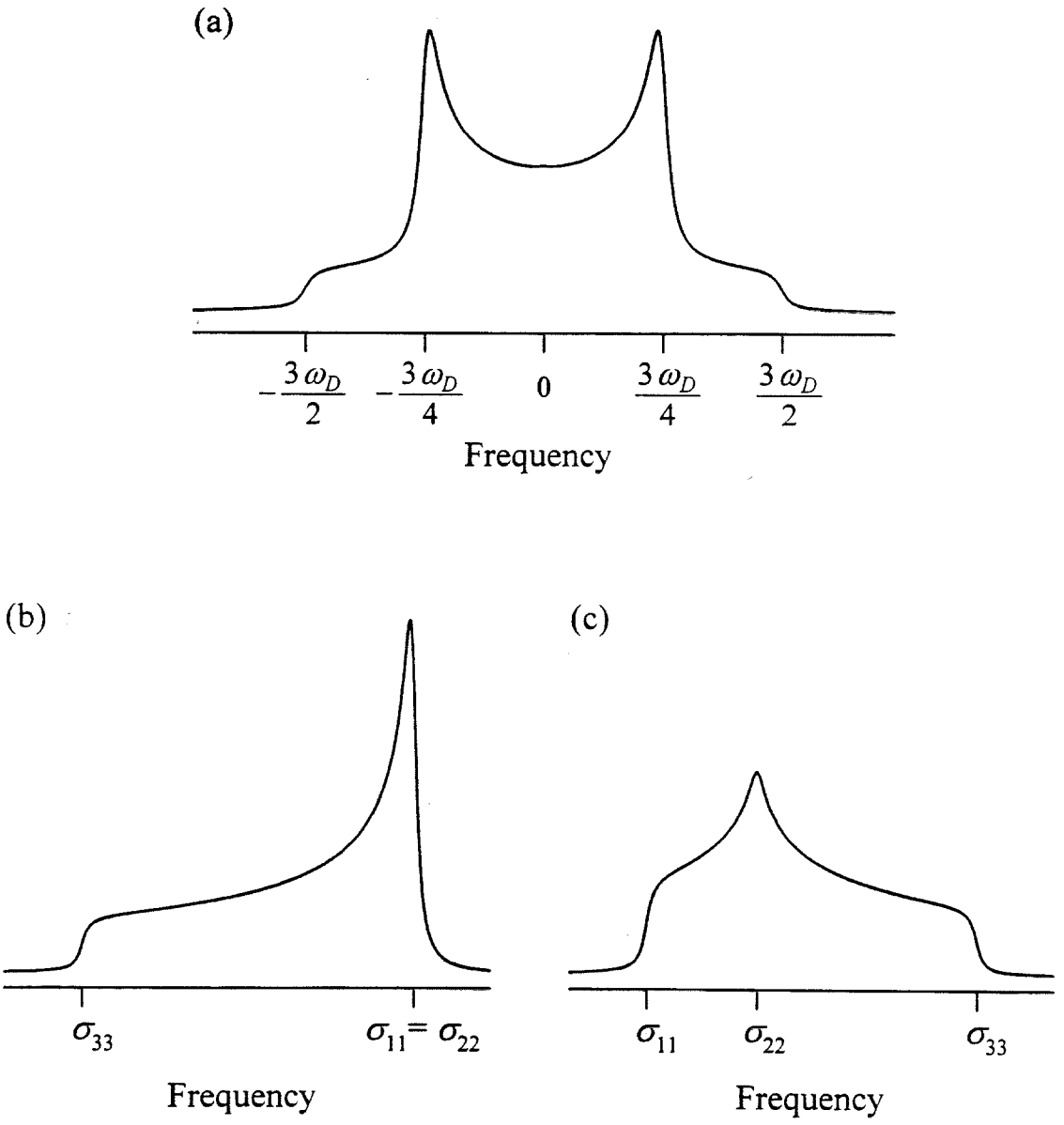

Fig. 3. Simulated spectra showing the variety of PASADENA lineshapes possible in powdered systems. The interproton distance, and the corresponding dipolar coupling parameter $\nu_D = \omega_D/(2\pi) = \gamma_n^2\hbar/(2\pi r^3)$ are shown below, along with the shift tensor parameters. The principal components for spin j are given by σ_{ii}^j (in kHz), and the Euler angles are given by Ω_j (in degrees). Note that the ordering of the principal components deviates from convention. The spectra have been convoluted with a Lorentzian lineshape of width 1 kHz. The flip angle in each simulation is 45°.

(a) r = 2.7 Å (ν_D = 6 kHz), σ_{ii}^1={5, 3, -1}, Ω_1={0, 90, 110},
σ_{ii}^2={-11, -6, 10}, Ω_2={220, 100, 250}

(b) r = 2.3 Å (ν_D = 10 kHz), σ_{ii}^1={2, 1, -12}, Ω_1={0, 100, 160},
σ_{ii}^2={-2, -1, 12}, Ω_2={210, 150, 340}

(c) r = 2.4 Å (ν_D = 9 kHz), σ_{ii}^1={-2, -1, 0}, Ω_1={0, 160, 130},
σ_{ii}^2={-5, -2, 9}, Ω_2={150, 10, 230}

(d) r = 1.9 Å (ν_D = 18 kHz), σ_{ii}^1={8, 3, -4}, Ω_1={0, 30, 100},
σ_{ii}^2={-1, -1, -5}, Ω_2={120, 100, 210}

(e) r = 2.1 Å (ν_D = 13 kHz), σ_{ii}^1={-6, 2, 17}, Ω_1={0, 40, 310},
σ_{ii}^2={-12, -7, 10}, Ω_2={240, 60, 230}

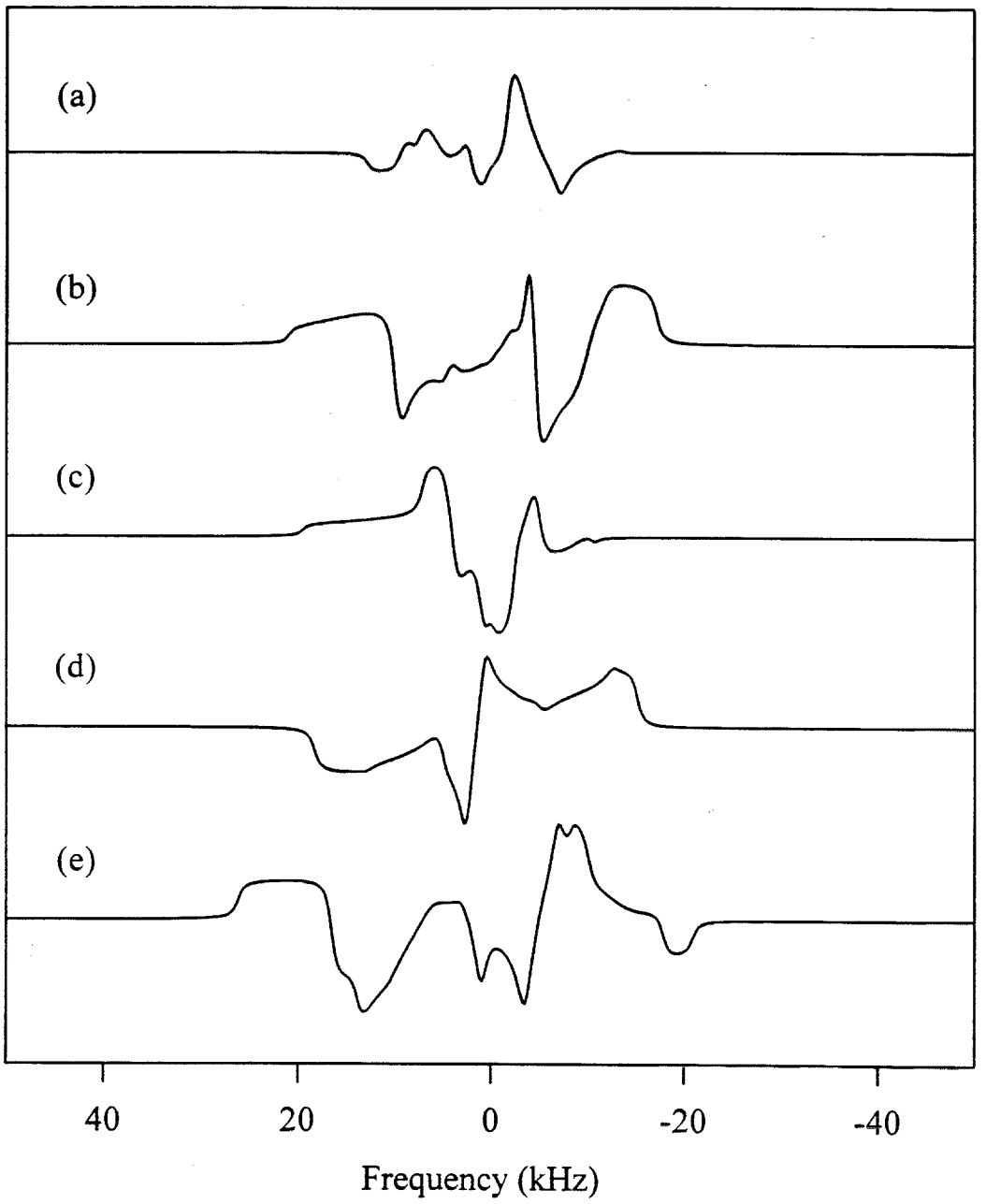
(a)
(b)
(c)
(d)
(e)
40
20
0
-20
-40
Frequency (kHz)

Fig. 4. Simulation of the dependence of the powder-PASADENA spectrum on the isotropic chemical shift difference Δ_0. The spectra are simulated with chemical shift tensor parameters of $\sigma^1 = \{1, 1, -2\}$ kHz, and $\sigma^2 = \{1, 0, -1\}$ kHz, corresponding to the $\Delta_0 = 0$ case (not shown). The anisotropies and asymmetries of the tensors are held constant as Δ_0 is changed. The alignment of the tensors is given by $\Omega_1 = \Omega_2 = \{0, 0, 0\}$, where the z-axis is defined by the internuclear vector. The dipolar coupling parameter is $\omega_D = 6$ kHz and the pulse flip angle is $\Theta = \pi/4$. The J coupling is set to zero. The spectra are broadened by 1 kHz as described in Fig. 3.

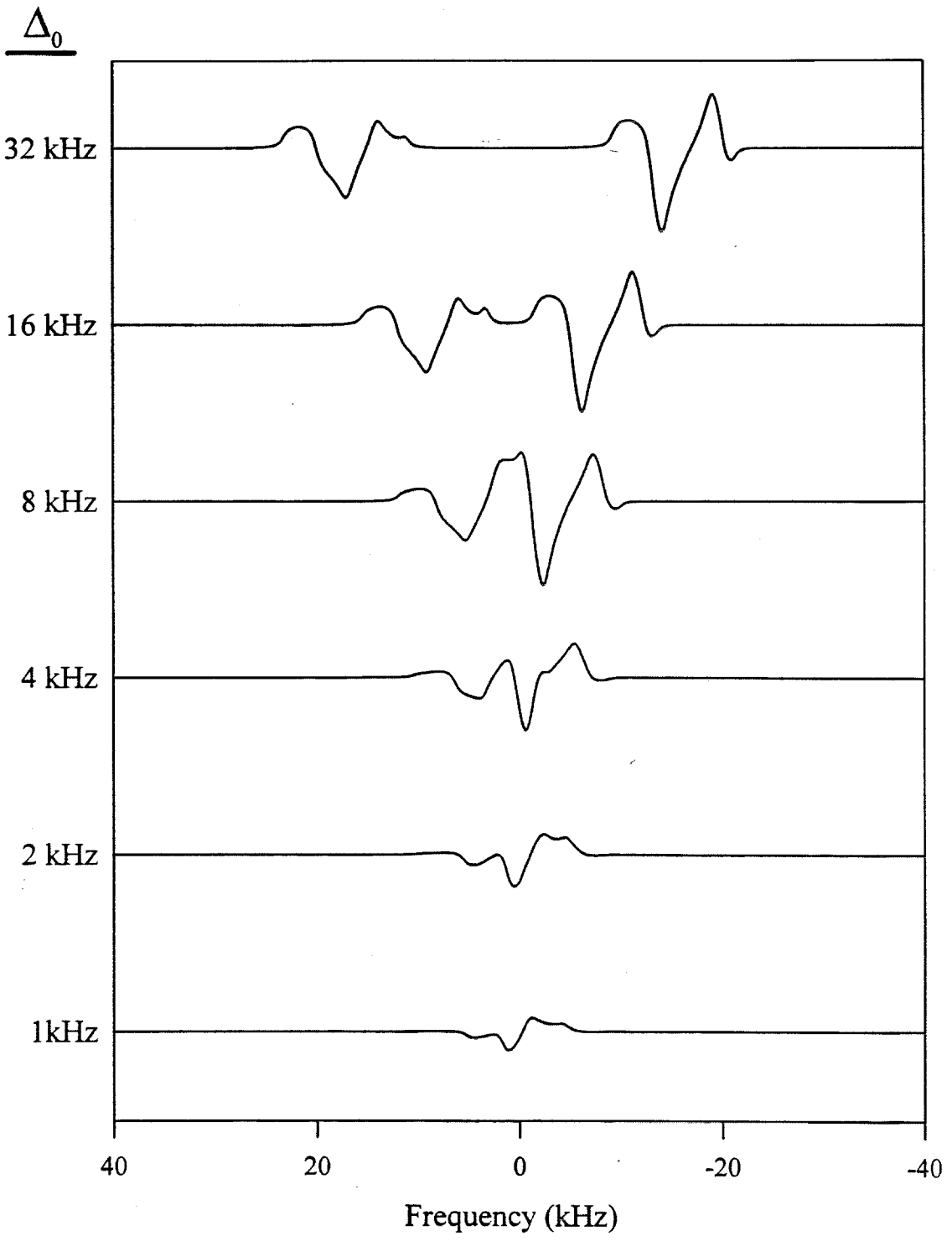
Δ_0
32 kHz
16 kHz
8 kHz
4 kHz
2 kHz
1kHz
40
20
0
-20
-40
Frequency (kHz)

Fig. 5. Simulation of the dependence of the powder-PASADENA spectrum on the dipolar coupling parameter ω_D. The same chemical shift tensors and pulse flip angle as in Fig. 4 are used, with the isotropic chemical shift difference fixed at $\Delta_0 = 2$ kHz. The J coupling is set to zero. The spectra are broadened by 1 kHz as described in Fig. 3.

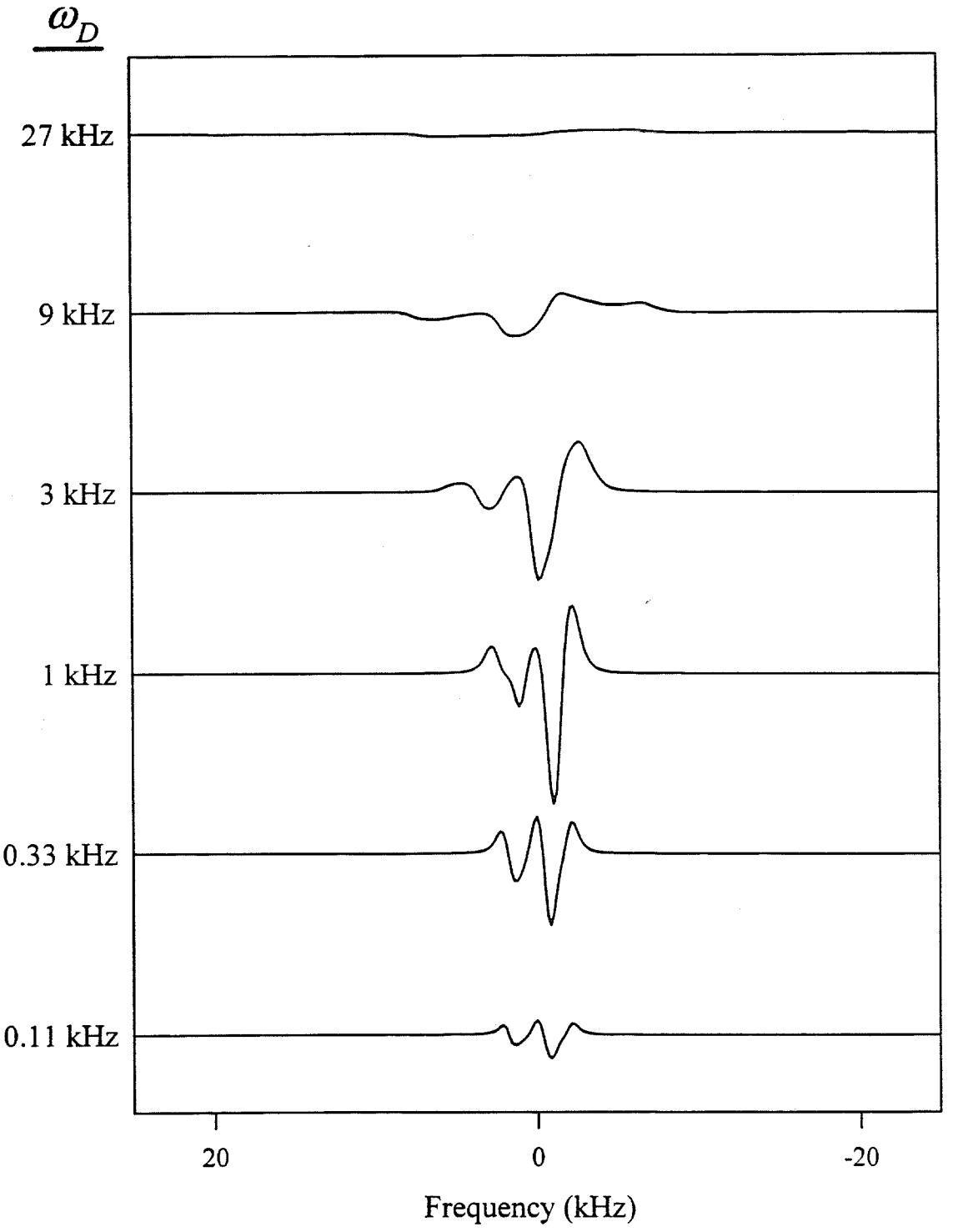

Fig. 6. Simulation of the dependence of the powder-PASADENA spectrum on the pulse flip angle Θ. The same chemical shift tensors as in Fig. 4 are used, with the isotropic chemical shift difference fixed at $\Delta_0 = 2$ kHz. The dipolar coupling is fixed at $\omega_D = 6$ kHz. The spectra are broadened by 1 kHz as described in Fig. 3.

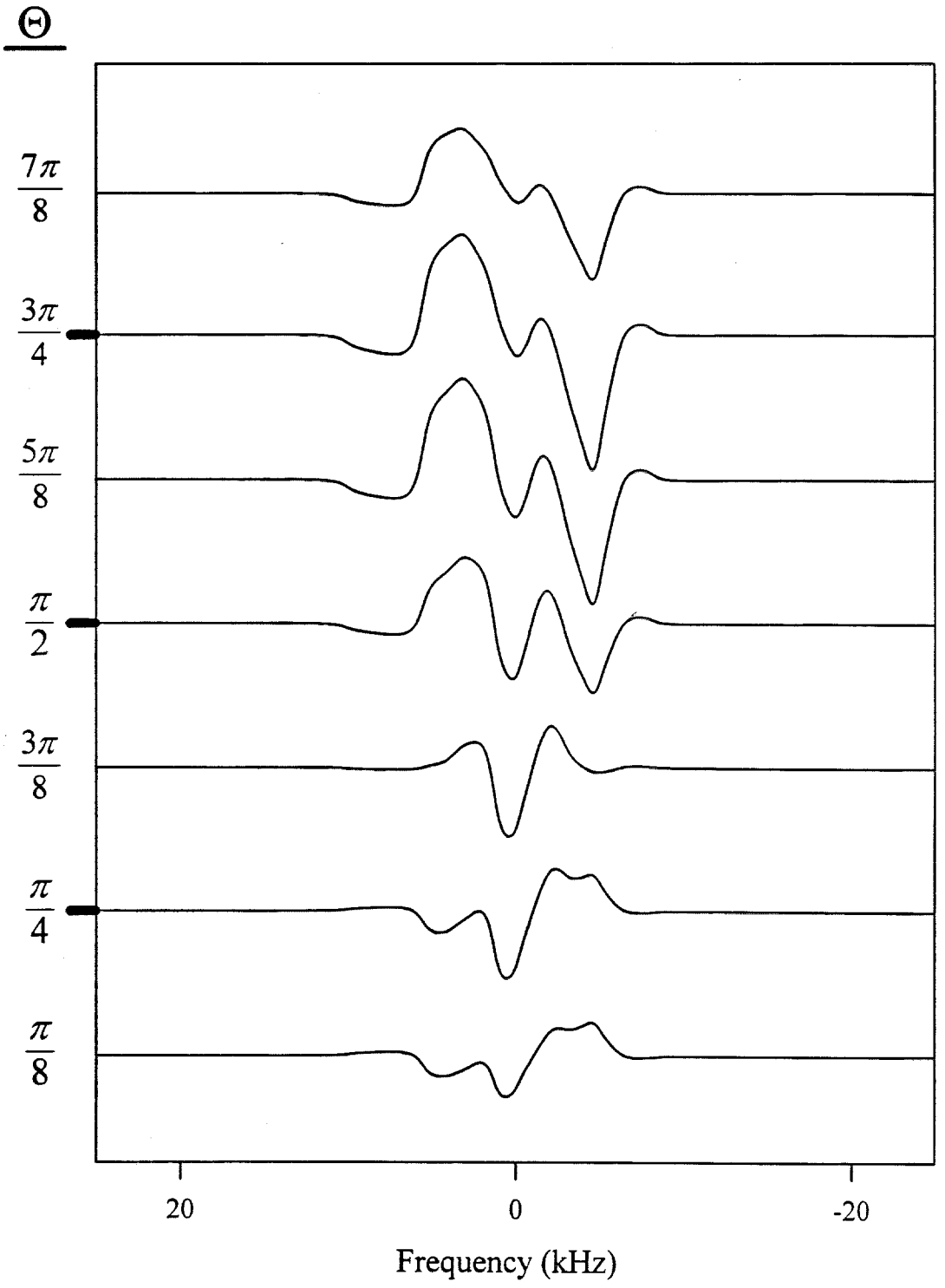

Fig. 7. Theoretical calculation of the integrated magnitude of the powder-PASADENA spectrum as function of pulse flip angle Θ. The same chemical shift tensors as in Fig. 4 are used, with the isotropic chemical shift difference fixed at $\Delta_0 = 2$ kHz. The dipolar coupling is fixed at $\omega_D = 6$ kHz. The spectra were broadened by 1 kHz as described in Fig. 3 before taking the absolute value and integrating.

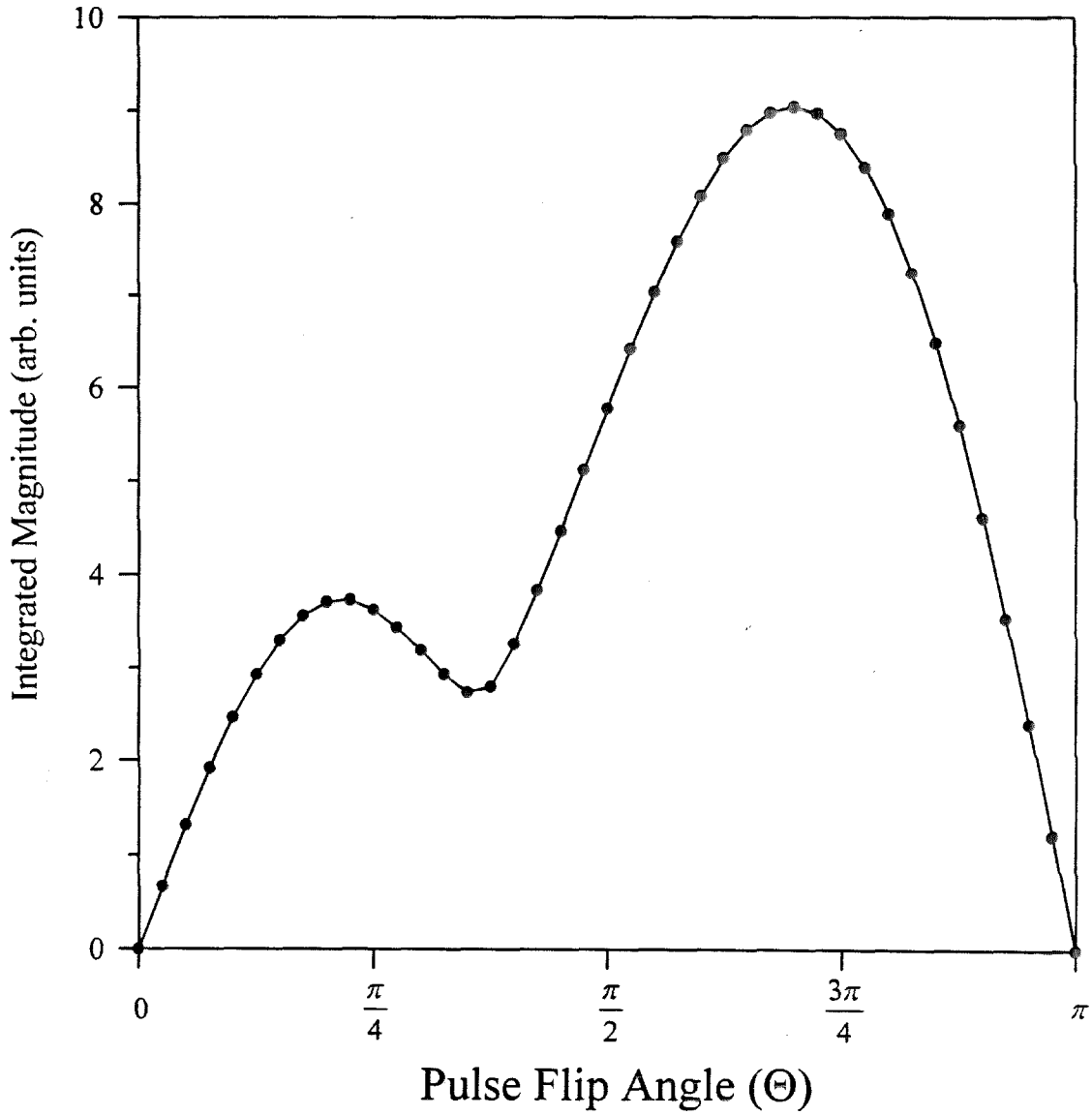

Chapter III. Parahydrogen-Enhanced NMR of H_2 Chemisorption at a Solid Surface

1. Heterogeneous Catalysis and the Active Sites on ZnO

Metal oxides are important constituents of many heterogeneous hydrogenation catalysts, either acting alone or in conjunction with metals or other oxides. Zinc oxide, in particular, is an important component in methanol synthesis catalysts, as well as olefin hydrogenation catalysts. Adsorption, kinetic, and infrared studies have all contributed to the construction of models for the active sites and intermediates.

The chemisorption of H_2 on ZnO is known to be accompanied by the appearance of O–H and Zn–H absorption bands in the IR spectrum.[1] This suggests the formation of the surface species:

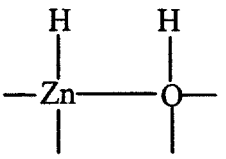

Fig. 1 shows a proposed reaction pathway for the catalytic hydrogenation of a generalized olefin by ZnO.[2]

Isotope studies [2] have shown that with a mixture of H_2 and D_2 added to the surface simultaneously during the olefin hydrogenation, the products alkane-d_0 and alkane-d_2 predominate. This is evidence that the two protons remain in close proximity to each other once adsorbed. Such a situation is important for the application of parahydrogen spin labeling since both atoms from a single H_2 molecule must remain coupled to each other long enough for the enhanced spin order to be detected. Conversely, this property of PASADENA will allow it to discriminate against catalytically irrelevant surface sites.

Two main types [3] of hydrogen adsorption on ZnO are observed at room temperature. Type 1 is fast and reversible. Type 2 is initially fast but then slows and is irreversible. Type 1 adsorption is accompanied by the occurrence of O–H and Zn–H bands in the IR whereas Type 2 is not. Type 1 was also found [3] to be the only one of the two types to directly participate in ethylene hydrogenation. The density of Type 1 sites on ZnO has been measured [4,5] to be roughly 10^{18} sites/m^2 with variation depending on the method of synthesis of the ZnO during manufacture.

Models for the active Type 1 sites have focused largely on the clean, reconstructed surfaces exposed in the polycrystalline material. ZnO crystallizes in a hexagonal wurtzite structure.[6] The three natural faces [7] of ZnO are the polar (0001) surface with Zn ions more outwardly exposed than O ions, the polar $(000\bar{1})$ surface with O ions more outwardly exposed than Zn ions, and the nonpolar $(10\bar{1}0)$ surface with Zn and O ions lying in the same plane.

Combined IR and kinetic studies,[8] as well as IR studies using coadsorption of CO [9] have led to the proposal that the Type 1 adsorption sites for H_2 are located on

the $(000\bar{1})$ surface. Evidence from coverage-induced IR frequency shifts [10] has led to the alternative suggestion that the Type 1 sites may be located on the (0001) surface. For illustration, a diagram depicting the sites proposed on the (0001) surface is shown in Fig. 2. Attention has also been given [5,11] to the role that surface defects, steps, and edges between faces may play in the catalytic activity of ZnO.

Combined temperature programmed desorption and IR studies [4] have revealed details in the energetics of Type 1 binding. In particular, this work has led to the subdivision of Type 1 binding into two distinct room-temperature binding states, distinguished by their desorption activation energies, while sharing the same IR spectra and nearly the same binding energies. A third Type 1 state, populated only at low temperatures, has also been found which differs from the other two in its IR spectrum and binding energy, as well as its desorption activation energy.

There is also evidence that Type 1 sites, correlated with ZnO-catalyzed ethylene hydrogenation,[3] may not be active in multicomponent catalysts containing ZnO. In particular, temperature-programmed desorption, combined with IR, and selective site blocking studies have led to the conclusion [12] that methanol synthesis on mixed Cu/ZnO catalysts probably does *not* involve Type 1 sites on ZnO.

Clearly, probes with greater structural discrimination are needed to reveal the locations of catalytic activity and characterize their structure. The high degree of chemical specificity obtainable with NMR, combined with its unique ability to measure internuclear distances (via the dipolar coupling interaction) in the solid state, make it attractive as such a probe. However, the poor sensitivity of NMR due to the small size of the energy quantum involved (both in the generation of spin order by the Curie law and in

the detection of the signal), combined with the relative diluteness of surface-bound species in a given volume of sample, hamper the use of NMR in surface studies. The PASADENA effect serves to ameliorate one of these sensitivity limiting factors, that of weak spin order as used in traditional NMR, with potentially orders-of-magnitude enhancement realizable.

2. Experimental Methods

The apparatus and methods for detecting reversible H_2 adsorption on ZnO using the PASADENA technique are described here. All experiments were performed at room temperature, employing moderate vacuum conditions for sample degassing. Powdered ZnO was used with the following specifications:[1] a purity of 99.8%, a mean surface area of 3.5 m^2/g, and a mean particle size of 0.31 μm.

Two different custom sample holders were used in the experiments. The first sample holder consisted of a 2 cm long NMR tube (diameter 5 mm) sealed at one end and fused at the other to a 6 cm Pyrex tube with a $\pi/2$ bend to allow connection to a combination evacuation and H_2 delivery line running parallel to the bore of the magnet. The second sample holder was similar but the glass elbow was replaced with a right-angle "Ultra-Torr" fitting connected to a straight section of NMR tube (also sealed at one end) that held the sample.

A 0.3 g sample of ZnO was packed into the tip of the NMR tube and held in place by a permeable glass wool plug. The sample was prepared by heating under vacuum in

[1] Strem Chemicals, Inc. (Newburyport, MA)

the sample holder to 673-723 K for > 4 hrs. Moderate vacuum was achieved with a belt-driven mechanical pump separated from the valve and sample arrangements by a liquid nitrogen trap. After activation, the sample tube was positioned in the probe while under continuous evacuation and the probe arrangement positioned in the magnet. A schematic of the apparatus is shown in Fig. 3.

Para-enriched hydrogen was prepared by equilibration of the ortho-para mole fractions at 77 K using a paramagnetic salt for the catalyst. To accomplish this, the catalyst, Apachi nickel silica gel,[2] was packed into a section of coiled glass tubing and then activated by heating to 200°C for several hours in a stream of He gas. The coils were then immersed in liquid nitrogen and H_2 gas was passed through the coils prior to delivery to the sample. The calculated para mole fraction resulting from equilibration at 77 K is 0.5. The para-enriched H_2 was allowed to come to room temperature before introduction to the sample tube.

NMR was performed at 4.7 T, with a proton resonance frequency of 198 MHz. Two different spectrometers were employed for the experiments reported here: one a homebuilt heterodyne spectrometer and the other a Bruker MSL-200. The NMR probe incorporated a 6-turn solenoid (length 1.7 cm, i.d. 0.7 cm) for radiofrequency excitation and detection. The coil Q was ~300, and the pulse time for a $\pi/2$ flip of sample magnetization was 3.6 μs.

A three-way solenoid valve allowed alternation between evacuation of the sample and exposure to p-H_2. The valve was controlled by the pulse programmer of the spectrometer, allowing bursts of p-H_2 to be delivered to the sample in synchrony with the

NMR experiments. Standing pressure in the p-H_2 line feeding the Apachi catalyst coils was 1.6×10^5 Pa. The typical sequence for the valve state consisted of a period of evacuation of the sample, typically several minutes, followed by a brief burst of p-H_2, and then immediate re-evacuation. Hydrogen burst lengths reported refer to the nominal time the valve was open. The valve was connected to the sample tube by >1 m of plastic tubing (i.d. 4 mm) and 20 cm of stainless steel tubing of roughly the same diameter. For burst lengths of tens or hundreds of milliseconds, as reported here, the H_2 pressure at the sample during the burst may be assumed to be highly transient. A resonant rf pulse to excite coherence was delivered at the end of the nominal burst time, followed by detection of precessing magnetization.

The free induction decay was sampled at a rate of 10 μs/point (100 kHz quadrature bandwidth). The delay before the first data point on the MSL-200 was 10 μs and sampling of the imaginary points (from the observable $\langle I_+ \rangle$) was shifted relative to the real points by 5 μs, requiring special Fourier transformation. The delay before the first data point on the homebuilt spectrometer was 20 μs and sampling of complex pairs was simultaneous. Typically 128 to 256 data points were collected and the transients were zero-filled to double the number of collected points before Fourier transformation. No apodization was used. Pure PASADENA transients (after subtraction of background resonances) were corrected for the sampling delay by setting the point at true $t = 0$ to zero, according to theory, and by estimating the missing point at 5 μs or 10 μs (depending on the sampling delay) by interpolation between $t = 0$ and the first data point collected (t

[2] Houdry, Division of Air Products and Chemicals, Inc. (Philadelphia, PA)

= 15 μs for the first imaginary point collected on the Bruker spectrometer and t = 20 μs for the first complex pair collected on the homebuilt spectrometer). The superiority of this method of correcting for the sampling delay (which is applicable only to PASADENA spectra with background resonances subtracted out) over traditional first-order phasing is confirmed by simulation. Experiments with n-H_2 (non-PASADENA experiments) were corrected for the sampling delay by fitting in the time domain and reconstructing the missing first two data points from the model.

3. Detection of Surface PASADENA

Hydrogen chemisorption experiments were performed on ZnO using both normal and para-enriched H_2. Fig. 4(a) shows the spectrum observed when a burst of n-H_2 of nominal length 50 ms is delivered to the sample. Fig. 4(b) shows the same experiment repeated with para-enriched H_2. Both spectra were acquired with a $\pi/4$ (flip angle) excitation pulse and represent single unaveraged shots. A prominent pattern of antiphase transitions is seen in Fig. 4(b). The antiphase character of these transitions is consistent with the PASADENA initial condition. The spectrum is interpreted as the parahydrogen-enhanced NMR of H_2 chemisorbed on ZnO. Signal from these same adsorption sites is not detected in the n-H_2 spectrum, nor is it discernible in previous NMR studies of H_2 on ZnO.[13,14]

The n-H_2 spectrum in Fig. 4(a) shows a 1 kHz-wide line on top of a broad low lying resonance. This broad background, itself made up of a 3.7 kHz-wide line and a 26 kHz-wide line, is also seen in spectra taken when the sample is under vacuum (not

shown). The background is attributed to protonated species adsorbed before the H_2 burst, as well as to probe contamination. The major feature of the n-H_2 spectrum cannot arise from dissociatively adsorbed H_2 at the same sites seen in the PASADENA spectrum, which would be expected to give a multiplet of peaks spanning the same spectral range. Furthermore, no nondissociative physisorption of H_2 is expected at room temperature.[1] This leads to the interpretation of the 1 kHz-wide line as attributed primarily to the NMR of gas-phase o-H_2 (p-H_2 in the gas-phase is not NMR active). The possibility exists that dissociatively adsorbed H atoms—which either occupy sites that are magnetically equivalent or which do not remain magnetically coupled to their original molecular partners—contribute to the narrow line. Signal from sites such as these are not expected to contribute significantly to the spectrum and will be treated as equivalent to gas-phase signal for the purposes of obtaining the pure PASADENA spectrum as described below.

The p-H_2 spin isomer does not possess a net magnetic moment and as such is not NMR detectable in the absence of a reaction which breaks the symmetry of the two spins. The o-H_2 isomer, however, behaves as a net spin 1 particle in the NMR experiment, without the need for symmetry breaking. As a result, only the ortho mole fraction can contribute to the gas-phase signal. To obtain the pure PASADENA signal the two spectra in Fig. 4(a) and Fig. 4(b) were subtracted from each other as follows. A fit to the broad background resonances from spectra taken under vacuum was subtracted from both the n-H_2 spectrum and the p-H_2 spectrum. A fit to the gas-phase peak in the n-H_2 spectrum was weighted by a factor of 2/3, since the ortho mole fraction is 1/2 in the para-enriched H_2 and is 3/4 in n-H_2, and then subtracted from the p-H_2 spectrum. The resulting pure PASADENA spectrum is shown in Fig. 4(c). Although the highly transient pressures at

the sample during a burst were not measured, the possibility exists that these pressures differed between the n-H_2 experiment and the p-H_2 experiment, since the p-H_2 experiment required a packed coil of ortho/para conversion catalyst submerged in N_2 to be in line with the H_2 supply and the control valve. This could lead to an inaccurate estimate of the size of the background gas-phase peak in the PASADENA spectrum.

Experiments in which ZnO is exposed to continuous p-H_2 atmosphere, show that the enhancement disappears over a period of tens of seconds leaving a spectrum similar to the n-H_2 spectrum shown in Fig. 4(a) (but with a larger gas-phase peak since the spectrum in Fig. 4(a) represents a transient pressure burst). The time constant for ortho-para equilibration over ZnO, however, is on the order of 10 minutes[15], so that the disappearance of enhanced signal cannot be attributed to the loss of para enrichment. This suggests that the sites observed in the PASADENA spectrum fill up over a period of several seconds and that no significant amount of dissociative adsorption takes place after this. This is qualitatively consistent with data [3] which show that rapid Type 1 adsorption (known to be dissociative) saturates on a similar time scale of tens of seconds. The transient nature of the enhancement at the sites that initially show a PASADENA signal is consistent with the expected decay of enhanced spin order by ordinary spin-lattice relaxation. The experiment in which a short burst of p-H_2 is preceded by evacuation was consistently repeatable after several seconds. This indicates a reversible binding site, also consistent with Type 1 adsorption at room temperature.

Experiments in which the time of the hydrogen burst is varied show changes in the appearance of the PASADENA spectrum. Fig. 5 shows the pure PASADENA spectra for nominal burst lengths of 50 ms, 100 ms, and 200 ms. These spectra, and all others

presented in this section, were acquired with a $\pi/4$ pulse. Growth in the signal amplitude as a function of burst length indicates that the detected amount of adsorbed hydrogen is increasing with exposure time. In addition, the powder line shape of the enhanced spectrum is seen to change with exposure time. These data suggest the intriguing possibility that different adsorption sites are coming into occupation at different rates. Alternatively, spin diffusion is transferring order to spectroscopically distinct protons near the binding site. On top of either of these possibilities is the effect of ordinary spin-lattice relaxation, which may differ in rate between different types of sites due to differences in magnetic coupling to their environments.

Experiments in which the period of evacuation between p-H_2 bursts was made sufficiently small show that a "steady-state" PASADENA lineshape is achieved that differs from the initial lineshape that is observed after a long period (minutes) of evacuation. This is illustrated in the series of spectra shown in Fig. 6 which were acquired 29 s apart from each other, with evacuation between shots. The relatively featureless background resonances are not removed from these spectra (nor from the spectra of Fig. 7-Fig. 9 to follow). Also, conventional first-order phasing was applied to these spectra (and as well to the spectra of Fig. 7-Fig. 9) since the interpolation method described in Section 2 only applies to PASADENA data without background resonances.

The first spectrum in the sequence in Fig. 6, indicated with open circles, is seen to differ noticeably from all subsequent shots, which do not significantly change from one shot to the next. This indicates the possibility that the experiment is discriminating between sites that have different desorption times and yet are still reversible. Fig. 7 shows a similar series of spectra but with the time between shots 12 s. The same result is seen

that the first shot of the series (indicated with open circles) differs significantly from subsequent shots, which do not differ from each other. The inset illustrates the reproducibility of the first-shot of a closely spaced series of shots. "First shots" of a series were typically preceded by at least several minutes of evacuation. The smaller steady-state amplitude of at least portions of the spectra taken 12 s apart relative to the spectra taken 29 s apart indicate that even the more rapidly desorbing sites are not completely freed of adsorbate between p-H_2 bursts separated by the shorter time.

Fig. 8 shows a series of spectra in which the length of the p-H_2 burst was varied between 50 ms and 500 ms. As in Fig. 5, the spectra show changes not only in the overall amplitude as a function of burst length, which is expected because more sites become occupied due to increased exposure time, but also in the relative amplitudes of spectral features. Fig. 9 shows a series of spectra in which the delay between the end of a 500 ms p-H_2 burst and the rf excitation pulse is varied from 50 ms to 800 ms. The end of the burst is defined as the nominal time at which the control valve was closed to p-H_2 and opened simultaneously to vacuum. These spectra are each four scan averages preceded by a single dummy scan (achieving, as demonstrated above, a periodic "steady-state" in the adsorption kinetics). The loss of signal as a function of increasing delay before the pulse is attributed in part to spin-lattice relaxation of the enhanced spin order. Another source of the loss of signal can be assumed to be desorption during the delay after the burst and before the rf pulse. The change in the relative amplitudes of the spectral features indicates several possibilities, including (1) different spin-lattice relaxation times for different types of sites, (2) spin diffusion between different types of sites, (3) different desorption kinetics for different types of sites.

The experiments in Fig. 4 and Fig. 5 were all performed on the homebuilt spectrometer with one of two different experimental setups (of nominally the same apparatus). The experiments in Fig. 6-Fig. 9 were all performed on the Bruker spectrometer with the second of these two setups. The two setups differed most importantly in the length of tubing that separated the control valve from the sample (~1 m for the first setup and ~3-4 m for the second setup). This presumably resulted in significantly different pressure transients for the same p-H_2 "burst" lengths, as evidenced, for example, by the different appearance of the spectra following a 50 ms burst on the two setups (compare Fig. 4(c) and the first spectrum in Fig. 8). Another possible source of differences in spectra is the variation from run to run and between the two setups in sample activation conditions (temperature, pressure, time of degassing, and initial sample contamination).

4. Simulations and Modeling

Powder-averaged PASADENA spectra have been simulated by integrating the theoretical PASADENA lineshape for an oriented, isolated two-spin system over all possible crystallite orientations, as described in Chapter II. Using this simulation capability a random search of parameter space for near matches to the data was performed. The spectrum following a 50 ms burst of p-H_2 was taken to be more likely to represent a single type of site than a spectrum following a longer burst and was used in the search for fits to the data.

The range of interproton distances sampled was 1.3 Å to 3.5 Å. The ranges of the chemical shift tensor parameters sampled were as follows: 0 to 8 kHz (0 to 40 ppm) isotropic shift difference, −16 to 16 kHz (−80 to 80 ppm) anisotropy, 0 to 1 asymmetry parameter, and all possible unique sets of Euler angles. The average isotropic shift was optimized for χ^2 after each simulation by shifting the simulated spectrum in increments of the number Hz per point in the spectrum, saving computation time by not requiring a separate powder average calculation for each different average isotropic shift. The linewidth for a single cyrstallite orientation was estimated from the data to be 1 kHz and was kept fixed. The simulated spectra were broadened with this linewidth by convolution with a Lorentzian lineshape.

Out of 2×10^6 random simulations, the best 100 fits to the data (ranging in reduced χ^2 value from roughly 2.3 to 3.5) were chosen for analysis of their Hamiltonian parameters. These top 100 are termed "near matches" to the data. None of the randomly generated simulations was iteratively optimized beyond finding the best average isotropic shift after the powder average calculation (by sliding the simulation from side to side). Such iterative optimization on top of the random search would increase the computation time likely by several orders of magnitude.

Fig. 10 shows the distribution of interproton distances, as well as the distribution of reduced χ^2 values among the near matches. Distinct clustering of interproton distances is seen around 1.8 Å and 2.5 Å, suggesting that one or both of these distances may be represented in the data.

Fig. 11-Fig. 14 show the distribution among the near matches of the average isotropic shift, the isotropic shift difference, the reduced anisotropy, and the asymmetry

parameter. The distributions of these parameters are computed separately for near matches that fall into the two clusterings of interproton distances. In all of the distributions shown, spin 1 refers to the spin with the more downfield (larger positive resonance frequency) isotropic shift. Distinct distributions of all of the chemical shift tensor parameters shown (except the asymmetry parameter which shows no significant clustering of its possible values) are seen for the two groupings of possible interproton distances.

Averages of the two clusterings of near matches according to their interproton distance and the standard deviations of these simulations are shown in Fig. 15. It is important to recognize that these averages do not themselves represent fits to the data, since they each derive from disparate sets of chemical shift tensor parameters. The standard deviations within each grouping indicate their closeness in lineshape to each other. Taken together the average and standard deviation illustrate visually the closeness of the near matches to the data. A smaller, less precise random search (2×10^5 parameter sets), showed no near matches between 3.5 Å and 7 Å. This smaller search differed in the range of interproton distances sampled (1.5 Å to 7 Å) as well as in the level of convergence of the powder spectra (not considered to be significant) and used flat sampling of the angle β in the shift tensors instead of spherically-weighted sampling (also not considered to be significant).

While this random search analysis cannot be used to rigorously exclude possible interproton distances represented in the data, it nonetheless strongly suggests that the reversible chemisorption sites detected on the surface of ZnO in these experiments have interproton distances near either 1.8 Å or 2.5 Å or a combination of both. This may

(although not necessarily) rely on the assumption that a single site geometry (i.e., a single spin Hamiltonian) dominates the appearance of the one-pulse PASADENA spectrum used in the random search.

5. Isolating Terms in the Initial Condition Based on Nutation Frequency

The initial condition in the PASADENA experiment, given by the density operator in Chapter I, Eq. 32, contains both linear terms (linear in the two I_z operators) and bilinear terms. The linear terms nutate (for a strong rf pulse on resonance) at the frequency ω_{rf} corresponding to the strength of the resonant component of the rf field, owing to the straightforward dynamics of spin operators under rotation. The bilinear terms, for the same reason, nutate at $2\omega_{rf}$. The presence of terms in the initial condition that nutate at different frequencies is a feature of the PASADENA experiment that is not found in a simple, conventional NMR experiment. This feature allows the independent selection of these different terms for evolution under the full Hamiltonian.

One method for obtaining the spectrum due to either the difference magnetization or the dipolar order alone is to simply acquire PASADENA spectra at two different pulse flip angles (where this angle refers by convention to the angle at which magnetization, arising from linear terms, is rotated by the pulse) and perform the appropriate linear combination of the two spectra. For example, the spectrum due to dipolar order in the initial condition can be obtained by subtracting a full PASADENA spectrum acquired with a $\pi/2$ pulse from a similar spectrum acquired with a $\pi/4$ pulse, with each spectrum weighted by the reciprocal sine of its pulse angle.

Another method, based essentially on the same principle but different in execution, is to Fourier transform a series of spectra acquired with incremented pulse angles in the dimension of the nutation time. The slice in this 2D spectrum at ω_{rf} corresponds to the spectrum of the difference magnetization (plus background resonances) evolving under the full Hamiltonian. The slice in the 2D spectrum at $2\omega_{rf}$ corresponds to the spectrum of the dipolar order, free of background signal, evolving under the full Hamiltonian.

Simulations of spectra arising from difference magnetization are shown in Fig. 16. The Hamiltonian parameters used for the simulations are the same parameters used to generate the full PASADENA spectra shown in Fig. 3 of Chapter II, with correspondence between parts (a)-(e) of the two figures. Fig. 17 shows simulations of spectra arising from dipolar order corresponding, respectively, to the same parameter sets as Fig. 16. The lineshapes of the spectra from the two terms in the initial condition are seen to differ dramatically from each other for the same Hamiltonian. Note that the spectra in Fig. 17 are scaled independently from those in Fig. 16, as well as from each other. Only one of the simulations of pure dipolar order in the initial condition, Fig. 17(d), shows the obvious character of an antiphase Pake doublet, affording easy visual estimation of the dipolar coupling parameter (equal to 2/3 of the splitting between the two major peaks in the antiphase doublet).

A low-resolution nutation experiment of this type was performed on the surface PASADENA system described in the section above and the spectrum arising from dipolar order obtained. A series of fourteen spectra were collected with the rf pulse length incremented for each successive spectrum. The nominal pulse length for the first

spectrum was 0.67 μs and the length was incremented by 0.67 μs. For reference, the measured $\pi/2$ pulse length for this experimental run was 2 μs. The p-H_2 burst length was 500 ms and the experiment was performed on the same experimental setup as that used for Fig. 6-Fig. 9 (described above). Background resonances were not subtracted from the spectra since they were not independently measured. However, as mentioned above, the background resonances, which necessarily arise from terms that are linear in spin operators, do not appreciably contribute to the slice of interest in the nutation spectrum.

The 2D Fourier transform (FT) that was performed was effectively a complex transform in the free evolution dimension (t_2) followed by a real transform in the nutation dimension (t_1). The way in which it was performed, however, was modified from convention in order to be able to apply the interpolation method for correction for the sampling delay in the t_2 dimension, as described in Section 2. The order of FT operations described above was reversed while still retaining quadrature information in the t_2 dimension, but at the same time assuring that the FT in the t_1 dimension was performed on real data. This was accomplished using the following identity:

$$\mathcal{F}_1\left\{\mathrm{Re}\left(\mathcal{F}_2\left\{S(t_1,t_2)\right\}\right)\right\} = \mathcal{F}_2\left\{\mathcal{F}_1\left\{S(t_1,t_2)\right\}\right\} + \mathcal{F}_2^{-1}\left\{\mathcal{F}_1\left\{S^*(t_1,t_2)\right\}\right\} \qquad (1)$$

in which $S(t_1,t_2)$ is the complex 2D signal and $\mathcal{F}_i$ is the Fourier transform with respect to the t_i dimension. This allowed time-domain correction for the sampling delay to be applied to the slice at $2\omega_1$. The data were apodized in the t_1 dimension to force decay to zero by the end of the transient and were zero filled to 128 points before Fourier transformation to make selection of the slice at $2\omega_{rf}$ more precise.

The 2D nutation spectrum obtained reveals featureless peaks (not shown) in the nutation dimension corresponding to ω_{rf} and $2\omega_{rf}$, since the spectrum is low resolution in this dimension. The slice at $2\omega_{rf}$, which is high-resolution in the free evolution dimension is shown in Fig. 18. A lineshape is seen which strongly hints at having the dominant character of an antiphase Pake doublet, with some extra features. Measuring the splitting between the large absorptive peak and the average position of the two emissive peaks as a rough starting point would predict a dipolar coupling parameter (assuming that the signal arises primarily from sites with the a single spin Hamiltonian) of ~9 kHz which would correspond to an interproton distance of ~2.4 Å.

A random search of parameter space for fits to the spectrum in Fig. 18 arising from dipolar order was performed. The search was completely identical in description and ranges of parameters sampled to the search performed in Section 3 for fits to the full PASADENA spectrum. The only differences were in the terms used in the initial condition and the spectrum used for the χ^2 calculation to determine goodness of fit. The results presented here represent the top 100 "near matches" to the data (ranging in reduced χ^2 from 4.4 to 7.4) for a total of 8×10^5 random simulations.

Fig. 19 shows the distribution of interproton distances and the distribution of reduced χ^2 values among the near matches. Clustering of interproton distances is seen around 2.3 Å, differing slightly from one of the clusters seen in the random search for fits to the full PASADENA spectrum. Notably absent is the cluster around 1.8 Å seen in the full PASADENA search.

Fig. 20-Fig. 23 show the distributions of the average isotropic shift, the isotropic shift difference, reduced anisotropy, and asymmetry parameter resulting from the random

search to the dipolar order data. As in the previous search, spin 1 refers to the spin with the more downfield isotropic shift. The distributions of these parameters all strongly resemble the analogous distributions seen among near matches to the full PASADENA spectrum for the group with interproton distances in the region of 2.5 Å (shown in Fig. 11-Fig. 14).

The average and standard deviation of lineshapes represented in the top 100 near matches to the dipolar order data are shown in Fig. 24. As mentioned for the near matches to the full PASADENA spectrum, this average does not represent a fit to the data. Together with the standard deviation the average summarizes visually the closeness of the near matches to the data.

The different results of the random searches for fits to the dipolar order spectrum and the full PASADENA spectrum have at least two possible explanations. The first stems from the different experimental conditions under which the two spectra were acquired. The dipolar order spectrum was acquired after a 50 ms burst and the experiment was preceded by at least several minutes of evacuation. The full PASADENA spectrum was acquired after a 500 ms burst and the repetition of the experiment while incrementing the pulse duration (and also while signal averaging) leads, as seen in Section 3, to a periodic steady-state in occupation numbers of the sites observed that is different from the distribution of sites observed in a single shot following a long period of evacuation.

The second possible reason for differences in the distribution of interproton distances found in the two searches is that the lineshape for the dipolar order spectrum for this particular system is more unique when compared to other lineshapes in parameter space than is the lineshape for the full PASADENA spectrum. The PASADENA

lineshape observed here may somehow be more generally attainable, to within the values of χ^2 achieved here, by more than one region of parameter space.

6. Enhancement and Sensitivity

Theoretical enhancement factors in the powder-PASADENA experiment are highly dependent on the degree of destructive interference between antiphase spectra arising from individual crystallites in the powder. This destruction of enhanced signal is unavoidable to some degree for any large number of randomly oriented crystallites (the definition of a powder) even if the lines in the individual crystallite spectra are well resolved. Its unavoidability is due in part to the near continuous distribution of orientations represented in the powder combined with the sign change in the dipolar coupling as the angle between the internuclear vector of the two protons and the magnetic field passes through its critical angle (the "magic angle," equal to ~54.7°). It is also, in general, greatly affected by the chemical shift anisotropy, as well as by the linewidths of resonances in the individual crystallites.

The enhancement factor for powder-PASADENA is defined here as the ratio of the integrated magnitudes of the PASADENA spectrum and the corresponding Curie-law ("ordinary NMR") spectrum. The enhancement calculations presented here neglect spin-lattice relaxation. The simulated Curie-law spectra for these calculations assume equilibrium magnetization at 300 K in a 4.7 T magnetic field, with a pulse flip angle of $\pi/2$ to maximize signal. The simulated PASADENA spectra assume a parahydrogen mole

fraction of $x_p = 0.5$ (corresponding to an enrichment factor in the initial condition of $f = 0.33$), with a pulse flip angle of $\pi/4$ (to match the data) unless otherwise specified.

A simulated PASADENA spectrum that roughly fits the data in Fig. 4(c) is shown in Fig. 24(a), along with the corresponding Curie-law spectrum. The calculated enhancement factor for this spin Hamiltonian is 724. The degree of destructive interference in this system is illustrated in Fig. 25, which shows powder-averages of the individual spin transitions for the spectrum in Fig. 24(a) and their sum. The spectra in Fig. 25(a) and (b) are plotted on the same scale as each other, illustrating the loss in signal intensity that results from powder averaging. For comparison, the corresponding individual transitions for the Curie-law spectrum are shown in Fig. 26, along with their sum. The differences in lineshape of the respective individual transitions for the PASADENA case and the Curie-law case arise from the unique orientation dependence of the PASADENA initial condition.

Theoretical enhancement factors for PASADENA spectra that start with the same Hamiltonian parameters as those used in Fig. 25 and vary either the dipolar coupling parameter ω_D or the isotropic shift difference Δ_0 are shown in Fig. 28 for two different pulse flip angles Θ. The functional form of this dependence of enhancement factor on the ratio ω_D / Δ_0, as well as its overall scale, is specific to the particular values of the Hamiltonian parameters which are not varied, namely the anisotropies, asymmetries, and Euler angles of the two shift tensors. The enhancement also depends, as mentioned above, on the underlying linewidths of the spectra from individual crystallites.

A few general observations about the dependence of the enhancement factor on the ratio ω_D / Δ_0 can be made. For fixed chemical shift parameters, the enhancement goes

to zero as ω_D goes to zero due to the destructive interference *within* each crystallite. The enhancement also goes to zero as ω_D goes to infinity since transitions between eigenstates with large population differences become increasingly dipole-forbidden (i.e., the degree of symmetry breaking upon reaction becomes increasingly diminished). For fixed ω_D, the enhancement reaches its maximum as Δ_0 goes to infinity (i.e., as ω_D/Δ_0 goes to zero) since this allows maximal separation (and hence minimal destructive interference) between spectral intensity due to spin 1 transitions and intensity due to spin 2 transitions. The case in which Δ_0 goes to zero is somewhat less interesting, since, in general, the spins will remain chemically inequivalent in this limit because of other shift tensor components that remain unequal.

In general, the enhancement factor for a given spin system can be manipulated by the appropriate application of multiple-pulse NMR sequences to scale the ratio ω_D/Δ_0. This is useful if it can be determined, either from a theoretical model for the spin Hamiltonian or empirically, that the enhancement factor is less than optimal. For example, if the dipolar coupling is too large relative to the chemical shifts, a pulse sequence such as WAHUHA or MREV, with tailored changes in delay times, can be used to scale it down. Less likely is the situation in which scaling the chemical shift down would significantly improve the enhancement. Spectroscopic first principles dictate, of course, that neither the dipole coupling nor the chemical shift can be scaled *up*, making traversal in Fig. 28 to the left along open circles or to the right along closed circles and impossibility.

The results of the random search for fits to the PASADENA spectrum, presented in Section 4, can be used as a basis for estimating the enhancement observed. Since the Curie-law spectrum from sites contributing to the PASADENA spectrum is not detected, the enhancement cannot be calculated directly. Its calculation thus depends on a model. On the assumption that the near matches found in the random search tend, on average, to approximate the true (unknown) model, the enhancement can be approximated using the near-match parameters. Calculated enhancements for each of the top 100 near matches are shown in Fig. 29(a) plotted versus interproton distance for the same near match. The median enhancement for near matches with $r < 2.1$ Å is 710 and for near matches with $r > 2.1$ Å is 970.

The sensitivity of the PASADENA experiment can be estimated in a similar fashion. The narrow, gas-phase peak in the n-H_2 spectrum at equilibrium pressure (not shown) gives a calibration point for spin counting (using a rough estimate of the volume of gas occupying the dead space in the sample tube). The sensitivity in the PASADENA experiment is estimated by taking the ratio of the integrated area of the Curie-law spectrum corresponding to the same parameters and the integrated area of the gas-phase peak. The ratio is then multiplied by the estimate of the number of spins in the gas-phase peak. Estimated sensitivities for each of the top 100 near matches to the PASADENA spectrum in Fig. 4(c) are shown in Fig. 29(b) versus interproton distance. The median sensitivity (reported as the number of protons observed) for near matches with $r < 2.1$ Å is $\sim 8\times10^{16}$ and for near matches with $r > 2.1$ Å is $\sim 4\times10^{16}$. Taking 10^{17} spins as an order of magnitude sensitivity estimate, the density of sites observed on the surface is estimated to be 10^{13} sites/cm^3, corresponding to roughly 1% of the available surface sites.[4]

7. References

[1] R.P. Eischens, W.A. Pliskin and M.J.D. Low, J. Catal. **1**, 180 (1962).

[2] K. Tanaka, Adv. Catal. **33**, 99 (1985).

[3] A.L. Dent and R.J. Kokes, J. Chem. Phys. **73**, 3772 (1969).

[4] G.L. Griffin and J.T. Yates, J. Catal. **73**, 396 (1982).

[5] C. Chauvin, J. Saussey, J.C. Lavalley and G. Djegamariadassou, Appl. Catal. **25**, 59 (1986).

[6] D.A. King and D.P. Woodruff, The chemical physics of solid surfaces and heterogeneous catalysis, (Elsevier, Amsterdam, 1984).

[7] S. Akhter, K. Lui and H.H. Kung, J. Phys. Chem. **89**, 1958 (1985).

[8] A.L. Dent and R.J. Kokes, J. Phys. Chem. **73**, 3781 (1969).

[9] F. Boccuzzi, E. Garrone, A. Zecchina, A. Bossi and M. Camia, J. Catal. **51**, 160 (1978).

[10] G.L. Griffin and J.T. Yates, J. Chem. Phys. **77**, 3744 (1982).

[11] V. Bolis, B. Fubini, E. Giamello and A. Reller, J. Chem. Soc., Faraday Trans 1 **85**, 855 (1989).

[12] D.L. Roberts and G.L. Griffin, J. Catal. **101**, 201 (1986).

[13] M. Watanabe and T. Ito, Japan. J. Appl. Phys. **19**, 1863 (1980).

[14] P.R. Dennison, K.J. Packer and M.S. Spencer, J. Chem. Soc., Faraday Trans. 1 **85**, 3537 (1989).

[15] W.C. Conner and R.J. Kokes, J. Phys. Chem. **73**, 2436 (1969).

Fig. 1. Schematic diagram of a proposed reaction pathway for olefin hydrogenation on the surface of ZnO. (From Ref. [2])

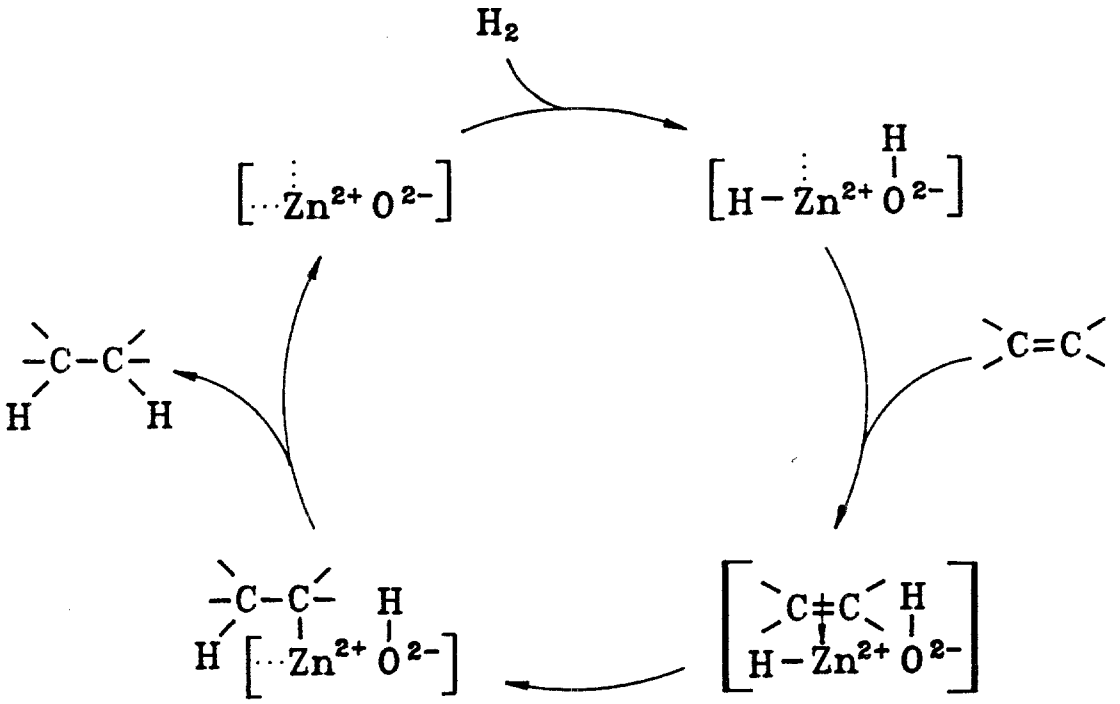

Fig. 2. Diagram of (2×2) reconstructed (0001) surface on ZnO, showing the possible location of Type 1 H_2 adsorption sites. (From Ref. [10])

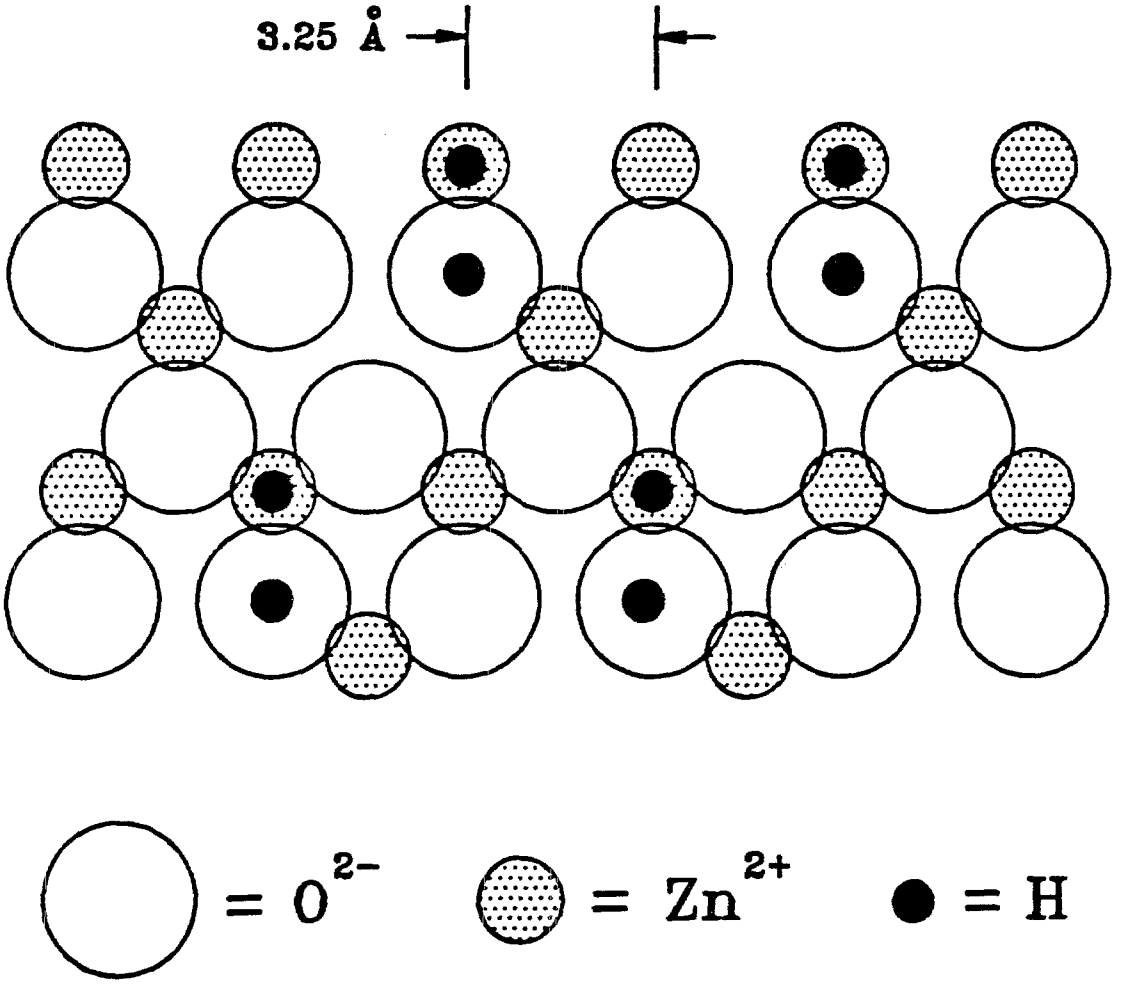

Fig. 3. Schematic diagram of apparatus used in solid-state PASADENA experiments. The box around the NMR probe indicates the portion of the apparatus that is inserted into the bore of a high-field magnet after sample activation.

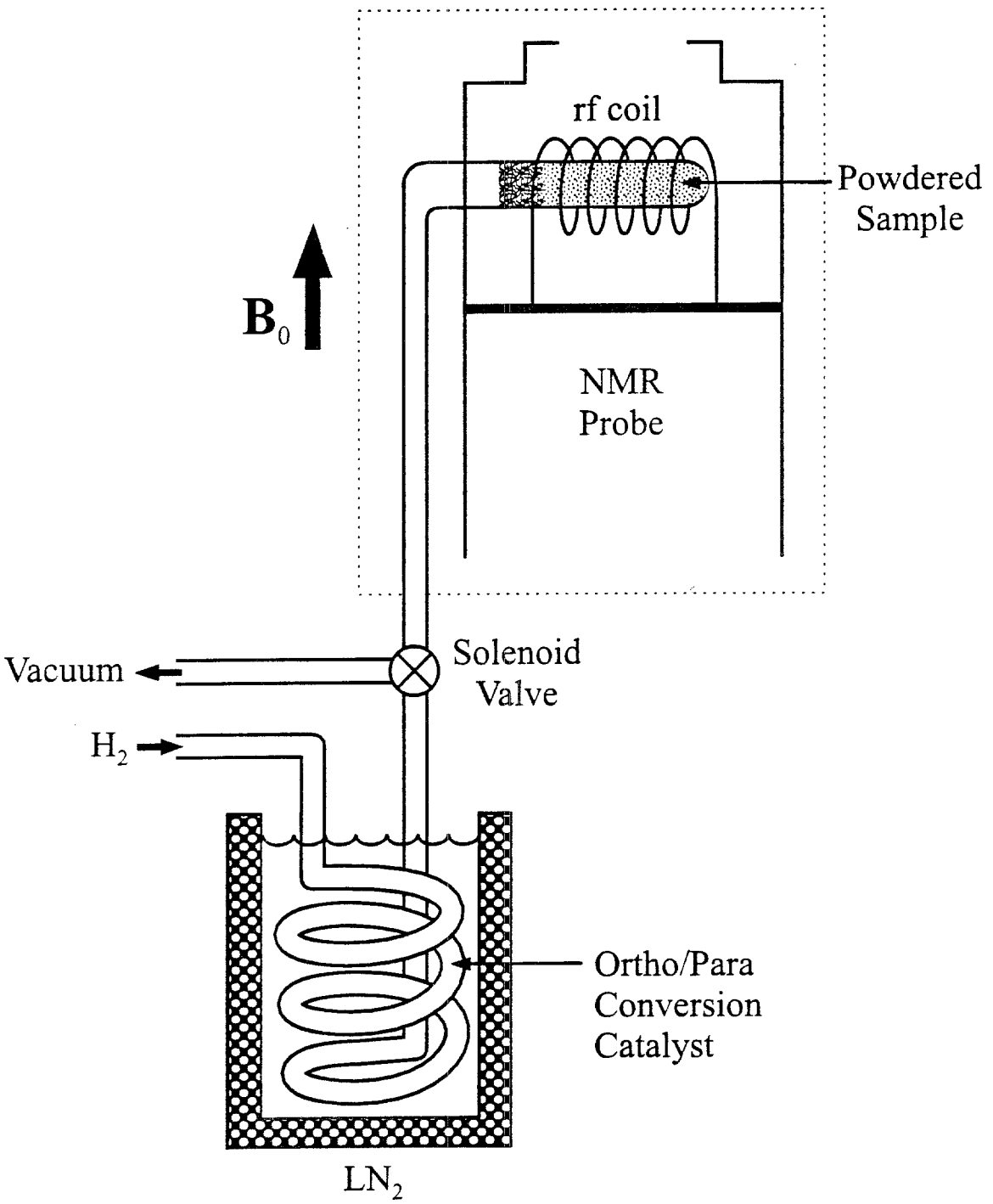

Fig. 4. (a) ^{1}H NMR spectrum immediately after a nominal 50 ms burst of n-H_2 delivered to polycrystalline ZnO. The spectrum represents a single scan acquired after a $\pi/4$ pulse. (b) Spectrum taken under the same conditions as in (a) but using para-enriched H_2 instead of n-H_2. Strong PASADENA enhancement is seen for sites not detectable in the n-H_2 experiment. (c) Pure PASADENA spectrum obtained by taking the ortho-weighted difference of (a) and (b), as described in the text.

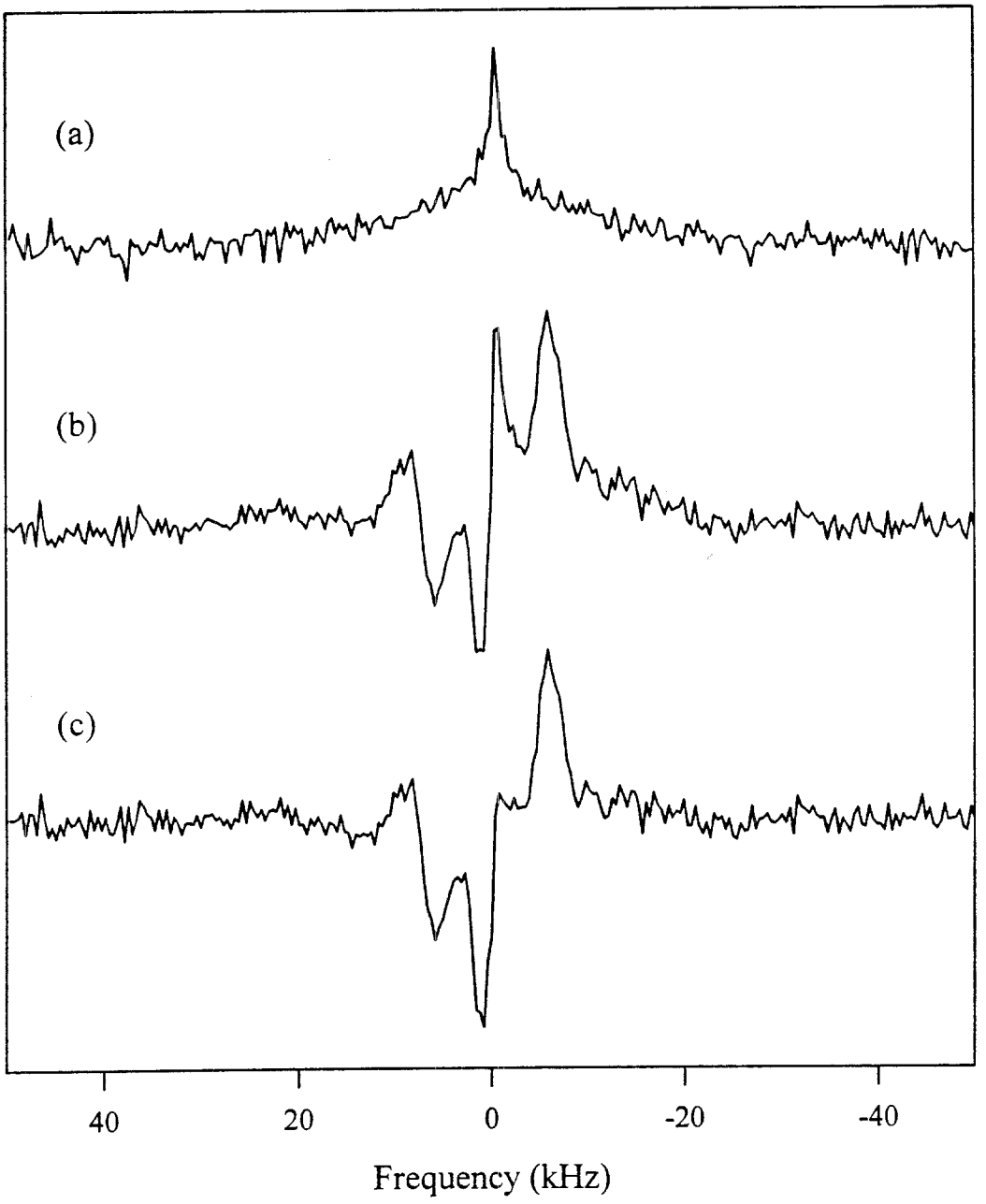

Fig. 5. PASADENA spectra of hydrogen chemisorption sites on ZnO after p-H_2 burst lengths of (a) 50 ms, (b) 100 ms, and (c) 200 ms.

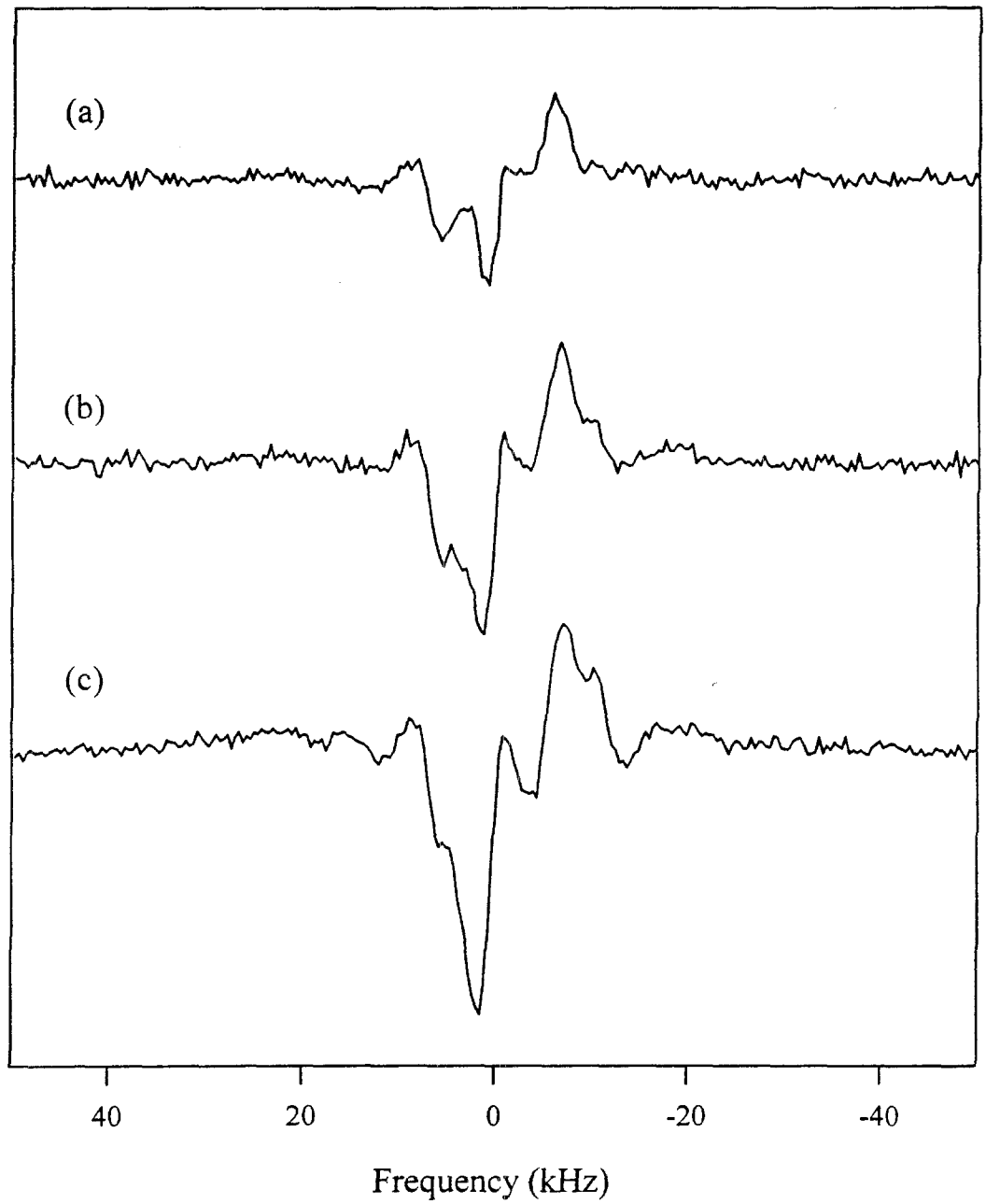

Fig. 6. A series PASADENA spectra, each following a 500 ms burst of p-H_2, taken 29 s apart from each other with evacuation between shots. The first spectrum acquired in the series is highlighted with open circles.

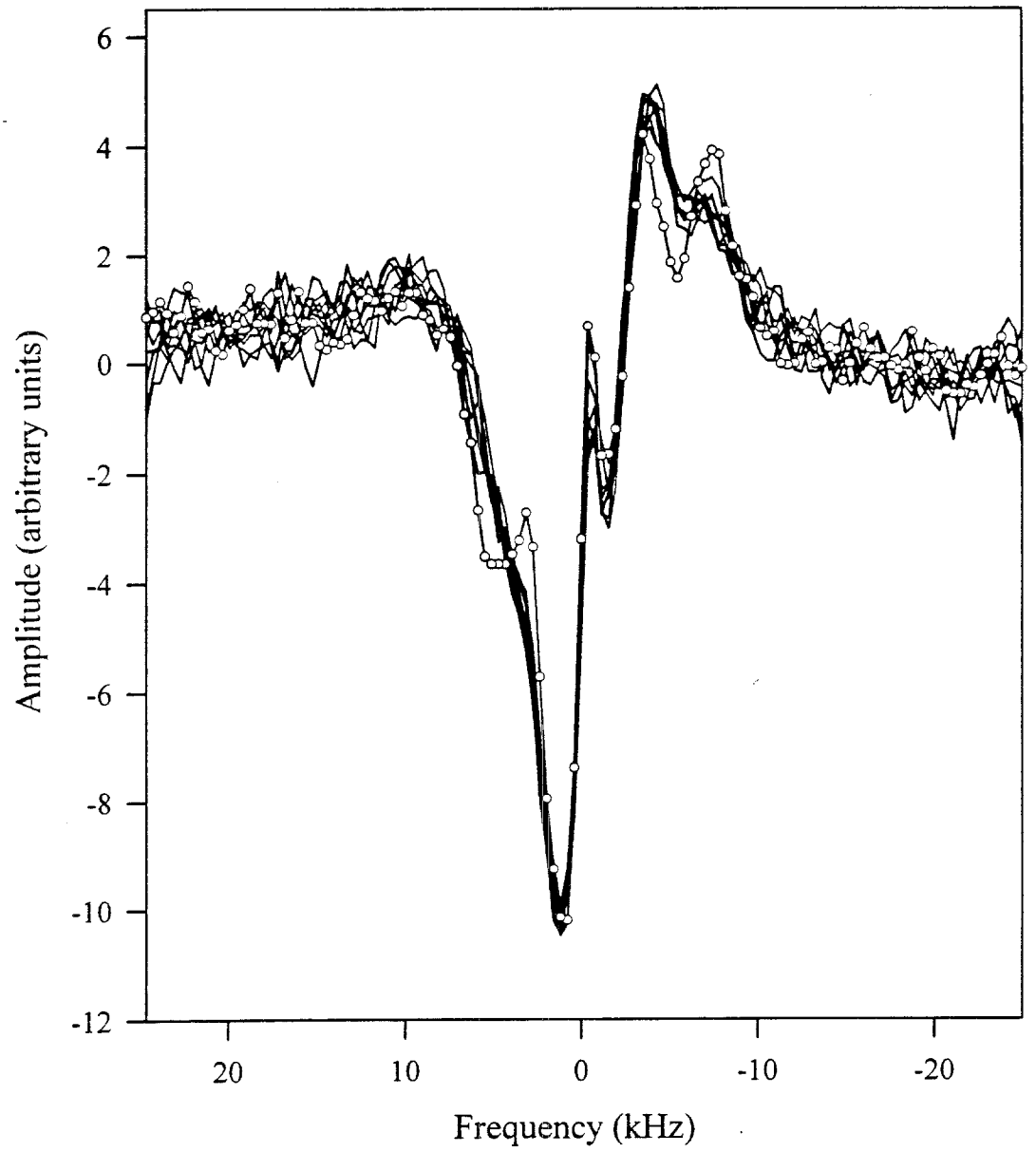

Fig. 7. A series PASADENA spectra, each following a 500 ms burst of p-H_2, taken 12 s apart from each other with evacuation between shots. The first spectrum acquired in the series is highlighted with open circles. The inset shows the first shot of the series (open circles) superimposed on the first shot of the series shown in Fig. 6 (filled circles), illustrating their closeness in lineshape to each other, relative to the shots that follow abbreviated evacuation periods in each figure.

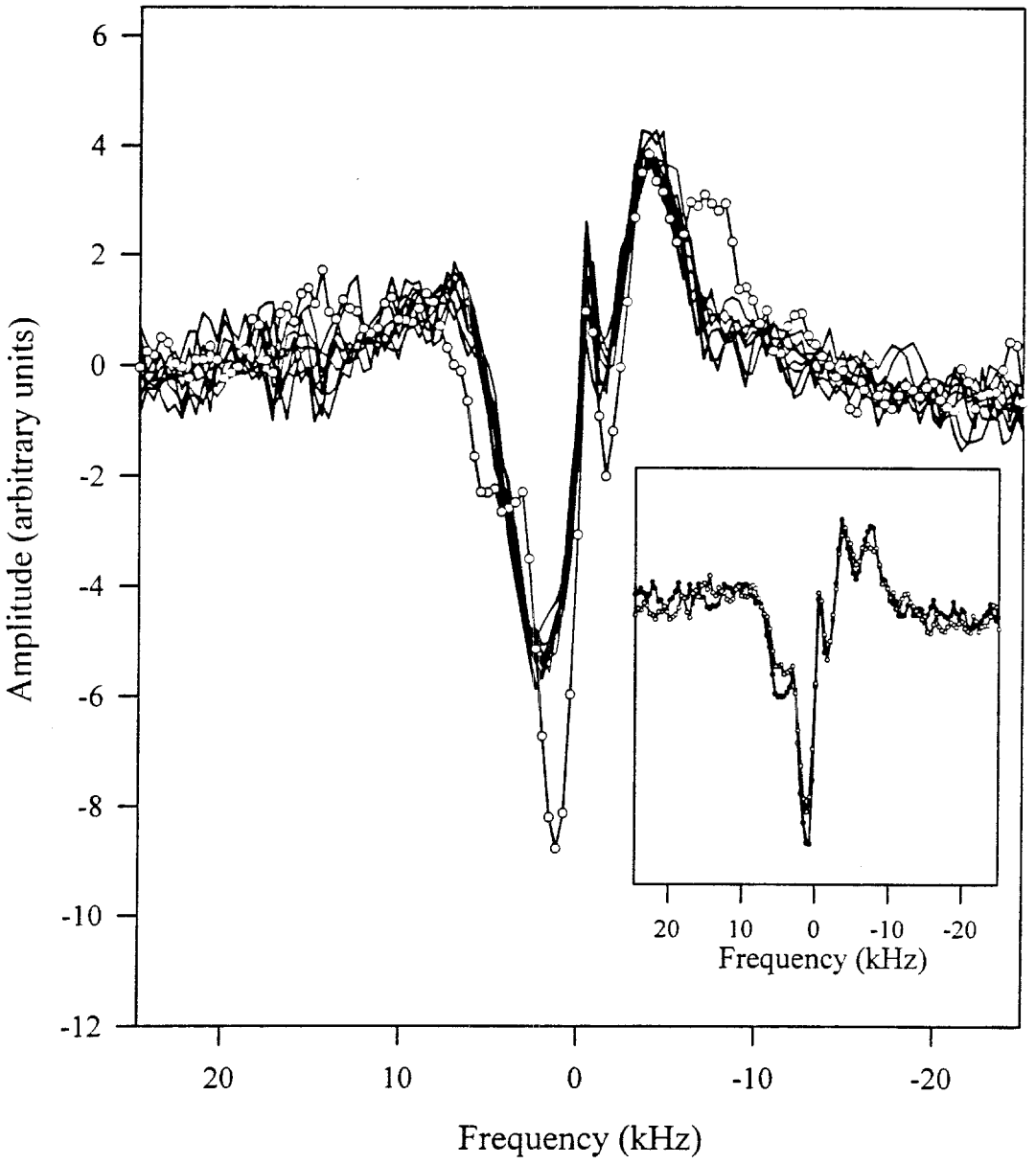

Fig. 8. A series PASADENA spectra in which the length of the p-H_2 burst is varied. The spectra are taken 29 s apart from each other with evacuation between shots. The first spectrum acquired in the series is the spectrum following a 50 ms burst.

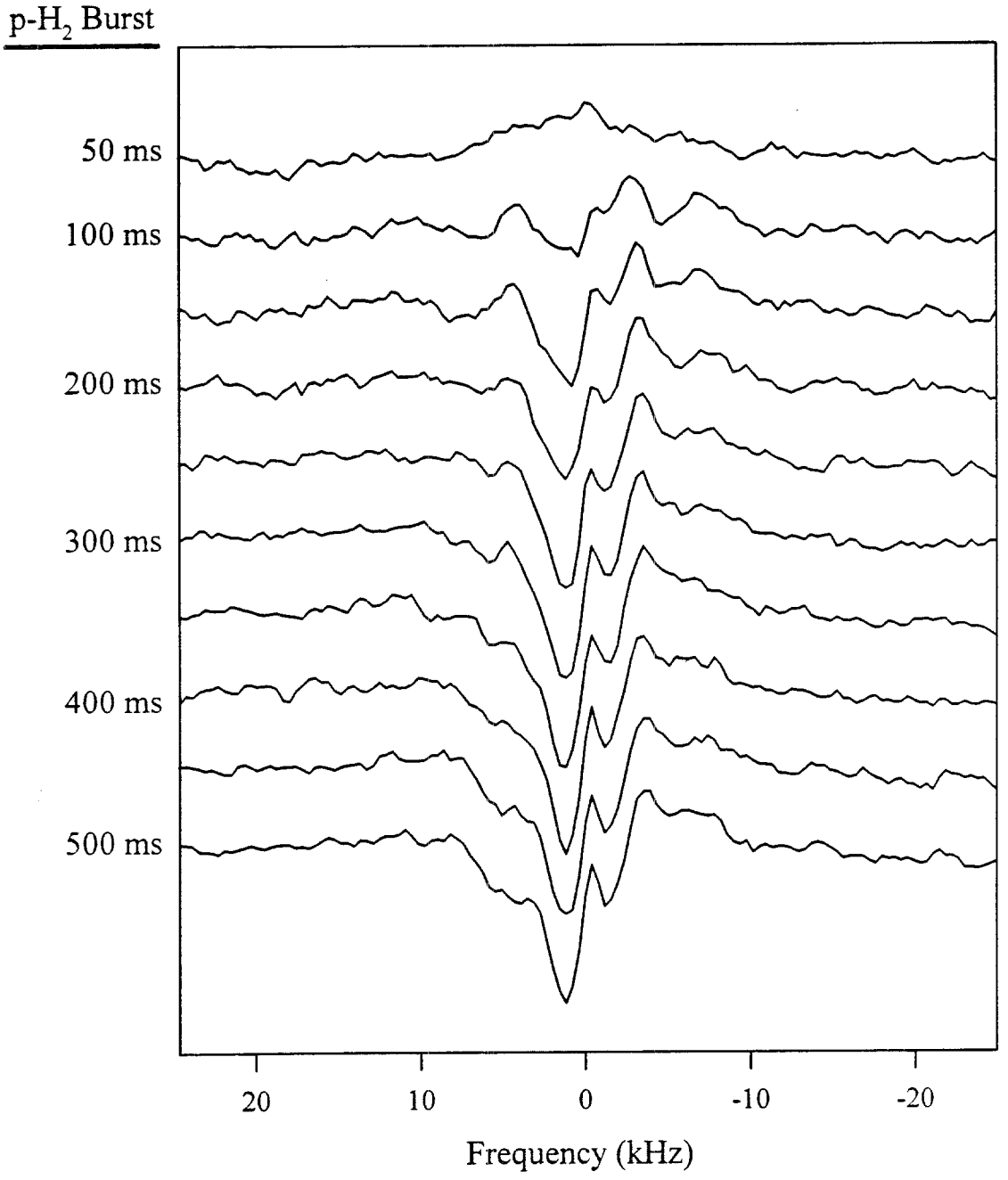

Fig. 9. A series PASADENA spectra in which the delay between a p-H_2 burst of 500 ms and the rf excitation pulse is varied. The spectra are taken 29 s apart from each other with evacuation between shots. The first spectrum acquired in the series is the spectrum following a 50 ms delay. All spectra are four scan averages, with one preceding dummy scan.

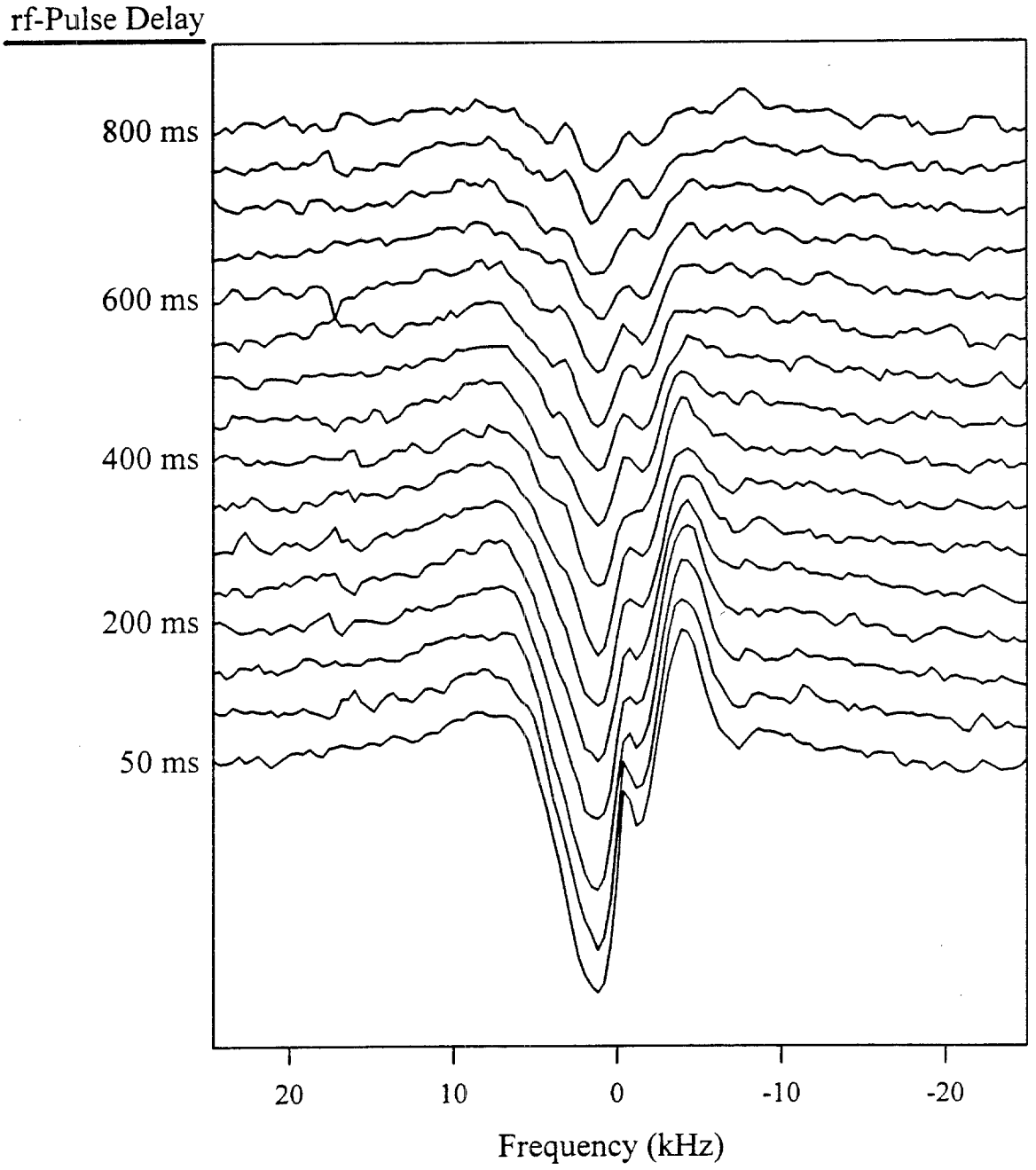

Fig. 10. (a) Scatter plot showing the reduced χ^2 and interproton distance for each of the simulations in the top 100 near matches to the one-pulse PASADENA spectrum in Fig. 4(c), taken from a large random search of 2×10^6 parameter sets spanning parameter space. (b) Distribution of the interproton distances represented in (a). Sampling of interproton distances was flat in the range shown and the distances were collected in contiguous bins centered at the points shown.

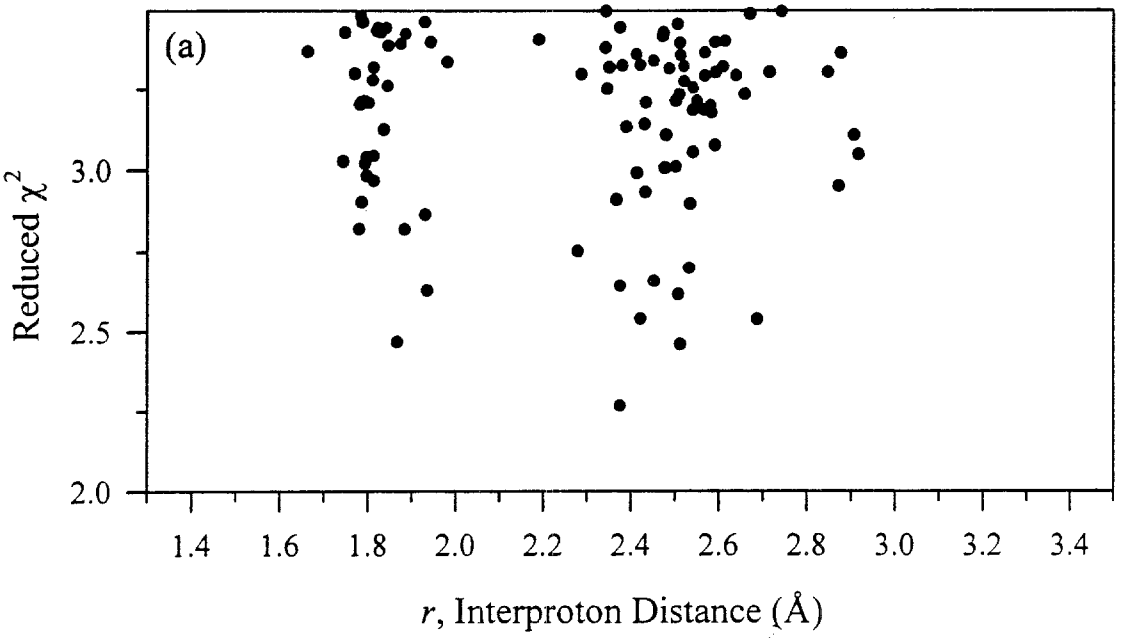

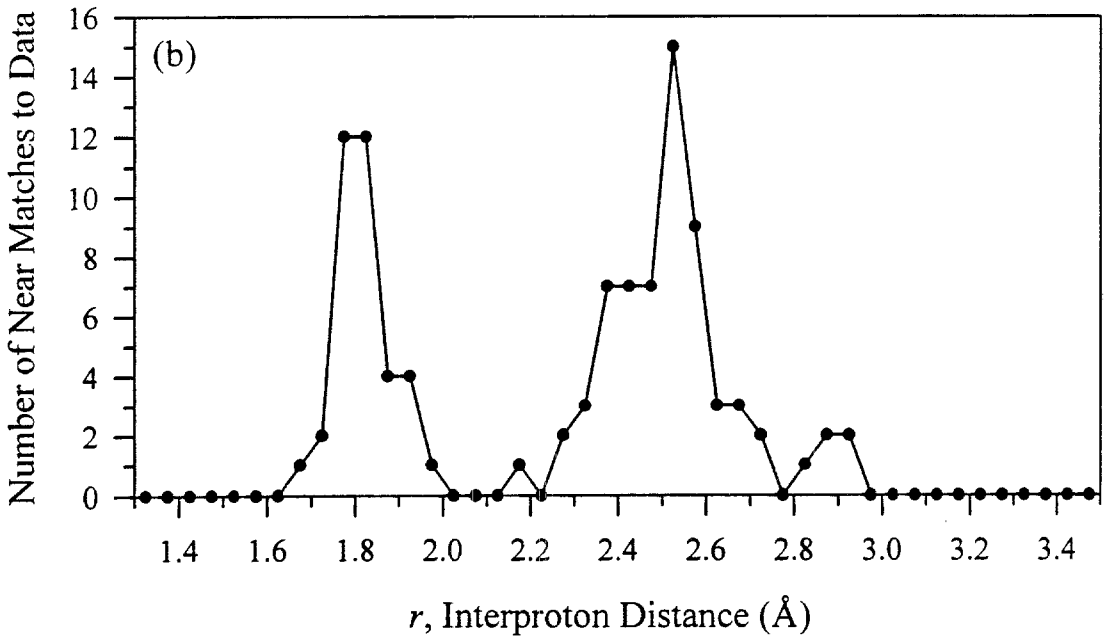

Fig. 11. (a) Distribution of average isotropic shifts represented in the top 100 "near-match" simulations of the one-pulse data in Fig. 4(c) that have interproton distances (r) less than 2.0 Å. (b) Distribution of average isotropic shifts among near matches that have interproton distances greater than 2.0 Å.

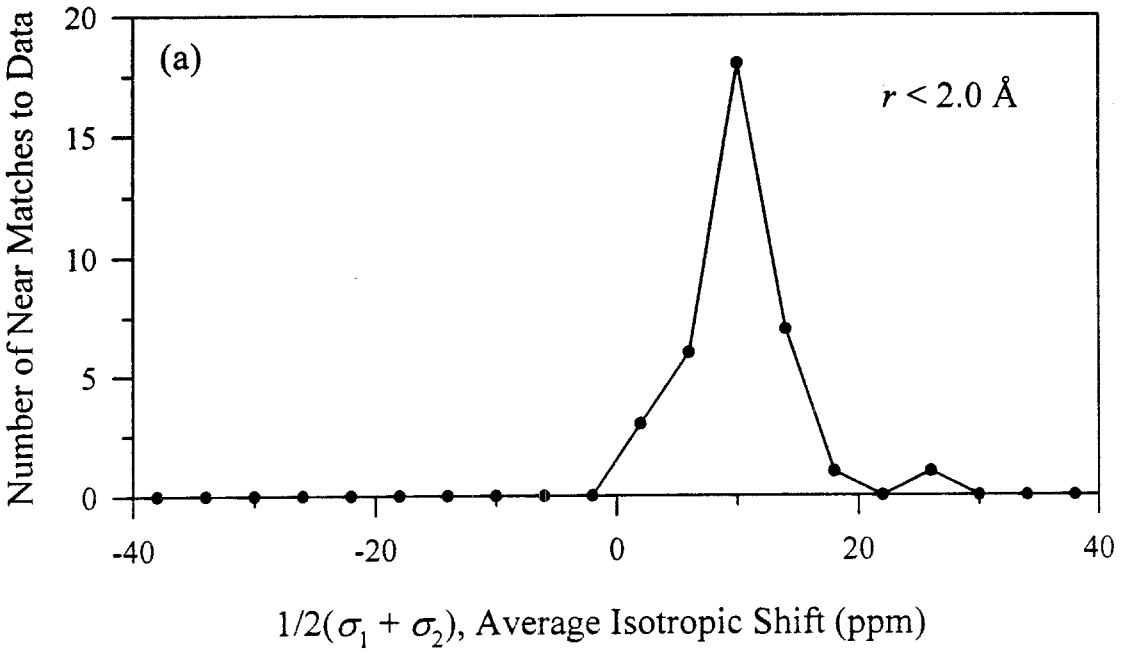

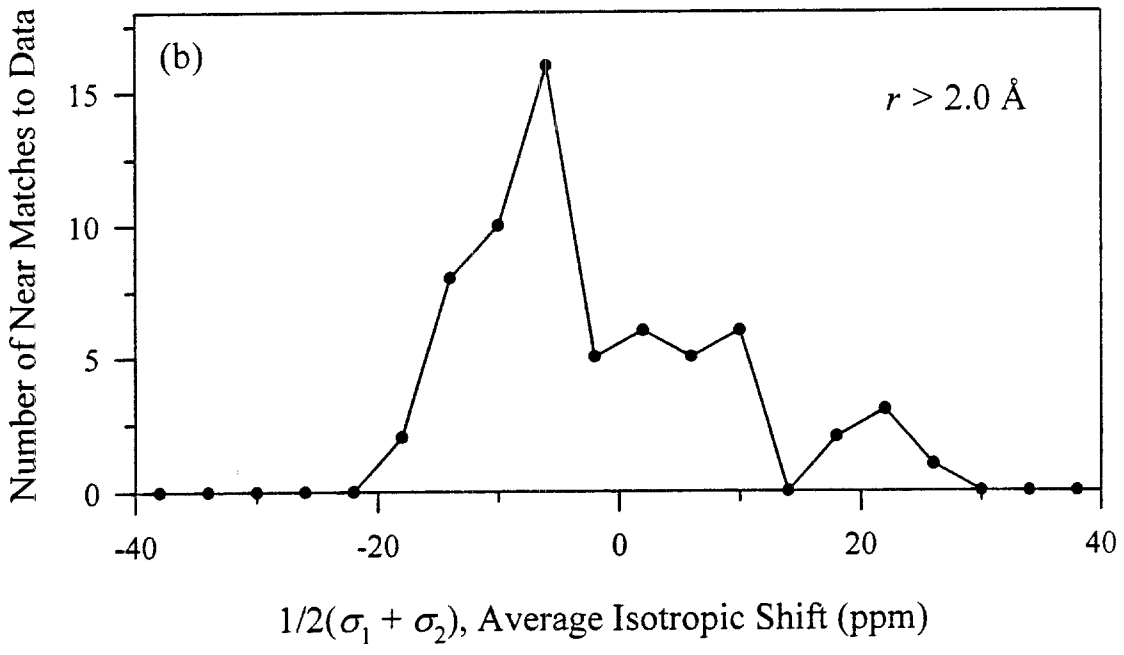

Fig. 12. (a) Distribution of isotropic shift differences represented in the top 100 "near-match" simulations of the one-pulse data in Fig. 4(c) that have interproton distances (r) less than 2.0 Å. (b) Distribution of isotropic shift differences among near matches that have interproton distances greater than 2.0 Å.

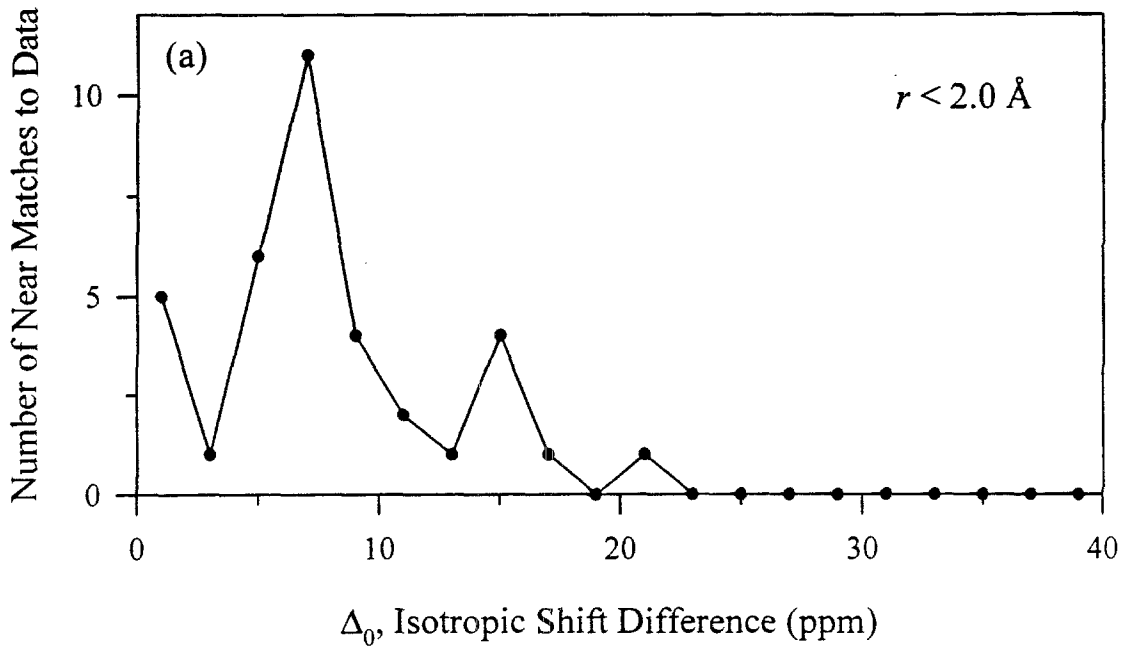

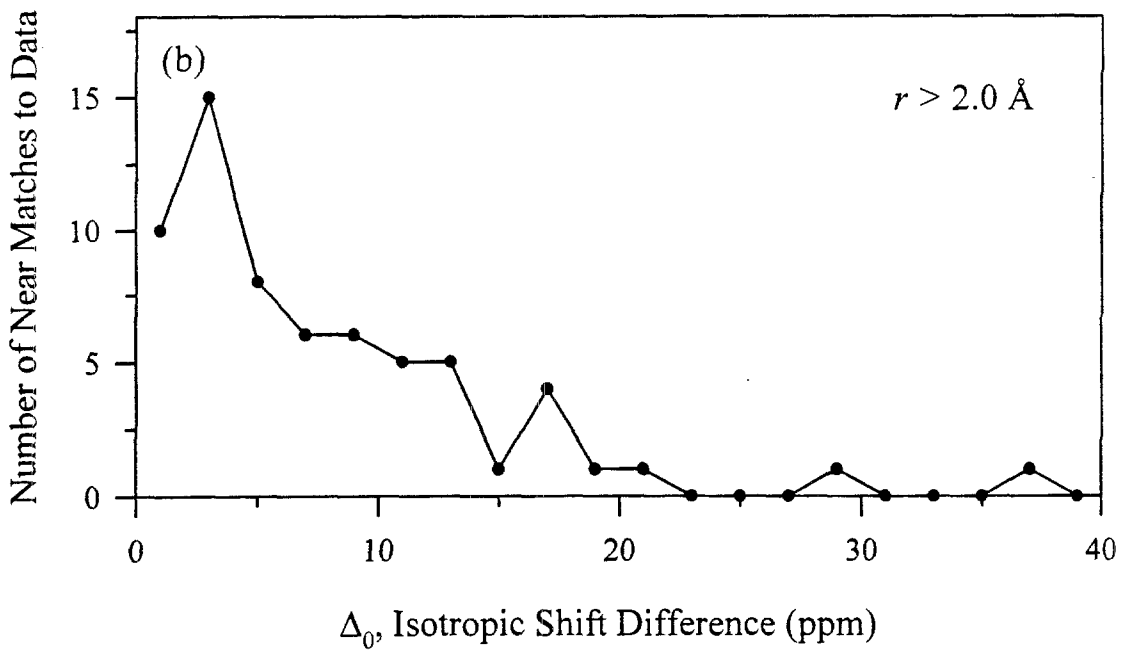

Fig. 13. (a) Distribution of reduced anisotropies represented in the top 100 "near-match" simulations of the one-pulse data in Fig. 4(c) that have interproton distances (r) less than 2.0 Å. (b) Distribution of reduced anisotropies among near matches that have interproton distances greater than 2.0 Å.

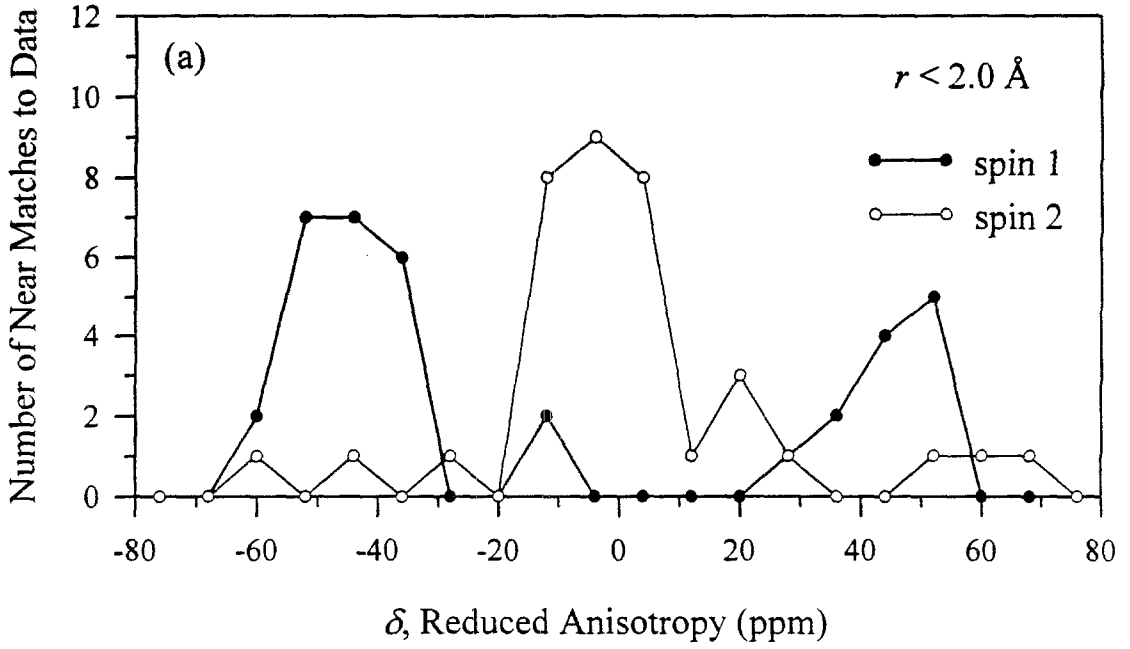

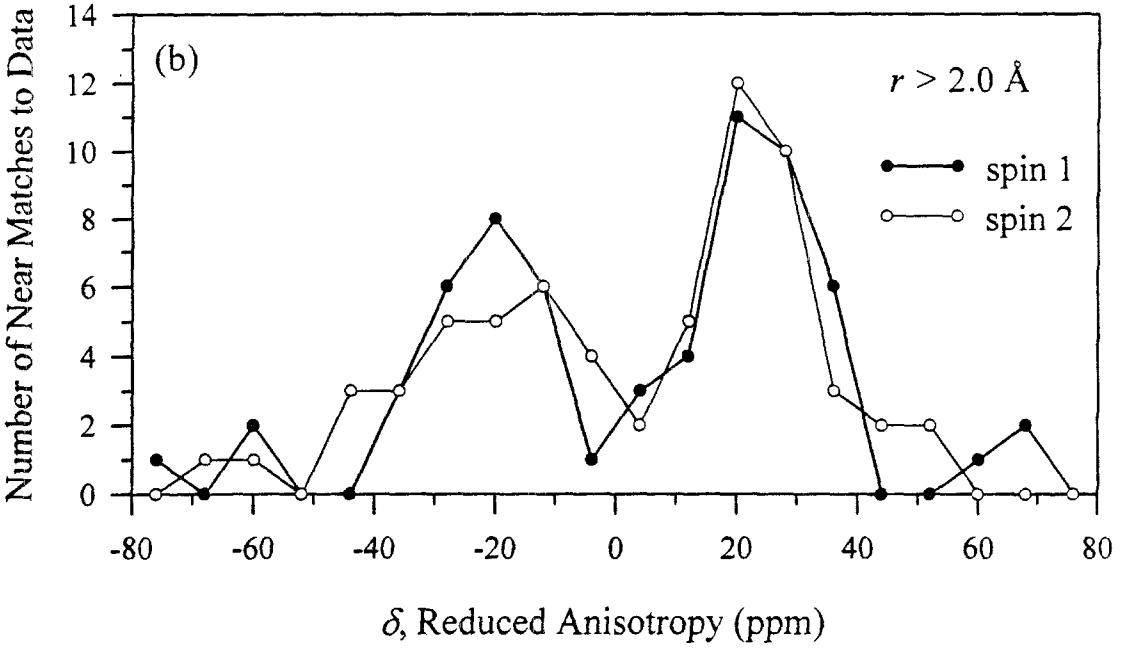

Fig. 14. (a) Distribution of asymmetry parameters represented in the top 100 "near-match" simulations of the one-pulse data in Fig. 4(c) that have interproton distances (r) less than 2.0 Å. (b) Distribution of asymmetry parameters among near matches that have interproton distances greater than 2.0 Å.

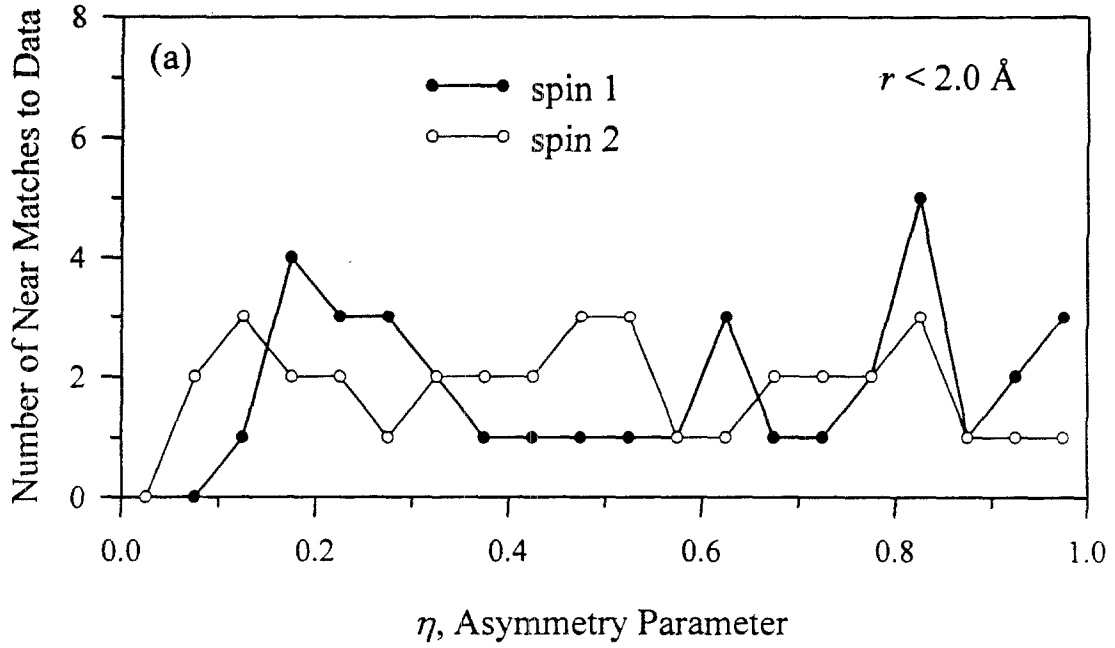

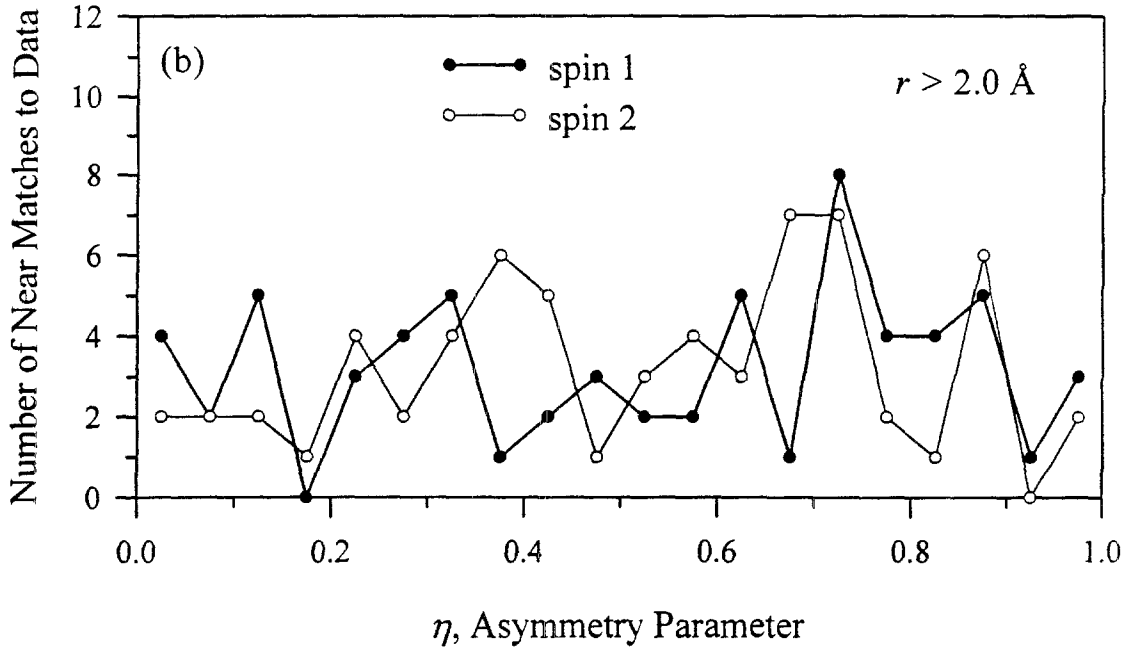

Fig. 15. (a) PASADENA spectrum after a 50 ms burst of p-H_2. (b) Average of "near-match" simulations having $r < 2.0$ Å. (c) Standard deviation as a function of frequency of near-match simulations in (b). (d) Average of near-match simulations having $r > 2.0$ Å. (e) Standard deviation of near-match simulations in (d). Note that (c) and (e) are not residuals, but show the closeness of the near matches (in each interproton grouping) to each other.

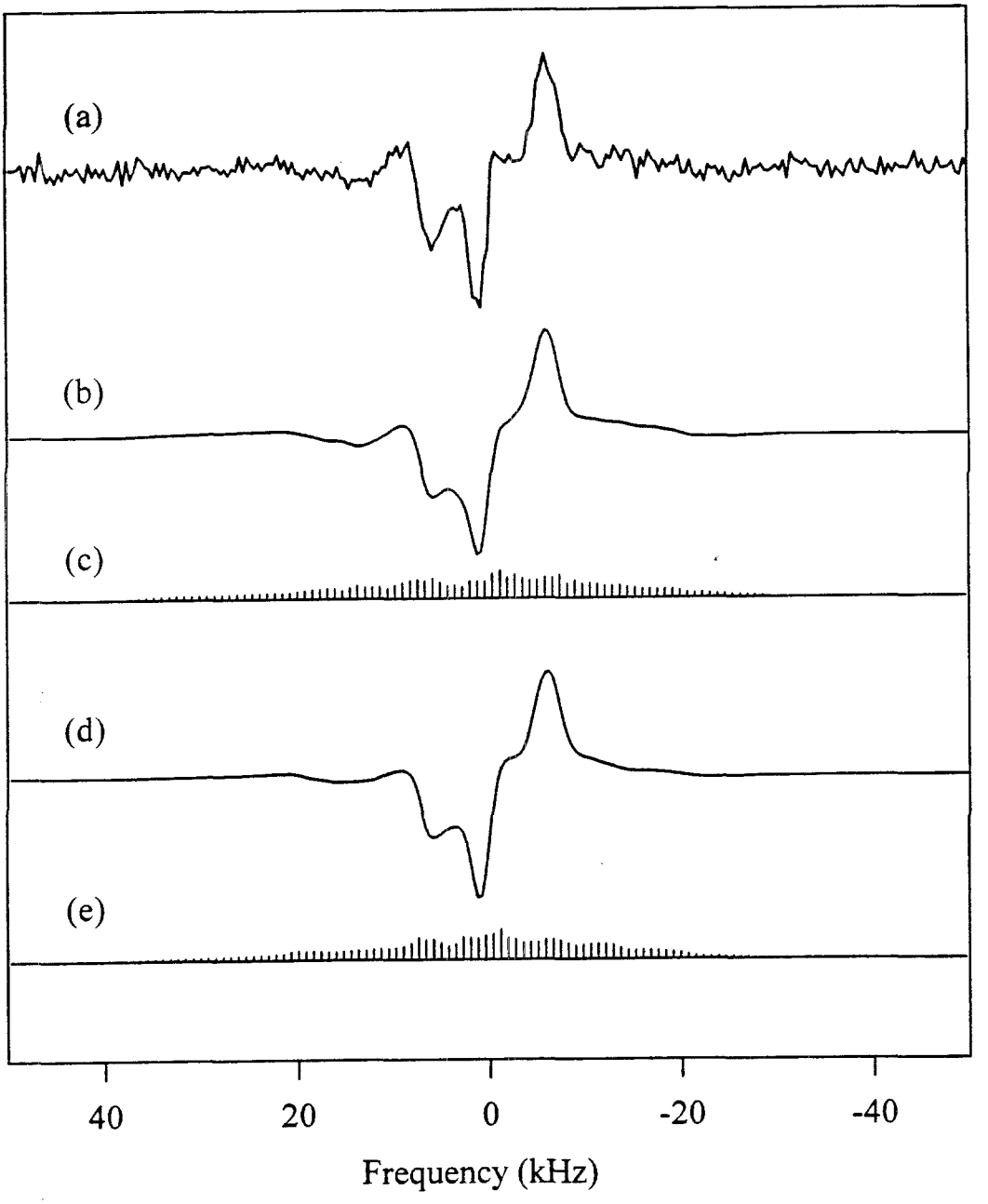

Fig. 16. Random simulations of spectra arising from difference magnetization only (nutation slices at ω_{rf}) corresponding, respectively, to the same sets of parameters used to generate the full PASADENA spectra in Fig. 3 of Chapter II.

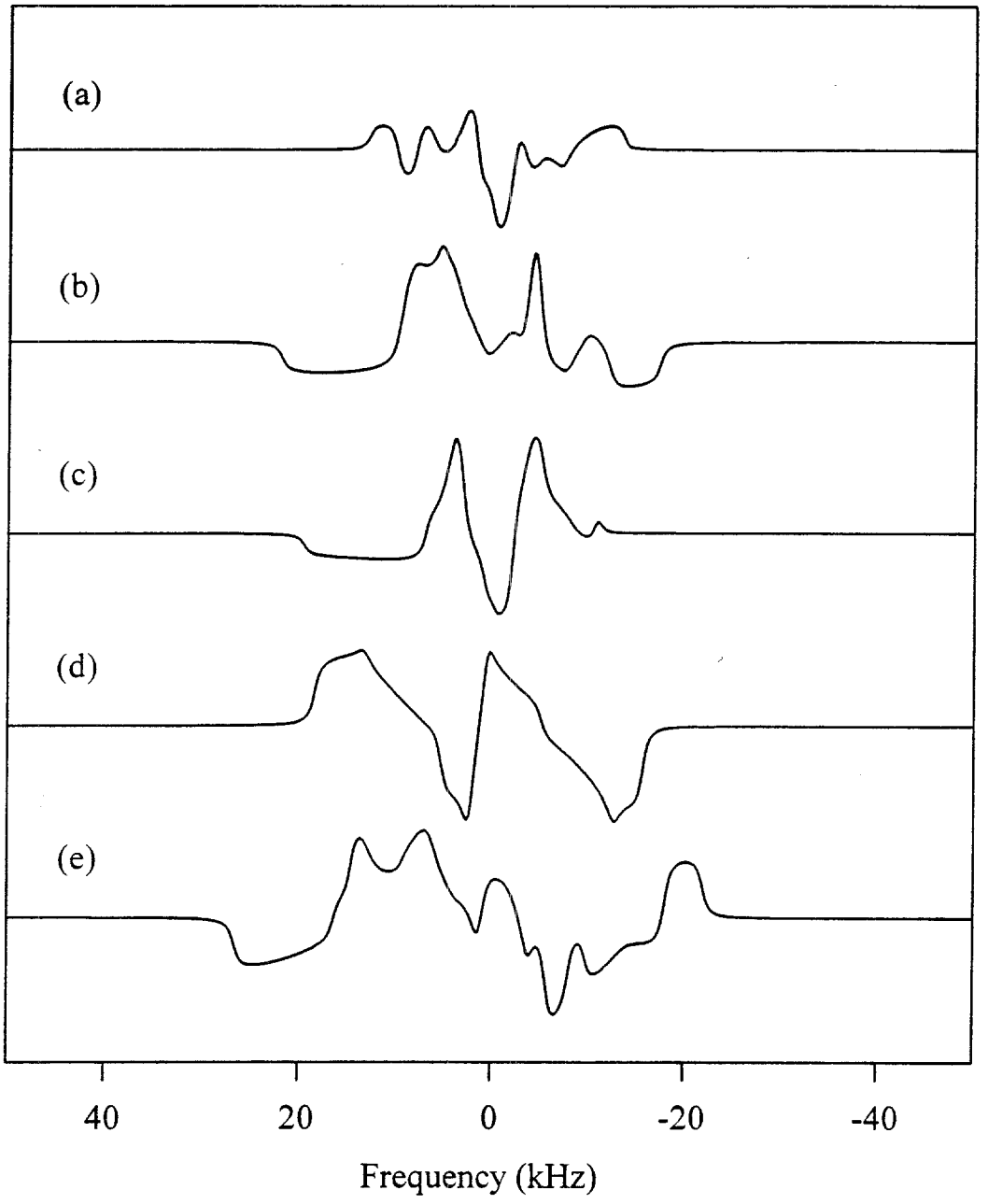

Fig. 17. Random simulations of spectra arising from dipolar order only (nutation slices at $2\omega_{rf}$) corresponding, respectively, to the same sets of parameters used to generate the full PASADENA spectra in Fig. 3 of Chapter II.

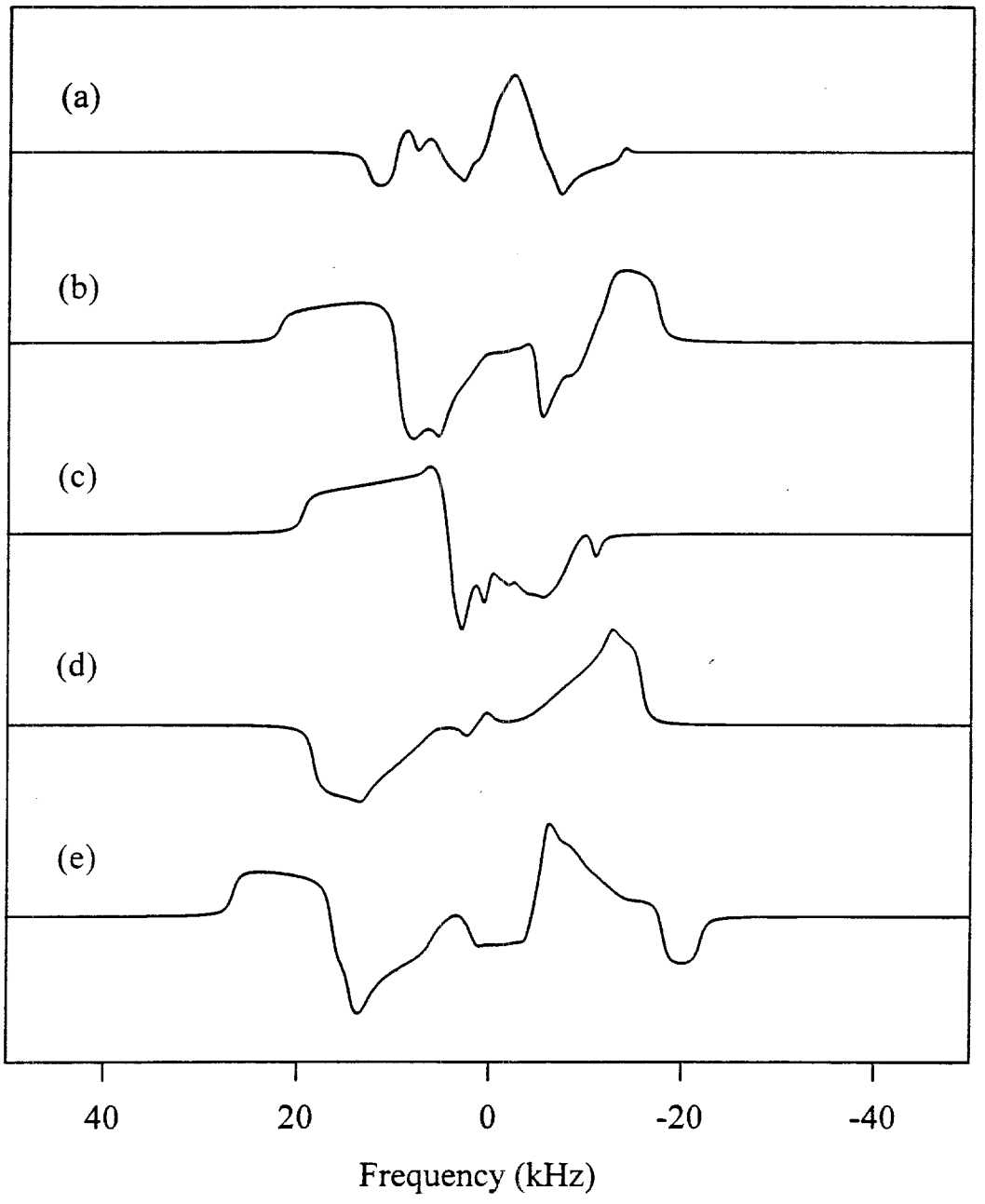

Fig. 18. Slice from a 2D PASADENA nutation spectrum taken at $\omega_1 = 2\omega_{rf}$, where ω_1 is the frequency in the nutation dimension and ω_{rf} is the strength of the resonant component of the rf field in units of rad/s. The frequency axis of the slice corresponds to the free evolution dimension (ω_2). The spectrum corresponds to the free evolution spectrum of the dipolar order present in the initial condition.

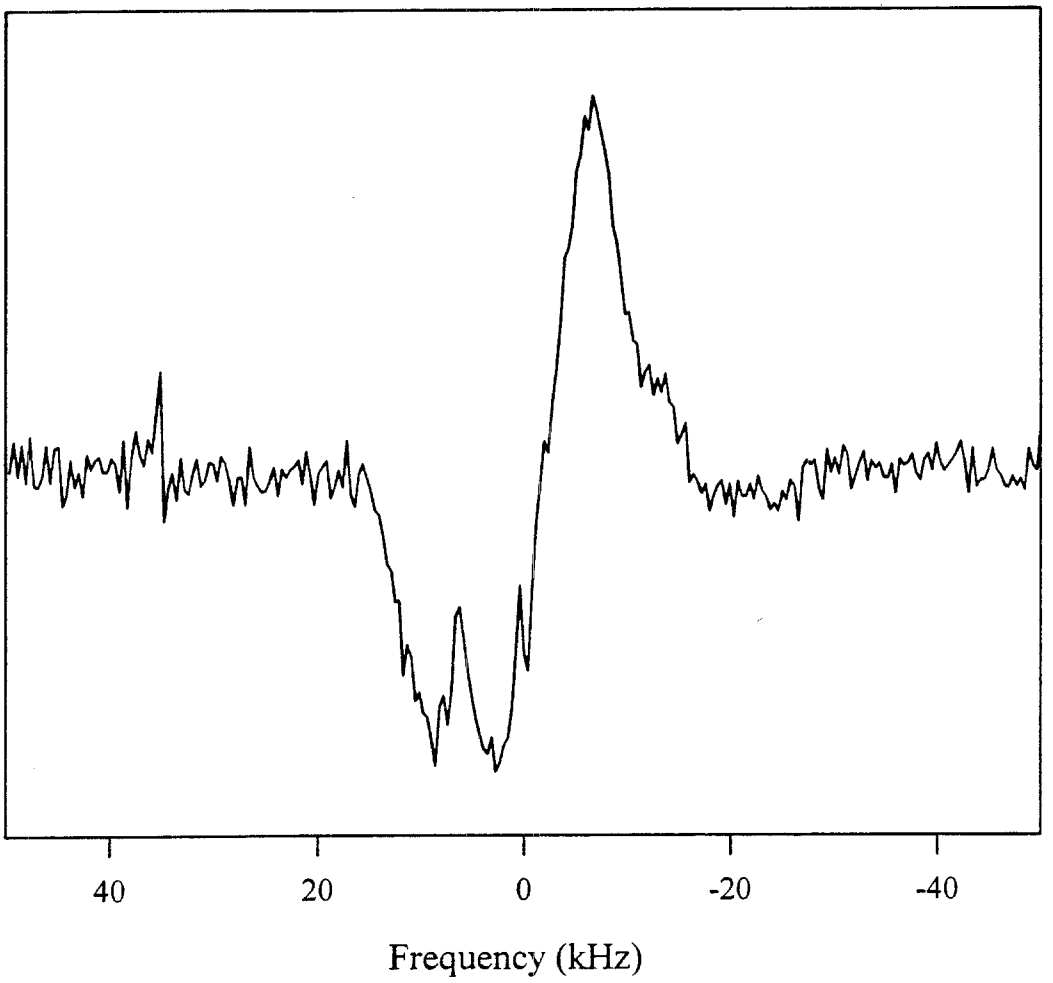

Fig. 19. (a) Scatter plot showing the reduced χ^2 and interproton distance for each of the simulations in the top 100 near matches to the nutation slice at $2\omega_{rf}$ in Fig. 18, taken from a random search of 8×10^5 parameter sets spanning parameter space. (b) Distribution of the interproton distances represented in (a). Sampling of interproton distances was flat in the range shown and the distances were collected in contiguous bins centered at the points shown.

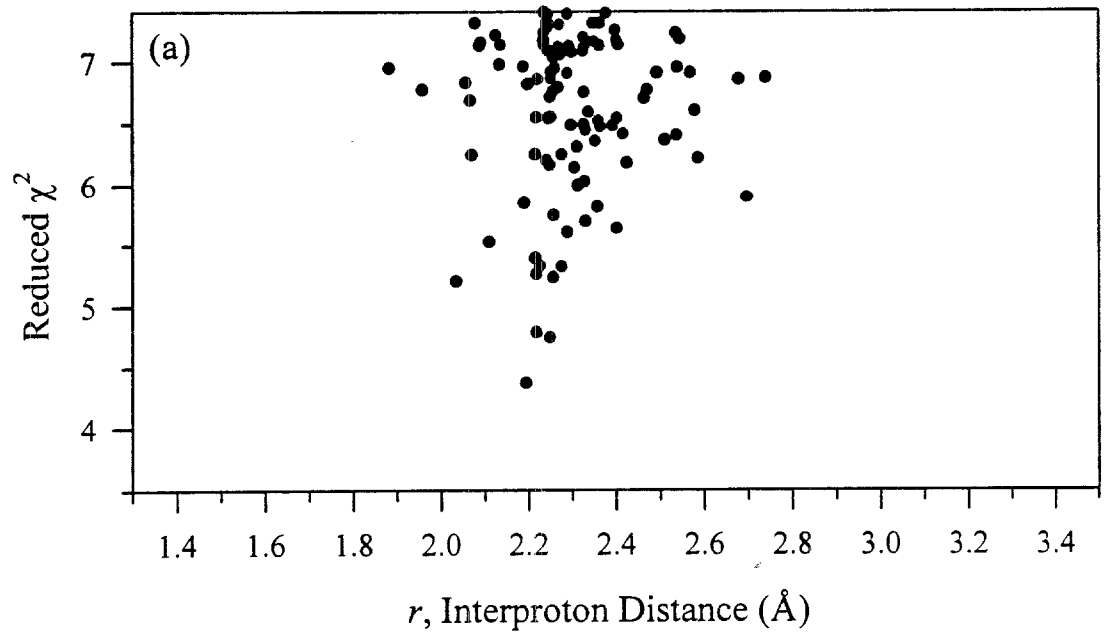

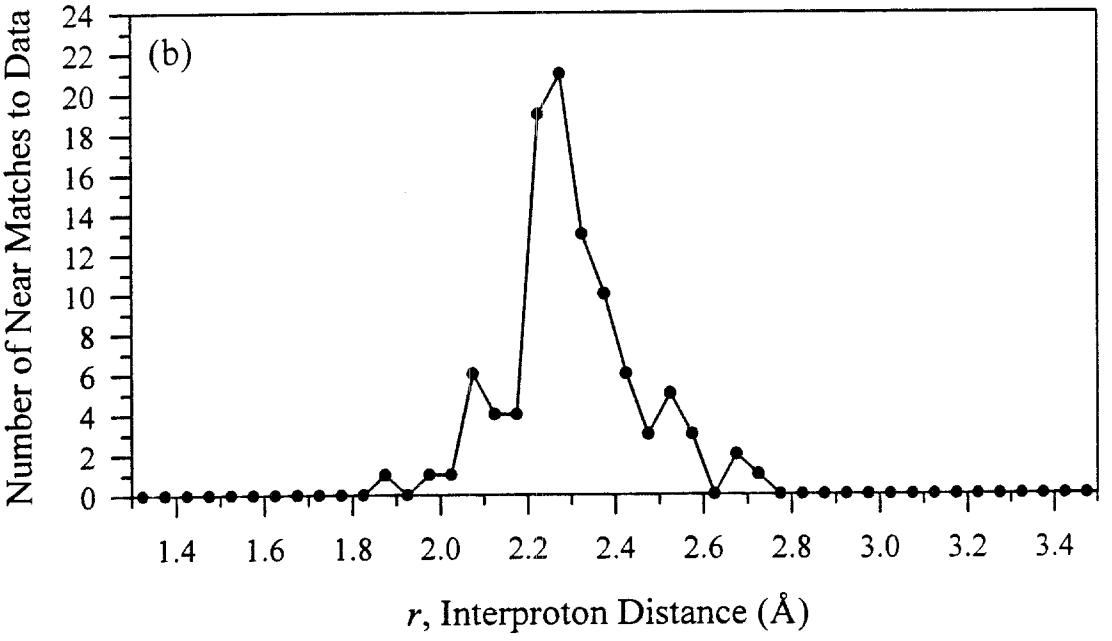

Fig. 20. Distribution of average isotropic shifts represented in the top 100 "near-match" simulations of the nutation slice at $2\omega_{rf}$ in Fig. 18.

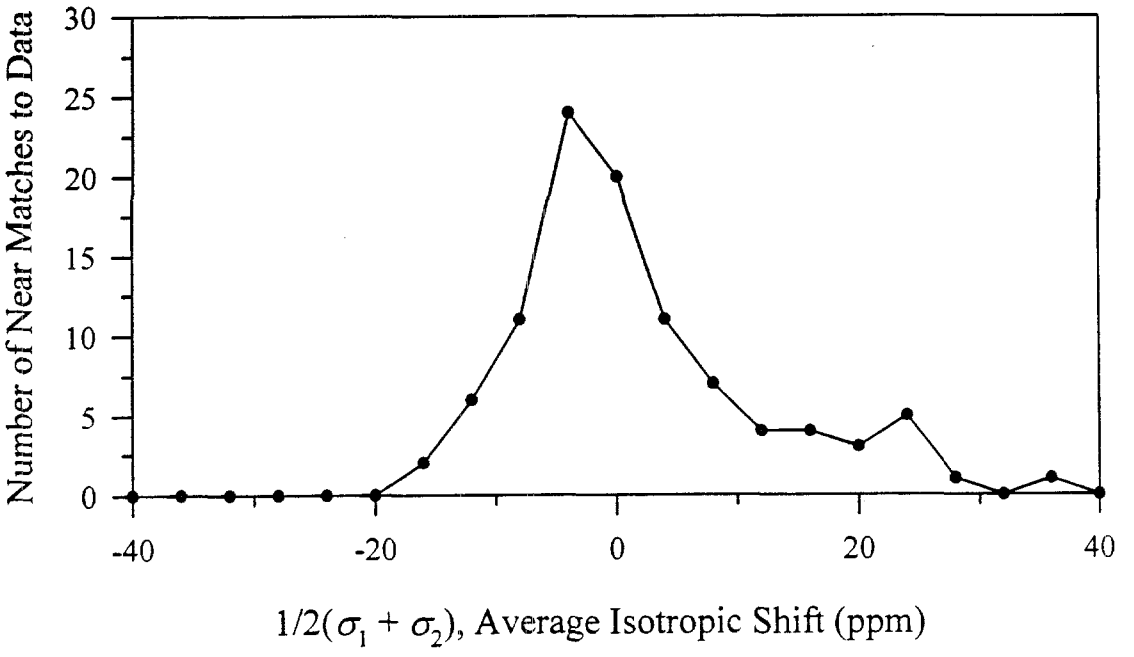

Fig. 21. Distribution of isotropic shift differences represented in the top 100 "near-match" simulations of the nutation slice at $2\omega_{rf}$ in Fig. 18.

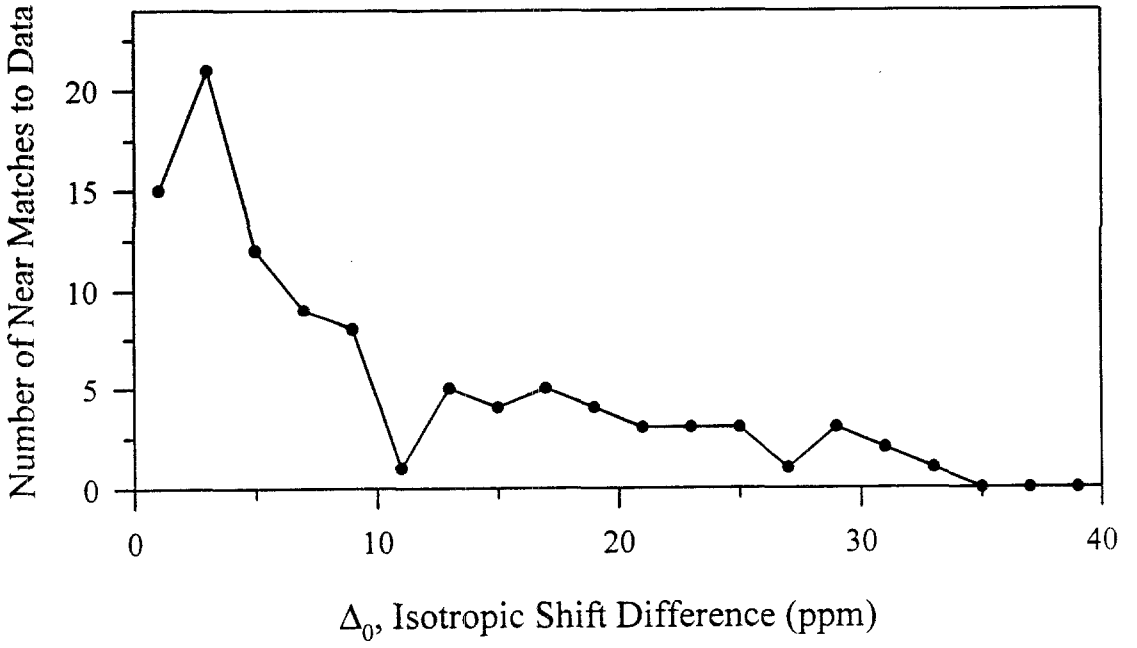

Fig. 22. Distribution of reduced anisotropies represented in the top 100 "near-match" simulations of the nutation slice at $2\omega_{rf}$ in Fig. 18.

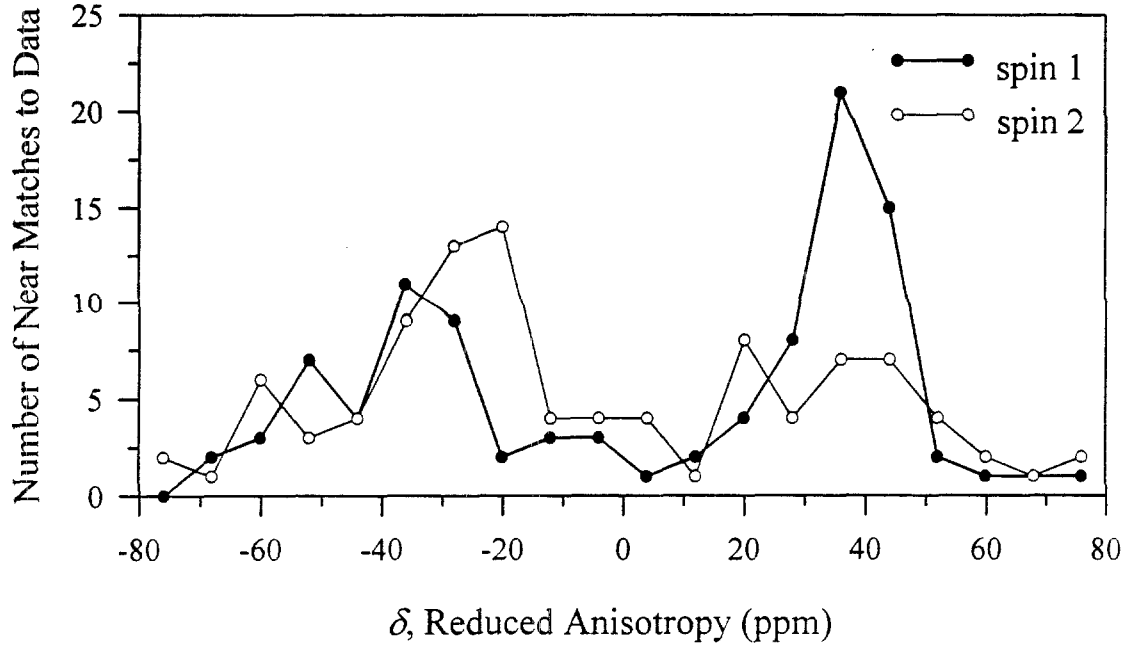

Fig. 23. Distribution of asymmetry parameters represented in the top 100 "near-match" simulations of the nutation slice at $2\omega_{rf}$ in Fig. 18.

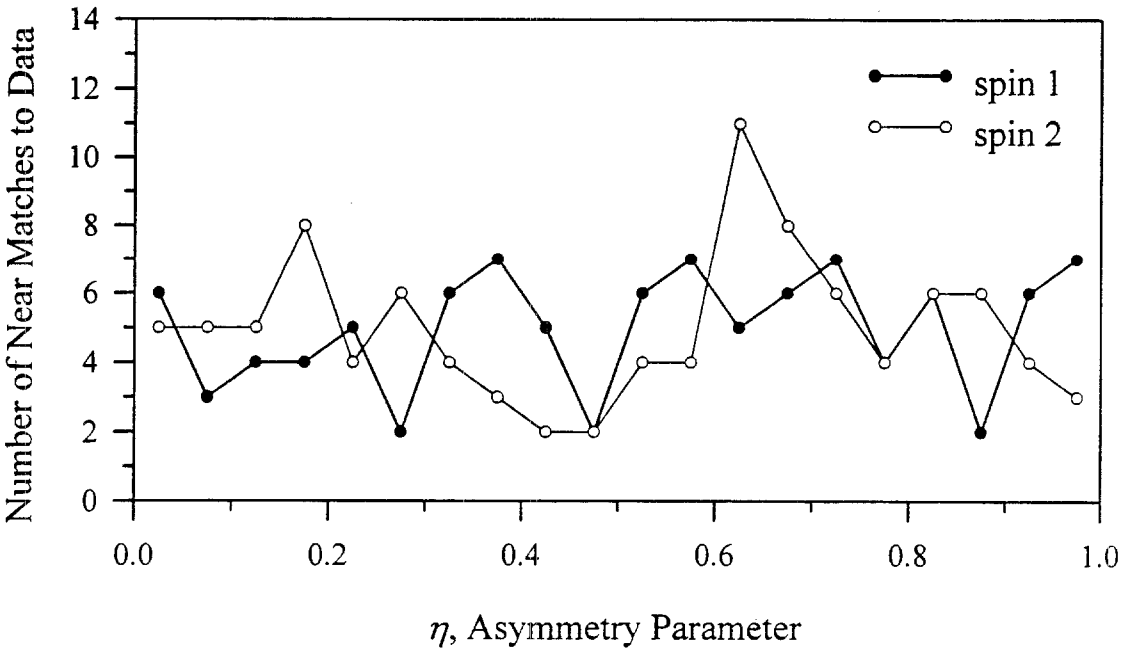

Fig. 24. (a) Slice from a 2D PASADENA nutation spectrum shown in Fig. 18. (b) Average of "near-match" simulations. (c) Standard deviation as a function of frequency of near-match simulations in (b). Note that this standard deviation is not a residual, but serves to show the closeness of the near matches to each other.

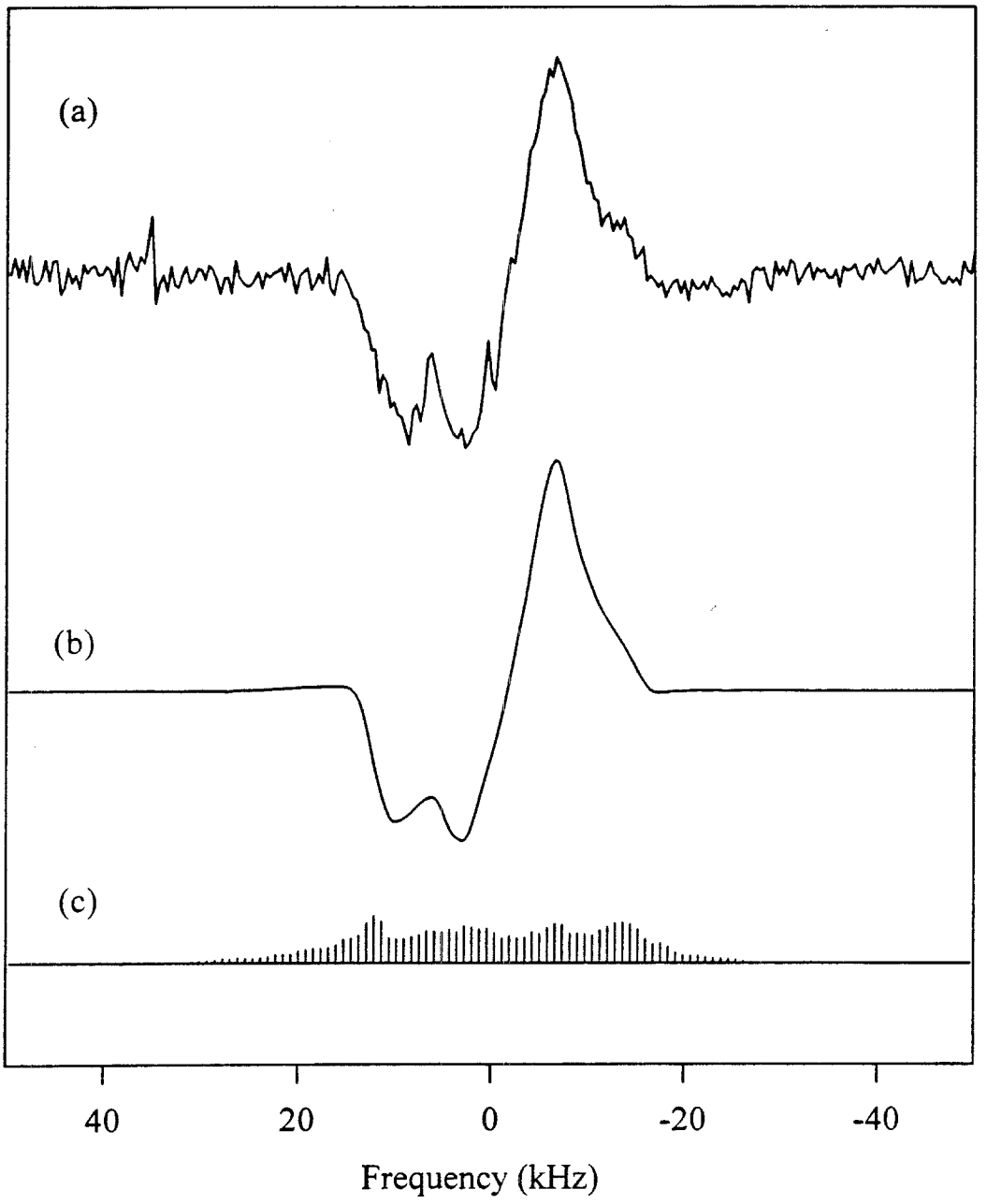

Fig. 25. Simulated spectra illustrating the enhancement factor for the powder PASADENA experiment for a particular set of Hamiltonian parameters that give a near fit to the PASADENA spectrum in Fig. 4(c). The spectrum using para-enriched H_2 ($x_p = 0.5$) and a $\pi/4$ pulse is shown in (a). The corresponding spectrum using Curie-law magnetization at 300 K in a 4.7 T field, with a $\pi/2$ pulse, is shown in (b). The two spectra are plotted on the same scale as each other after multiplication of the n-H_2 spectrum by the enhancement factor shown. The simulations are convoluted with a 1 kHz-wide Lorentzian line. The parameters used in the simulations are listed below, with the principal components σ_{ii}^j given in kHz and the Euler angles Ω_j given in degrees.

$r = 2.75$ Å ($\nu_D = 5.79$ kHz), $\sigma_{ii}^1 = \{0.77, 6.30, 0.18\}$, $\Omega_1 = \{0, 57, 52.8\}$,

$\sigma_{ii}^2 = \{0.37, -4.62, 4.96\}$, $\Omega_2 = \{41.9, 152.3, 134.9\}$

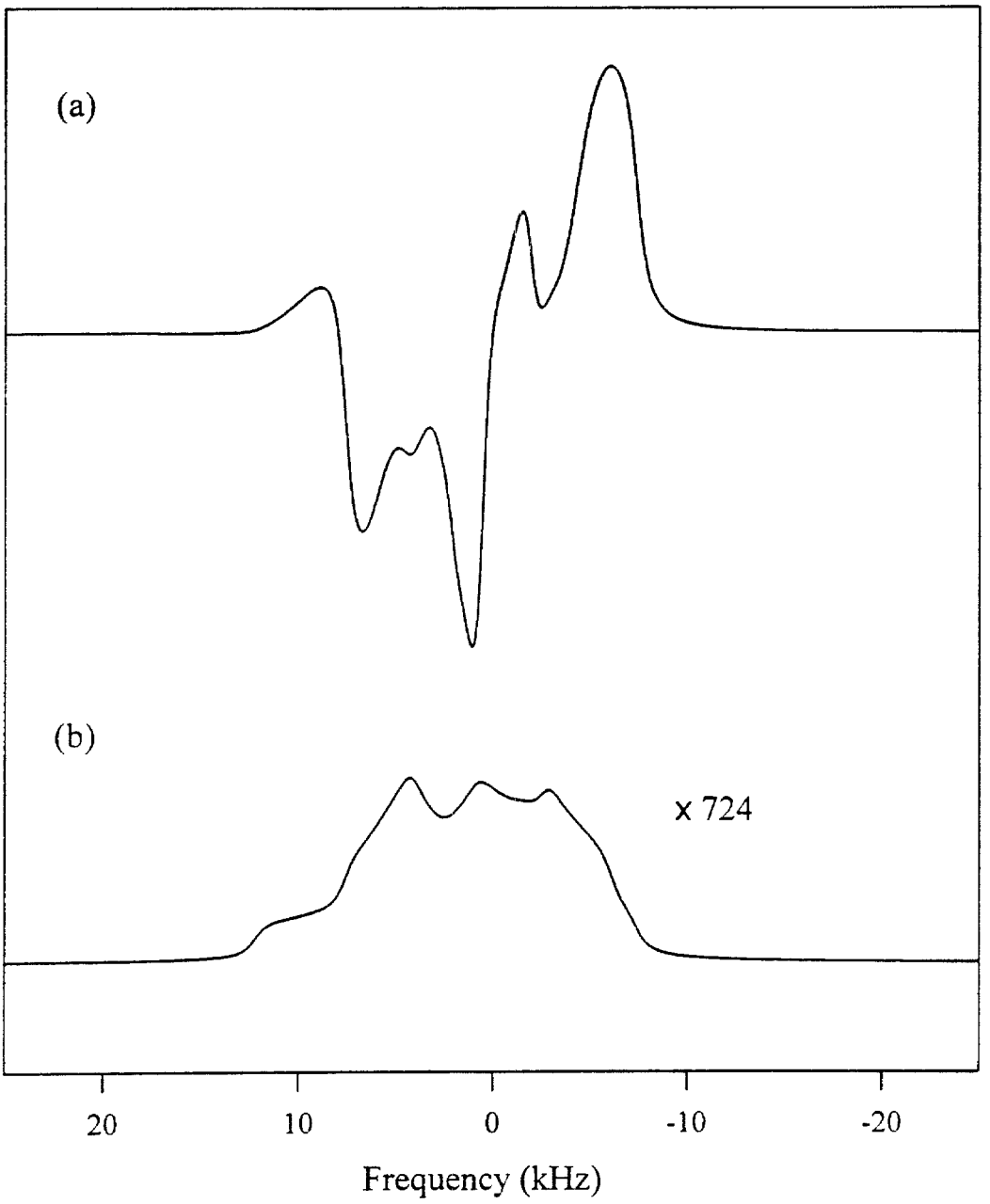
(a)
(b)
x 724
20
10
0
-10
-20
Frequency (kHz)

Fig. 26. (a) Separate powder averages of the four individual spin transitions in the PASADENA spectrum shown in Fig. 25(a). (b) The sum of the four transitions shown in (a), giving the same spectrum as in Fig. 25(a). The spectrum in (b) is plotted on same scale as the spectra for the individual transitions in (a), illustrating the degree of destructive interference between antiphase signals in the powder average.

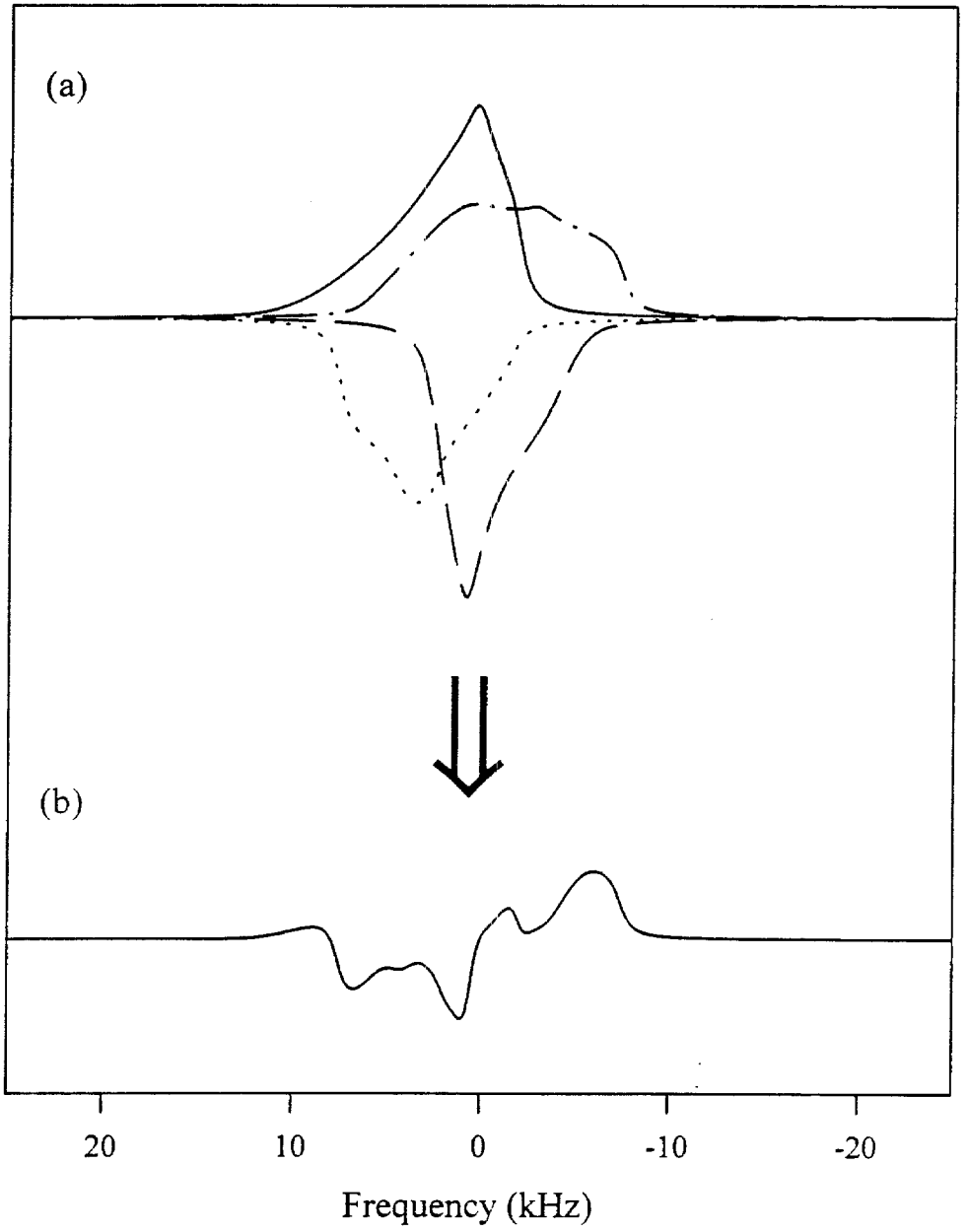

Fig. 27. (a) Separate powder averages for the four individual transitions in the ordinary NMR spectrum shown in Fig. 25(b). (b) The sum of the four transitions shown in (a), giving the same spectrum as Fig. 25(b). The spectrum in (b) is plotted on the same scale as the spectra in (a). Graphical line patterns (dotted, dashed, etc.) in (a) correspond to the same transitions in this figure as they do in Fig. 25(a).

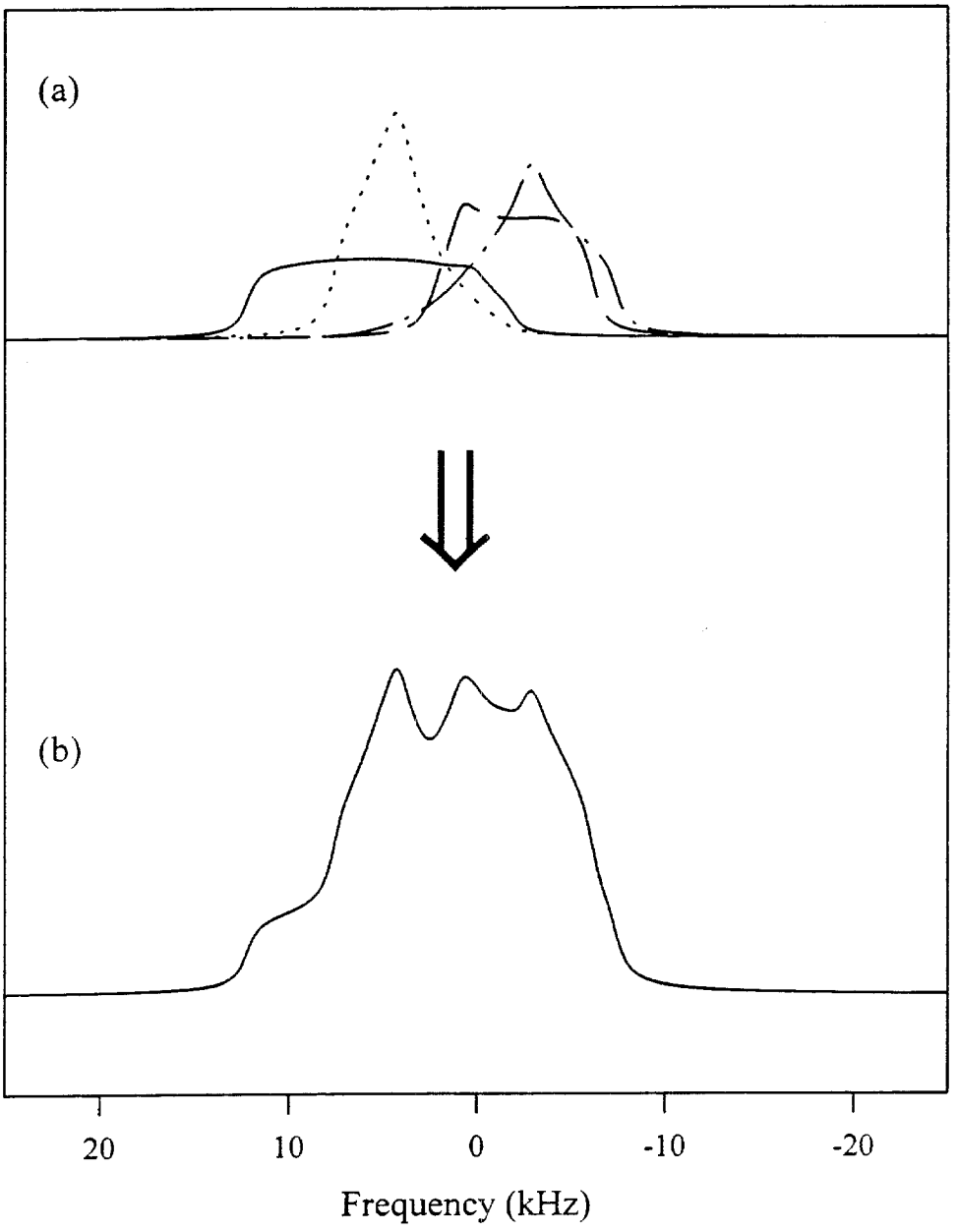

Fig. 28. Enhancement factors for the powder-PASADENA spectrum as a function of the ratio ω_D/Δ_0 using the same parameters as those in Fig. 25 but with variation in ω_D or Δ_0, with the other of these two fixed as indicated by the legend. The two arrows indicate the ratio on the horizontal axis that exactly matches the parameters used in Fig. 25. A line broadening of 1 kHz was applied to all spectra before calculation of enhancement factors. (a) Pulse flip angle: $\pi/4$. (b) Pulse flip angle: $3\pi/4$.

(a)

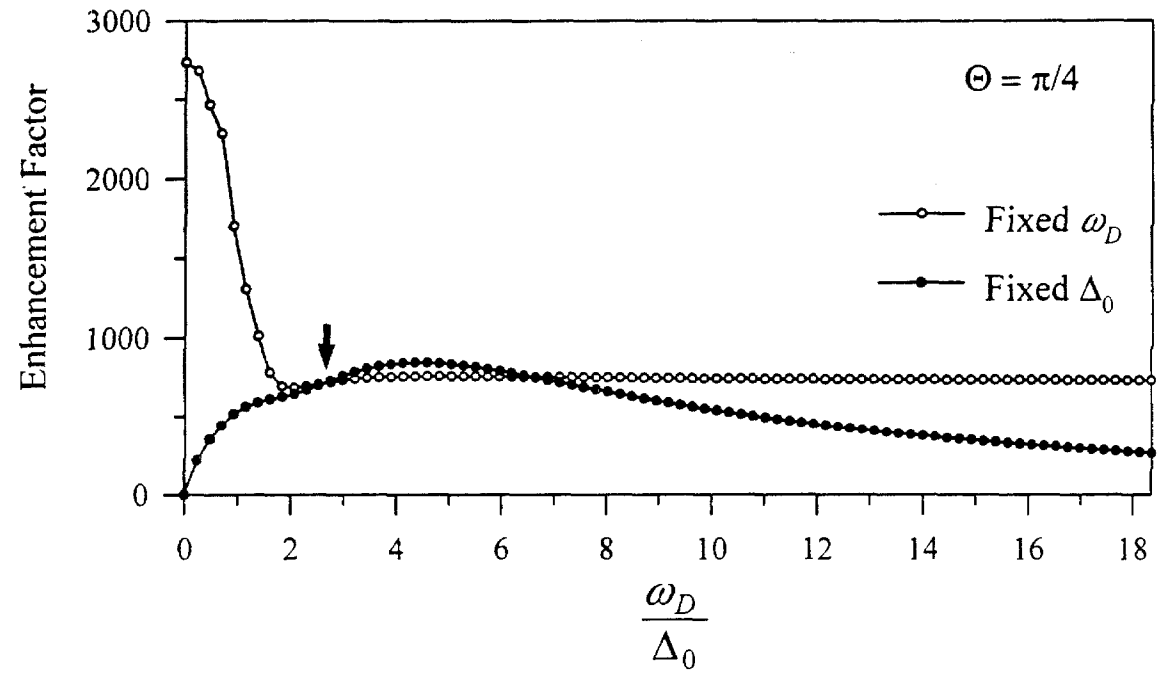
Enhancement Factor
3000
2000
1000
0
Θ = π/4
Fixed ω_D
Fixed Δ_0
0
2
4
6
8
10
12
14
16
18
$\frac{\omega_D}{\Delta_0}$

(b)

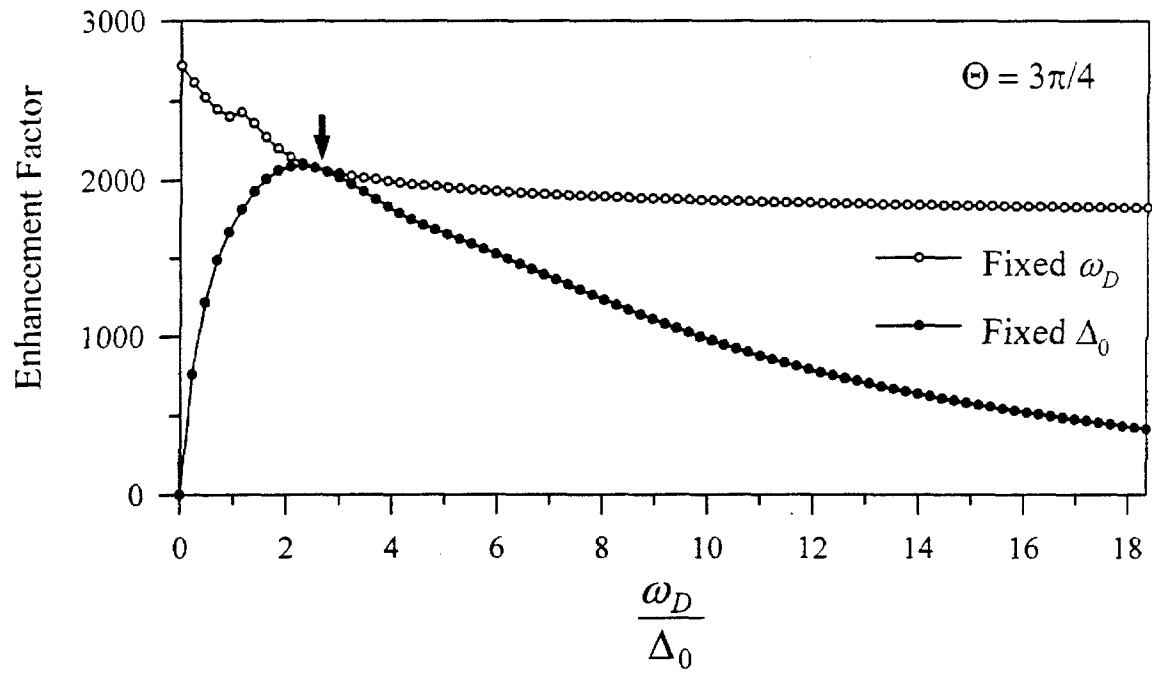
Enhancement Factor
3000
2000
1000
0
Θ = 3π/4
Fixed ω_D
Fixed Δ_0
0
2
4
6
8
10
12
14
16
18
$\frac{\omega_D}{\Delta_0}$

Fig. 29. (a) Estimated enhancement factors corresponding to the top 100 near matches to the PASADENA spectrum shown in Fig. 4(c), from a large random search of parameter space as described in Section 4. (b) Sensitivity estimates corresponding the same near matches as in (a).

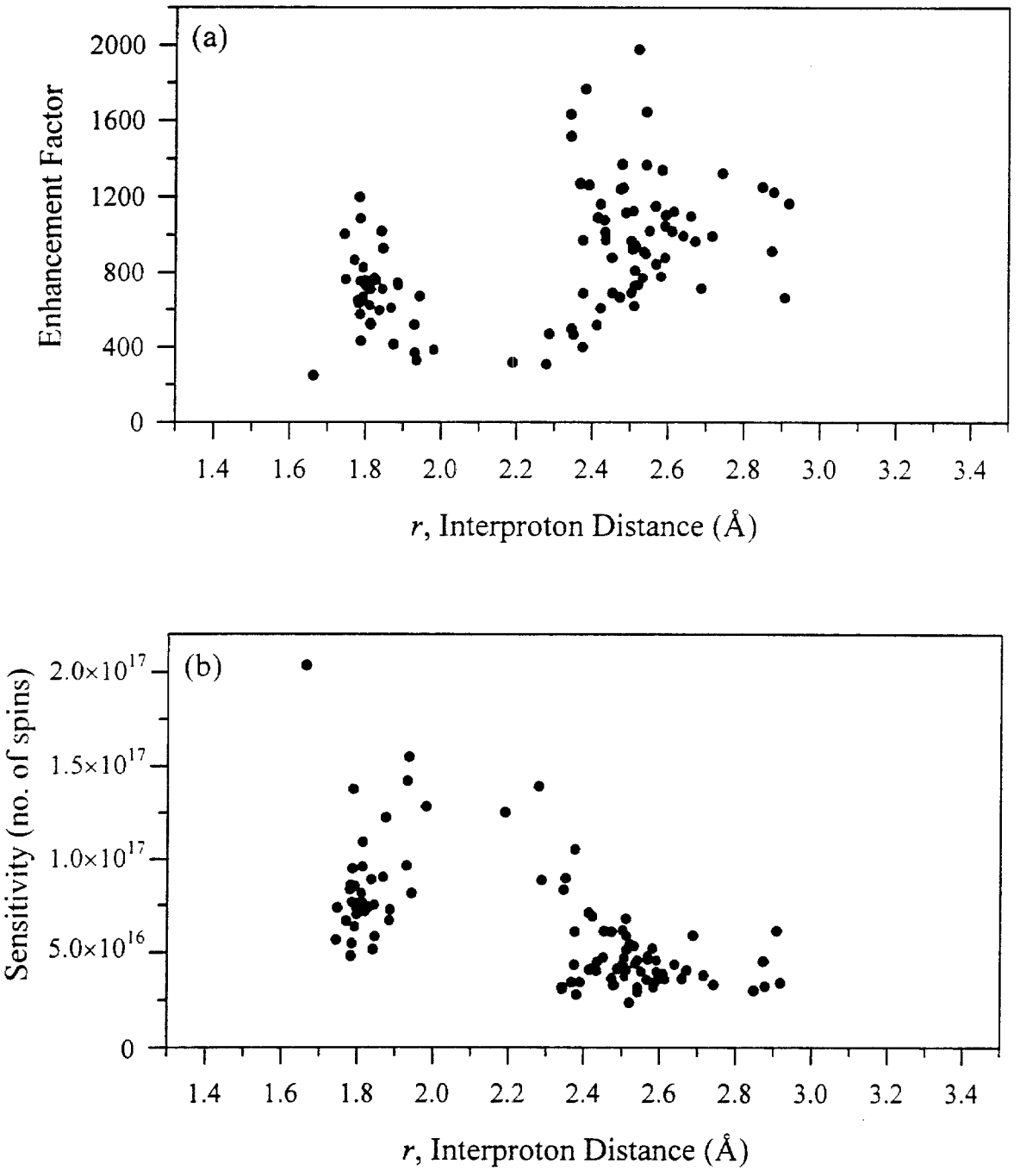

Chapter IV. Surface PASADENA with Selective Averaging and Multiple-Quantum NMR

1. Introduction

The spin Hamiltonian of the surface-bound proton pair treated in Chapters II and III contains twelve independent parameters that report on the structure of the binding site. As discussed in Chapter II, these parameters are the internuclear distance (manifested in the dipolar coupling), the three principal components of each spin tensor, and five of the six total Euler angles that relate the orientations of the spin tensors to the molecular frame. It was seen in Chapter III that the number of independent parameters is large enough, and their apparent correlation with each other (in dictating powder lineshapes) is strong enough, that unique fitting to powder-PASADENA data acquired with a single rf pulse is difficult at best and perhaps impossible in general. Although this does not preclude the use of single-pulse surface PASADENA in kinetic and mechanistic studies of heterogeneous catalysis, it does make the conclusive determination of binding-site structure more difficult.

Techniques are described in this chapter which are designed to selectively reduce the number of free parameters in the Hamiltonian contributing to the spectral lineshape. The techniques fall into two categories, both of which are well-developed fields of NMR spectroscopy and are described briefly below.

The first technique is selective averaging using multiple-pulse NMR.[1,2] The principle behind multiple-pulse line narrowing is the manipulation of the spin state with rf pulses, separated by regular periods of evolution under the full Hamiltonian, to achieve a desired average, or effective, Hamiltonian that describes the net evolution when the manipulation period is taken as a whole. A typical multiple-pulse sequence may consist of anywhere from two to forty-eight or more pulses. The pulses are usually strong $\pi/2$ pulses, but a sequence can also contain of pulses of flip angle π or other angles. The pulse sequence is repeated for each data point in the time-domain transient, with sampling performed in the evolution window between each full repetition of the sequence. Dipolar couplings, quadrupole couplings, and chemical shift interactions can all be averaged away to zeroth order in the rotating frame, with varying degrees of suppression of higher-order terms, depending on the design of the multiple-pulse sequence.

The second category of techniques described in this chapter for effectively reducing the number of parameters in the observed Hamiltonian is multiple-quantum NMR.[3,4] In multiple-quantum NMR, a period of preparation, usually involving both pulses and free evolution, generates a mixture of coherences of differing orders. Coherence of a desired order is selected by phase-cycling—that is, by repeating the experiment with appropriately chosen phases for the preparation period and adding the separate experiments. The net effect is generally to isolate a particular coherence order n

at the beginning of the multiple-quantum evolution period. A mixing period at the end of this evolution period, consisting of at least one rf pulse converts the *n*-quantum coherence encoded during evolution into observable single-quantum coherence which is measured in real time as a decaying transient. The entire experiment, with phase cycling, is repeated to map out each point in the multiple-quantum evolution period.

Two different possible applications of each of two general parameter-reduction techniques described above are treated in this chapter. The multiple-pulse applications treated are dipolar averaging and chemical-shift averaging. The multiple-quantum applications treated are zero-quantum and double-quantum NMR. Demonstrations of these techniques on the PASADENA system are shown where available (demonstrations of dipolar averaging and zero-quantum NMR have both been performed).

2. Dipolar Averaging

Multiple-pulse line-narrowing sequences such as the four pulse WAHUHA-4 and the eight pulse MREV-8 selectively average the dipolar coupling Hamiltonian to zero. The MREV-8 sequence is chosen here because its superior insensitivity to pulse imperfections. The sequence consists of the following train of $\pi/2$ pulses and delays, where pulses are identified by their rotation axes in the rotating frame (with a bar indicating a negative rotation angle) and delays are given as multiples of a user-selected base of length τ:

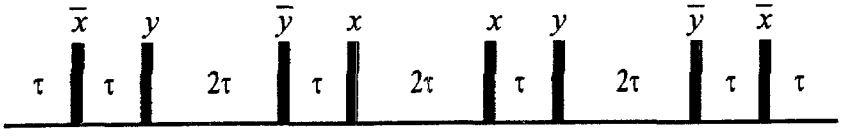

Sampling is performed between each repetition of the entire eight-pulse sequence.

If the full internal Hamiltonian governing evolution during the delays of the pulse sequence is that of Chapter I, Eq. (13), neglecting scalar (or "J") coupling, then the average Hamiltonian describing net evolution during a full cycle of the pulse sequence is given by

$$\overline{\mathcal{H}}_{\mathrm{MREV}} = \frac{1}{3}\omega_{1z}(I_{1z} + I_{1x}) + \frac{1}{3}\omega_{2z}(I_{2z} + I_{2x}) \tag{1}$$

The most important feature of this Hamiltonian is the absence of the dipolar coupling interaction. Two usually undesirable, although minor, consequences of the averaging process for the MREV-8 sequence are the scaling of the chemical shifts and the tilting of the quantization axis, both of which are seen in Eq. (1).

The initial condition is taken as the standard initial PASADENA density operator in Chapter I, Eq. (32). Only the difference magnetization in the initial condition evolves into observable magnetization under the Hamiltonian of Eq. (1). The signal for a single crystallite orientation is

$$S_{\mathrm{MREV}}(t) = -\frac{f}{4}\sin\kappa\cos\kappa(\sin\beta - \cos\beta)\left(e^{i(\sqrt{2}/3)\omega_{1z}t} - e^{i(\sqrt{2}/3)\omega_{2z}t}\right) \tag{2}$$

Depending on the overlap of the chemical shift powder patterns for the two spins, some or all of the principal components of the two chemical shift tensors may be directly (visually) obtainable from the spectrum.

Fig. 1 shows a series of simulations of MREV spectra for the powdered PASADENA system using the same sets of parameters, respectively, as the simulations of the full PASADENA spectra shown in Chapter II, Fig. 3. The frequency scale is the same

for the two figures, showing the dramatic narrowing of the powder lineshape that results from dipolar averaging.

Fig. 2(a)-(c) shows a series of full PASADENA simulations in which only the dipolar coupling is varied, while the chemical shift tensors remain fixed. The corresponding MREV spectra are shown in Fig. 2(d)-(e). Since only the chemical shift interaction is observed during evolution, the three MREV spectra are substantially the same, despite their widely disparate dipolar couplings. The only reason (assuming perfect averaging of the dipolar coupling) that the lineshapes differ at all is that the *initial condition* still retains its full orientation dependence on the dipolar coupling, despite its absence during evolution. This is a feature of the PASADENA effect which is not seen in conventional NMR.

An experimental demonstration of the MREV-PASADENA experiment is shown in Fig. 3(b), along with the corresponding full PASADENA experiment in (a), both using a 50 ms burst of p-H_2 delivered to powdered ZnO. A reduction in overall "linewidth" by roughly an order of magnitude is achieved using line-narrowing. It should be noted that the MREV spectrum is not free of background resonances from gas-phase o-H_2 and contaminant species. Also, there is a significant amount of ghosting (reflection of signal across zero) due to the tilted quantization axis of the MREV experiment. For comparison, an analogous pair of simulations for the two experiments in Fig. 3 is shown in Fig. 4, using a set of parameters chosen to give a qualitatively similar lineshape for the full PASADENA spectrum. The predicted MREV lineshape for this same Hamiltonian is likewise similar to the experimentally observed MREV lineshape. The simulations contain no background and no ghosting.

3. Chemical-Shift Averaging

Multiple-pulse sequences can also be used to selectively average the chemical shift interaction to zero, while preserving the dipolar coupling interaction. Such a sequence is the Carr-Purcell sequence, and variants thereof, which consists of a train of π pulses delivered to the sample. The average Hamiltonian in this case (again neglecting J coupling) is

$$\overline{\mathcal{H}}_{\text{C.S.Avg.}} = \frac{\omega_D}{2}\left(1-3\cos^2\theta\right)\left(3I_{1z}I_{2z}-\mathbf{I}_1\cdot\mathbf{I}_2\right) \tag{3}$$

Under this Hamiltonian only the dipolar order in the PASADENA initial condition will evolve into observable magnetization. The signal for the chemical-shift averaging experiment is given by

$$S_{\text{C.S.Avg.}}(t) = \frac{f}{2}\cos^2\kappa\,\sin\beta\cos\beta\left(e^{-i(3D/2)t}-e^{i(3D/2)t}\right) \tag{4}$$

Fig. 5 shows a series of simulations of the PASADENA chemical-shift averaging experiment, using the same sets of parameters, respectively, as the simulations of the full PASADENA spectra shown in Chapter II, Fig. 3, as well as the MREV simulations in Fig. 1 of this chapter. The simulations in Fig. 5 show that in most cases, chemical-shift averaging yields a lineshape that can be described as an antiphase Pake doublet, with the splitting between the two sharpest antiphase peaks ~$(3/2)\omega_D$. In one of the cases shown, namely Fig. 5(c), the remaining dependence of the initial condition on the full, unaveraged Hamiltonian is seen to dominate the powder lineshape and may, in practice, preclude the use of this experiment to obtain directly the dipolar coupling without a fit to the full Hamiltonian.

Fig. 6(a)-(c) shows a series of full PASADENA simulations in which only the isotropic shift difference is varied, while the dipolar coupling and the other chemical shift tensor parameters remain fixed. The corresponding chemical-shift averaging spectra are shown in Fig. 6(d)-(e). For the two larger isotropic shift differences, chemical-shift averaging is seen to return nearly the same spectral lineshape. For the smallest isotropic shift difference (for this particular set of parameters), the chemical shift dependence in the initial condition is seen to significantly affect the spectral lineshape.

4. Zero-Quantum Surface PASADENA

The PASADENA initial condition is unique in that it contains terms that are bilinear in spin angular momentum operators. As such, the usual extended preparation period for multiple-quantum NMR can be replaced with a single pulse to generate a mixture of zero and double quantum coherence (along with single-quantum coherence and residual bilinear population terms). The preparation pulse is then phase-cycled to eliminate either the zero or double quantum coherence, while allowing the other to remain. One such scheme for observing zero-quantum coherence is the following:

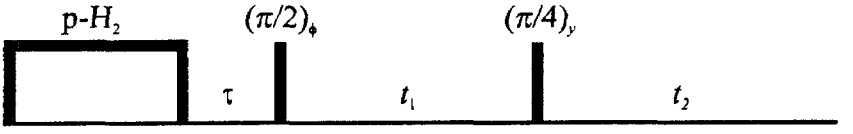

The delay τ allows for gas-phase p-H_2 to be cleared so that no new adsorbed spin order can be created after the first rf pulse but before the second pulse. The phase ϕ of the first pulse is cycled as follows, with plus signs indicating that each of the experiments is added: $(+x,+\bar{x},+y,+\bar{y})$.

The scheme above results in the desired zero-quantum coherence that derives from each of the bilinear terms in the initial condition, as well as J order ($I_{1z}I_{2z}$) that is contributed by the rotationally insensitive $\mathbf{I}_1 \cdot \mathbf{I}_2$ terms. The zero-quantum coherence evolves during t_1 with the characteristic frequency

$$\omega_{23} = \frac{E_2 - E_3}{\hbar} = \sqrt{(J - D)^2 + \Delta^2} \tag{5}$$

which is notably independent of the average chemical shift and also does not depend on the sign of the chemical shift difference Δ or the sign of the dipolar coupling D (assuming the scalar coupling J is negligible). In a variation of this experiment, multiple-pulse line-narrowing can be applied during t_1, leaving zero-quantum evolution only under the chemical shift difference tensor.

Fig. 7 shows an experimental demonstration of the 2D zero-quantum experiment for p-H_2 chemisorbed on powdered ZnO, along with a projection of the data onto the zero-quantum evolution axis f_1. Fig. 8 shows a simulation of the same experiment using the same Hamiltonian parameters used to generate the spectra in Fig. 4. The zero-quantum simulation shows a qualitative similarity to the main features of the data in Fig. 7, neglecting the intensity near f_1, which is not due to zero-quantum coherence. The intensity near f_1 is due to the J order that survives phase cycling and remains as populations during t_1, but which is converted to observable magnetization during t_2.

5. Double-Quantum Surface PASADENA

The scheme below can be used to observe double quantum coherence generated from the PASADENA initial condition.

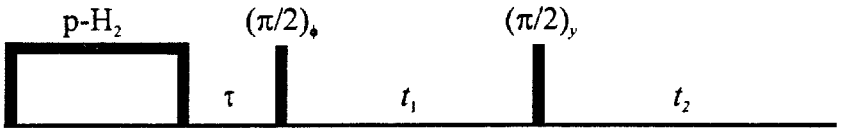

The phase ϕ is cycled as follows, with a minus sign indicating that the experiment of the corresponding phase is subtracted instead of added: $(-x,-\bar{x},+y,+\bar{y})$. Unlike the zero-quantum PASADENA experiment described above, no population differences are stored during t_1. The phase-cycled density operator during t_1 contains only double quantum coherence, which evolves purely at the frequency

$$\omega_{14} = \frac{E_1 - E_4}{\hbar} = \omega_{1z} + \omega_{2z} \tag{6}$$

yielding a powder pattern in the f_1 dimension that depends only on the sum of the chemical shift tensors. Fig. 9 shows a simulation of the 2D double-quantum experiment using the same Hamiltonian parameters used in Fig. 4.

6. References

[1] U. Haeberlen, High Resolution NMR in Solids: Selective Averaging, (Advances in Magnetic Resonance Supplement I, J. S. Waugh, Series Ed.), (Academic Press, New York, 1976).

[2] M. Mehring, High Resolution NMR in Solids, Second Edition, (Springer-Verlag, Berlin, 1983).

[3] D.P. Weitekamp, Adv. Magn. Reson. **11**, 111 (1983).

[4] R.R. Ernst, G. Bodenhausen and A. Wokaun, Principles of Nuclear Magnetic Resonnace in One and Two Dimensions, (Clarendon Press, Oxford, 1987).

Fig. 1. Simulated spectra for which the dipolar coupling is selectively averaged to zero by a multiple-pulse sequence such as MREV-8 (described in the text). The parameters correspond, respectively, to the same sets of parameters used to generate the full PASADENA spectra in Fig. 3 of Chapter II.

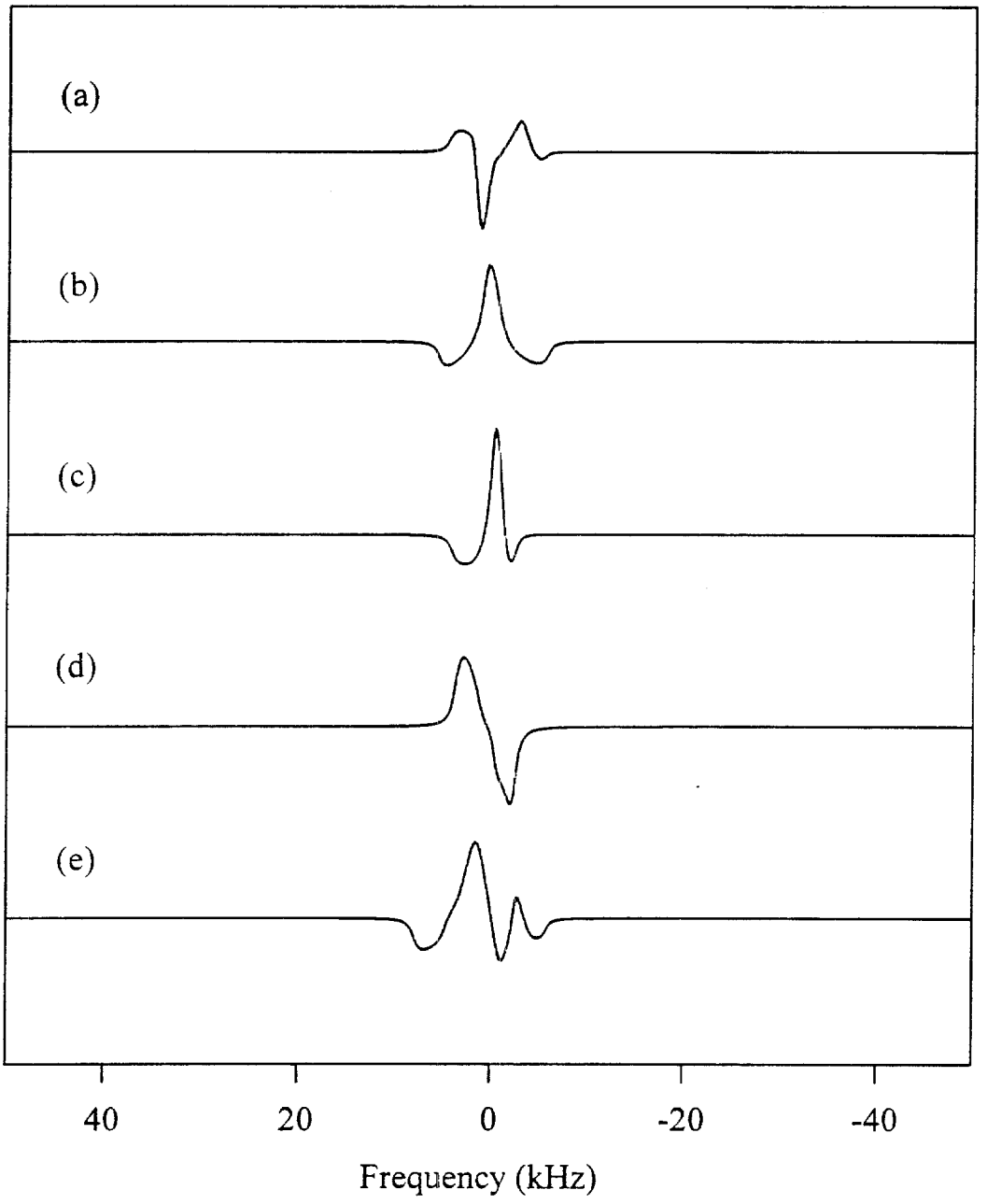

Fig. 2. (a)-(c) Simulated PASADENA spectra with varying dipolar couplings, shown as $\nu_D = \omega_D/(2\pi)$. (d)-(f) Simulated PASADENA spectra with the dipolar averaging sequence MREV-8, using the same parameter sets as (a)-(c), from top to bottom, respectively. All six simulations use the following chemical shift tensor parameters: σ_{ii}^1={1.2, 3.2, 5.2}, Ω_1={0,0,0}, σ_{ii}^2={-3.2,-1.2,1.8}, Ω_2={0,0,0}, where the chemical shifts are given in kHz.

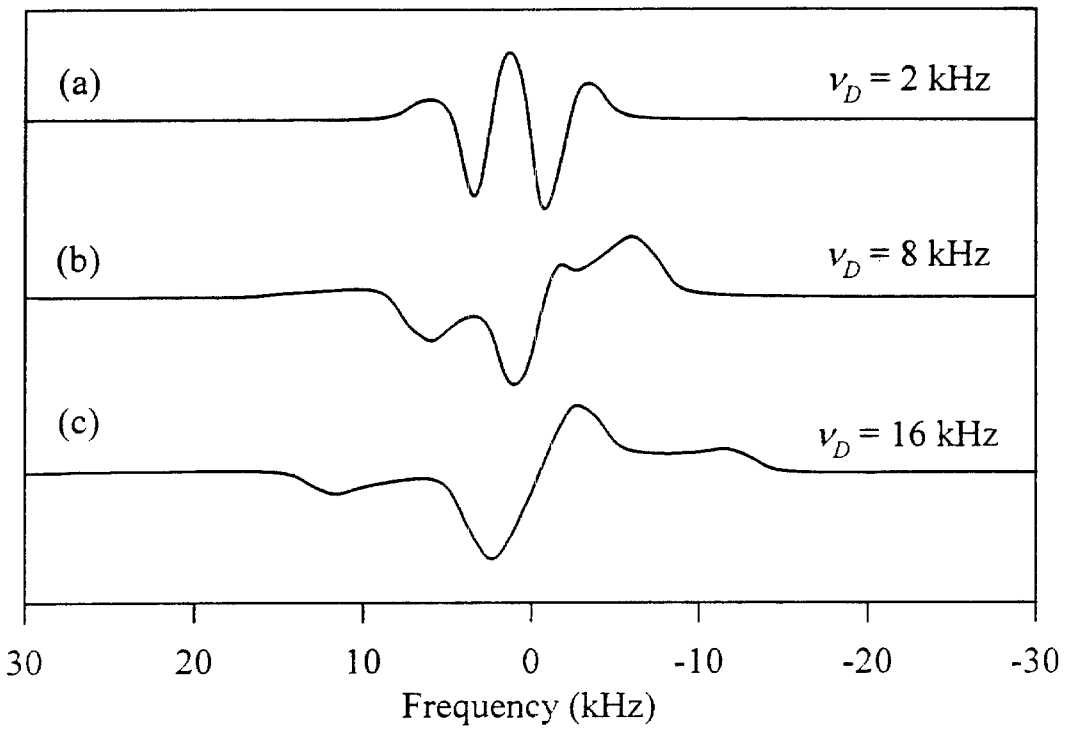
(a)
ν_D = 2 kHz
(b)
ν_D = 8 kHz
(c)
ν_D = 16 kHz
30
20
10
0
-10
-20
-30
Frequency (kHz)

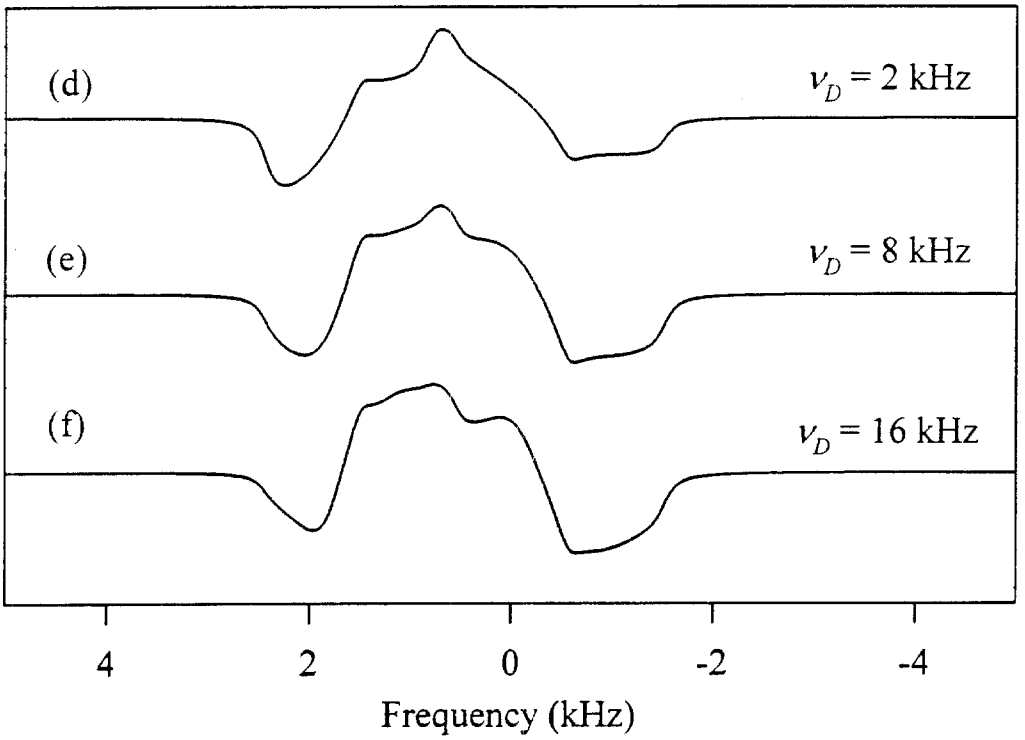
(d)
ν_D = 2 kHz
(e)
ν_D = 8 kHz
(f)
ν_D = 16 kHz
4
2
0
-2
-4
Frequency (kHz)

Fig. 3. (a) PASADENA spectrum for a 50 ms burst of p-H_2 on ZnO. (b) Dipolar averaged spectrum using MREV-8, acquired under the same conditions as the spectrum in (a).

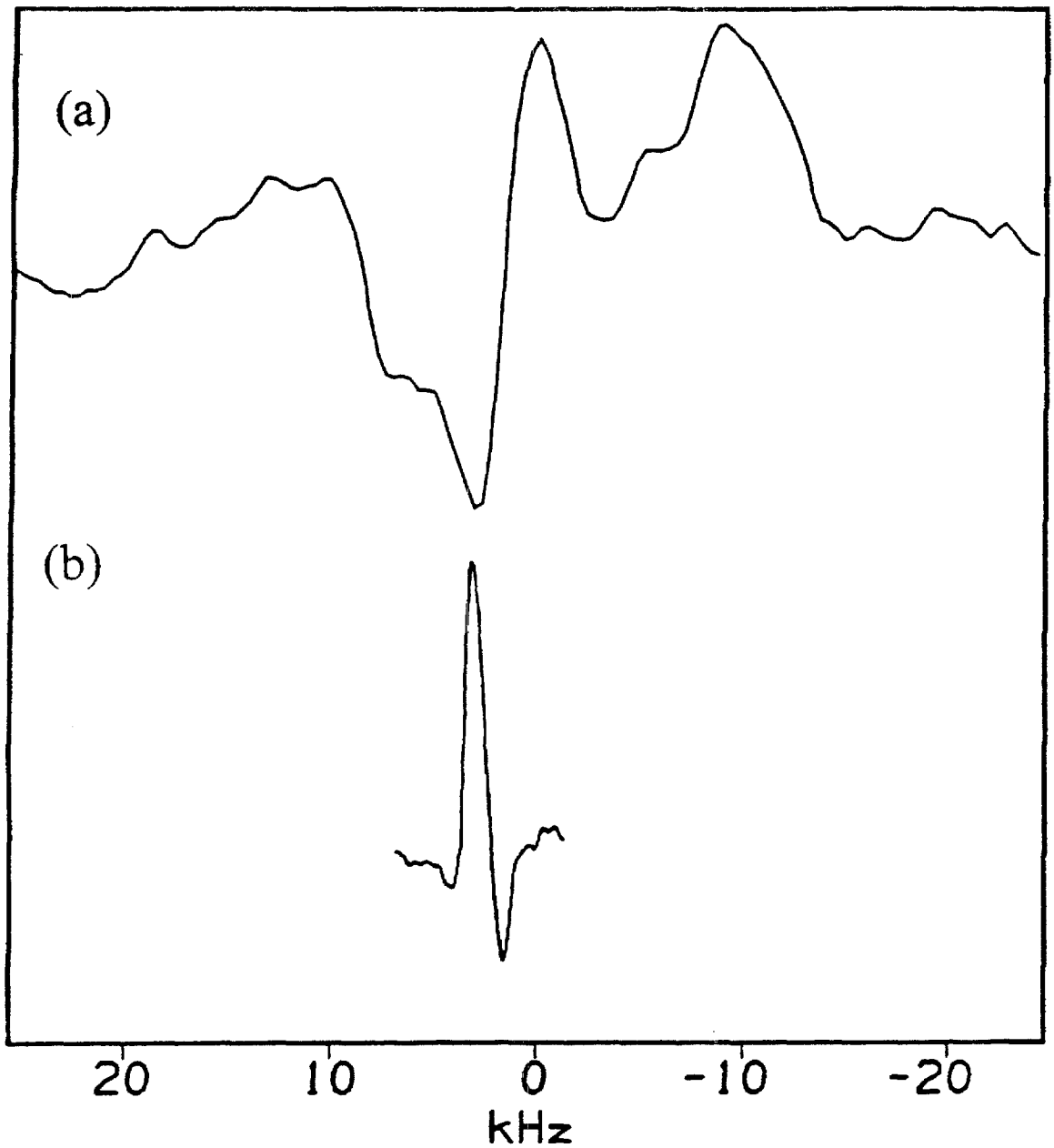

Fig. 4. (a) Simulated PASADENA spectrum using the same chemical shift parameters as the simulations in Fig. 2, with a dipolar coupling parameter of ν_D = 8 kHz. (b) Simulation of dipolar averaged spectrum (using MREV-8), with the same parameters as in (a).

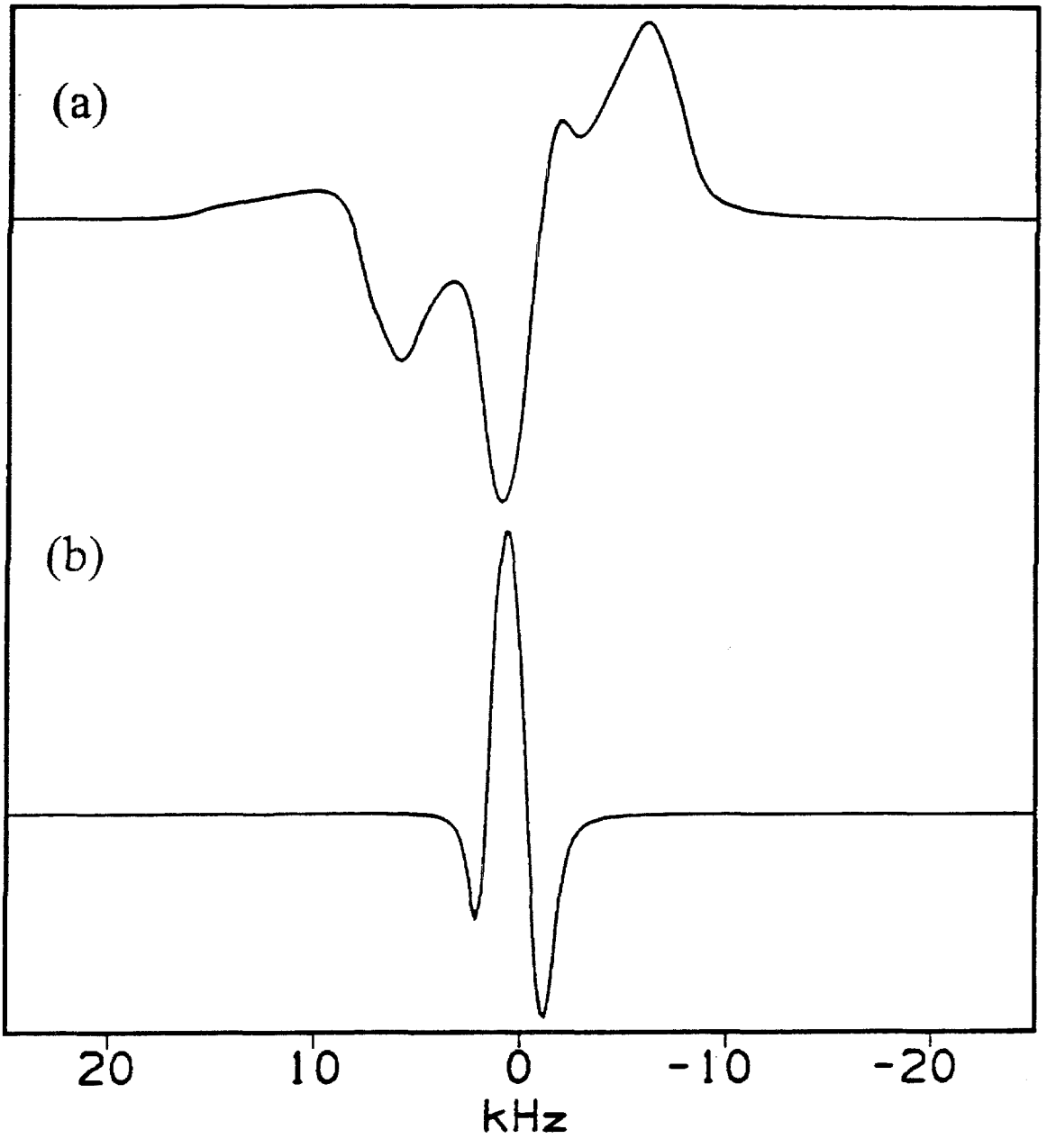

Fig. 5. Simulated spectra for which the chemical shift interaction is selectively averaged to zero by a multiple-pulse sequence such as a train of π pulses. The parameters correspond, respectively, to the same sets of parameters used to generate the full PASADENA spectra in Fig. 3 of Chapter II.

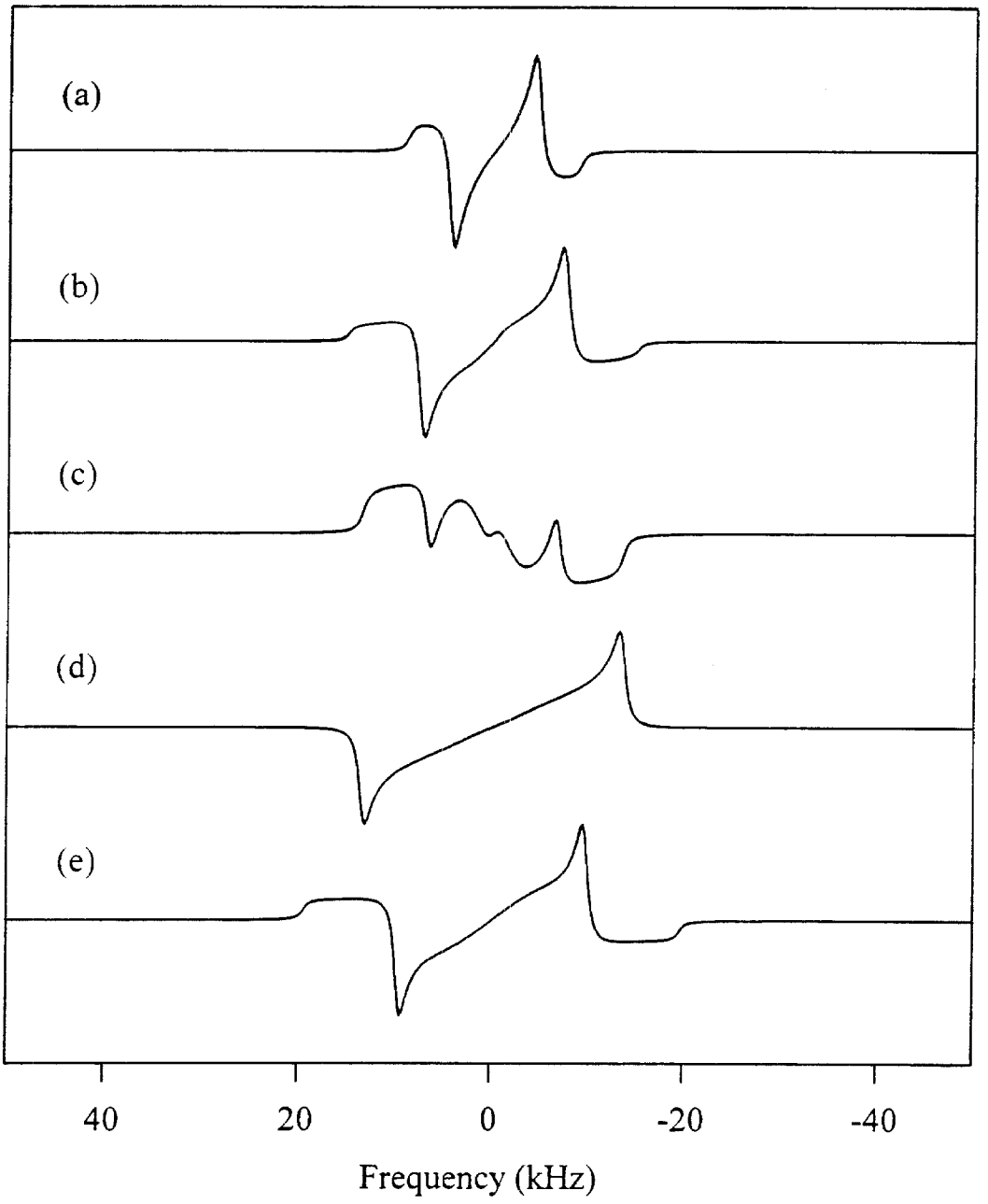

Fig. 6. (a)-(c) Simulated PASADENA spectra with varying isotropic shift difference, shown as Δ_0. (d)-(f) Simulated PASADENA spectra with a chemical shift averaging sequence (such as a train of π pulses), using the same parameter sets as (a)-(c), from top to bottom, respectively. All six simulations use the following chemical shift tensor parameters, except with the isotropic shift difference as specified in the figure: σ_{ii}^1={1.2, 3.2, 5.2}, Ω_1={0,0,0}, σ_{ii}^2={-3.2,-1.2,1.8}, Ω_2={0,0,0}, where the chemical shifts are given in kHz. The dipolar coupling for all six simulations is ν_D = 8 kHz.

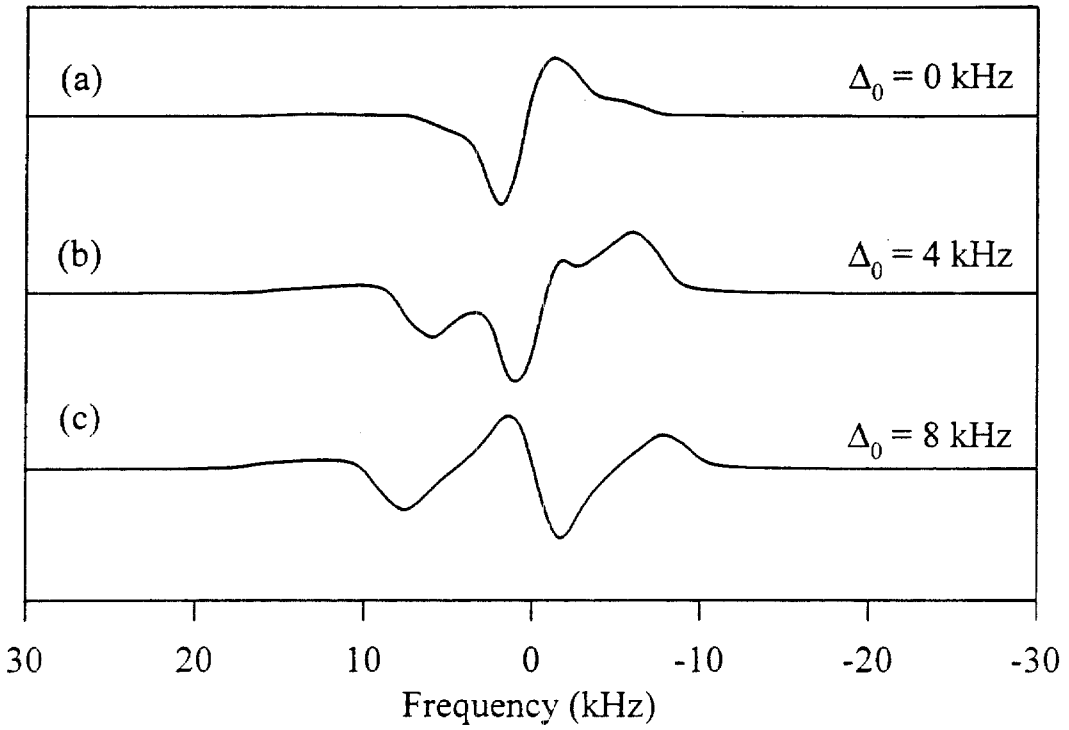
(a)
Δ_0 = 0 kHz
(b)
Δ_0 = 4 kHz
(c)
Δ_0 = 8 kHz
30
20
10
0
-10
-20
-30
Frequency (kHz)

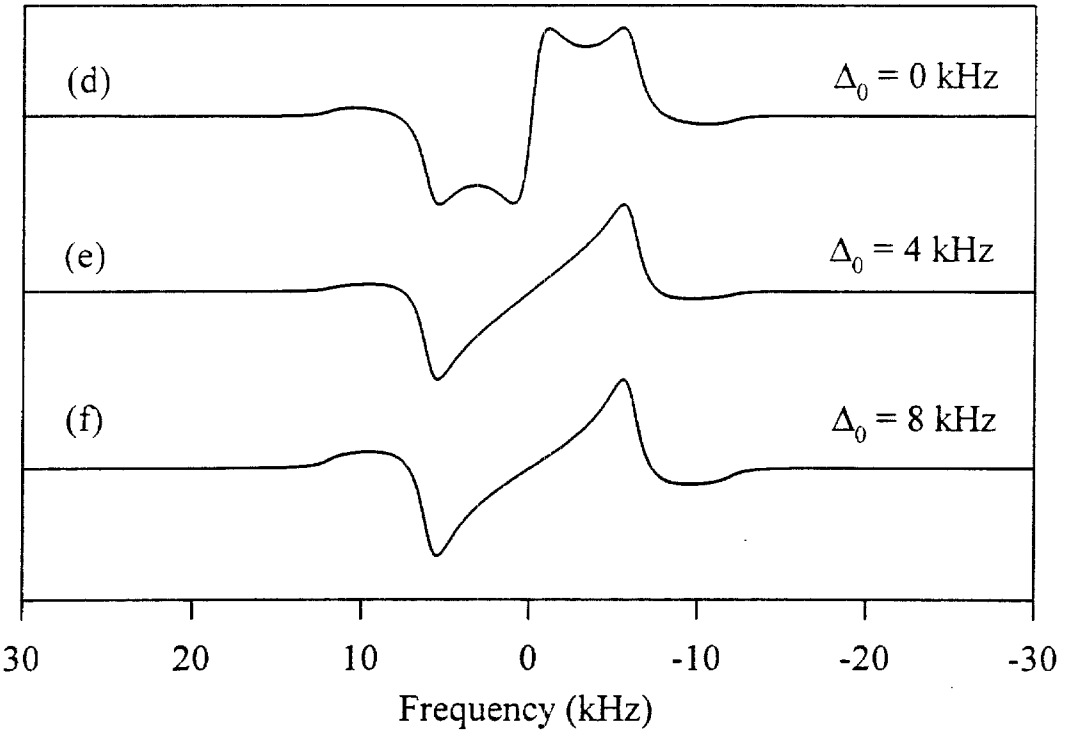
(d)
Δ_0 = 0 kHz
(e)
Δ_0 = 4 kHz
(f)
Δ_0 = 8 kHz
30
20
10
0
-10
-20
-30
Frequency (kHz)

Fig. 7. (a) Two-dimensional zero-quantum spectrum of p-H_2 on ZnO, plotted in magnitude mode. The f_1 axis represents Fourier transformation in the zero-quantum evolution dimension, and the f_2 axis represents Fourier transformation in the free evolution dimension. (b) The projection of the data onto the zero-quantum evolution axis.

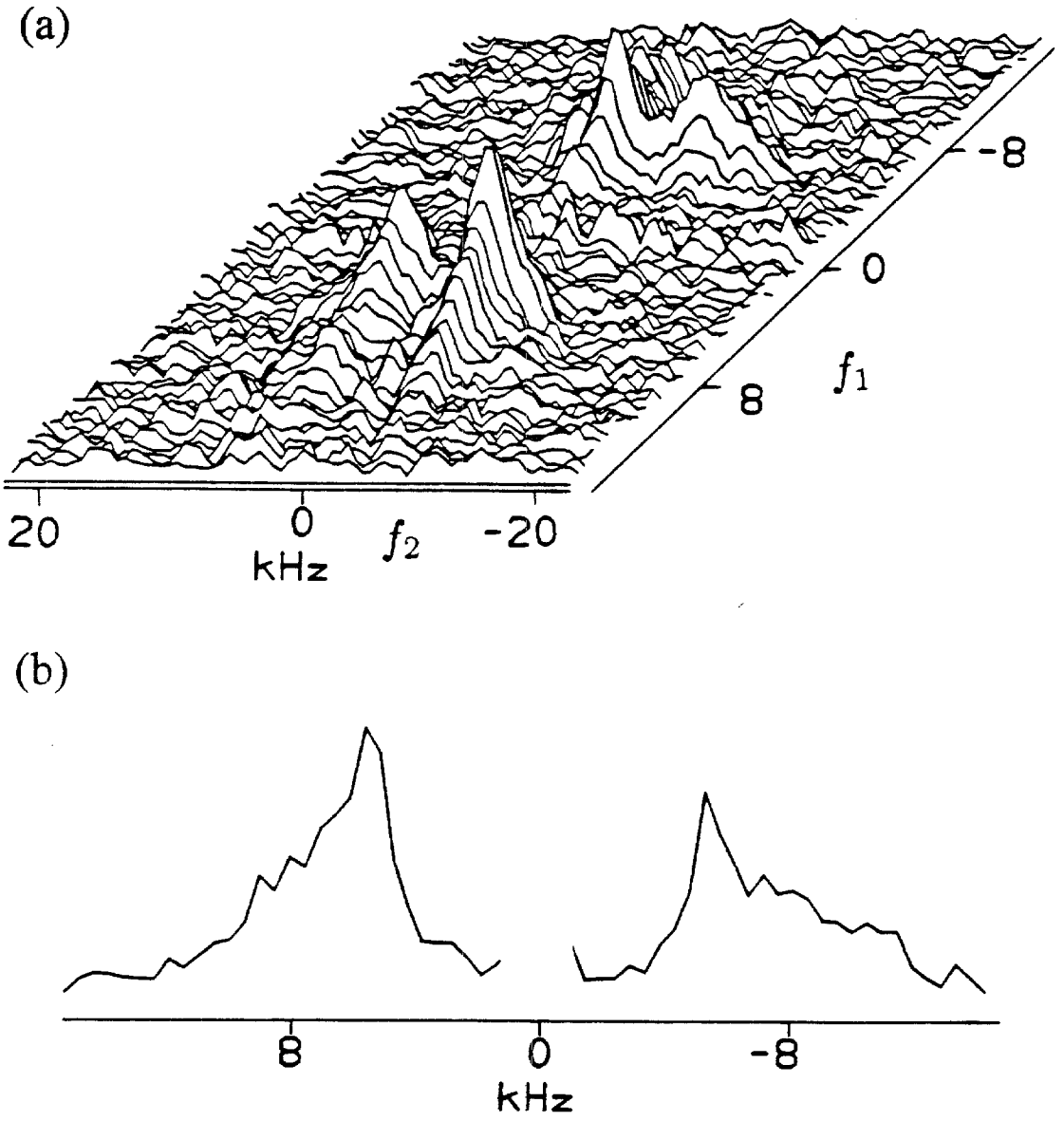

Fig. 8. (a) Simulated two-dimensional zero-quantum PASADENA spectrum, plotted in magnitude mode. The f_1 axis represents zero-quantum evolution, and the f_2 axis represents free evolution. (b) The projection of the spectrum onto the zero-quantum evolution axis.

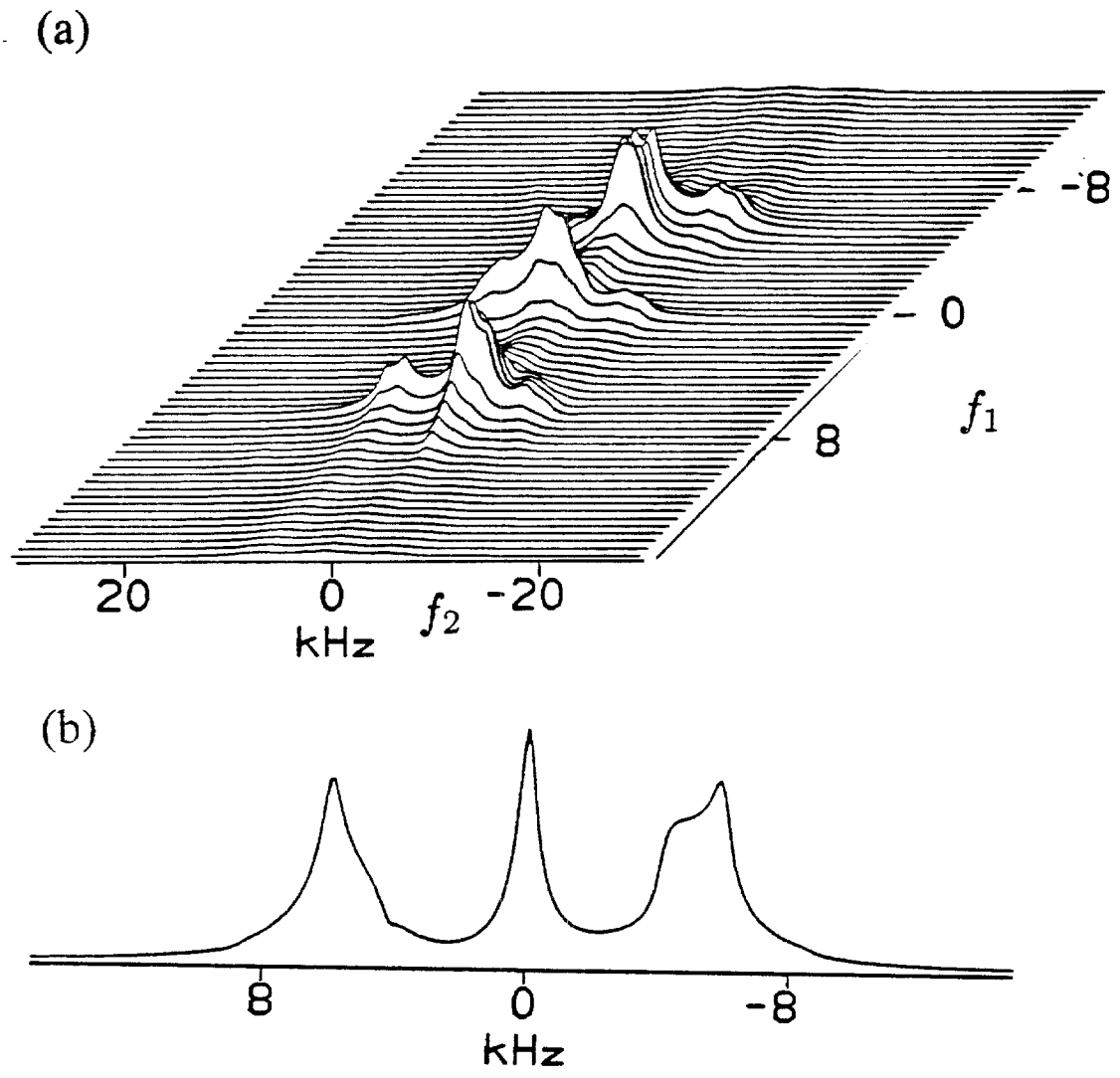

Fig. 9. (a) Simulated two-dimensional double-quantum PASADENA spectrum, plotted in magnitude mode. The f_1 axis represents zero-quantum evolution, and the f_2 axis represents free evolution.

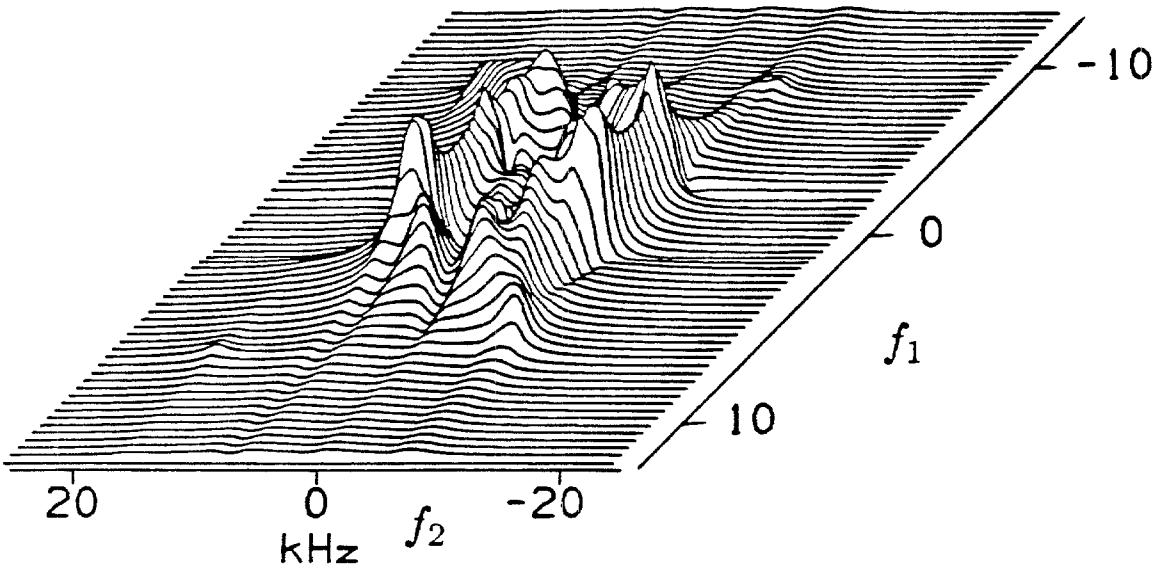

Chapter V . NMR by Measuring the Spin-Symmetry Branching Fraction of Desorbed Hydrogen

1. Introduction

The success of the surface PASADENA effect described in previous chapters provides a tool for orders of magnitude enhancement of surface NMR. It nonetheless requires powdered samples to provide a large enough surface area to detect signals from the surface. As seen in Chapter III, the powder average makes spectral interpretation far more difficult than it would be in liquid-like spectra, including spectra from single crystal surfaces. With ~10^5 fewer spins than powders, however, single-crystal studies present a new and far more daunting sensitivity challenge.

Sensitivity in NMR is traditionally limited by the small degree of spin ordering in the initial condition (which typically derives from equilibrium magnetization in a strong field at temperatures far above the equivalent temperature of the spin transition), as well as by the thermal noise that is unavoidable in detecting the relatively small quantum of the spin transition. The PASADENA effect solves the first of these two limitations but does not address the second. Bowers and Weitekamp [1-4] have proposed that the second

limitation can be solved by changing the detected observable from that of a weak rf quantum to the molecular rotational state (correlated with spin-symmetry) of species desorbed after NMR spin evolution. This observable can be detected far more sensitively, using optical methods, than can precessing magnetization from the same spins. This "inverse-PASADENA" phenomenon is briefly explored further in this chapter.

2. NMR by Detecting the Spin-Symmetry Branching Fraction

In the one variation [5] of the proposed spin-symmetry branching fraction (SSBF) experiment, parahydrogen is allowed to react with a substrate that breaks the magnetic equivalence of the two protons. The initial density operator for the NMR experiment is taken to be just that of the PASADENA experiment. For an oriented system, such as a single crystal surface, and for a spread of reaction times that averages away zero-quantum coherence initiated by the reaction, this initial condition is described by Chapter I, Eq. (32). Spin evolution starting from this state is initiated by a resonant rf pulse and the spin state of the surface bound system after evolution is encoded into free molecular states by rapid molecular desorption of the bound spins. The observable in the experiment is then the expectation value for measuring the free molecule to be in, say, the para state:

$$x_p(t) = \mathrm{Tr}\left\{\rho(t)\left(\frac{1}{4}1 - \mathbf{I}_1 \cdot \mathbf{I}_2\right)\right\} \tag{1}$$

where $\rho(t)$ is the state of the system after evolution. Fourier transformation of the $x_p(t)$ transient yields the zero-quantum NMR spectrum of the spins on the surface.

In another variation, a multiple-pulse line-narrowing sequence that suspends all spin evolution [6,7] is applied during adsorption and then stopped to synchronously initiate evolution of the zero-quantum coherence of the surface bound ensemble. This has the advantage of not wasting the extra spin order represented by the zero-quantum coherence that would otherwise be averaged incoherently over the adsorbing ensemble. The parahydrogen branching fraction, again computed according to Eq. (1), is found in this optimal case to have the following dependence on Hamiltonian parameters:

$$x_p(t) = \frac{1+f}{4} + \frac{f}{2}\left(\sin^2\kappa + \cos^2\kappa \cos\omega_{23}t\right) \tag{2}$$

where $\kappa = \mathrm{Arg}[\Delta + i\,(J\text{–}D)]$, with the chemical shift difference given by $\Delta = \omega_{1z} - \omega_{2z}$, and J and D representing the scalar coupling and orientation-dependent dipolar coupling, respectively. The zero-quantum evolution frequency is given by

$$\omega_{23} = \frac{E_2 - E_3}{\hbar} = \sqrt{(J-D)^2 + \Delta^2} \tag{3}$$

The parameter f quantifies the degree of enrichment of the precursor in one of the two spin-symmetry isomers ($f = x_p - x_o/3$). As seen in Eq. (2), the SSBF experiment has the advantage over the PASADENA experiment in that a coupling between the spins is not required in order to see enhanced signal.

3. Using Strong Zeeman Order as an Alternate Source of Spin Order

The use of spin-symmetry enriched precursors as a source of near-unity spin order has the advantage of relative ease of preparation. For example, as mentioned in previous chapters, equilibration of H_2 at liquid nitrogen temperatures (77 K) in the presence of a

conversion catalyst yields 50% parahydrogen, which translates to an enrichment factor of $f = 0.33$. Using spin-symmetry order has the limitation, however, that the two protons which originated from a single H_2 molecule in the gas phase must remain associated with each other on the surface and desorb as a pair, in order for the enhanced order to be exploited. If the protons scramble on the surface after adsorption and lose their molecular partners, the effect is the same is if normal H_2, with a three to one ortho/para ratio had been added to the surface. This situation is illustrated in Fig. 1. The density operator for the ensemble after scrambling will then be nearly the identity operator (as in the Curie-law experiment) and NMR will not appreciably modulate the fraction of ortho and para desorbed from the surface.

If, on the other hand, highly Zeeman ordered hydrogen is used as the precursor for the SSBF experiment, scrambling does not affect the spin order. This situation is illustrated in Fig. 2, which shows that in this case NMR is still able to modulate the projection of the bound spin state of ultimate molecular partners onto the ortho and para spin states. A pulse sequence for observing SSBF-detected NMR is the following:

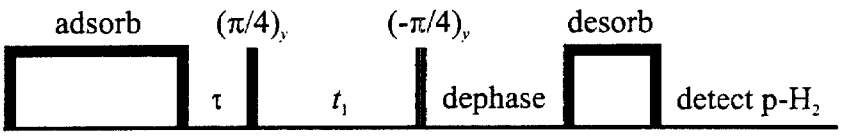

For near unity polarization of the precursor hydrogen (either atoms or molecules), the first $\pi/4$ pulse excites all three possible orders of coherence (zero, single, and double-quantum) in the two-spin system formed by any pair that will ultimately desorb as a molecule. These coherences then evolve during the time period t_1 after which another $\pi/4$

pulse and a dephasing period allow encoding of all orders of coherent evolution into the projection of the state onto either para or orthohydrogen upon desorption.

A simulated single-crystal SSBF spectrum using the pulse sequence shown above is shown in Fig. 3 for a particular choice of chemical shifts and no coupling between the protons during evolution. The linewidth is conservatively estimated to be 200 Hz. The main feature of this spectrum is that the lines are "liquid-like" and hence well resolved, unlike the case of powders, needed for the PASADENA experiment. In general, the spectrum reports on all thirteen internal parameters in the Hamiltonian (the internuclear distance, and six parameters from each shift tensor) as well as the two polar angles orienting the magnetic field in the molecular frame, for a total of fifteen parameters. The internal parameters can be delineated by rotation studies in which a separate SSBF spectrum is acquired for each orientation of the crystal in the magnetic field and the line positions are fit to a theoretical model for the orientation dependence of the Hamiltonian.

As shown in Chapter I, the equilibrium density operator for a two-spin system at temperature T can be written

$$\rho_{eq} = \frac{1}{4}\mathbb{1} + \frac{\zeta}{2}\left(I_{1z} + I_{2z}\right) + \frac{\zeta^2}{2} I_{1z} I_{2z} \tag{4}$$

where

$$\zeta = \tanh\left(\frac{\hbar\omega_0}{2k_B T}\right) \tag{5}$$

and ω_0 is the Larmor frequency. For the experiment simulated in Fig. 3, the bilinear term in Eq. (4) contributes all orders of coherence that contribute to the measured signal. Using Eqs. (4) and (5), the amplitudes of the various lines in the spectrum can be computed as a

function of spin temperature. Fig. 4 shows the relative line intensities as a function of $1/T^2$. The polarization corresponding to each spin temperature T is shown on the axis below the figure. In the case of a two spin-1/2 system, the polarization is given by $P_{eq} = \langle I_z \rangle = \zeta$. The figure shows that a spin temperatures as low as ~ 3×10^{-3} K (corresponding to a polarization of ~0.9) are needed to approach the asymptotic limit for maximum intensity. It also shows that in the limit of high spin temperatures (small polarizations) the spectral intensities are linear in $1/T^2$ as expected from (4) and the high-temperature limit for ζ:

$$\zeta \rightarrow \frac{\hbar\omega_0}{2k_B T} \tag{6}$$

4. Approaches to SSBF Detection

In this section, the essential elements of a proposed SSBF apparatus are discussed. A schematic of the apparatus is shown in Fig. 5. The arrangement at the top left of the figure allows for variable sample orientation relative to a strong static magnetic field. Variable sample temperature is also possible with this arrangement. The detection of ortho and para mole fractions of desorbed molecular hydrogen is performed with extreme sensitivity using laser induced fluorescence in an optical cell that can be distant from the NMR magnet. The experimental sequence is as follows.

The target species is formed by chemisorption of spin-ordered hydrogen (e.g., parahydrogen, Zeeman polarized H_2, or nuclear-spin polarized H atoms) on the surface of interest. The adsorption time of the ensemble is restricted to be shorter than the spin

lattice relaxation time on the surface. Excess gas-phase hydrogen is evacuated and the desired NMR pulse sequence is delivered, thereby modulating the spin populations of the target species and more importantly, modulating the projection of the spin state onto the states of the spin-symmetry isomers. The surface bound hydrogen is then desorbed from the surface, for example by rapid sample heating through contact with a resistive plate or by laser heating. The NMR transient, or "FID," is thus encoded in pointwise fashion into the ortho and para mole fractions of the H_2 desorbed from the surface. The experiment is repeated for each point in interferogram, stepping the evolution time accordingly.

The desorbed H_2 gas (containing a roughly estimated 10^{10} molecules per shot for ZnO, or 10^{-8} torr in a volume of 100 cm^3) is compressed by first expanding into the cavity of a piston whose volume after the sample is sealed off is much larger than the volume above the crystal sample and the tubing connecting the sample chamber to the piston. Nearly all of the desorbed molecules can then be compressed into a small volume for optical detection with optimum sensitivity.

The two main requirements for any optical detection scheme to be used in the SSBF experiment are that para (even j_{rot}) and ortho (odd j_{rot}) states be resolved and that detection with sensitivity well below the number of molecules desorbed per shot be possible.

One possibility for optical detection that meets these requirements is laser induced fluorescence (LIF) of hydrogen [8-12] in the vacuum ultraviolet. Typically XUV or VUV radiation is used to excite bands in the Lyman, $B\,^1\Sigma_u^+ - X\,^1\Sigma_g^+$, system, as shown in Fig. 6, and the resulting VUV fluorescence is measured. The excitation and fluorescence processes conserve spin-state parity, enabling detection of ortho and para mole fractions.

Parker and Kuppermann [12] have achieved LIF sensitivity to 10^7 states. A schematic of their apparatus is shown in Fig. 7. A dye laser was used to generate light at 660 nm which was then frequency doubled using appropriate doubling crystals. Third-harmonic generation of VUV light from the UV light was accomplished in a Kr gas cell adjacent to the H_2 target cell. The pulse length achieved was 5 ns with a pulse energy of 300 pJ (1.7×10^8 photons at 110 nm), and a repetition rate of 20 Hz. Fluorescence in the VUV was detected with a photomultiplier tube, with a geometric collection efficiency of ~0.5%.

The VUV absorption spectrum [12] acquired using this apparatus shown in Fig. 8 (acquired using the above apparatus) demonstrates the rotational resolution needed to detect the ortho and para branching fractions of H_2 desorbed after NMR evolution. The LIF spectrum was obtained by scanning the frequency of the incident light and collecting the undispersed fluorescence. The signals are normalized to correct for fluctuations of the intensity of each laser pulse, which is measured separately. The noise level (3σ) corresponds to ~10^7 states. The NMR of surface species using the SSBF method combined with LIF for the detection of ortho and para mole fractions will thus be possible at this sensitivity.

5. References

[1] C.R. Bowers and D.P. Weitekamp, J. Am. Chem. Soc. **109**, 5541 (1987).

[2] C.R. Bowers, D.H. Jones, N.D. Kurur, J.A. Labinger, M.G. Pravica and D.P. Weitekamp, Adv. Magn. Reson. **14**, 269 (1990).

[3] C.R. Bowers, Ph.D. Thesis, California Institute of Technology (1991).

[4] C.R. Bowers, S.K. Buratto, P.J. Carson, H.M. Cho, J.Y. Hwang, L.J. Mueller, P.J. Pizarro, D.N. Shykind and D.P. Weitekamp, SPIE Optical Methods for Ultrasensitive Detection and Analysis: Techniques and Applications **1435**, 36 (1991).

[5] C.R. Bowers and D.P. Weitekamp, in preparation .

[6] D.P. Weitekamp, J.R. Garbow and A. Pines, J. Chem. Phys. **77**, 2870 (1982).

[7] H.M. Cho, C.J. Lee, D.N. Shykind and D.P. Weitekamp, Phys. Rev. Lett. **55**, 1923 (1985).

[8] E.E. Marinero, C.T. Rettner, R.N. Zare and A.H. Kung, Chem. Phys. Lett. **95**, 486 (1983).

[9] F.J. Northrup, J.C. Polanyi, S.C. Wallace and J.M. Williamson, Phys. Lett. **105**, 34 (1984).

[10] W. Meier, H. Rottke, H. Zacharias and K.H. Welge, J. Chem. Phys. **83**, 4360 (1985).

[11] W. Meier, G. Ahlers and H. Zacharias, J. Chem. Phys. **85**, 2599 (1986).

[12] G.R. Parker, Ph.D. Thesis, California Institute of Technology (1988).

Fig. 1. Schematic illustration of the effect of scrambling after adsorption of parahydrogen to a substrate surface. Scrambling prevents modulation of the spin-symmetry isomer projections by NMR.

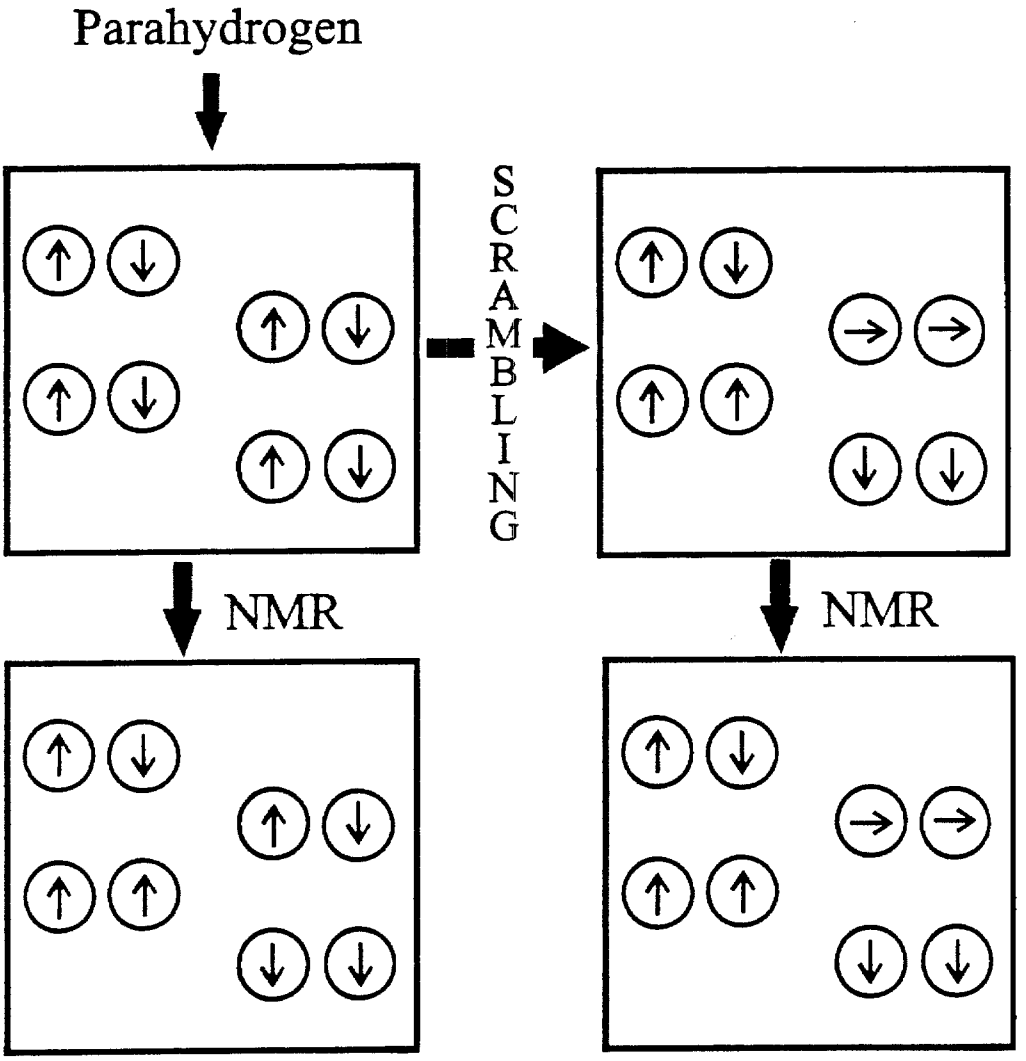

Fig. 2. Schematic illustration of the effect of scrambling after adsorption of highly Zeeman order H_2 to a substrate surface. Scrambling does not prevent modulation of the spin-symmetry isomer projections by NMR.

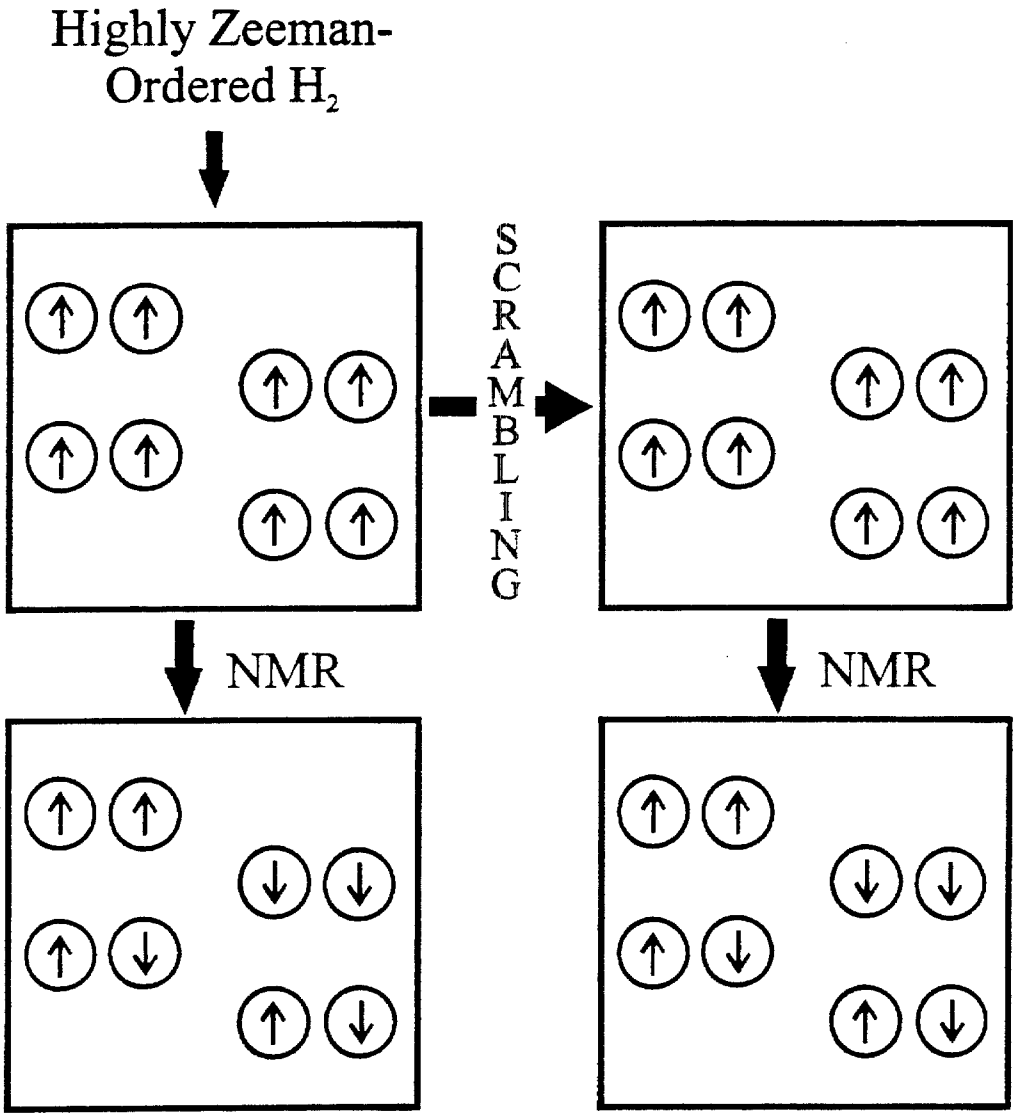

Fig. 3. Simulated single-crystal SSBF spectrum, starting with highly Zeeman ordered hydrogen precursor. The chemical shifts of the two protons on the surface are $\omega_{1z} = 8$ kHz and $\omega_{2z} = 10$ kHz.

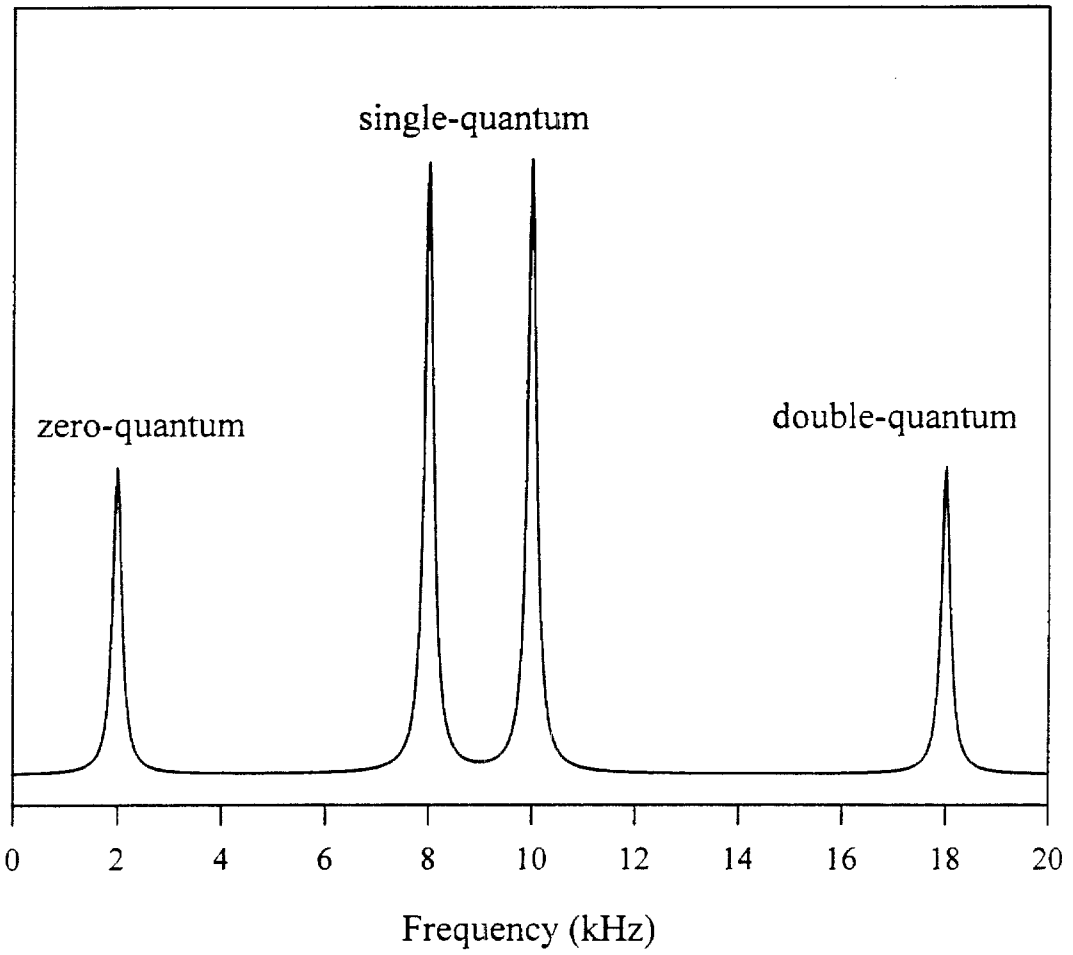

Fig. 4. Relative intensities of the spectral lines in the SSBF spectrum shown in Fig. 3, starting from highly Zeeman ordered hydrogen, as a function of $1/T^2$, where T is the spin temperature. The calculation assumes a static field strength of 4.7 T (corresponding to a proton Larmor frequency of 200 MHz).

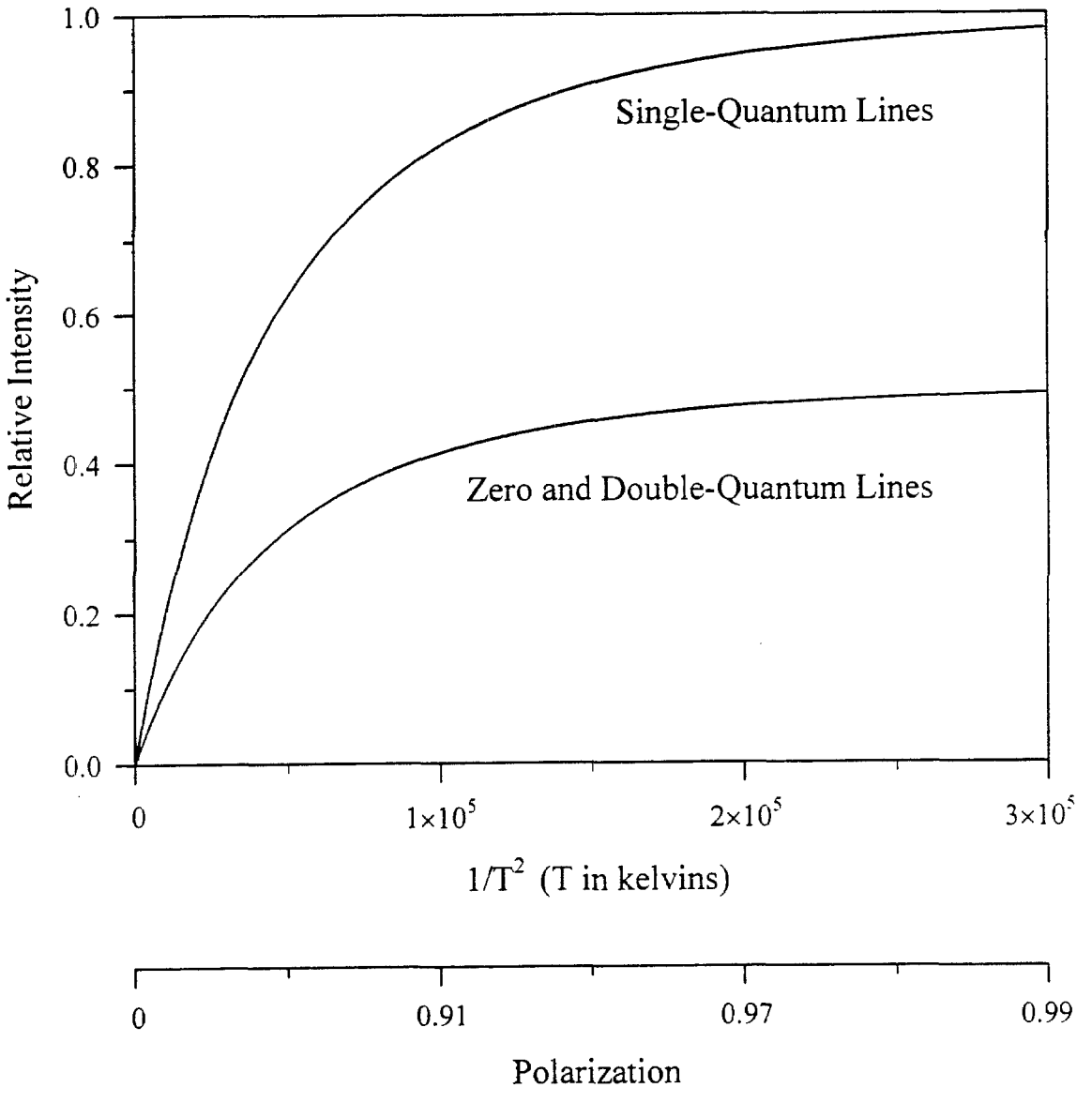

Fig. 5. Schematic diagram of the proposed apparatus for detecting NMR by measuring the spin-symmetry branching fraction (SSBF) of molecules desorbed after NMR evolution on a single crystal surface.

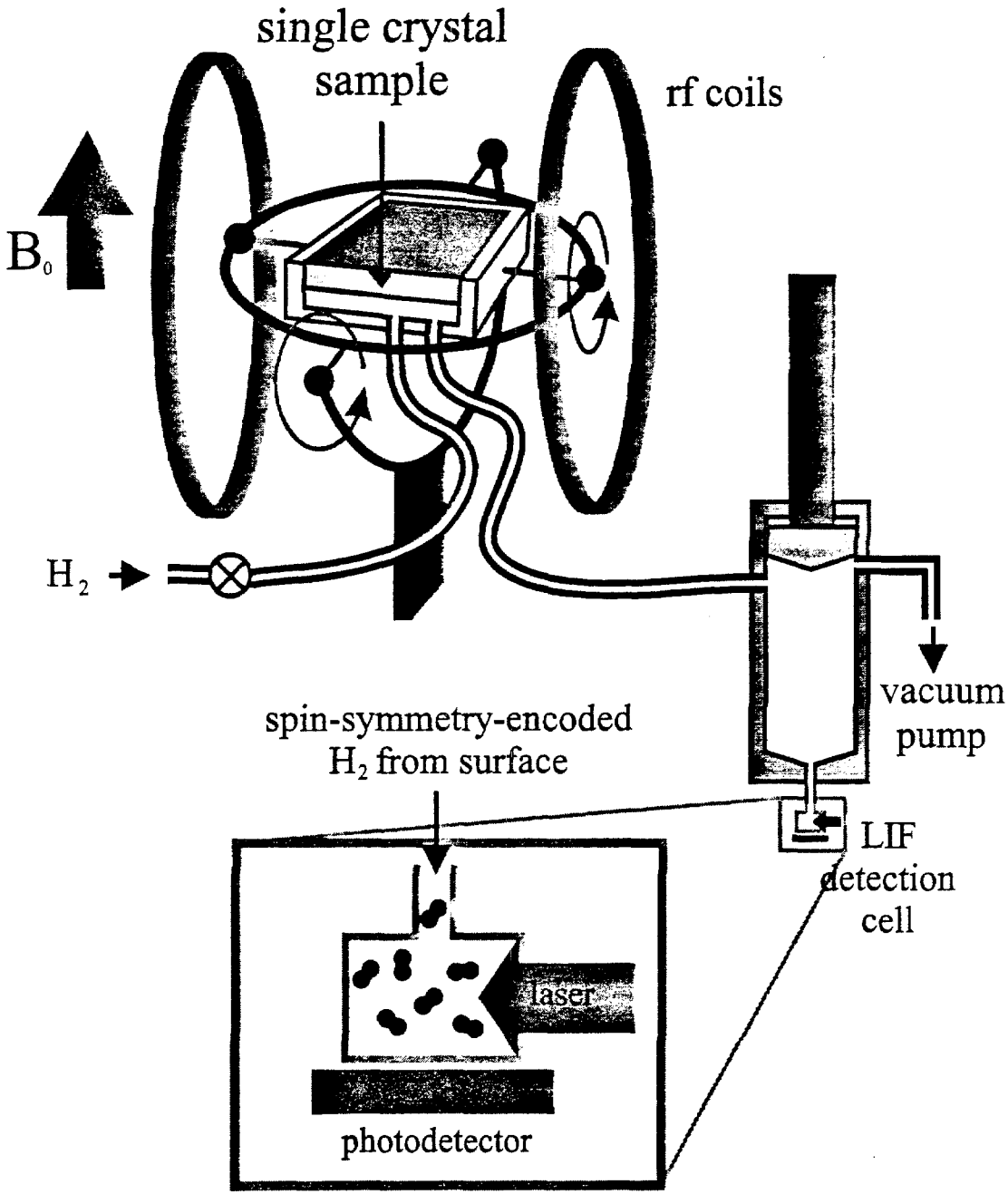

Fig. 6. Lyman band system of molecular hydrogen used for quantum-state-specific detection of H_2 via laser induced fluorescence.

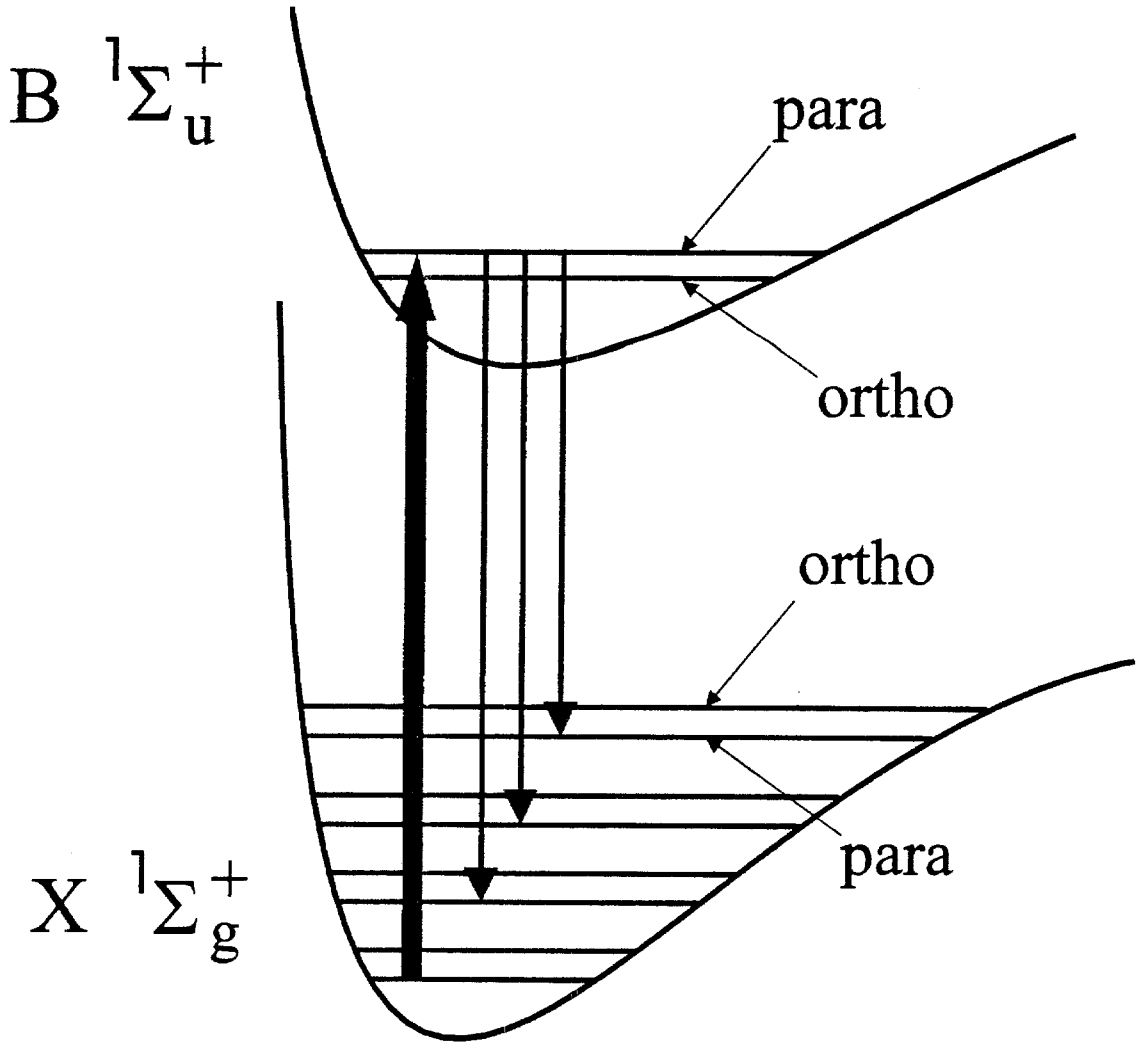

Fig. 7. Schematic diagram of apparatus [12] for generation of VUV light and detection of laser induced fluorescence of molecular hydrogen.

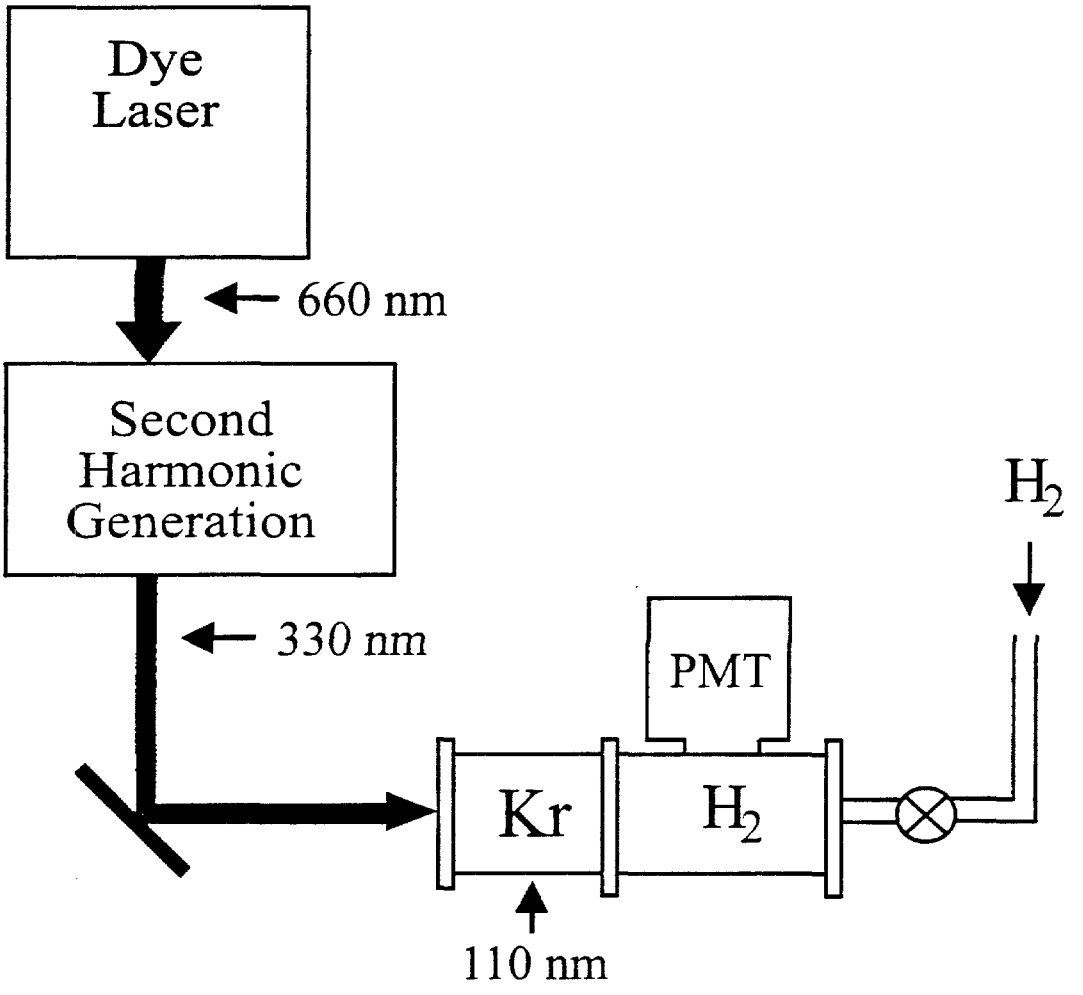

Fig. 8. LIF experiment by Parker and Kuppermann [12] showing the rotational resolution required to measure ortho and para mole fractions in the SSBF NMR experiment. The spectrum is an average of six scans, with 7-8 laser pulses per point.

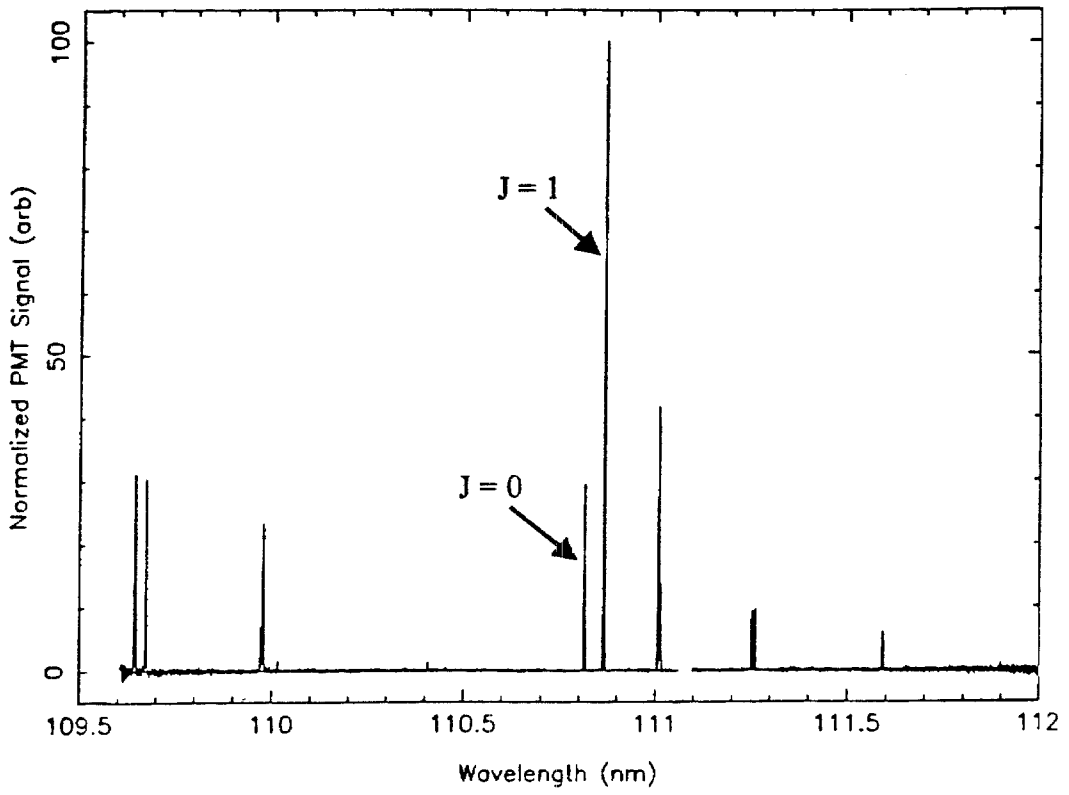

Chapter VI. Optical Larmor Beat Detection

1. Introduction

Nuclear magnetic resonance is unique among the spectroscopies in its ability to discriminate between subtle differences in electronic environment and bonding geometry. As such, it is well-suited for obtaining information in semiconductors on both structure and excited-state electronic wavefunctions. Through the nuclear electric quadrupole interaction, it provides the ability to measure electric field gradients due, for example, to point defects or interfacial bonding. The quadrupole interaction also reports on strain arising from either lattice mismatch or external stress. The Knight shift measures electron spin polarization and probability density at nuclear sites. Even electric fields that are homogeneous from one unit cell to the next can be measured as quadrupole splittings through a linear Stark effect.

Electronic and optical devices grown from III-V semiconductors are prime targets for nuclear magnetic resonance spectroscopy, but conventional NMR using Curie-law magnetization and rf detection lacks the sensitivity required to probe the approximately

10^{12} nuclei/mm^2 present in a single epitaxial structure. Optical pumping with circularly polarized light at the bandgap provides large nonequilibrium nuclear polarizations,[1,2] effectively solving the first part of the sensitivity problem. Optical detection of NMR [3-12] through the Hanle effect overcomes the second part. In this technique, the polarization of photocarriers in the conduction band, and hence the circular polarization of subsequent luminescence, is sensitive to the nuclear spin polarization.

The quasi-steady-state experiment of these early optically-detected NMR studies, however, lacks the resolution necessary to exploit the exquisite discrimination and ease of spectral interpretation of NMR. This problem was overcome by Burratto and Weitekamp [13,14] using a time-sequencing technique in which optical nuclear polarization, nuclear spin evolution (to encode the spectrum), and optical detection of the final nuclear spin state are divided into successive periods and are thus separately optimizable. The result is an order-of-magnitude improvement in resolution, as well as improvement in sensitivity. In abandoning the steady-state approach, it also makes available to the study of single epitaxial structures the full power of modern time-domain multiple-pulse NMR techniques.

The time-sequenced technique for optical NMR (ONMR) is necessarily pointwise since the quantizing magnetic field applied during detection stops precession. To obtain the NMR interferogram a period of coherent NMR evolution is incremented on successive shots, with each shot contributing one time-domain point. This has the effect of limiting experimental throughput, and also has the potential for introducing random shot to shot variation (which translates into noise in the spectrum) that is larger than detection noise.

This chapter describes a new technique [15] for optically detected NMR of III-V semiconductors in which luminescence polarization is modulated at the difference frequency between two precessing nuclear fields. The nuclear field of one isotope is spin locked to provide a reference field of known frequency while the free precession of the isotope of interest is effectively measured via the differences between its Fourier components and the reference field. This Larmor beat detection (LBD) method lifts the previous pointwise restriction of time-sequenced ONMR and allows the collection of NMR transients in real time.

2. Optical Absorption and Emission

The band structure for GaAs is shown in Fig. 1. The conduction band ($J = 1/2$) in GaAs is ~1.5 eV above the top of the valence band. The heavy-hole ($J = 3/2$) and light-hole ($J = 1/2$) bands are degenerate at $k = 0$, and the spin-orbit coupling separating these two bands from the split-off band ($J = 1/2$) is $\Delta \sim 0.3$ eV at $k = 0$.

The selection rules [7] for photon absorption in GaAs are shown in Fig. 2. The selection rules show that an excess of one of the two spin orientations of the conduction band electrons results from illumination with either right-hand or left-hand circularly polarized light. The ratio of transition probabilities for a single polarization of light for degenerate heavy-hole and light-hole bands is 3:1. The result is a spin polarization immediately after absorption of $|\mathbf{P}_e| = 1/2$, with the vector polarization defined as

$$\mathbf{P}_e \equiv \frac{n_+ - n_-}{n_+ + n_-} \mathbf{n}_E \qquad (1)$$

where n_+ and n_- are the number of spin-up and spin-down electrons, respectively, and $\mathbf{n}_E$ is the unit vector in the direction of excitation. Spin relaxation competes with recombination to dictate the net polarization of the conduction electrons. If the rate of recombination is $1/\tau$ and the rate of electron spin relaxation is $1/\tau_s$, then the expectation value for electron spin angular momentum in steady-state is given by

$$\mathbf{S} = \frac{1}{2}\frac{\tau_S}{\tau + \tau_S}\mathbf{P}_e \tag{2}$$

One consequence of the conduction-electron polarization, along with the selection rules for optical transitions, is that the subsequent luminescence is also polarized. The degree of circular polarization of luminescence is given by the quantity

$$\rho = \frac{I_+ - I_-}{I_+ + I_-} \tag{3}$$

where I_+ is the intensity of right-hand circularly polarized luminescence and I_- is the intensity of left-hand circularly polarized luminescence. The selection rules dictate that the degree of circularly polarized luminescence and the polarization of the conduction electrons are related by

$$\rho = -\frac{1}{2}\mathbf{P}_e \cdot \mathbf{n}_D = -\mathbf{S} \cdot \mathbf{n}_D \tag{4}$$

where $\mathbf{n}_D$ is the unit vector in the direction of the detection axis.

3. Optical Nuclear Polarization and Optical Detection of NMR

Polarized conduction electrons are able to share their polarization with the lattice nuclei through the Fermi-contact hyperfine interaction. The spin Hamiltonian for the hyperfine interaction can be written:[16]

$$H_{\mathrm{HF}} = \frac{2}{3}\mu_0 \hbar^2 \gamma_e \sum_j \gamma_j |\psi(\mathbf{r}_j)|^2 \mathbf{S}\cdot\mathbf{I}_j \tag{5}$$

where μ_0 is the permeability of free space, γ_e is the electron gyromagnetic ratio, γ_j is the nuclear gyromagnetic ratio of the j^{th} nucleus, $\Psi(\mathbf{r}_j)$ is the electronic wavefunction at the position of the j^{th} nucleus, and $\mathbf{S}$ and $\mathbf{I}_j$ are the electron and nuclear spin angular momentum operators, respectively.

For the case of a quantizing magnetic field in the same direction as the optical orientation axis, dynamic nuclear polarization via the hyperfine interaction results in an expectation value for nuclear spin angular momentum of

$$< I > = \frac{4}{3} I(I+1) < S > \tag{6}$$

neglecting nuclear spin relaxation. In the GaAs experiments described in this thesis, nuclear spin polarizations of ~ 10% have been observed with less that 5 sec of optical nuclear polarization.

The hyperfine interaction also provides a means of optical detection of nuclear fields [2] via the Hanle effect, in which the degree of circular polarization of luminescence is sensitive to the size of the nuclear fields. The case of two nuclear hyperfine fields transverse to the direction of luminescence observation will be treated here, since this is the basis of the Larmor beat detection method. For the moment, these

two fields will be assumed to be static and will be written as $\mathbf{B}_N^{sig}$ and $\mathbf{B}_N^{ref}$, where "sig" and "ref" will later denote signal and reference fields. In this case the Hanle-effect luminescence polarization is given by

$$\rho = \rho_0 \frac{B_H^2 + |\mathbf{B}_0 + \mathbf{B}_N^{misc}|^2}{B_H^2 + |\mathbf{B}_0 + \mathbf{B}_N^{misc}|^2 + |\mathbf{B}_N^{ref} + \mathbf{B}_N^{sig}|^2} \tag{7}$$

where $\mathbf{B}_0$ is the applied static magnetic field and $\mathbf{B}_N^{misc}$ refers to any remaining nuclear fields parallel to the applied field. The characteristic "Hanle-width" is given by B_H and is measured in the GaAs heterojunction of Chapter VII to be ~80 gauss.

The mechanism of Hanle depolarization of luminescence is the precession of photoelectrons around the total magnetic field before recombination. When the total field contains transverse components, this precession results in a net decrease in average electron polarization in the longitudinal direction. This process is depicted in the time domain in Fig. 3, showing that larger the transverse field (and hence the larger the precession frequency) the smaller the average electron polarization in the longitudinal direction z, and vice versa.

The effect of longitudinal magnetic fields, both applied fields and nuclear hyperfine fields, is to effectively increase the Hanle width, as shown in Fig. 4. The result is that a larger net transverse field is needed to achieve the same depolarization as without longitudinal fields.

The Hanle effect provides the basis for optical detection of NMR in semiconductors. In traditional steady-state methods for optically detecting NMR, an applied radiofrequency magnetic field is swept in frequency and resonance is detected as Hanle depolarization due the resulting transverse nuclear hyperfine fields. Alternatively, a

resonantly spin-locked nuclear field is swept through the transverse plane using adiabatic rapid passage and the luminescence depolarization is measured to record the cw NMR spectrum.

4. Larmor Beat Detection

In the steady-state methods for optically detecting NMR described above, the measured luminescence depolarization is insensitive to the orientation of the nuclear fields *within* the transverse plane. This is a direct result of Eq. (7), which shows that Hanle depolarization depends only on the *magnitude* of net transverse field and not on its direction.

The basis of the Larmor beat detection method is the introduction of a transverse reference field, in addition to the transverse field that is being measured, so that *magnitude* of the vector sum field (reference plus signal) is modulated at the difference frequencies of its Fourier components. This, in turn, modulates the circular polarization of luminescence at the difference frequencies.

To optimize both sensitivity and linearity, the reference field is chosen to be larger than the signal field and comparable in size to the total longitudinal field. In GaAs, this is achieved by spin locking one of the nuclear fields to serve as the reference field, while the NMR of the nucleus of interest is recorded. The resulting Hanle depolarization is described by Eq. (7), with reference and signal fields now time dependent.

Figure 5(a) shows the evolution of the reference and signal hyperfine fields during Larmor beat detection. The reference field is shown as a precessing cone about the z axis

parallel to the static magnetic field. The signal field is shown as a purely transverse field precessing about the static field, but whose vector is translated to show addition with the reference field. The vector sum of the two fields is shown as an elevated rosette, along with its projection onto the transverse plane, of relevance to the Hanle effect. Fig. 5(b) shows the transverse component of the vector sum trajectory projected onto the 2D Hanle curve describing luminescence depolarization. The vertical component of the projected curve gives ρ, which now oscillates in time, primarily at the Larmor beat frequency.

For two precessing nuclear hyperfine fields, the Fourier component of luminescence polarization at the difference in Larmor frequencies is given by

$$\rho(t) = -2\rho_0 \sum_i \left(\frac{b_N^{ref}(t)}{\left\{ [b_N^{ref}(t)]^2 + 1 \right\}^2} b_N^{sig,i}(t) + O[(b_N^{sig,i})^3] \right) \cos \omega_i t \qquad (8)$$

where ρ_0 is the steady-state luminescence polarization and ω_i is the Larmor beat frequency, with i indexing lines in the spectrum of the signal nucleus. The "reduced" nuclear hyperfine fields whose magnitudes appear in Eq. (8) are given (in vector form) by

$$\mathbf{b}_N^{ref,sig} = \frac{\mathbf{B}_N^{ref,sig}}{\sqrt{B_H^2 + |\mathbf{B}_0 + \mathbf{B}_N^{misc}|^2}} \qquad (9)$$

The circularly polarized luminescence signals given by Eq. (8) are demodulated by a heterodyne rf spectrometer and digitized to record the NMR spectrum of the signal nucleus.

Figure 6 shows schematically the sequence of events in real-time optical NMR using Larmor beat detection. A period of optical nuclear polarization is followed by resonant rf pulses to the nuclei, after which the reference nucleus is spin locked and the signal nucleus undergoes free precession, modulating luminescence polarization at the

difference between the reference frequency and all of the spectral frequencies of the signal nucleus.

It is also possible to use the LBD method as a pointwise method by spin locking the signal nuclear field after a period of spin evolution and measuring the Larmor beat frequency between the two simultaneously spin-locked fields. The NMR transient is then mapped out by stepping the evolution period and repeating the experiment. This has the advantage,[17] as in ordinary NMR, of improving the sensitivity of the experiment by prolonging the transverse signal nuclear field. The sequence of events for the pointwise experiment is shown in Fig. 7. Here NMR evolution to encode the spectrum is followed by a pulse which stores coherences as populations (corresponding to vertical nuclear fields) which are then read out by a pulse and subsequent spin locking of each nuclear field simultaneously.

Figure 8 shows the resolution obtainable in a GaAs heterostructure with multiple-pulse line-narrowing using Larmor beat detection. For comparison, spectra using steady-state and Fourier-transform time-sequenced NMR (without line narrowing) are shown. The line-narrowed LBD spectrum (recorded in a static magnetic field of 0.2 T) achieves a linewidth of ~50 Hz. It has been proposed [18] that imaging of the excited-state electronic wavefunction can be achieved in a quantum well by using multiple-pulse line narrowing and reintroducing the Knight-shift interaction with optical pulses during the windows of the NMR pulse sequence. The linewidth achieved to date using multiple-pulse LBD is not far from the ~10 Hz resolution needed to resolve individual atomic layers using this imaging method.

5. References

[1] G. Lampel, Physical Review Letters **20**, 491 (1968).

[2] F. Meier and B.P. Zakharchenya, Eds. (1984). *Optical Orientation.* Modern Problems in Condensed Matter Sciences. Amsterdam, Elsevier.

[3] M.I. Dyakonov and V.I. Perel, Soviet Physics JETP **33**, 1053 (1971).

[4] M.I. Dyakonov and V.I. Perel, Soviet Physics JETP **36**, 995 (1973).

[5] M.I. Dyakonov and V.I. Perel, Soviet Physics-JETP **38**, 177 (1974).

[6] M.I. Dyakonov, V.I. Perel, V.L. Berkovits and V.I. Safarov, Soviet Physics - JETP **40**, 950 (1974).

[7] M.I. Dyakonov and V.I. Perel (1984). Theory of Optical Spin Orientation of Electrons and Nuclei in Semiconductors. *Optical Orientation.* F. Meier and B. P. Zakharchenya. Amsterdam, North-Holland: 11.

[8] V.L. Berkovits, A.I. Ekimov and V.I. Safarov, Sov. Phys.-JETP **38**, 169 (1974).

[9] D. Paget, G. Lampel, B. Sapoval and V.I. Safarov, Physical Review B **15**, 5780 (1977).

[10] D. Paget, Physical Review B **24**, 3776 (1981).

[11] D. Paget and B.L. Berkovits (1984). Optical Investigation of Hyperfine Coupling Between Electronic and Nuclear Spins. *Optical Orientation.* F. Meier and B. P. Zakharchenya. Amsterdam, North-Holland. **8:** 173.

[12] V.K. Kalevich, V.L. Korenev and O.M. Fedorova, JETP Letters **52**, 349 (1990).

[13] S.K. Buratto, D.N. Shykind and D.P. Weitekamp, Physical Review B **44**, 9035 (1991).

[14] S.K. Buratto, J.Y. Hwang, N.D. Kurur, D.N. Shykind and D.P. Weitekamp, Bulletin of Magnetic Resonance **15**, 190 (1993).

[15] J.A. Marohn, P.J. Carson, J.Y. Hwang, M.A. Miller, D.N. Shykind and D.P. Weitekamp, Physical Review Letters **75**, 1364 (1995).

[16] A. Abragam, Principles of Nuclear Magnetism, 1st Edition, (International Series of Monographs on Physics(Clarendon Press, Oxford, 1961).

[17] D.P. Weitekamp, Adv. Magn. Reson. **11**, 111 (1983).

[18] S.K. Buratto, D.N. Shykind and D.P. Weitekamp, Journal of Vacuum Science and Technology B **10**, 1740 (1992).

Fig. 1. GaAs band structure. The conduction band is labeled "c." The valence bands are labeled as follows: "hh" is the heavy-hole band, "lh" is the light-hole band, and "sh" is the split-off band.

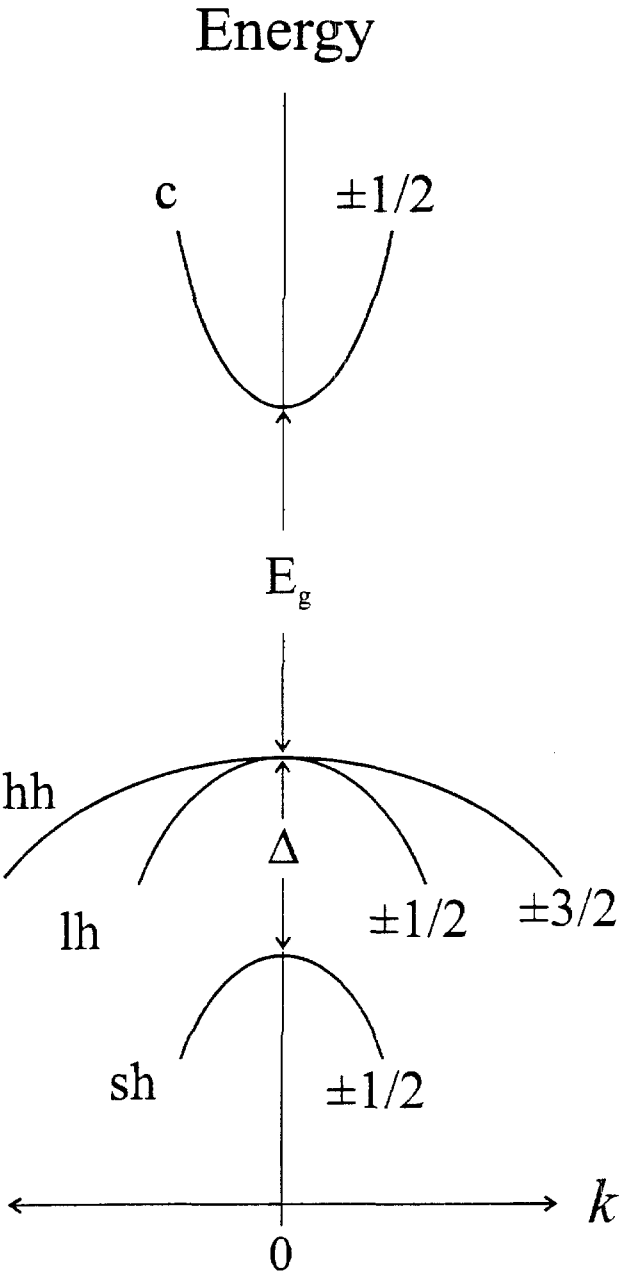

Fig. 2. Selection rules for absorption of circularly polarized light in GaAs. The relative probabilities of the transitions are shown next to each right-handed or left-handed polarization arrow.

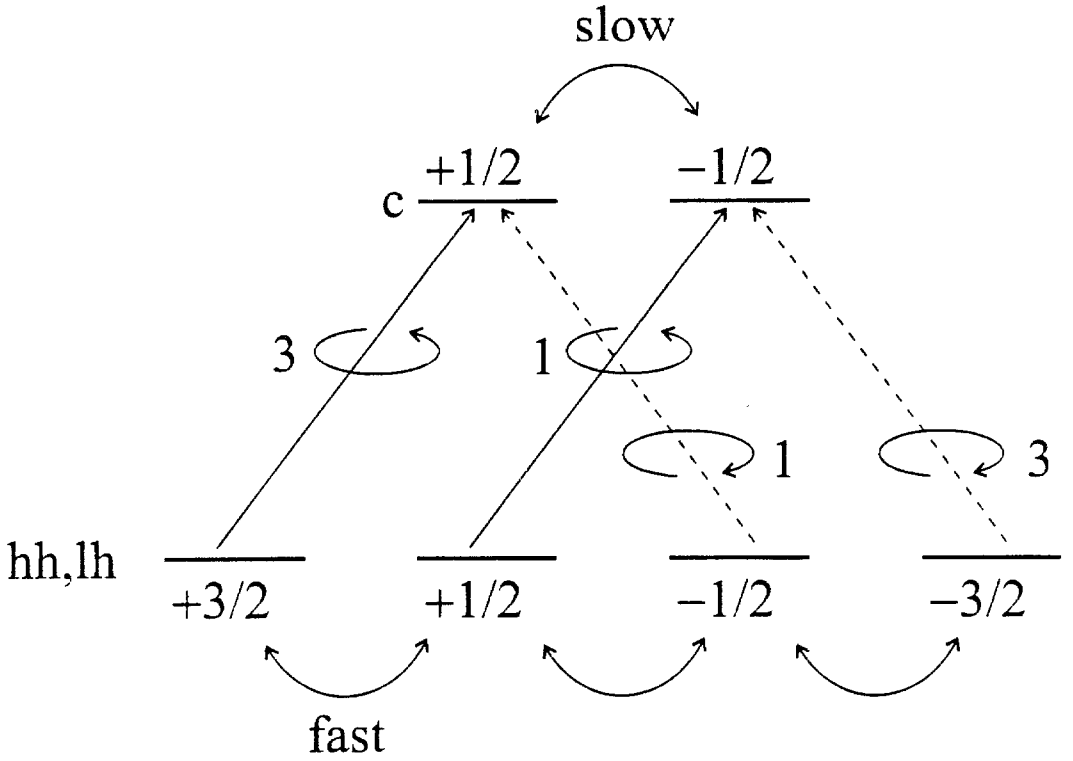

Fig. 3. Time-domain depiction of the Hanle effect. (a) A large electron precession frequency due to a large transverse magnetic field results in a small average electron polarization in the detection direction z, and hence a large depolarization of luminescence. (b) A small electron precession frequency due to a small transverse field results in a large electron polarization and hence a small depolarization of luminescence.

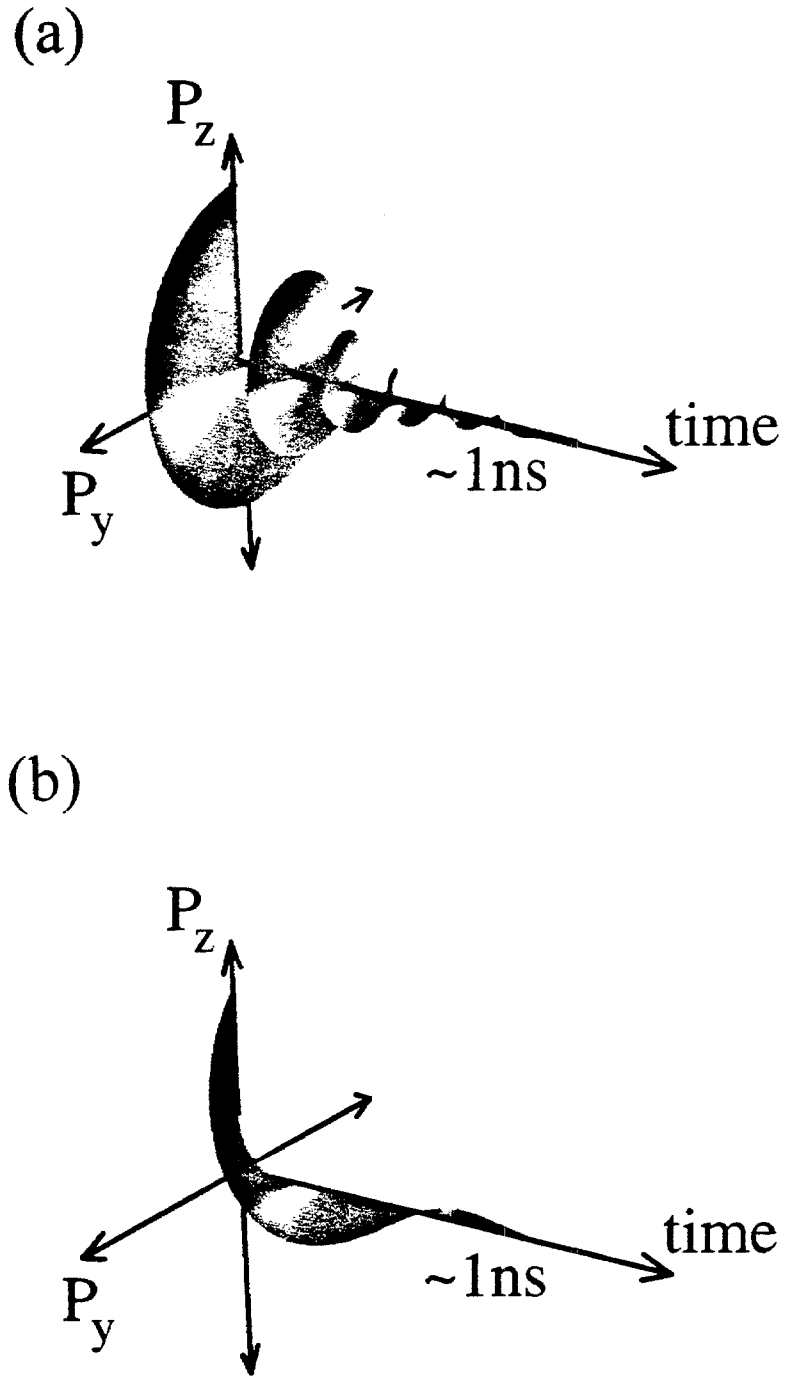

Fig. 4. (a) Hanle depolarization curve without longitudinal magnetic fields. (b) Hanle depolarization curve with longitudinal fields, either applied fields or nuclear hyperfine fields.

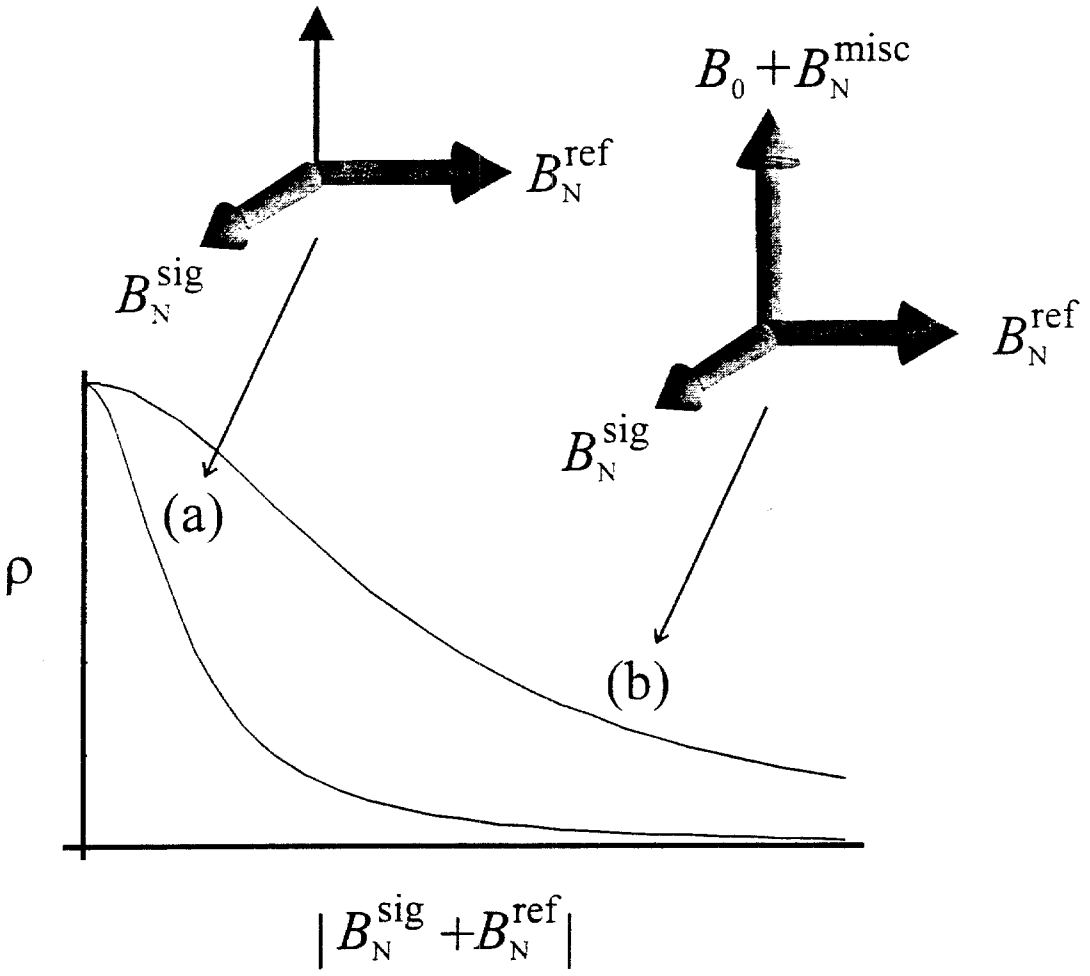

Fig. 5. (a) Schematic depiction of the evolution of the reference and signal nuclear hyperfine fields in the Larmor beat detection method of optical NMR (see text for a description of the vectors). (b) Projection of the transverse component of the vector sum of the two nuclear fields onto a 2D Hanle curve, showing modulation of luminescence at the difference in Larmor frequencies.

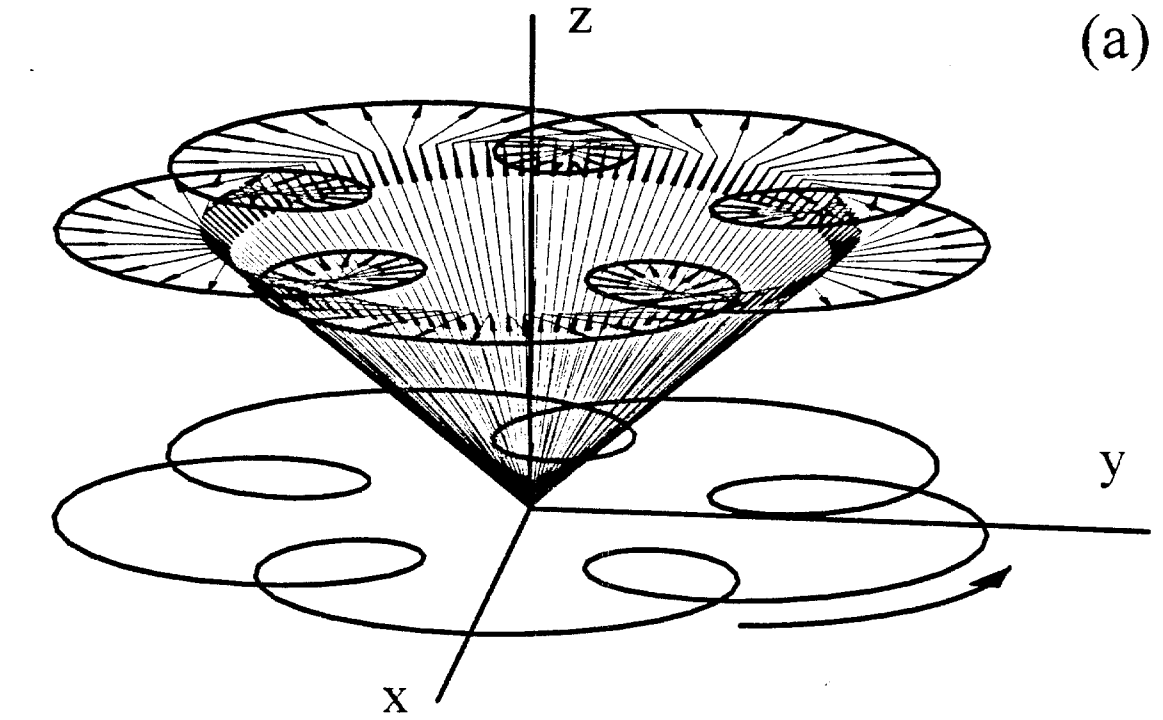

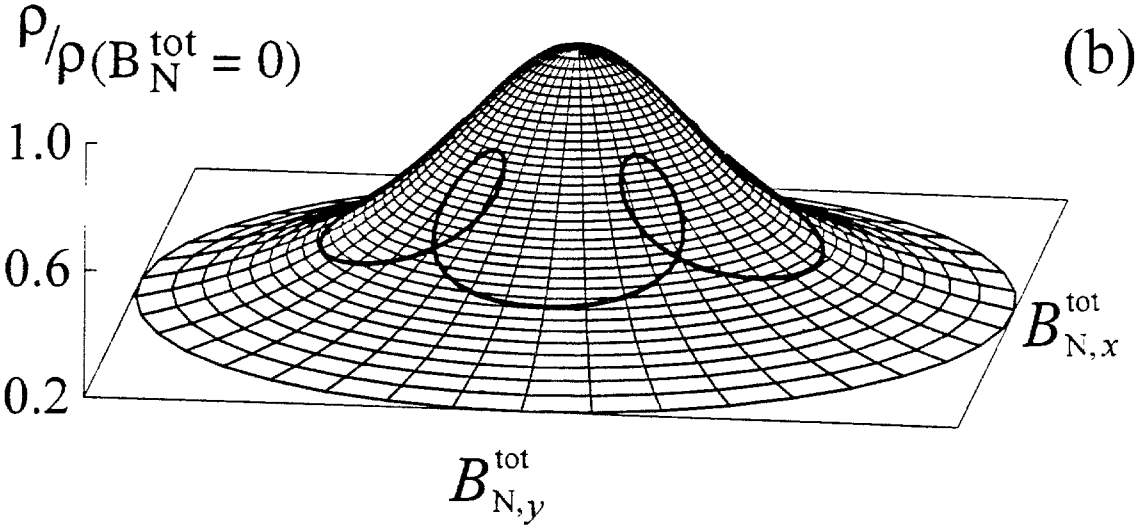

Fig. 6. Sequence of events for real-time detection of NMR using the Larmor beat method.

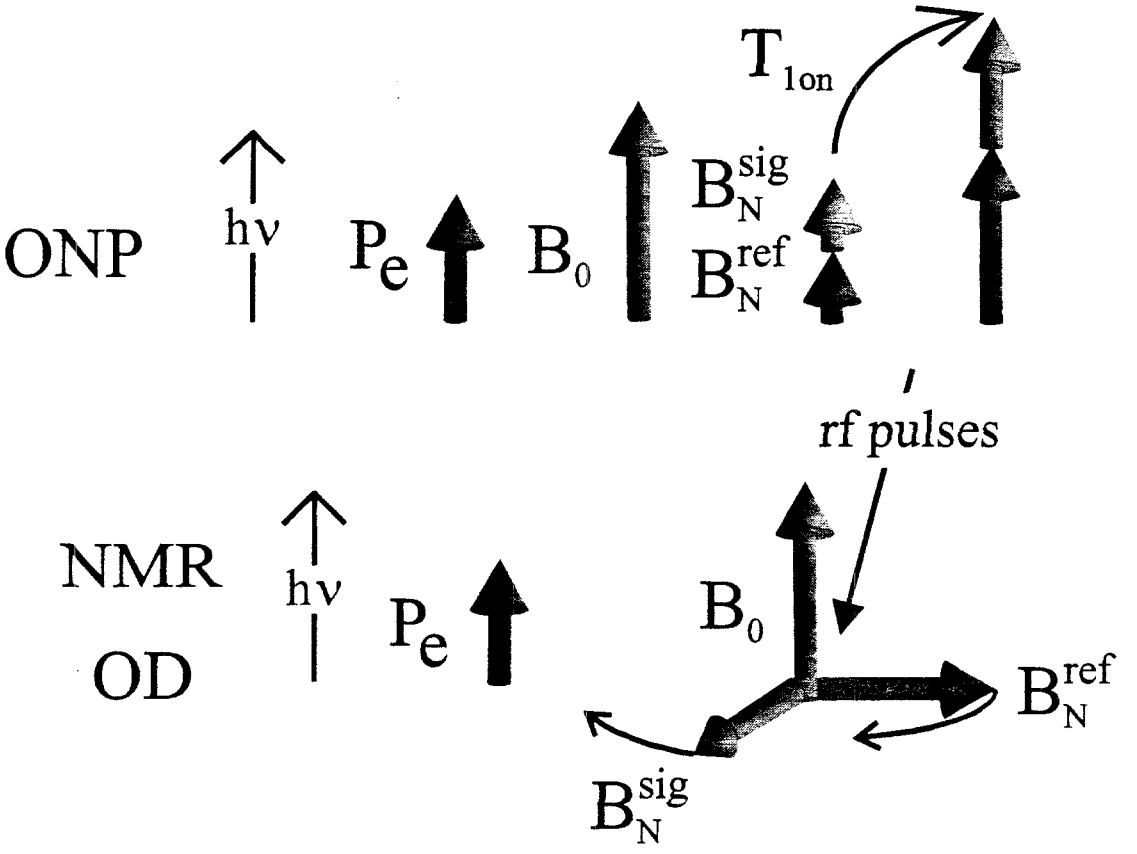

Fig. 7. Sequence of events for pointwise detection of NMR using the Larmor beat method.

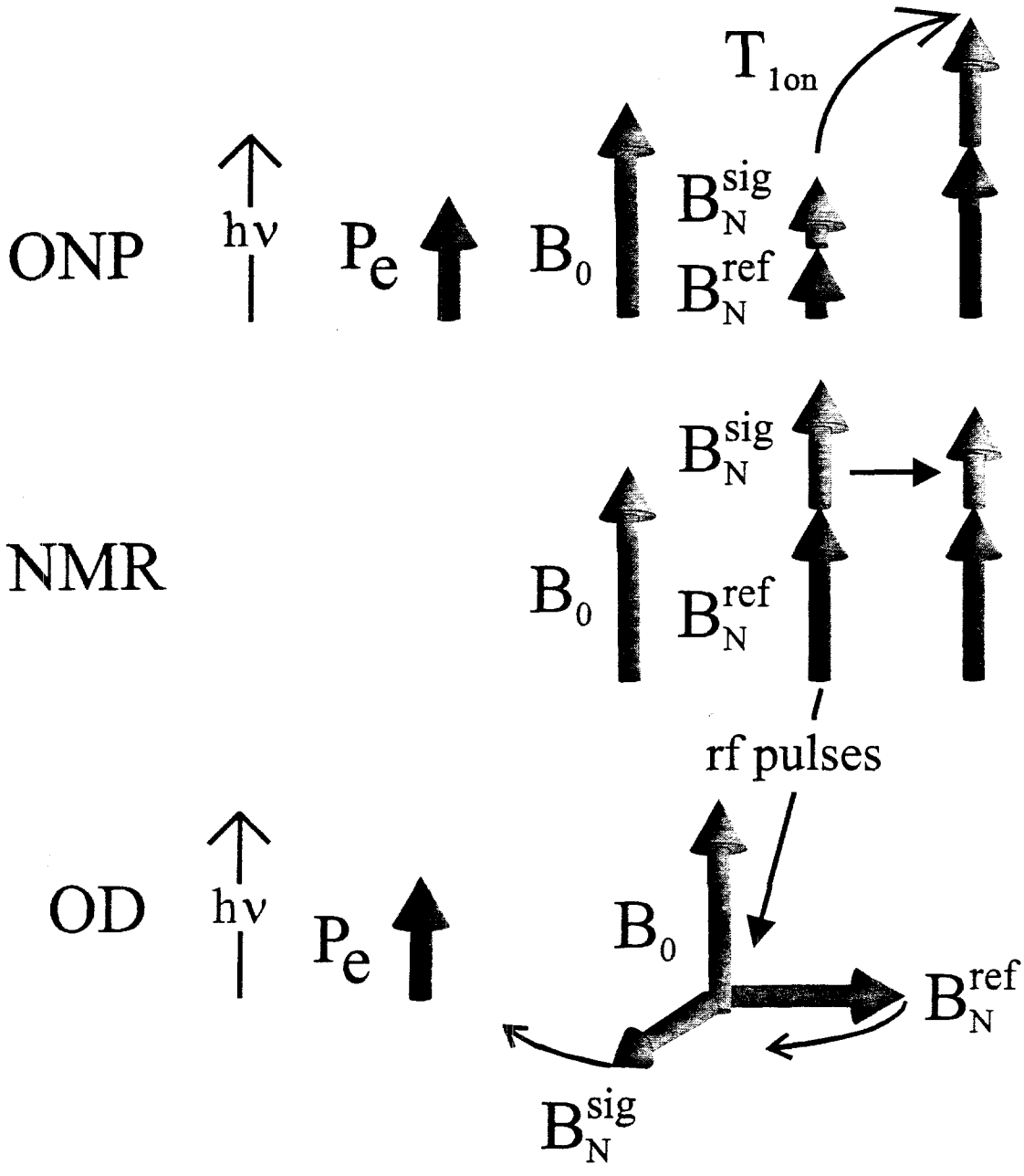

Fig. 8. Optically detected NMR of GaAs. (a) Steady-state optical detection of ^{69}Ga NMR (A. I. Ekimov and V. I. Safarov, 1972). (b) Time-sequenced Fourier-transform optical NMR of ^{71}Ga (S. K. Buratto, D. N. Shykind, and D. P. Weitekamp, 1991). (c) ^{71}Ga NMR spectrum using Larmor beat detection in conjunction with multiple-pulse line narrowing (J. A. Marohn, P. J. Carson, J. Y. Hwang, M. A. Miller, D. N. Shykind, and D. P. Weitekamp, 1995).

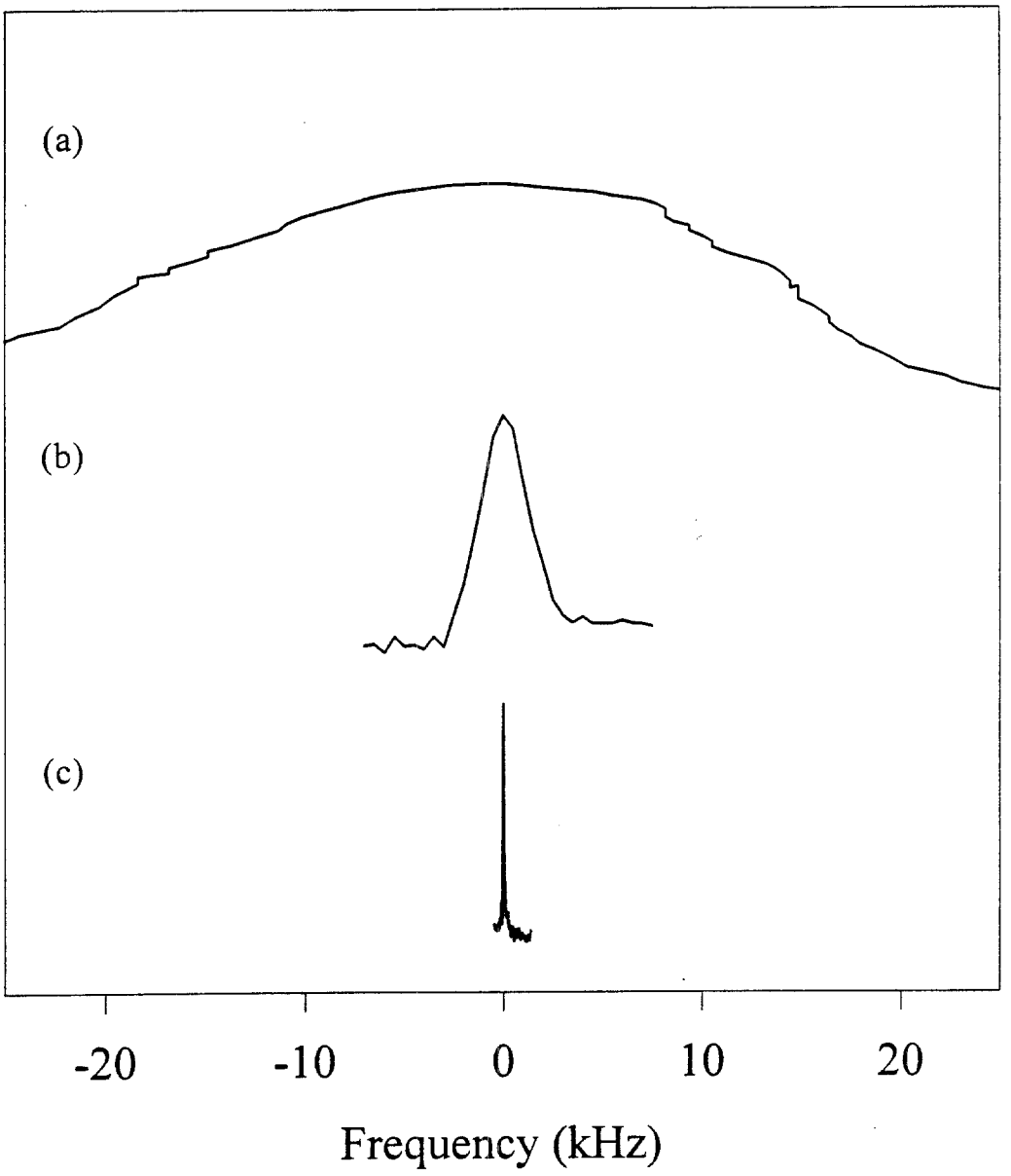

Chapter VII. Optical NMR of III-V Heterostructures Using Larmor Beat Detection

1. Sample and Experimental Methods

Optical Larmor beat detection has been used to study the NMR of a single p-channel GaAs/AlGaAs heterojunction. A diagram of the sample is shown in Fig. 1. The sample was grown on a semi-insulating GaAs substrate along the [001] axis by molecular beam epitaxy. The heterostructure consists of a 6.5 nm layer of undoped $Al_xGa_{1-x}As$ (x = 0.36) on top of a 2500 nm layer of undoped GaAs, followed by a 30 nm layer of p-type $Al_xGa_{1-x}As$ (x = 0.36) doped with $6 \times 10^{17}/cm^3$ of Be, and a 21 nm layer of undoped GaAs.

A schematic diagram of the apparatus used for optical nuclear magnetic resonance is shown in Fig. 2. Experiments were performed in an optical cryostat at a temperature of ~ 2 K by immersion of the sample in liquid helium pumped below the λ point. A static magnetic field of 240 mT was supplied by a superconducting Helmholtz pair. Figure 3 shows the arrange of optics for optical nuclear polarization and subsequent detection of

the circular polarization of luminescence. The sample growth axis was nominally parallel to both the optical detection axis and the static magnetic field axis. The sample was irradiated with ~ 5 mW cw of circularly polarized 780 nm light from a GaAs/AlGaAs diode laser. The irradiation was incident at an angle of 15° relative to the detection axis and covered an area of ~ 1 mm^2. Sample luminescence was detected with a silicon avalanche photodiode in linear mode after passing through a 50 kHz photoelastic modulator (PEM), a linear polarizer, and an 830 nm bandpass filter (FWHM 10 nm) to select the *d* line of *H*-band luminescence.

For steady-state optical NMR experiments, the photocurrent was demodulated by a lock-in amplifier by the PEM frequency before digitization. For Larmor beat experiments, the photocurrent was demodulated by an rf heterodyne spectrometer by the PEM frequency plus the relevant Larmor beat frequency.

2. Detection of Optical NMR Using the Larmor Beat Method

Figure 4 shows the real-time free induction decay of ^{71}Ga in the heterojunction following 5 s of optical nuclear polarization. The transients were obtained with a 3.6μs, 3.152 MHz, $\pi/2$ pulse ^{71}Ga, the signal nucleus. The reference field was provided by ^{75}As, spin locked 54 kHz off resonance with a 0.6 mT, 1.824 MHz rf field. The transients represent 100-scan averages each taken in 10 min total time. The rise time observed on the FIDs is due to filter response.

Pointwise experiments were performed in which both the reference and signal fields were spin locked after a period of NMR evolution of the signal nuclear field. The experiment was repeated, stepping the period of evolution, for each point in the transient.

A timing diagram for a pointwise spin echo experiment on ^{71}Ga is shown in Fig. 5, along with the resulting t_1 transient after integration of the signal in the spin-lock dimension t_2. The transients of a spin-echo experiment before integration in t_2 are shown in Fig. 6.

Figure 7 shows a variety of Larmor beat detected ^{71}Ga spectra along with a steady-state cw spectrum, demonstrating the dramatic improvement in resolution realized with the Larmor beat method. Fig. 7(a) shows the quasi-steady state CW ^{71}Ga optical NMR spectrum (τ_L = 30 s) of the heterostructure, reproducing the result of Ref. [1] on our sample. The signal grows in during optical nuclear polarization with a time constant of 500 s. This steady-state spectrum is featureless even for ^{71}Ga Rabi frequencies small compared to the dipolar local field, while in contrast the Fourier transform (τ_L = 5 s) of the ^{71}Ga FID recorded using Larmor beat detection shows a well-resolved triplet (Fig. 7(b)). Since a spin-echo experiment (Fig. 7(c)) refocuses evolution due to static field inhomogeneity, chemical shifts, and heteronuclear dipolar couplings, the surviving triplet structure is shown to be due to quadrupole coupling. Splittings observed in the ^{69}Ga spectra (not shown) scale with nuclear quadrupole moment, verifying this conclusion. The nutation spectrum (Fig. 7(d)) in which the triplet splitting is half as large also verifies a quadrupole coupling and reveals an ω_1 of 35.1 kHz (where $\omega_1 = \gamma_N^{sig} B_1$ and B_1 is the magnitude of the circular component of the applied rf field). The lack of a peak at 52.6 kHz, where $2\omega_1$ would fold into the nutation spectrum, proves that there are no strongly quadrupole-perturbed sites ($\omega_Q >> \omega_1$) contributing to the spectrum.

The spectra of Fig. 7(b-d) are consistent with a roughly Gaussian distribution of ^{71}Ga quadrupole splittings (mean splitting of -18.6 ± 0.1 kHz and FWHM of 4.6 ± 0.3 kHz) corresponding to an electric field gradient whose principal component along [001] is $V_{zz} = -6.76 \times 10^{18}$ V/m^2 (where the sign is obtained as discussed below). The

quadrupole splitting is seen to change or disappear from run to run and is sensitive to sampling mounting procedures. This evidence is used to conclude that the splittings observed in Fig. 7 are due to sample strain and not to interfacial *E*-fields. The narrow distribution of splittings is inconsistent with electric field gradients due to distorted bonds near the interface or point defects in the bulk.

The dependence of the spin-echo spectrum on preparation-pulse tip angle, θ, measures the spin temperature due to the relatively large contribution in the initial density operator following ONP of a term proportional to I_z^2. Figure 8 shows a series of ^{71}Ga spin-echo spectra with variable pulse tip angles used for spin thermometry. Assuming that the initial spin-state populations are described by a single spin temperature, the satellite ratio measured as a function of pulse angle indicates a spin temperature on the order of 1 mK at a Zeeman splitting of 3.2 MHz, corresponding to nuclear polarizations on the order of 10%. The calculated spin polarization enhancement due to ONP is approximately 2000.

3. *Shot-Noise-Limited Detection*

In experiments where t_1 noise is negligible compared to noise during Larmor beat detection (t_2 noise), calculations show that the dominant source of noise in the experiment is shot noise [2] from the detected luminescence. Two other possible sources of noise during Larmor beat detection are found to be negligible. They are (1) noise from the pre-amplifier of the heterodyne rf spectrometer used to mix down the luminescence signal modulated at the Larmor beat frequency, and (2) thermal Johnson noise in the feedback resistor of the avalanche photodiode (at room temperature).

Shot noise in this experiment has two contributing sources: the photon counting statistics (Poisson statistics) associated with optical detection, and the current counting statistics (also Poisson) associated with the dark current in the avalanche photodiode. The optical shot noise current is given by

$$I_{\text{n,optical}} = \left[2qP_{\text{o}}R^{\text{o}}M^2FB_{\text{c}}\right]^{1/2} \tag{1}$$

where q is the electronic charge, P_{o} is the optical power, R^{o} is the unity gain responsivity of the photodiode, M is the avalanche gain, F is the excess noise factor intrinsic to the avalanche process, and B_{c} is the bandwidth cutoff frequency. The unity gain responsivity is given by

$$R^{\text{o}} = \frac{\eta q}{h\nu} \tag{2}$$

where η is the quantum efficiency of the photodiode, and $h\nu$ is the photon energy. For these experiments, $\eta = 0.77$, $M = 124$, and $F = 4.43$. In a typical experiment, the total luminescence power detected (P_{o}) is 1.5 nW (6×10^9 photons/sec for λ = 830nm). The resulting optical shot noise density is

$$\tilde{I}_{\text{n,optical}} = 2.9 \text{ pA}/\sqrt{\text{Hz}} \tag{3}$$

where

$$\tilde{I}_{\text{n}} = I_{\text{n}}/\sqrt{2B_{\text{c}}}\ . \tag{4}$$

The shot noise associated with the dark current of the avalanche photodiode is given by

$$I_{\text{n,dark}} = \left[2q\left(I_{\text{ds}} + I_{\text{db}}M^2F\right)B_{\text{c}}\right]^{1/2} \tag{5}$$

where I_{ds} is the dark surface current and I_{db}, the dark bulk current. For these experiments the dark current shot noise density is

$$\tilde{I}_{\text{n,dark}} = 0.8 \text{ pA}/\sqrt{\text{Hz}} = (\text{NEP})R^0M\ , \tag{6}$$

where the second equation relates it to noise equivalent power (NEP).

The total shot noise density $\tilde{I}_{n,shot}$ is the rms sum of the optical and dark current shot noise contributions:

$$\tilde{I}_{n,shot} = \left(\tilde{I}^2_{n,optical} + \tilde{I}^2_{n,dark}\right)^{1/2} = 3.0 \text{ pA}/\sqrt{\text{Hz}} \tag{7}$$

The measured noise during Larmor beat detection (i.e., during t_2) is found to be

$$\tilde{I}_{n,measured} = 3.3 \text{ pA}/\sqrt{\text{Hz}} \tag{8}$$

which is within 10% of the calculated shot noise. The sensitivity is thus said to be shot noise limited. Another point of reference is that the resulting SNR is within a factor of 2 of a hypothetical ultrafast photon counter with the same quantum efficiency. This indicates that the sources (e.g., laser fluctuations at the Larmor beat frequency) are no more than 50% of the shot noise density (accounting for rms summation of the two noise densities).

4. References

[1] G.P. Flinn, R.T. Harley, M.J. Snelling, A.C. Tropper and T.M. Kerr, Semiconductor Science and Technology **5**, 533 (1990).

[2] S.M. Sze, Physics of Semiconductor Devices, 2nd Edition, (John Wiley and Sons, NY, 1981).

Fig. 1. Schematic diagram of the GaAs/AlGaAs heterojunction structure.

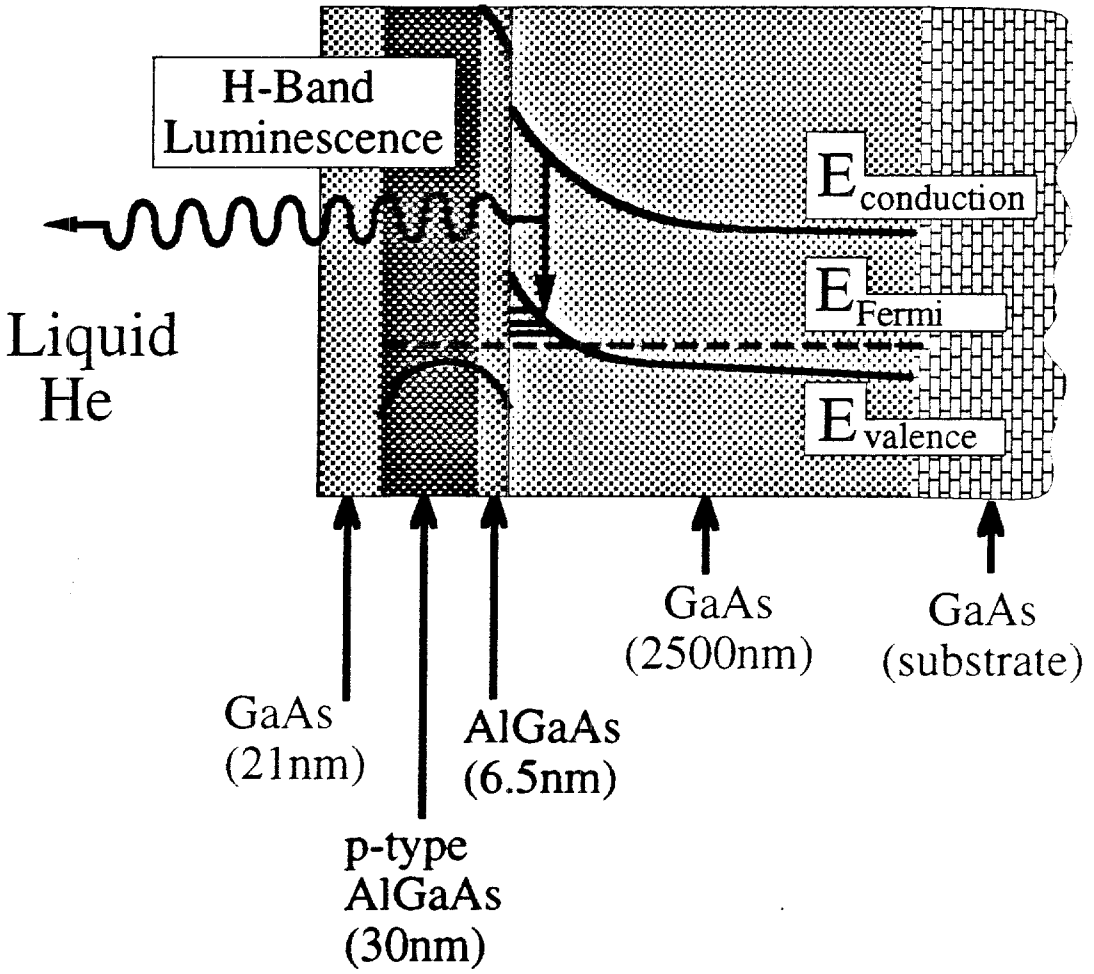

Fig. 2. Schematic diagram of the optical nuclear magnetic resonance apparatus.

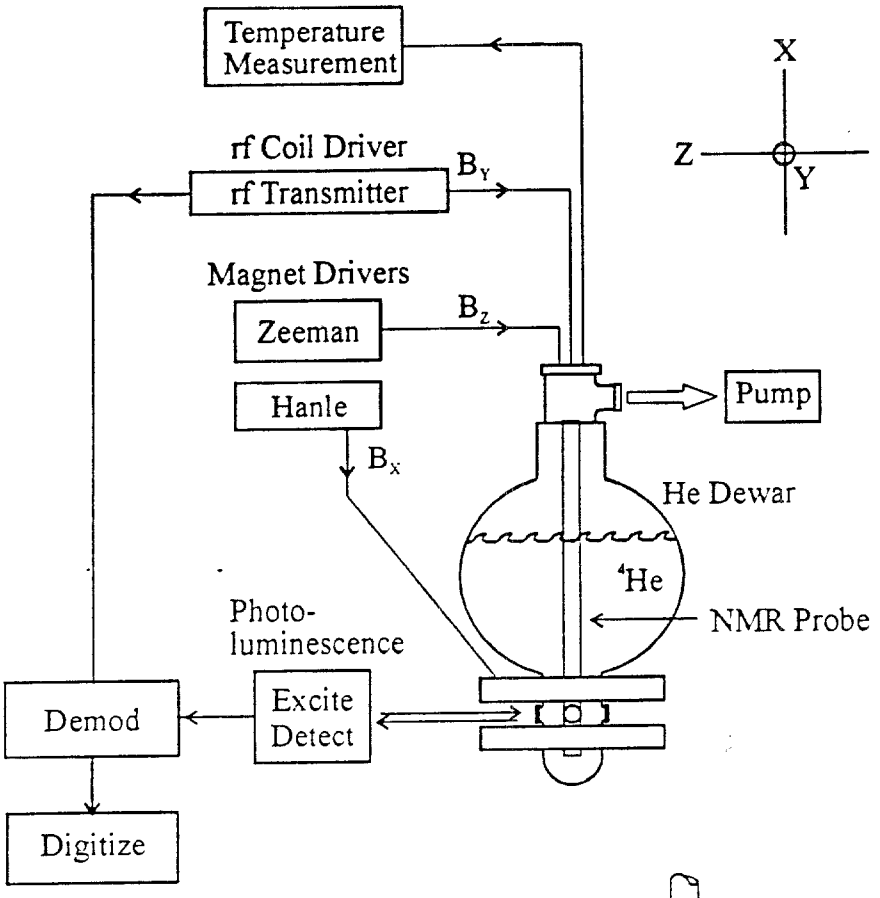

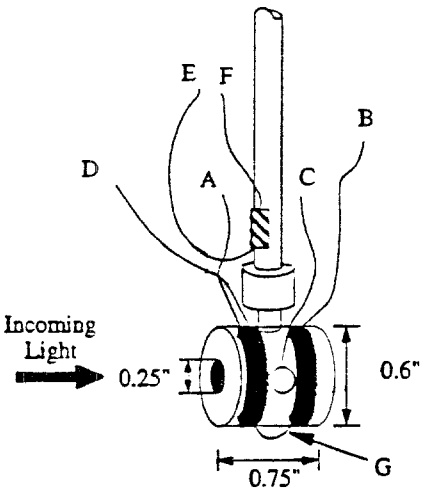

Fig. 3. Optics for optical pumping and detection of circular polarization of luminescence.

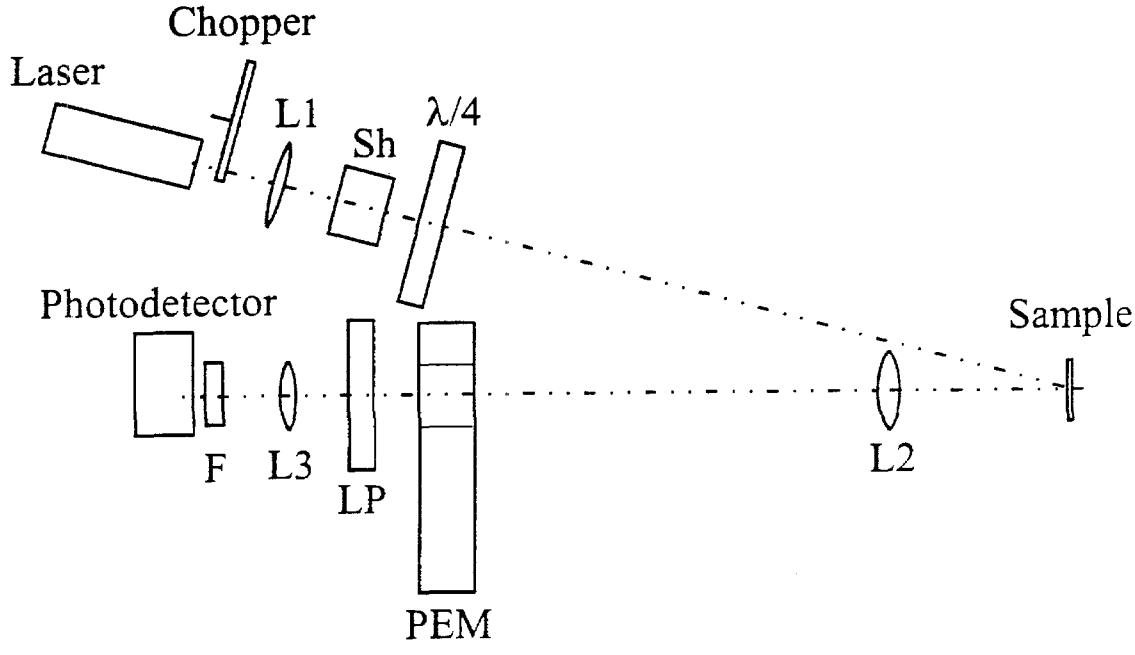

Fig. 4. Real-time optical detection of the ^{71}Ga free induction decay in the heterojunction for two different carrier offset frequencies.

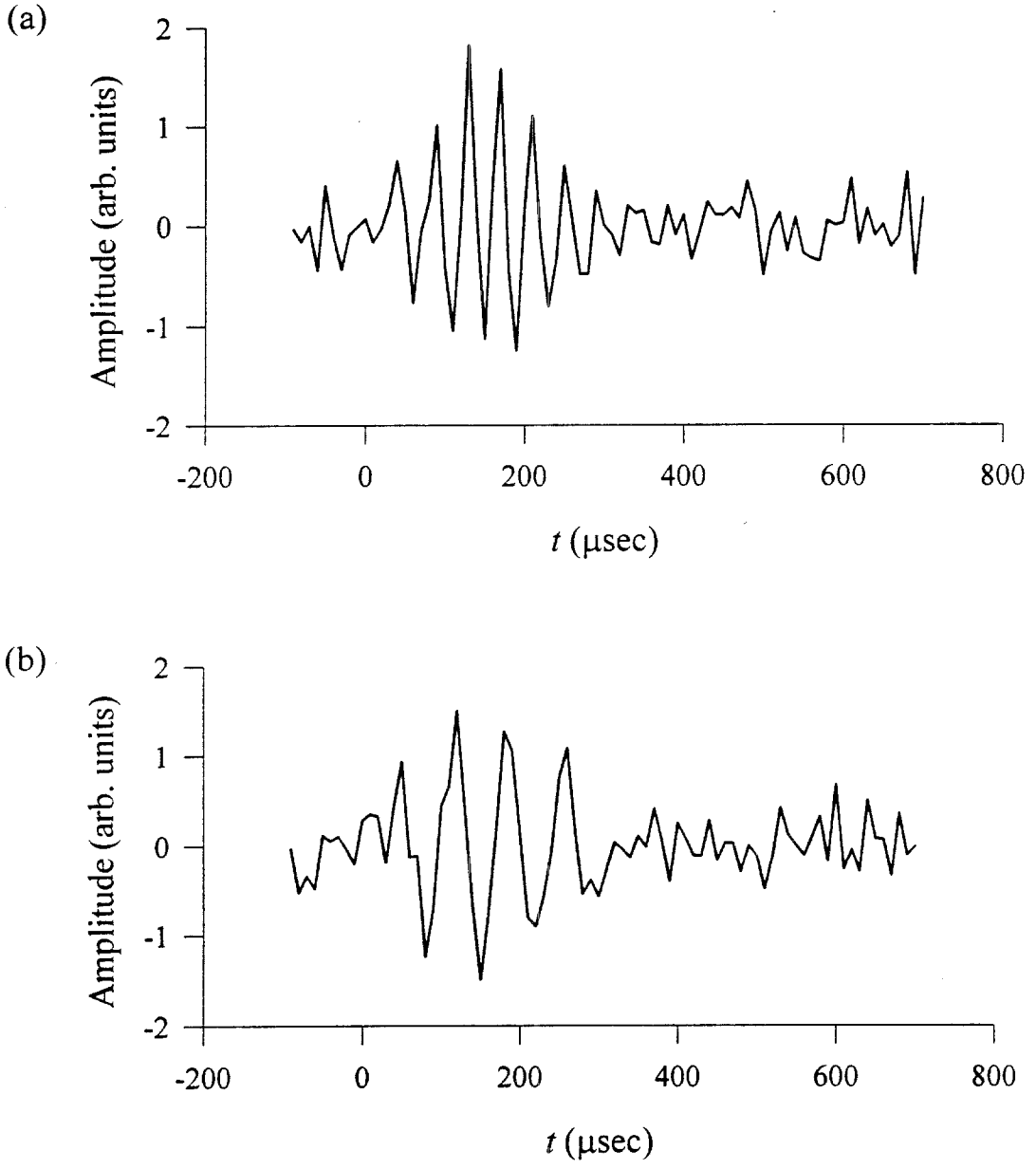

Fig. 5. Timing diagram for a pointwise spin echo experiment on ^{71}Ga. The spin echo transient is shown below.

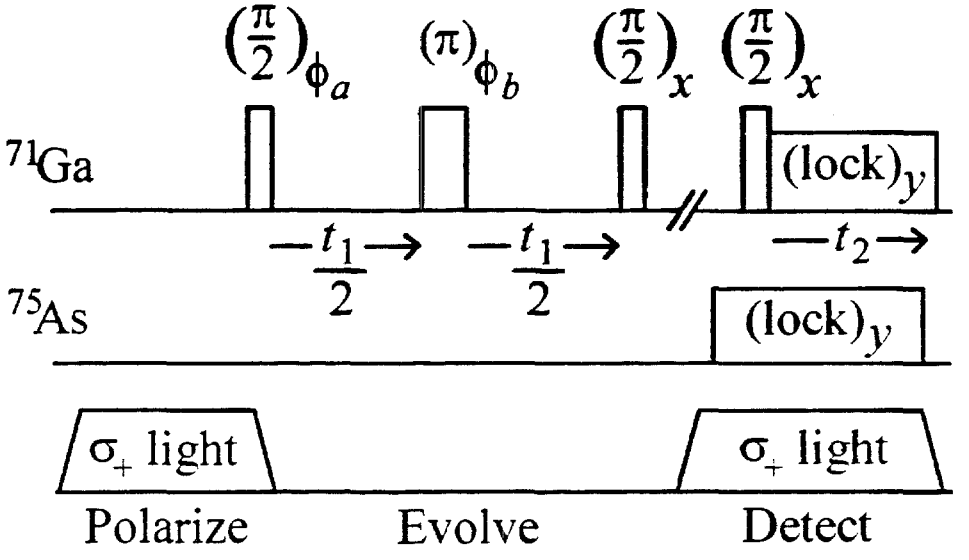

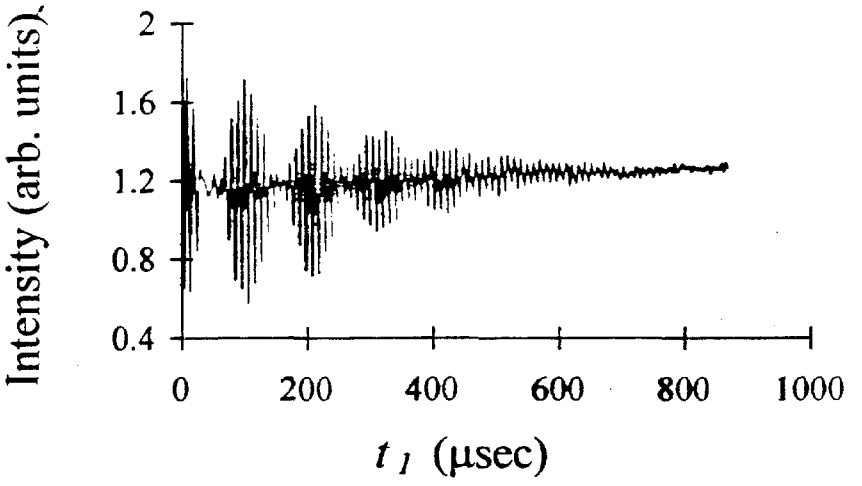

Fig. 6. Pointwise spin-echo transients before integration and Fourier transformation.

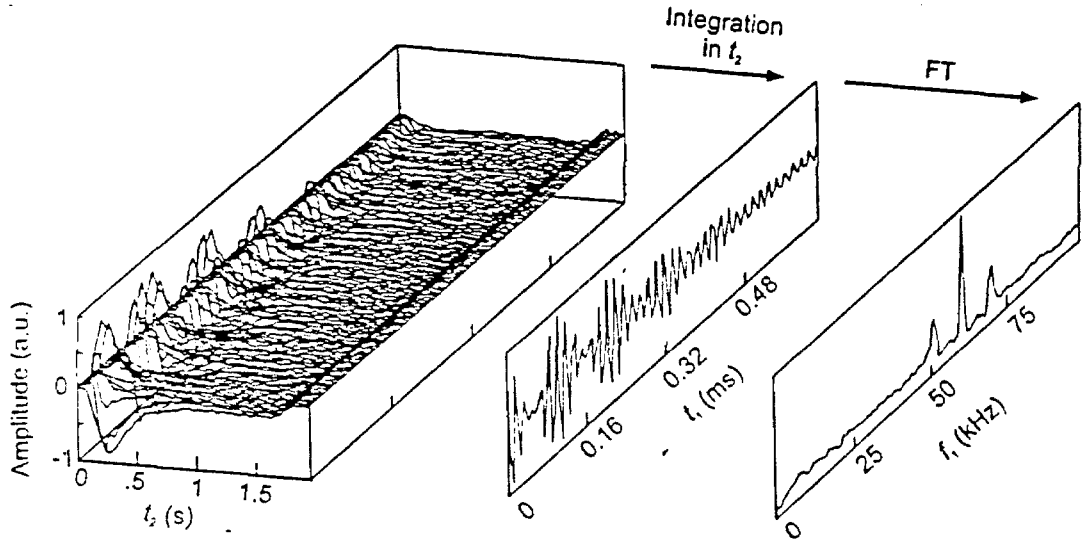

Fig. 7. Optical NMR spectra of the heterostructure. (a) Steady-state CW ^{71}Ga optical NMR spectrum. (b) Fourier transform of ^{71}Ga free induction decay in t_1, following a $\theta = \pi/2$ pulse, recorded by Larmor beat detection in t_2. (c) Spin echo spectrum. (d) Nutation spectrum. Each spectrum (b)-(d) results from a t_2 transient at each t_1 point, with the entire set of transients taken in 30 minutes.

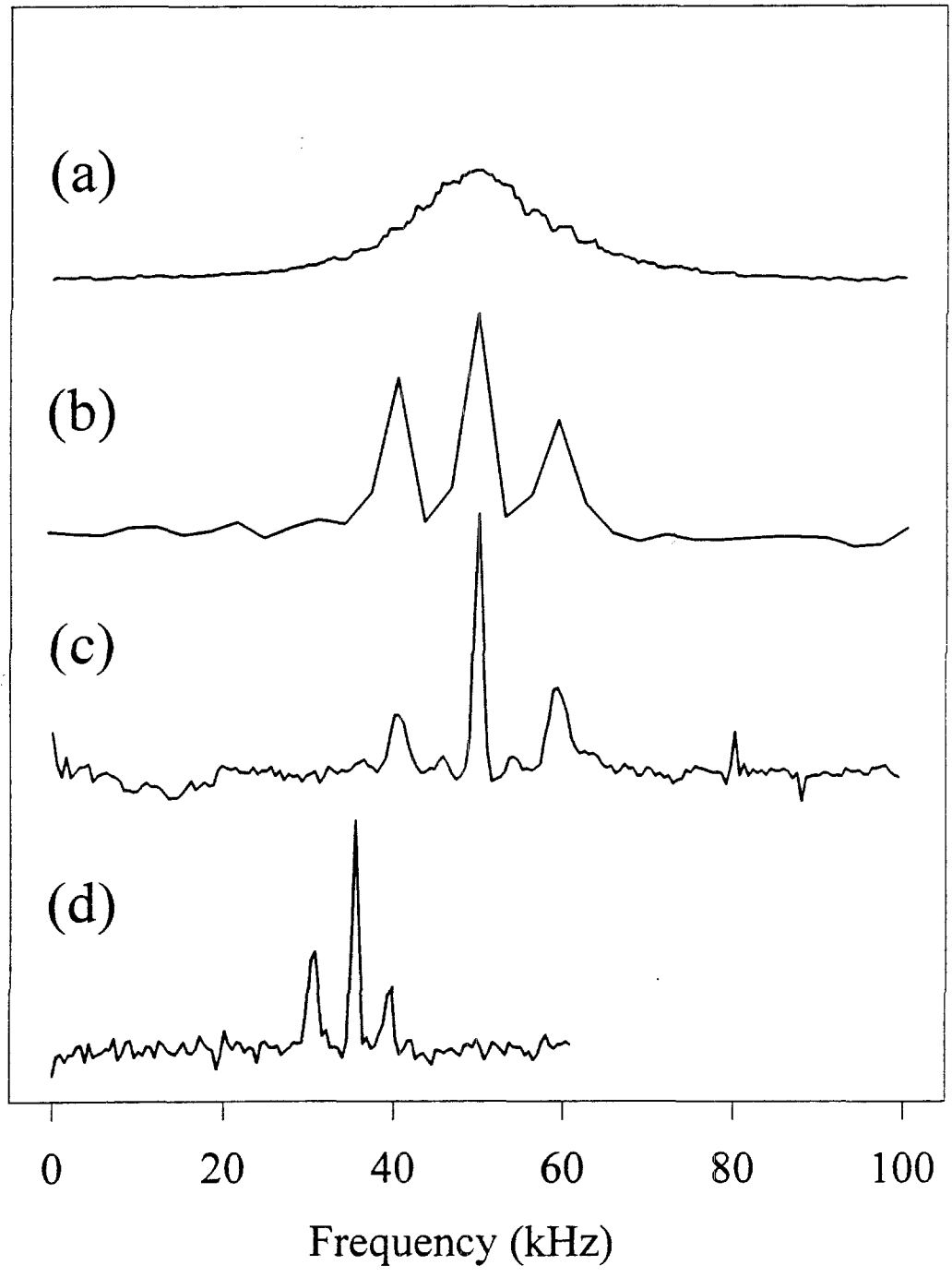

Fig. 8. Spin-echo spectra of ^{71}Ga in the heterojunction used for spin thermometry.